Influence of Ion Solvation on Charge Storage Behavior of MXene in Aqueous Electrolytes

Important note
To cite this publication, please use the final published version (if applicable).
Please check the document version above.

Influence of Ion Solvation on Charge Storage Behavior of MXene in Aqueous Electrolytes
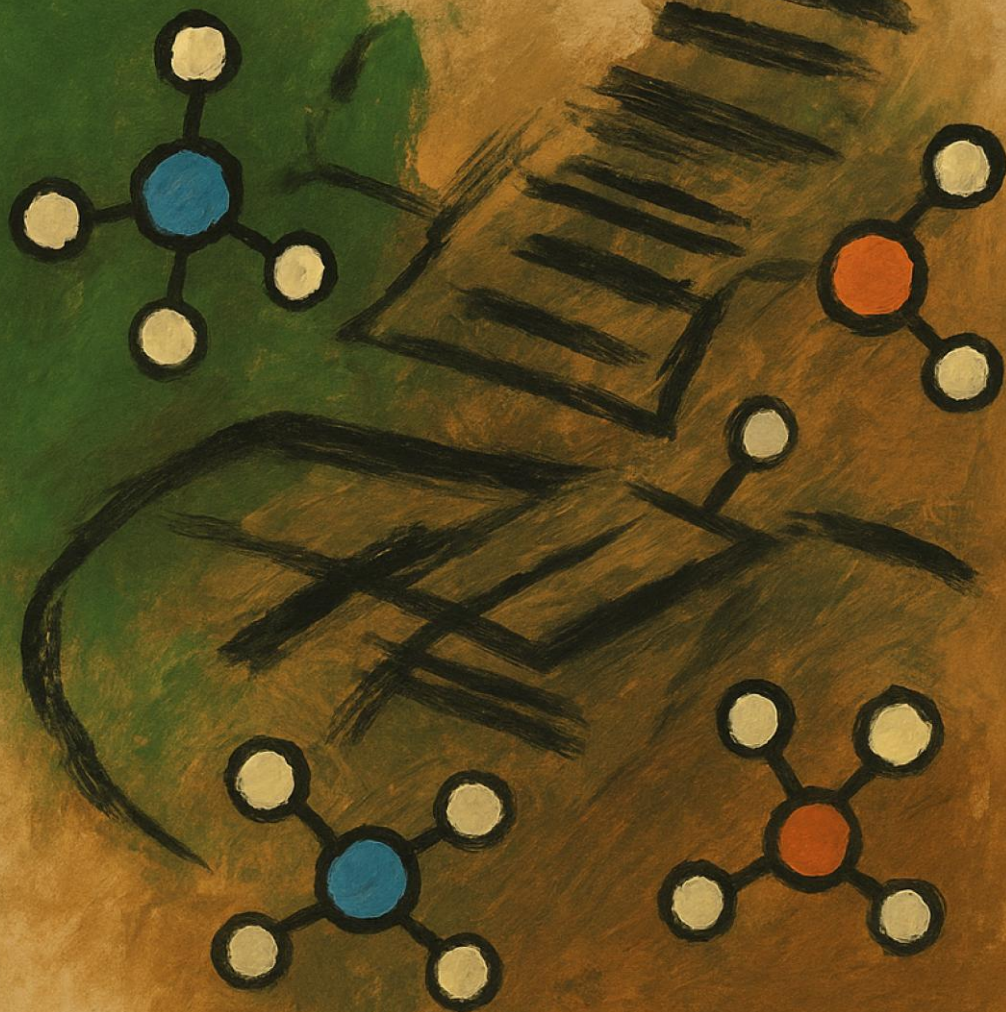
Chaofan CHEN

Influence of Ion Solvation on Charge Storage Behavior of MXene in Aqueous Electrolytes

Dissertation

for the purpose of obtaining the degree of doctor

at Delft University of Technology

by the authority of the Rector Magnificus, Prof.dr.ir. T.H.J.J. van der Hagen

chair of the Board for Doctorates

to be defended publicly on

Thursday 08 January 2025 at 12:30 o'clock

by

Chaofan CHEN

Master of Science in Physics

Jilin University, China

Born in Henan, China

This dissertation has been approved by the promotors.

Composition of the doctoral committee:

Rector Magnificus	Chairperson
Prof. dr. ir. M. Wagemaker	Delft University of Technology, promotor
Dr. X. Wang	Delft University of Technology, copromotor

Independent members:

Prof. dr. F. M. Mulder	Delft University of Technology, the Netherlands
Dr. drs. ir. L. J. Bannenberg	Delft University of Technology, the Netherlands
Prof. dr. Y. Gogotsi	Drexel University, the United States
Dr. Y. Gao	Jilin University, China
Dr. rer. nat. S. Fleishmann	Karlsruhe Institute of Technology, Germany
Prof. dr. E. H. Brück	Delft University of Technology (reserve member)

Cover designed by Chaofan. Artwork generated with ChatGPT-5.1. Inspired by the album Summer/Fever by Sodagreen,

An electronic version of this dissertation is available at https://repository.tudelft.nl

Contents

1 Introduction

1.1 Overview of electrochemical energy storage devices

As global energy sources shift toward renewable energy such as solar and wind, which generate electricity intermittently based on environmental conditions, there is a growing need for efficient energy storage devices to buffer fluctuations and maintain a stable balance between energy supply and demand. Electrochemical energy storage (EES) systems convert electrical energy into chemical energy and release it on demand, enabling reliable power supply. These systems are essential not only for integrating renewable energy into the grid but also for powering portable electronics and electric vehicles[1,2]. The two primary categories of EES devices are secondary batteries and capacitors. Batteries, particularly lithium-ion batteries (LIBs), are widely used due to their high energy density (up to 300 Wh kg^{-1}), a key requirement for mobile and transport-related applications where space and weight are constrained. However, they often suffer from limited charge/discharge rates (a few minutes) and finite cycle life (a few thousand cycles). In contrast, capacitors offer high power density (~ 10 kW kg^{-1}) and excellent cycling stability ($\sim 10^6$ cycles), but their energy density (~ 5 Wh kg^{-1}) is relatively low. Pseudocapacitors are expected to bridge the gap between batteries and conventional capacitors. They combine higher energy density (~ 10 Wh kg^{-1}) than capacitors with greater rate capability (a few seconds) and longer cycle life ($\sim 10\ 000$ cycles) than batteries, making them effective in complementing batteries and, in some cases, replacing them in various energy storage applications such as uninterruptible power supplies.

1.2 Charge storage characteristics of batteries, capacitors and pseudocapacitors

The electrochemical performance of EES devices is fundamentally governed by their charge storage mechanisms. In commercial LIBs, charge storage mainly occurs through the intercalation of ions into the electrode. As a result, the rate performance is limited by slow ion diffusion process in the bulk structure. Meanwhile, the electrode may undergo solid-solution reactions or phase transitions. These structural changes often induce substantial volume expansion or contraction during cycling, potentially compromising the mechanical integrity of the electrode and negatively impacting its long-term cycling stability[3]. These underlying mechanisms are reflected in electrochemical features, which are characterized by well-defined redox peaks in cyclic voltammograms (CV) and distinct voltage plateaus in galvanostatic charge-discharge (GCD) profiles (**Figure 1.1 c & f**). In battery systems, electrochemical performance is commonly quantified by the capacity (C or mAh), which represents the amount of charge stored[4].

In contrast, electric double-layer capacitors (EDLCs) store charge through rapid physical adsorption/desorption of ions at the electrode/electrolyte interface, without involving any

redox reaction or phase transition[5]. The performance of EDLC is highly dependent on the accessible surface area of the electrode. Porous materials with large specific surface area, such as activated carbons, are commonly used in EDLCs to maximize charge storage[6,7]. Unlike batteries, performance of EDLC is evaluated using specific capacitance (F), which is potential-independent and reflects a constant charge storage per unit voltage. Generally, EDLCs exhibit nearly rectangular CVs and triangular GCD curves (**Figure 1.1 a & d**).

Pseudocapacitors store charge through surface redox reactions at the surface or near surface region (surface redox pseudocapacitance) or through fast ion intercalation into the electrodes without phase transition (intercalation pseudocapacitance)[5,8,9]. This mechanism allows pseudocapacitive materials to provide higher capacitance than EDLCs, while maintaining fast kinetics. Among pseudocapacitive materials, ruthenium dioxide (RuO2) and niobium pentoxide (Nb2O5) are widely studied as typical surface redox-type and intercalation-type materials, respectively[10,11]. RuO2 exhibits outstanding performance owing to rapid, reversible surface redox reactions, particularly in acidic electrolytes. It is commonly used in thin-film form to maximize surface area and enhance charge transfer. However, its high cost and toxicity hinder large-scale applications. In contrast, Nb2O5 stores charge through the fast intercalation of small cations (e.g., Li^+, Na^+) into its crystalline structure. Despite its favorable structural properties, Nb_2O_5 suffers from intrinsically low electronic conductivity, which often necessitates nanostructuring or introducing conductive additives to improve the performance[12].

Typically, pseudocapacitive materials show broad and symmetric redox peaks in CV curves and quasi-linear GCD curves[8]. These electrochemical signatures distinguish pseudocapacitive process from purely capacitive or battery-type processes and are critical for interpreting the charge storage mechanism of electrode materials. For many emerging materials, especially for those that exhibit characteristics between conventional batteries and capacitors, it's important to determine whether charge storage is dominated by surface-controlled process or limited by ion diffusion. A common way is analyzing CV data using the power-law relationship between peak current (i) and scan rate (v)[13], expressed as:

$$i(V) = av^b$$

Here, a and b are adjustable parameters, and the exponent b provides insight into the underlying mechanism. A b value close to 1 reflects capacitive-controlled nature, where the current response scales linearly with scan rates due to fast surface redox reactions or double-layer charging. In contrast, a b value near 0.5 indicates that diffusion through the bulk material is the rate-limiting factor, typical of battery-type EES device.
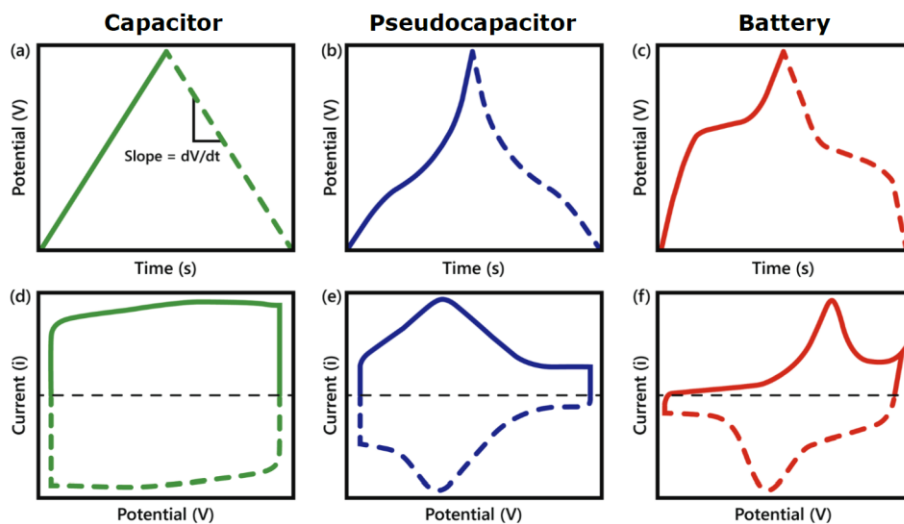
Figure 1.1 Electrochemical signatures of (a, d) capacitors, (b, e) pseudocapacitors and (c, f) batteries, shown by schematic GCD (a–c) and CV (d–f) profiles[4].

To obtain a more quantitative breakdown of current contributions, a more detailed method is often used to separate the capacitive and diffusion-limited components. This approach, commonly referred to as Dunn's method[14], assumes that the total current at a given potential (V) is the sum of two terms:

$$i(V) = k_1 v + k_2 v^{1/2}$$

In this expression, $k_1 v$ represents the capacitive current contribution, and $k_2 v^{1/2}$ accounts for the diffusion-controlled current at a given potential. This analysis is especially valuable for materials like pseudocapacitive electrodes, where both processes may contribute simultaneously.

Electrochemical impedance spectroscopy (EIS) provides valuable insight into charge storage kinetics by analyzing the current response to a small sinusoidal voltage (5-10 mV) over a wide frequency range. A typical Nyquist plot features a high-frequency semicircle, which reflects the charge transfer resistance (R_{ct}), and a low-frequency region associated with ion diffusion or capacitive storage[15,16]. If the low-frequency portion appears as a vertical line, it indicates ideal capacitive behavior. A 45-degree slope, on the other hand, is characteristic of the Warburg impedance, which arises from diffusion-limited ion transport. Fitting these curves to an equivalent circuit model yields parameters such as R_{ct}, double-layer capacitance

(C_{dl}), or the Warburg component, offering unique information about the dominant rate-limiting steps in the system.

1.3 Two-dimensional MXenes: structure, synthesis, and electronic properties

Two-dimensional (2D) materials have emerged as promising candidates for pseudocapacitive energy storage due to their rich surface redox activity and open structure for ion diffusion[17]. Among these, MXenes, a family of early transition metal carbides/nitrides, stand out due to their unique combination of high electrical conductivity, redox-active surface, and open interlayer with good ion accessibility[18,19]. The general chemical formula of MXenes is $M_{n+1}X_nT_x$, where M stands for the transition metal, X is C and/or N, and T_x represents the surface functional groups (e.g., -F, -Cl, -OH, and =O)[20]. Since the first MXene $Ti_3C_2T_x$ was discovered in 2011, more than 40 MXenes have been synthesized experimentally[21,22]. Their unique physicochemical properties have positioned MXenes promising candidates in diverse application fields, including energy storage, electromagnetic interference shielding, catalysis, sensors, and optoelectronic devices[12-14].

1.3.1 Structure and composition of MXenes

Generally, MXenes are derived from their parent materials, MAX phases, which are layered ternary compounds (**Figure 1.3 a**) with the general formula of $M_{n+1}AX_n$ (n=1, 2, 3, 4), where A is typically an element from groups IIIA or IVA (e.g., Al, Si) in the periodic table (**Figure 1.2**). These compounds adopt a close-packed hexagonal structure with a space group symmetry of $P6_3/mmc$[23]. In MAX structure, the X-site atoms (typically carbon and/or nitrogen) reside in the interstitial positions formed by the surrounding transition metal atoms, forming edge-sharing M_6X octahedra, while A atoms are interleaved between the $M_{n+1}X_n$ slabs. The metallic M-A bond in MAX phases is generally weaker than the stronger ionic/covalent M-X interaction, which allows selective removal of A layer while preserving the $M_{n+1}X_n$ framework[26]. Upon the transformation from MAX to MXenes, the transition metal atoms undergo a noticeable increase in valence state, whereas the carbon atoms remain chemically unaffected[27].

MXenes can be classified into three different categories based on the distribution of transition metal atoms in their lattice: single-M element, M-site solid solutions, and ordered double-M elements (**Figure 1.2**)[18,22,28] Solid solution MXenes are characterized by random distribution of two or more transition metals within the M layers. This category includes both double-metal solid solutions, such as $(Ti_{1-y}Nb_y)_2CT_x$ and $(V_{1-y}Cr_y)_3C_2T_x$, and high-entropy MXenes, which contain four or more transition metals, like $TiVNbMoC_3T_x$[29]. In contrast, ordered MXenes display a periodic arrangement of different metal atoms, either out-of-plane (o-

MXenes) or in-plane (i-MXenes). In o-MXenes, distinct transition metals occupy alternating atomic layers, typically with one metal (e.g., Ti) in the inner layers and another (e.g., Mo or Cr) at the outer surfaces. These structures are generally limited to $M_3X_2T_x$ and $M_4X_3T_x$. In-plane ordering features alternating metal atoms within the same atomic layer, as seen in i-MXenes, like $(Mo_{2/3}Y_{1/3})_2CT_x$. Because ordered arrangements are thermodynamically driven, only certain element pairings are capable of forming stable ordered phases. In addition to variation at the M site, compositional diversity at the X site can be achieved by partially or fully substituting carbon with nitrogen, leading to the formation of carbonitride or nitride MXenes. Compared to their carbide counterparts, nitride MXenes often exhibit enhanced electrical conductivity[30]. MXene structures are also characterized by surface terminations (T_x), which form spontaneously during the etching process and strongly influence their physicochemical properties. These terminations, including -F, -OH, and =O, typically bond to the outermost transition metal atoms on both sides of the MXene sheet. The type and distribution of terminations are influenced by the synthesis conditions and significantly affect the electronic, optical, and chemical properties of MXenes.
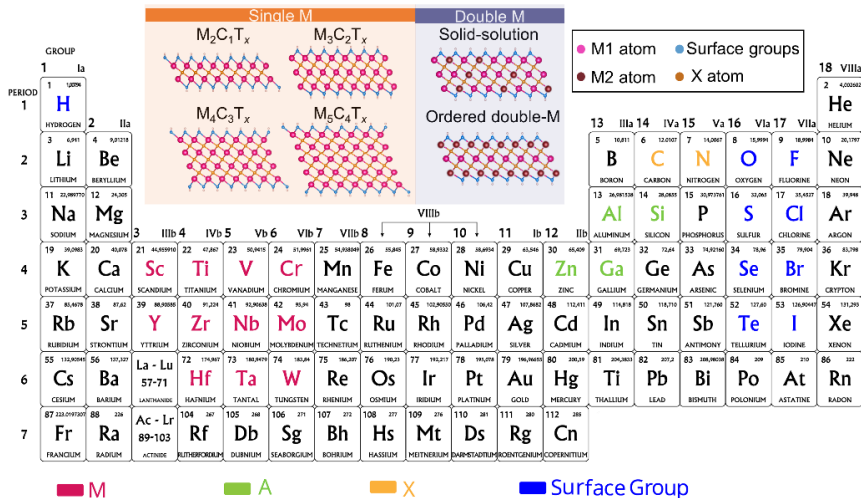
Figure 1.2 Periodic table showing the composition of MXenes. Color code in the periodic table: red (transition metal), yellow (X element), blue (surface groups), and green (A element in MAX phases). Schematics show the general structure of different types of MXenes.

1.3.2 Synthesis methods of MXenes

MXenes can be synthesized through both top-down and bottom-up approaches. The top-down methods are generally classified into two main categories: solution-based etching and molten salt etching. These synthesis approaches involve two main steps: first, chemical

exfoliation of the parent MAX phase to obtain multilayered MXene, and second, delamination to produce single-layered or few-layered nanosheets.

1.3.2.1 Solution-based synthesis of MXene

Solution-based etching methods employing fluorine-containing etchants remained the most established approach for synthesizing MXenes. Hydrofluoric acid (HF) is the earliest and most widely used etchant, typically applied in concentrations ranging from 10% to 50%[31]. The etching process generally proceeds under ambient or mildly elevated temperatures, with reaction time and temperature carefully controlled to optimize the yield and preserve MXenes' structural integrity. During the etching process, the A-site metal (Al) is oxidized by protons, while fluoride ions coordinate with the resulting metal cations to form soluble AlF_3. Concurrently, surface terminations are introduced through reactions with HF and water, yielding surface groups such as -F, -OH. Taking the synthesis of $Ti_3C_2T_x$ MXene as an example, the reactions between the Ti_3AlC_2 MAX phase and HF can be described as[21]:

$Ti_3AlC_2 + 3\ HF \rightarrow AlF_3 + 3/2\ H_2 + Ti_3C_2$

$Ti_3C_2 + 2\ H_2O \rightarrow Ti_3C_2(OH)_2 + H_2$

$Ti_3C_2 + 2\ HF \rightarrow Ti_3C_2F_2 + H_2$
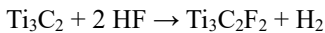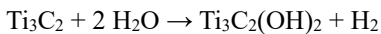
The etching process typically initiates at the particle edges, adsorption of proton and fluorine ions at the reaction front and their diffusion facilitates the progressive removal of aluminum atoms from the central regions of the particle, enabling complete exfoliation. The reaction is accompanied by the generation of hydrogen gas, which opens the layer gallery, producing the characteristic accordion-like morphology of multilayered MXenes (**Figure 1.3 b**)[32]. A similar approach, involving the mixture of HF with hydrochloric acid (HCl), has also been explored to reduce the concentration of HF while maintaining the etching efficiency[33].
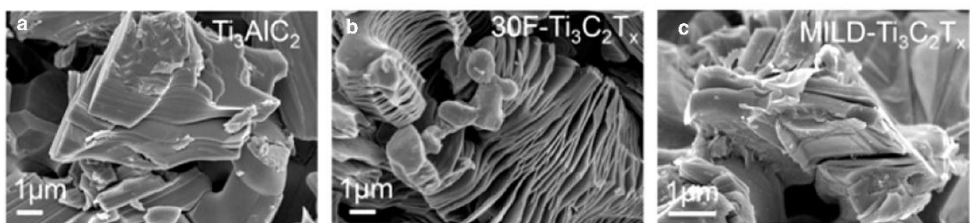
Figure 1.3 Morphology of (a) Ti_3AlC_2, (b) 30% HF-etched $Ti_3C_2T_x$ MXenes and (c) LiF/HCl etched $Ti_3C_2T_x$ MXenes[31].

Despite its effectiveness, hydrofluoric acid poses significant safety risks due to its highly corrosive and hazardous nature[34]. To minimize the direct handling of concentrated HF, one widely adopted approach involves the use of mild etchants that combine fluoride salts (LiF, NaF, NH₄F, etc.) with hydrochloric acid (HCl) to generate HF in situ. The presence of Li^+ and Cl^- ions influences the etching kinetic. Cl^-, due to its large ionic radius, is proposed to contribute to interlayer spacing expansion and stabilization of intermediates within the etching environment, meanwhile, Li^+ ions intercalated in between the layers, further expanding the interlayer spacing and promoting subsequent delamination[35]. MXenes synthesized via the LiF/HCl route exhibited larger lateral flake sizes, reduced surface roughness, and fewer structural defects than those produced using concentrated HF (**Figure 1.3 c**)[20,36]. The resulting open and uniform morphology enhances ion accessibility and transport, which are critical for electrochemical performance. Furthermore, LiF/HCl etched $Ti_3C_2T_x$ exhibited a higher proportion of oxygen-containing terminations (e.g., =O and -OH) and a lower fraction of fluorine terminations relative to HF-etched samples[37]. Noteworthy, while MAX phases are commercially produced at the kilogram scale, MXene synthesis, has been demonstrated at the tens of grams scale (for example, 50 g per batch) with good reproducibility. Moreover, industrial-scale production remains limited by batch-based processing, hazardous etchants, and the need for precise reaction control.

In recent years, several alternative solution-based etching strategies have been developed to synthesize MXenes while avoiding the introduction of fluoride-based surface terminations, which are often chemically inert and can limit certain applications. Among these methods, alkali etching, halogen etching and electrochemical exfoliation have emerged as promising fluoride-free approaches, each offering distinct surface chemistry.

Alkali etching typically employs alkaline solutions such as sodium hydroxide (NaOH) to selectively remove the A-site element from MAX phases. For instance, treatment of Ti_3AlC_2 in NaOH solution under hydrothermal condition can produce $Ti_3C_2T_x$ with surface groups primarily composed of -OH and =O[38]. However, due to sluggish reaction kinetics, an elevated temperature and concentrated alkaline solution are needed.

Halogen etching has emerged as another solution-based alternative to traditional fluorine-based methods for MXene synthesis, offering a -F-free and potentially safer approach for removing the A-layer from MAX phases. This method involves the use of molecular halogens (such as bromine and iodine) or interhalogen compounds (such as ICl and IBr) in organic solvents[28]. The etching mechanism involves direct oxidation of the A layer and the formation of volatile metal halides, which can be removed without destroying the MXene structure[29]. The resulting MXenes retain a compact multilayer morphology, distinct from the accordion-like structures typically formed via HF etching. Additionally, the nature of the termination

groups introduced by halogen etching, primarily -Br or -I groups, exhibit increased chemical uniformity.

Electrochemical etching presents a versatile and -F-free approach for synthesizing MXenes by selectively removing the A-site element through anodic oxidation. This process is generally carried out by applying a controlled anodic potential to MAX working electrode in acidic or basic electrolytes[41,42]. The etching progress can be effectively tracked using current-time profiles. Typically, a pronounced initial current corresponds to the active dissolution of aluminum, followed by a plateau phase associated with MXene formation[43]. As the reaction proceeds, the current gradually declines, reflecting the consumption of accessible aluminum. Compared to traditional chemical etching methods, MXenes produced by electrochemical etching tend to exhibit smooth surfaces, fewer structural defects, and larger flake size[44]. Moreover, the electrolyte composition, applied voltage, and temperature can be adjusted to optimize the reaction kinetics and tailor the resulting surface terminations.

To fully exploit the potential of MXenes, a subsequent delamination step is typically employed to obtain single-layered or few-layered flakes with significantly increased accessible surface area. This process is generally achieved by intercalating cations or organic molecules between the MXene layers to expand the interlayer spacing and weaken interlayer van der Waals interactions[31,45]. Further mechanical treatment, such as shaking or sonication, may also be applied to facilitate the physical separation of the layers into individual flakes. The choice of intercalants depends on the etching route and the specific MXene composition, as each intercalant exhibits distinct interactions with the MXene surface. Commonly used species include metal cations (e.g., Li^+), polar solvents such as dimethyl sulfoxide (DMSO), and bulky organic ions like tetrabutylammonium (TBA^+)[46]. In summary, different solution-based etching strategies not only determine the yield and flake sizes but also affect the surface chemistry and morphology of MXenes.

1.3.2.2 Molten salt etching

Lewis acid molten salt etching offers a -F-free and scalable strategy for synthesizing MXenes[47]. In this method, molten metal halide salts act as both reactants and solvents, operating at elevated temperatures (typically 550-750 $^\circ$C)[48]. During etching, the A-site element was selectively extracted from MAX phases through redox reaction or replacement mechanism[49]. For instance, when the $ZnCl_2$ is used as the molten salt etchant, the reaction initiated by replacing Al by Zn to form Ti_3ZnC_2., which further reacted with excess $ZnCl_2$ and yield $Ti_3C_2Cl_2$ [50]. The selection of molten salt is guided by the redox potential of the transition metal cation of Lewis acid salt (strong oxidizer) relative to that of the A-site atom[49]. This principle can also be applied for etching Si, Ga, and Zn-based MAX besides conventional Al-based precursor. A key advantage of this approach lies in the possibility of

post-synthetic substitution of surface terminations due to relatively weak binding energy of halogen terminations[51]. They can be partially or fully replaced by groups such as -NH$_2$, -OH, or -S through hydrothermal or chemical vapor treatments, enabling the tunability of surface charge and electronic structure[52]. Another strength of this approach is the concurrent reduction of metal cations from the etchant. During etching with copper or iron chloride, metallic copper or iron can form and embed within the MXene structure as nanoparticles. These metal particles can directly serve as active sites for catalysis or be further converted into compounds[53,54]. This capability enables the possibility of multifunctional MXene-based hybrid materials through facile synthesis protocol.

However, MXenes derived from molten salt method, particularly those terminated with -Cl or -Br, present significant delamination challenges. Unlike HF-etched MXenes, which are typically hydrophilic and dispersible in aqueous solvents, halogen-terminated MXenes exhibit strong interlayer van der Waals interactions and hydrophobic surfaces, which hinder water intercalation during synthesis and subsequent exfoliation. These characteristics result in poor dispersibility in polar solvents and necessitate harsh delamination conditions. For instance, extended sonication is required when using TBAOH as intercalant for delaminating MXenes produced by molten salt method, and a brittle film was obtained after filtrating the few-layer MXene solution[55]. Recent work has demonstrated that Li$^+$ preintercalated multilayer -Cl terminated MXenes undergo swollen when dispersed in polar aprotic solvents (NMF)[34]. The high dielectric constant of the NMF solvent is necessary for facilitating cation solvation and reducing interlayer cohesion. Following by subsequent sonication assisted delamination, few-layered Ti$_3$C$_2$Cl$_2$ suspensions can be obtained. However, all these processes were conducted under strictly anhydrous conditions. These results underline the importance of optimizing the delamination strategies for molten salt etched MXenes.

1.3.2.3 Bottom-up synthesis of MXene by chemical vapor deposition

Bottom-up synthesis offers a direct and scalable approach to fabricate MXenes by assembling molecular precursors into 2D carbides or nitrides. Unlike top-down etched MXenes, which are often terminated with a mixture of -F, -OH, and =O groups, bottom-up method allows better control over surface termination. Chemical vapor deposition (CVD) has been employed to produce Ti$_2$CCl$_2$ by reacting titanium halide (TiCl$_4$) and methane (CH$_4$) carbon source on Ti surface at elevated temperatures (950 $^\circ$C)[56]. Interestingly, at the first stage, the carpet-like Ti$_2$CCl$_2$ MXene sheets are grown perpendicular to the Ti substrate. As the thickness of TiCCl$_2$ increases, a flower-like morphology is formed, possibly caused by the negative surface tension. Moreover, replacing the methane with nitrogen gas enables the successful synthesis of phase-pure Ti$_2$NCl$_2$ which are challenged to produce from solution-based etching. The resulting MXene films synthesized via CVD generally exhibit excellent

crystallinity, minimal structural defects with controlled thickness[56]. A major concern of CVD for MXene synthesis is its requirement for high temperatures, which can impose thermodynamic constraints and limit substrate compatibility.

1.3.3 Electronic properties of MXenes

The electronic conductivity of MXenes is highly tunable and depends on their composition and surface chemistry. In unfunctionalized Ti_3C_2 monolayer, the electronic density of states (DOS) at the Fermi level is dominated by Ti 3d orbitals hybridized with C 2p states[57,58]. As a result, Ti-based MXenes typically feature metallic behavior, attributed to the high DOS near the Fermi level. Mo-containing MXenes like $Mo_2TiC_2T_x$, on the other hand, exhibit narrower d bands and reduced DOS, which may lead to semiconducting character[59]. Surface groups can further modulate the band structure by hybridizing the d orbitals with their p orbital states, reshaping the energy distribution near the Fermi level[60]. DFT studies have shown that electronegative surface terminations can significantly shift the Fermi level, with -OH terminated MXenes typically exhibiting lower work functions in the range of 1.6 to 2.8 eV [61]. Substituting carbon with nitrogen in the X-site also affects the electronic structure, leading to increased DOS near the Fermi level due to the hybridization of Ti 3d, N 2p, and C 2p orbitals[57].

In addition to intrinsic band structure, extrinsic factors such as intercalated species and flake stacking also play a role in determining overall conductivity, especially in film form. While individual flakes maintain high in-plane conductivity, the inter-flake electron transport is often hindered by the presence of intercalated species such as water molecules or bulky ions like tetrabutylammonium (TBA^+)[59]. These intercalants increase the spacing between MXene layers and introduce insulating barriers that limit electronic percolation across the stacked structure. Consequently, MXene films fabricated via solution-based processing may display semiconducting or resistive behavior, even when the intrinsic properties of the flakes are metallic. To mitigate this, post-treatment strategy has been employed to eliminate residual intercalants and improve electronic conductivity[59,62].

1.3.4 Chemical stability of MXenes

The chemical stability of MXenes remains a major concern as they are prone to oxidation and hydrolysis under ambient and aqueous conditions[63]. Water molecules can intercalate or absorb between MXene layers and coordinate with surface Ti atoms. This interaction facilitates the hydrolysis of Ti-C bonds, particularly at undercoordinated or defective sites, thereby exposing titanium to dissolved oxygen[64]. The degradation of $Ti_3C_2T_x$ results in the formation of TiO_2 nanoparticles and amorphous carbon layer[65]. These chemical

transformations are accompanied by distinct morphological changes, including pinhole formation, agglomeration on the edges, and structural collapse[65].

To mitigate such degradation, several stabilization strategies have been developed. The most widely approach is to store the MXene dispersions under argon and at low temperatures to suppress the oxidative degradation. At -20 °C, $Ti_3C_2T_x$ stored under inert conditions retains its layered structure, surface terminations, and electrical conductivity for over 700 days, with minimal signs of oxidation or structural degradation[66]. Additionally, reducing the amount of free water by replacing water with less reactive solvents such as isopropanol or introducing high concentrated salt to coordinate water molecules can significantly slow the hydrolysis during storage[67,68]. Since the degradation usually initiates at the edges and defects, another effective approach is to improve the quality of the MAX precursor by incorporating excess aluminum during synthesis, which yields larger and more ordered MXene flakes with fewer reactive defects[33]. Moreover, encapsulating MXenes with organic molecules or reducing agents, and constructing composite heterostructures can provide physical barriers against water and oxygen, therefore show great promise in eliminating the degradation process[69–71]. Noteworthy, the physical state of the MXene also impacts its chemical stability. MXenes in film form tend to be more resistant to oxidation compared to colloidal dispersions due to the reduced exposure to water molecules and oxygen in compact films[72]. Noteworthy, the chemical stability of MXenes, such as their resistance to oxidation in ambient or aqueous environments, directly influences their electrochemical stability, as structural or surface degradation under open-circuit conditions can be further accelerated under applied anodic potentials[89].

1.4 Charge storage mechanism of MXene in different electrolyte systems

MXenes typically exhibit capacitive or pseudocapacitive charge storage behavior, driven by surface ion adsorption and intercalation into the interlayer spacing. Their performance is determined by factors such as chemical composition, surface functional groups, and interlayer spacing. In addition to these intrinsic properties, the electrolyte plays a crucial role in modulating charge storage. By influencing ion solvation and intercalation, electrolytes directly affect how ions interact with surface terminations and access the interlayer space, thereby shaping both the capacitance and rate capability of MXene-based EES systems.

1.4.1 Pseudocapacitive behavior of MXene in organic electrolytes

Organic electrolytes offer key advantages for MXene-based energy storage, particularly their ability to support extended voltage windows (2.5 V). In these electrolytes, charge storage in MXenes is predominantly governed by surface-controlled redox reactions, often coupled with ion intercalation. The first experimental report on Li-ion storage in MXenes

demonstrated that HF-etched multilayer Ti_2CT_x delivered a reversible capacity of 225 mAh g^{-1} in carbonate-based electrolytes. The sloping charge-discharge profile, as well as the broad reversible redox peaks in CV, together suggested a pseudocapacitive process[73] (**Figure 1.4 a & b**). The charge storage mechanism was confirmed by the reversible shift of Ti K-edge XANES spectra upon charge/discharge[27]. Moreover, a shrinkage of Ti_2CT_x d-spacing by 0.4 Å was observed at charged state, which suggested the ion intercalation. Similar pseudocapacitive behavior has also been reported when using Ti_2CT_x for Na^+ ion storage[74]. However, Na^+ intercalation involves an initial activation step with a large interlayer expansion from 7.7 Å to 10.1 Å, followed by reversible cycling with minimal spacing change, distinguishing its intercalation mechanism from that of Li^+.

Surface groups play a critical role in determining the ion storage behavior. Systematic DFT studies performed on M_2C-type MXenes (M = Ti, V, Nb, Mo) revealed that =O terminated MXenes exhibit the most favorable thermodynamics for Li adsorption, enabling multilayer Li accommodation[75]. In contrast, -F terminations allowed only monolayer adsorption due to weaker binding and increased repulsive interactions at higher coverages. Such findings have motivated studies on surface engineering to optimize electrochemical performance. For instance, Lewis acid molten salt etching method has been used to produce -F-free MXene. When evaluated in 1 M LiPF$_6$/EC-DMC electrolyte, -Cl terminated Ti_3C_2 delivered a high specific capacity of 205 mAh g^{-1}, corresponding to approximately 0.4 electrons transferred per Ti atom, with minimal structural change[49]. In particular, introducing redox active -Br terminations has been shown to provide additional faradaic contributions, further boosting capacity beyond the intrinsic performance of -F/-OH terminated counterparts[76]. The electrochemical performance of MXenes is also strongly influenced by interlayer spacing, which governs both ion accessibility and transport dynamics[77,78]. For example, Sn^{4+} pillaring expanded the Ti_2CT_x interlayer from 11.5 Å to 12.7 Å, resulting in a significant increase in capacity and rate performance, owing to reduced steric hindrance and facilitated Li^+ diffusion within the expanded galleries[79]. Post-treatment on -F/-OH terminated MXene with Lewis basic salt (AlBr$_3$/NaBr/KBr) mixture can simultaneously tune the interlayer spacing and termination via nucleophilic reaction and ion intercalation, resulting a doubled capacity with improved rate capability compared to pristine MXene[80].
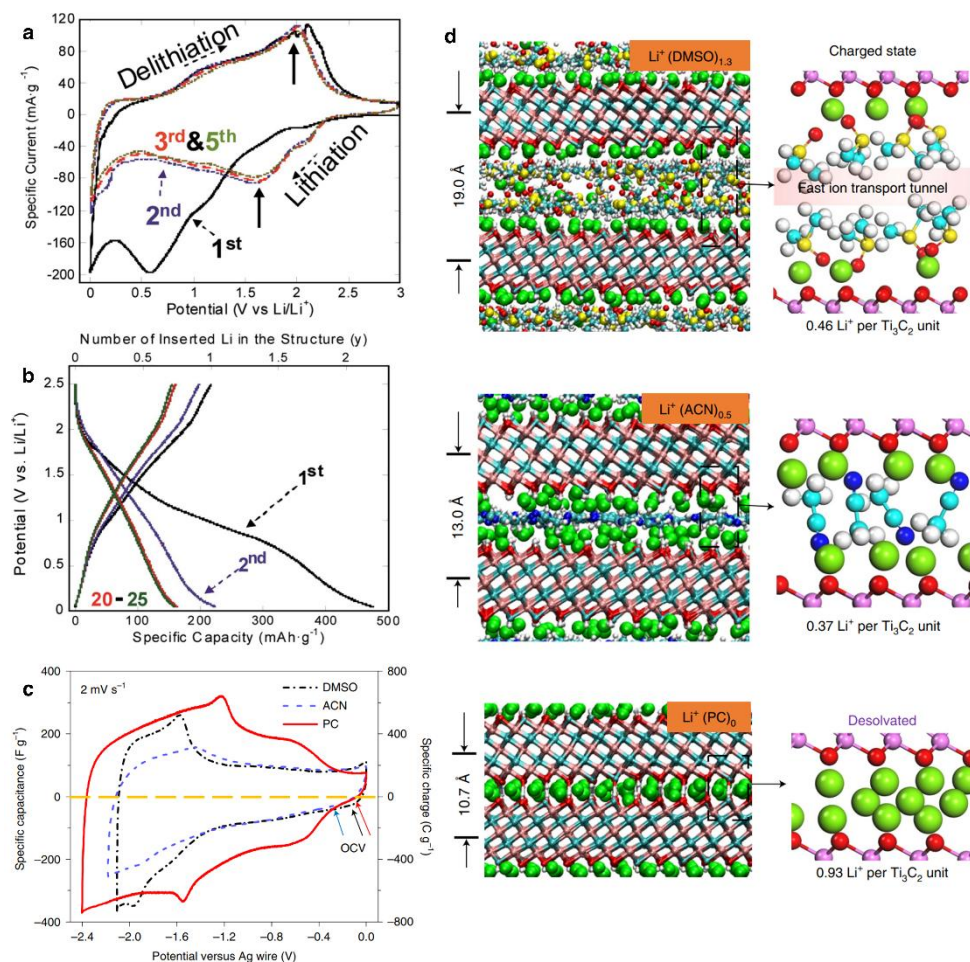
Figure 1.4 Pseudocapacitive charge storage of MXene in organic electrolytes. (a) CV and (b) GCD of multilayered Ti$_2$CT$_x$ in Li$^+$-based Carbonate electrolytes[73]. (c) CV of Ti$_3$C$_2$T$_x$ with 1 M LiTFSI in ACN, DMSO and PC solvents[82]. (d) MD simulation results showing ion/solvents arrangement under confinement of MXene (From top to bottom: in DMSO, ACN and PC)[82].

Another critical factor influencing charge storage is the ion desolvation prior to intercalation process, which determines how closely the ions can approach and interact with the surface functional groups of MXene and mediate the charge transfer at intercalated state[81]. This desolvation process is governed by both the solvents and the surface terminations of the MXene. When Ti$_3$C$_2$T$_x$ was cycled in propylene carbonate (PC), the interlayer spacing remained constant at 10.7 Å throughout charging and discharging, indicating that Li$^+$ ions

were fully desolvated prior to intercalation[82] (**Figure 1.4 d**). In contrast, when acetonitrile (ACN) and dimethyl sulfoxide (DMSO) were used, the interlayer spacing expanded from 13.0 Å and 18.8 Å to 13.4 Å and 19.3 Å under cathodic polarization, respectively, suggesting that Li$^+$ ions entered the interlayer along with solvent molecules. Molecular dynamics simulations further confirmed that a monolayer of ACN or a bilayer of DMSO was intercalated in the interlayer, which reduced ion-surface interactions and posted steric hinderance for further ion intercalation (**Figure 1.4 d**). Consequently, Ti$_3$C$_2$T$_x$ delivered a capacitance of 195 F g^{-1} in PC, compared to only 110 F g^{-1} and 130 F g^{-1} in ACN and DMSO, respectively, at a scan rate of 2 mV s^{-1}. In addition to solvent effects, surface terminations strongly affect desolvation by altering both the interfacial interaction and ion accessibility[83]. -O/-Cl terminated MXenes retained a fixed interlayer spacing of 11.0 Å throughout cycling, indicative of effective Li$^+$ desolvation and closer ion-surface interaction. While -F/-OH terminated Ti$_3$C$_2$ exhibited an interlayer expansion from 13.7 Å to 14.9 Å during first charge in carbonate-based electrolytes. This indicated solvent co-intercalation and incomplete ion desolvation, resulting in a denser and thicker solid electrolyte interphase (SEI) and less Li$^+$ intercalation. Consequently, -O/-Cl terminated Ti$_3$C$_2$ achieved a capacity of 873 C g^{-1}, far surpassing the 286 C g^{-1} delivered by -F/-OH terminated counterparts.

1.4.2 Capacitive behavior of MXene in ionic liquid

Ionic liquids (ILs) offer wide electrochemical window, their non-volatility, and excellent thermal stability further make them attractive electrolytes for achieving safety and high energy density simultaneously. Ti$_3$C$_2$T$_x$ MXene delivered a specific capacitance values around 84 F g^{-1} at a scan rate of 2 mV s^{-1} in neat EMIMTFSI over a wide potential range from -1.5 V to +1.5 V vs. Ag[84]. During negative polarization, a reversible increase in interlayer spacing from 13.3 Å to 14.4 Å was seen, attributed to the intercalation of EMIM$^+$ cations. In contrast, under positive polarization, a slight contraction occurred, due to the deintercalation of EMIM$^+$ or the adsorption of TFSI$^-$ anions to MXene's surface. DFT calculations showed that EMIM$^+$ intercalation is thermodynamically favorable, with a free energy of -14.5 eV and a preferred parallel alignment on the MXene surface, while TFSI$^-$ intercalation is energetically unfavorable with a positive free energy of 6.9 eV, excluding the possibility of anion intercalation[85]. To improve the ion accessibility, pillaring strategies have been used to expand MXene's interlayer spacing. When tested in neat EMIMTFSI, CTAB-pillared Ti$_3$C$_2$T$_x$ achieved a higher specific capacitance of 142 F g^{-1} at 5 mV s^{-1}. During cycling, CTAB-pillared Ti$_3$C$_2$T$_x$ showed a minimal interlayer change of 0.6 Å, indicating that the ion intercalation occurred with smaller structural change due to the pillaring effect. The effect of interlayer spacing and surface termination on charge storage in ionic liquid was further investigated using molecular dynamics simulations in [HEMIm][NTf$_2$][86]. The results revealed that narrow d-spacing of 7 Å suppressed electric double-layer (EDL) formation,

whereas large spacing of 10-14 Å facilitated ion adsorption near the MXene surfaces. Moreover, the distribution of ions was found to be highly dependent on surface chemistry. On =O terminated MXene, HEMIm$^+$ cations and NTf$_2^-$ anions aligned parallel to the surface under negative and positive potentials, respectively. Despite similar ion orientation, -OH terminated MXene showed a reduced ion-surface distance (0.8 Å compared to 2.0 Å for =O terminated surface) and stronger hydrogen bonding with ions. This strengthened interaction leads to an enhancement in differential capacitance. To understand the ion transport behavior, quasielastic neutron scattering was conducted at charge and discharged states in EMIMTFSI-acetonitrile (ACN) mixtures at varying concentrations[87]. The ion dynamics fitted with a Gaussian jump-diffusion model gave the highest mobility at intermediate acetonitrile contents (25-50%). Under these conditions, the ACN molecules disrupt strong ion pairing without overcrowding the electrode/electrolyte interface. These dynamics correlated with improved capacitance and minimal structural deformation upon cycling. These findings collectively highlight the importance of tailoring interlayer spacing, surface functionalization, and electrolyte composition to optimize charge storage in MXene-based systems using ionic liquids.

1.4.3 Pseudocapacitive behavior of MXene in acidic electrolytes

Compared to organic electrolytes, aqueous electrolytes are inherently non-flammable, non-toxic, and environmentally friendly, making them attractive for applications where safety and scalability are prioritized. In particular, acidic aqueous electrolytes usually have high ionic conductivity, making them suitable for high-power applications. Ti$_3$C$_2$T$_x$ MXenes exhibit exceptional electrochemical performance in acidic electrolytes, distinguished by high gravimetric and volumetric capacitance[88,89]. The CV profile of Ti$_3$C$_2$T$_x$ MXene in H$_2$SO$_4$ electrolytes exhibits nearly symmetric anodic and cathodic peaks with minimal peak separation (**Figure 1.5 a**). Specifically, a volumetric capacitance up to 900 F cm^{-3} was obtained, which is comparable to RuO$_2$. The superior performance is attributed to a unique charge storage mechanism combining both surface redox reactions and interlayer ion intercalation[90].

Proton intercalation during electrochemical cycling has been revealed via *in-situ* XRD measurements, as the interlayer spacing of Ti$_3$C$_2$T$_x$ shows significant change of 0.54 Å during charging/discharging process (**Figure 1.5 b**)[91]. Further insight into the nature of intercalated protons is revealed via *in-situ* FTIR. Multiple distinct peaks (e.g., at 1920, 2080, 2380, and 2840 cm^{-1}) appeared when immersing Ti$_3$C$_2$T$_x$ in acidic conditions, attributing to confined protons in MXene interlayer[92]. Upon proton intercalation, transformation of surface terminations from =O to -OH occurred, as confirmed by the redshift of characteristic A$_{1g}$ (Ti-C-T$_x$) Raman vibration mode of Ti$_3$C$_2$T$_x$ from 730 cm^{-1} to 722 cm^{-1} during cathodic

polarization[93]. Meanwhile, this reversible transformation of surface groups is accompanied by the valence change of transition metals[94]. The Ti K-edge XANES spectrum shows a shift in Ti oxidation state from 2.43 to 2.33 (0.3 V to -0.45 V), corresponding to a transfer of 0.1 electrons per Ti atom, or 0.3 electrons per $Ti_3C_2T_x$ unit (**Figure 1.5 c & d**). This electron transfer accounts for a theoretical capacitance of $205\,F\,g^{-1}$, which aligns well with experimental values, confirming that this reversible redox contributes significantly to charge storage process[95]. This pseudocapacitive behavior was also confirmed by in situ UV-Vis Spectroscopy. In 1 M H_2SO_4, the plasmonic peak of $Ti_3C_2T_x$ shifts drastically from 770 nm to 650 nm, with a relative absorption change of $-5.78\,V^{-1}\,\mu m^{-1}$, which is much more pronounced than that in neutral electrolytes[96]. First-principles simulations provide further insights by separating total charge storage into contributions from electric double-layer (EDL) and redox processes[97]. These calculations revealed a slight mismatch between proton and electron transfer, resulting in a net positive surface charge, thereby confirming the coexistence of EDL effects alongside dominant Faradaic reactions (**Figure 1.5 e**). Additionally, the electron transfer is facilitated by Ti sites near the Fermi level, while protons preferentially adsorb onto oxygen-terminated surfaces. The remarkable rate performance of $Ti_3C_2T_x$ MXenes in acidic electrolytes is closely linked to an efficient ion transport mechanism that enables both rapid proton mobility and fast surface redox kinetics. Within the confined interlayer space of the MXene, protons are transported through a Grotthuss-type hopping process, wherein they shuttle between water molecules via transiently formed hydrated structures such as Eigen and Zundel complexes[98]. Even under significant spatial confinement, this mechanism remains highly effective, with calculated ion diffusivity values reaching $5 \times 10^{-9}\,m^2\,s^{-1}$ when bi-layer water exists in MXene's interlayer, thereby ensuring rapid ion dynamics that support high rate performance. Beyond $Ti_3C_2T_x$, other MXenes such as Mo_2CT_x and V_2CT_x have also demonstrated promising electrochemical performance in acidic electrolytes[56,57]. To better understand the underlying factors controlling these performances, computational modeling has been used to identify meaningful descriptors. Among these, the shift in the potential of zero charge (PZC) during the transition from =O to -OH terminated surfaces emerges as a key indicator of redox activity[99]. It was found that a smaller shift in PZC (quantified as ΔV_{PZC}) and a moderate Gibbs free energy of hydrogen adsorption (ΔG_H) correlates with greater reversible pseudocapacitance and minimal hydrogen evolution reaction (**Figure 1.5 f**). Interestingly, Zr-based nitride MXenes have been

computationally identified to satisfy both criteria, highlighting them as promising candidates for future energy storage applications.
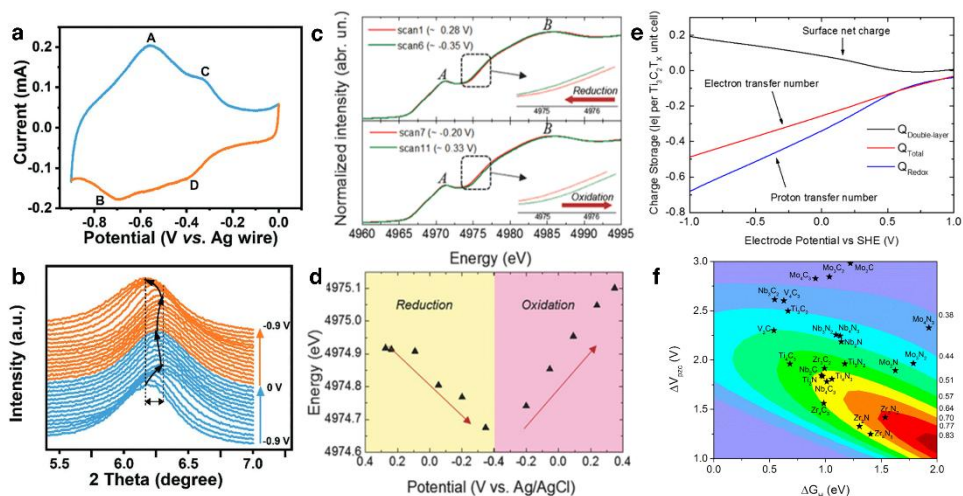

Figure 1.5 Charge storage mechanisms of MXene in acidic electrolytes. (a) CV curve of $Ti_3C_2T_x$ in 1 M H_2SO_4. (b) XRD patterns showing (0 0 2) reflection of $Ti_3C_2T_x$ during electrochemical cycling[91]. (c) Ti K-edge XANES of $Ti_3C_2T_x$ in H_2SO_4 during charging/discharging. (d) variation of Ti edge energy (at half height of normalized XANES spectra) at different potential[95]. (e) Charge transfer per $Ti_3C_2T_x$ unit cell at different potential[97]. (f) Charge storage per formula unit vs the shift in the potential at the point of zero charge (ΔV_{PZC}) and hydrogen adsorption free energy (ΔG_H)[99].

1.4.4 Capacitive behavior of MXene in non-acidic aqueous electrolytes

While prior studies reported substantial pseudocapacitive behavior with capacitances up to 900 F cm^{-3} in acidic electrolytes, only moderate capacitance around 300 F cm^{-3} was reported in alkaline/neutral aqueous electrolytes[100]. Nonetheless, clear evidence of reversible intercalation for various cations such as Li$^+$, Na$^+$, K$^+$, Mg^{2+}, NH$_4^+$, and Al^{3+}, was demonstrated using *in-situ* XRD. For instance, in MgSO$_4$ aqueous electrolytes, a reversible shrinkage of MXene interlayer spacing by 0.3 Å during cathodic scan was observed. This shrinkage is the result of intercalation of partial desolvated cations. The ion intercalation process induced a continuous, reversible mass uptake and a monotonic increase in electronic conductivity with more negative potential, as supported by electrochemical quartz crystal admittance (EQCA) and in situ conductance measurements[101]. It has been reported that ion size and charge influence the mechanical deformation during charging/discharging, with smaller, multivalent cations such as Li$^+$ and Mg^{2+} inducing layer contraction, while larger ions causing expansion. This is likely correlated with their different solvation structure. Ab initio molecular dynamics simulations demonstrated that cations undergo varying degrees of desolvation prior to adsorption/intercalation, dependent on ionic size and charge (**Figure 1.6 a**)[102]. Multiple

18

spectroscopic investigations have confirmed that redox activity is negligible in neutral aqueous electrolytes[90]. In situ Raman spectroscopy in 1 M Li_2SO_4 showed small, fully reversible shifts in characteristic vibrational modes, indicating minor structural change during cycling[93]. These experimental results are consistent with DFT predictions, showing that intercalating cations tend to retain part of their hydration shell, which suppresses orbital overlap with the MXene surface and prevents redox reactions (**Figure 1.6 b**)[103]. Given the relatively low specific surface area of MXenes (30 m^2 g^{-1}), the observed capacitance exceeding classical electric double-layer predictions is likely attributed to effects arising from nanoconfinement effect. Water confined within the interlayer spacing can exhibit a negative dielectric constant when small, strongly hydrated cations such as Li^+ are intercalated, a phenomenon ascribed to overscreening effects from densely packed hydration shells[104]. Collectively, a basic understanding of charge storage behavior in neutral aqueous electrolytes can be established. MXenes store charge primarily through rapid and reversible intercalation of partially hydrated cations, accompanied by modest structural changes and negligible redox activity.
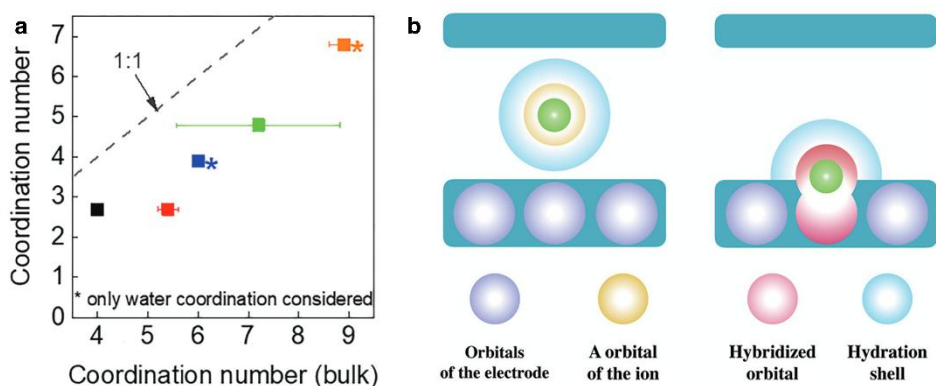
Figure 1.6 (a) Coordination numbers in bulk electrolytes and in MXene's interlayer spacing[102]. (b) Schematic illustration of capacitive (left) and pseudocapacitive (right) charge storage originating from orbital coupling in MXene electrodes[103].

The main limitation of aqueous electrolytes lies in their narrow electrochemical stability window (typically <1.23 V), which compromises the cell voltage and thus limits the achievable energy density. To address the limited energy density of neutral aqueous system, expanding the voltage window by electrolyte engineering and enhancing redox activity through surface modification or partial oxidation has been explored. Water-in-salt (WIS) electrolytes, such as 19.8 mol kg^{-1} LiCl, effectively suppress water activity, enabling $Ti_3C_2T_x$ to operate within a broad voltage window of 1.6 V, significantly larger than the 1.0 V typical of conventional neutral electrolytes[105]. In WIS electrolyte, two different ion intercalation

processes corresponding to different degrees of Li^+ desolvation dominated the charge storage process. In the initial stage, fully solvated Li^+ ions that are coordinated with approximately 2.85 water molecules intercalated and abruptly expanded the interlayer spacing from 11.0 Å to 12.9 Å. At more negative potentials, partially desolvated Li^+ ions (with 1.5 water molecules) began to intercalate, gradually increasing the spacing to 13.3 Å. Importantly, in situ UV-Vis spectroscopy shows no significant change in absorption throughout the cycle, indicating that the process involves minimal electron transfer[96]. Further improvement of the energy density can be achieved by enhancing redox activity via surface oxidation. Electrochemical oxidation of $Ti_3C_2T_x$ by extending the voltage to 1.2 V in 19.2 mol kg^{-1} LiBr can activate Ti-based Faradaic reactions at negative potential, as evidenced by a reversible Ti valence shift from +2.78 to +2.86 observed via *in-situ* Ti K-edge XANES [106]. Moreover, the partial oxidation is accompanied by an expansion in interlayer spacing from 12.6 Å to 15.7 Å, which can facilitate further ion insertion. Besides electrochemical oxidation, thermal oxidation can also improve the redox activity of MXenes in neutral electrolytes. Annealing in air under mild condition introduced amorphous surface oxide domains on $Mo_2Ti_2C_3$, as confirmed by the formation of Mo-O and Ti-O bonds[107]. The partially oxidized structure exhibits improved charge storage in 5 m LiCl, attributed to a combination of redox reaction from the oxide components and structural disorder. Modifying surface terminations is another strategy to enhance redox activity. Replacement of -F terminations with -OH groups through alkaline treatment can improve the ion-electrode interaction and ion intercalation kinetics, leading to enhanced capacitance and rate performance[108].

1.5 Research questions

As reviewed in Section 1.4, the charge storage behavior of MXenes is governed by both electrode material characteristics (surface terminations, interlayer spacing, and electronic structure) and electrolyte properties. In bulk electrolytes, ions are surrounded by solvent molecules that form solvation shells, stabilizing the ions and enabling their transport through the solution. Upon approaching the MXene/electrolyte interface, these solvated ions undergo partial or complete desolvation, which directly influences the subsequent charge storage process, including ion adsorption, intercalation, and even electrochemical deposition. Importantly, the solvation structure can be systematically tuned by varying the ionic size or through electrolyte engineering, offering a powerful strategy to modulate interfacial and bulk processes. However, a comprehensive understanding of how different ion solvation environments govern these mechanisms on MXene, particularly in non-acidic electrolytes, remains limited.

Accordingly, this work seeks to address the following key research questions: (1) How can electrolyte composition be engineered to regulate the solvation structure of metallic ions and, consequently, the electrochemical behavior of MXenes? (2) How do MXenes respond to non-metallic ion modulation in aqueous electrolytes, and what roles do ion size and solvation play in governing their intercalation behavior? (3) Beyond conventional ion adsorption and intercalation process, how does ion solvation influence electrochemical deposition at MXene/electrolyte interfaces? (4) How does the ion-desolvation process couple with MXenes' structure, and affect charge transfer and ion storage kinetics?

1.6 Thesis outline

This thesis aims to help understand how ion solvation influences the charge storage behavior of $Ti_3C_2T_x$ MXene in neutral aqueous electrolytes. This is achieved through two main approaches. First, electrolyte engineering strategy has been employed to tune ion solvation structures through varying ion species and solvents. This enables control over the intercalation behavior of both non-metallic and metallic ions into MXene's interlayer, as well as the deposition behavior of Zn^{2+} ions on $Ti_3C_2T_x$ surface. Second, the electrode architecture is modified by constructing a redox-active $Ti_3C_2T_x$/conjugated polyelectrolyte (CPE) heterostructure. This design alters the local interlayer environment and influences the desolvation behavior of ammonium ions.

The thesis is organized into three parts, the first part of this thesis focuses on the intercalation of non-metallic ions into $Ti_3C_2T_x$, starting with a systematic study on ammonium (NH_4^+) and tetraalkylammonium ions (TMA^+, TEA^+, and TPA^+) intercalation (chapter 2). These ions, with distinct sizes and solvation structures, provide a platform to understand how solvation influences non-metallic ion storage behavior of flexible 2D materials. Considering the moderate capacitance of $Ti_3C_2T_x$ for ammonium ion storage, we designed a redox-active heterostructure composed of $Ti_3C_2T_x$ and a n-type cationic conjugated polyelectrolytes (CPE) (chapter 3). In this chapter, we found that structural tuning at the electrode level can affect ion desolvation, which in turn affects the charge storage behavior.

The second part of the thesis investigates how electrolyte design can be used to control ion solvation structures, with the goal of tuning metallic ion intercalation behavior in $Ti_3C_2T_x$. In chapter 4, polyethylene glycol (PEG-400) is introduced as a molecular crowding agent in Li^+-based aqueous electrolytes. This modification extends the voltage window and tunes the Li^+ intercalation behavior at higher potential. In chapter 5, acetonitrile (ACN) was used as co-solvent to tune the solvation environment of Na^+ ions. By varying the ACN content, the strength of ion-solvent interactions is adjusted, leading to change in charge storage mechanism and electrochemical performance.

The third part (chapter 6) examines how ion solvation affects Zn^{2+} deposition behavior on $Ti_3C_2T_x$, which is used as a freestanding current collector in anode-free aqueous zinc metal batteries (AZMBs). By introducing Li-salts and propylene carbonate (PC) as electrolyte additives, the solvation structure of Zn^{2+} ions is altered, which directly influences interfacial chemistry at the MXene surface. This modulation leads to the formation of a ZnF_2-rich interphase that stabilizes Zn deposition and improves cycling efficiency. These findings demonstrate how tailoring ion solvation can serve as a powerful strategy to control not only intercalation, but also metal deposition behavior in MXene-based charge storage systems.

1.7 Reference:

1   B. Dunn, H. Kamath and J. Tarascon, *Science*, 2011, **334**, 928–935.

2   J. R. Miller and P. Simon, *Science*, 2008, **321**, 651–652.

3   Y. Liu, Y. Zhu and Y. Cui, *Nat. Energy*, 2019, **4**, 540–550.

4   T. S. Mathis, N. Kurra, X. Wang, D. Pinto, P. Simon and Y. Gogotsi, *Adv. Energy Mater.*, 2019, **9**, 1902007.

5   P. Simon and Y. Gogotsi, *Nat. Mater.*, 2008, **7**, 845–854.

6   D. Qu and H. Shi, *J. Power Sources*, 1998, **74**, 99–107.

7   J. Chmiola, G. Yushin, Y. Gogotsi, C. Portet, P. Simon and P. L. Taberna, *Science*, 2006, **313**, 1760–1763.

8   S. Fleischmann, J. B. Mitchell, R. Wang, C. Zhan, D. Jiang, V. Presser and V. Augustyn, *Chem. Rev.*, 2020, **120**, 6738–6782.

9   M. Mastragostino, C. Arbizzani and F. Soavi, *Solid State Ionics*, 2002, **148**, 493–498.

10   J. P. Zheng, P. J. Cygan and T. R. Jow, *J. Electrochem. Soc.*, 1995, **142**, 2699.

11   V. Augustyn, J. Come, M. A. Lowe, J. W. Kim, P.-L. Taberna, S. H. Tolbert, H. D. Abruña, P. Simon and B. Dunn, *Nat. Mater.*, 2013, **12**, 518–522.

12   V. Augustyn, P. Simon and B. Dunn, *Energy Environ. Sci.*, 2014, **7**, 1597–1614.

13   H. Lindström, S. Södergren, A. Solbrand, H. Rensmo, J. Hjelm, A. Hagfeldt and S.-E. Lindquist, *J. Phys. Chem. B*, 1997, **101**, 7717–7722.

14   J. Wang, J. Polleux, J. Lim and B. Dunn, *J. Phys. Chem. C*, 2007, **111**, 14925–14931.
22

15   V. Vivier and M. E. Orazem, *Chem. Rev.*, 2022, **122**, 11131–11168.

16   S. Wang, J. Zhang, O. Gharbi, V. Vivier, M. Gao and M. E. Orazem, *Nat. Rev. Methods Primers*, 2021, **1**, 41.

17   E. Pomerantseva and Y. Gogotsi, *Nat. Energy*, 2017, **2**, 17089.

18   X. Li, Z. Huang, C. E. Shuck, G. Liang, Y. Gogotsi and C. Zhi, *Nat. Rev. Chem.*, 2022, **6**, 389–404.

19   B. Anasori, M. R. Lukatskaya and Y. Gogotsi, *Nat. Rev. Mater.*, 2017, **2**, 16098.

20   M. Naguib, V. N. Mochalin, M. W. Barsoum and Y. Gogotsi, *Adv. Mater.*, 2014, **26**, 992–1005.

21   M. Naguib, M. Kurtoglu, V. Presser, J. Lu, J. Niu, M. Heon, L. Hultman, Y. Gogotsi and M. W. Barsoum, *Adv. Mater.*, 2011, **23**, 4248–4253.

22   A. Lakmal, P. B. Thombre and C. E. Shuck, *Acc. Chem. Res.*, 2024, **57**, 3007–3019.

23   A. VahidMohammadi, J. Rosen and Y. Gogotsi, *Science*, 2021, **372**, eabf1581.

24   F. Shahzad, M. Alhabeb, C. B. Hatter, B. Anasori, S. Man Hong, C. M. Koo and Y. Gogotsi, *Science*, 2016, **353**, 1137–1140.

25   W. Zhang, S. Li, X. Fan, X. Zhang, S. Fan and G. Bei, *Carbon Energy*, 2024, **6**, e609.

26   H. Chen, H. Ma and C. Li, *ACS Nano*, 2021, **15**, 15502–15537.

27   M. Okubo, A. Sugahara, S. Kajiyama and A. Yamada, *Acc. Chem. Res.*, 2018, **51**, 591–599.

28   B. Anasori, Y. Xie, M. Beidaghi, J. Lu, B. C. Hosler, L. Hultman, P. R. C. Kent, Y. Gogotsi and M. W. Barsoum, *ACS Nano*, 2015, **9**, 9507–9516.

29   S. K. Nemani, B. Zhang, B. C. Wyatt, Z. D. Hood, S. Manna, R. Khaledialidusti, W. Hong, M. G. Sternberg, S. K. R. S. Sankaranarayanan and B. Anasori, *ACS Nano*, 2021, **15**, 12815–12825.

30   H. Kumar, N. C. Frey, L. Dong, B. Anasori, Y. Gogotsi and V. B. Shenoy, *ACS Nano*, 2017, **11**, 7648–7655.

31   M. Alhabeb, K. Maleski, B. Anasori, P. Lelyukh, L. Clark, S. Sin and Y. Gogotsi, *Chem. Mater.*, 2017, **29**, 7633–7644.

32   K. R. G. Lim, M. Shekhirev, B. C. Wyatt, B. Anasori, Y. Gogotsi and Z. W. Seh, *Nat. Synth.*, 2022, **1**, 601–614.

33   T. S. Mathis, K. Maleski, A. Goad, A. Sarycheva, M. Anayee, A. C. Foucher, K. Hantanasirisakul, C. E. Shuck, E. A. Stach and Y. Gogotsi, *ACS Nano*, 2021, **15**, 6420–6429.

34   P. Lakhe, E. M. Prehn, T. Habib, J. L. Lutkenhaus, M. Radovic, M. S. Mannan and M. J. Green, *Ind. Eng. Chem. Res.*, 2019, **58**, 1570–1579.

35   C. A. Voigt, M. Ghidiu, V. Natu and M. W. Barsoum, *J. Phys. Chem. C*, 2018, **122**, 23172–23179.

36   Y.-J. Kim, S. J. Kim, D. Seo, Y. Chae, M. Anayee, Y. Lee, Y. Gogotsi, C. W. Ahn and H.-T. Jung, *Chem. Mater.*, 2021, **33**, 6346–6355.

37   M. A. Hope, A. C. Forse, K. J. Griffith, M. R. Lukatskaya, M. Ghidiu, Y. Gogotsi and C. P. Grey, *Phys. Chem. Chem. Phys.*, 2016, **18**, 5099–5102.

38   T. Li, L. Yao, Q. Liu, J. Gu, R. Luo, J. Li, X. Yan, W. Wang, P. Liu, B. Chen, W. Zhang, W. Abbas, R. Naz and D. Zhang, *Angew. Chem.*, 2018, **57**, 6115–6119.

39   A. Jawaid, A. Hassan, G. Neher, D. Nepal, R. Pachter, W. J. Kennedy, S. Ramakrishnan and R. A. Vaia, *ACS Nano*, 2021, **15**, 2771–2777.

40   H. Shi, P. Zhang, Z. Liu, S. Park, M. R. Lohe, Y. Wu, A. Shaygan Nia, S. Yang and X. Feng, *Angew. Chem.*, 2021, **60**, 8689–8693.

41   S.-Y. Pang, Y.-T. Wong, S. Yuan, Y. Liu, M.-K. Tsang, Z. Yang, H. Huang, W.-T. Wong and J. Hao, *J. Am. Chem. Soc.*, 2019, **141**, 9610–9616.

42   W. Sun, S. A. Shah, Y. Chen, Z. Tan, H. Gao, T. Habib, M. Radovic and M. J. Green, *J. Mater. Chem. A*, 2017, **5**, 21663–21668.

43   K. C. Chan, X. Guan, T. Zhang, K. Lin, Y. Huang, L. Lei, Y. Georgantas, Y. Gogotsi, M. A. Bissett and I. A. Kinloch, *J. Mater. Chem. A*, 2024, **12**, 25165–25175.

44   S. Yang, P. Zhang, F. Wang, A. G. Ricciardulli, M. R. Lohe, P. W. M. Blom and X. Feng, *Angew. Chem.*, 2018, **57**, 15491–15495.

45   O. Mashtalir, M. Naguib, V. N. Mochalin, Y. Dall'Agnese, M. Heon, M. W. Barsoum and Y. Gogotsi, *Nat. Commun.*, 2013, **4**, 1716.

46   A. Thakur, N. Chandran B.S., K. Davidson, A. Bedford, H. Fang, Y. Im, V. Kanduri, B. C. Wyatt, S. K. Nemani, V. Poliukhova, R. Kumar, Z. Fakhraai and B. Anasori, *Small Methods*, 2023, **7**, 2300030.

47   D. D. Kruger, H. García and A. Primo, *Adv. Sci.*, 2024, **11**, 2307106.

48   G. Ma, H. Shao, J. Xu, Y. Liu, Q. Huang, P.-L. Taberna, P. Simon and Z. Lin, *Nat. Commun.*, 2021, **12**, 5085.

49   Y. Li, H. Shao, Z. Lin, J. Lu, L. Liu, B. Duployer, P. O. Å. Persson, P. Eklund, L. Hultman, M. Li, K. Chen, X.-H. Zha, S. Du, P. Rozier, Z. Chai, E. Raymundo-Piñero, P.-L. Taberna, P. Simon and Q. Huang, *Nat. Mater.*, 2020, **19**, 894–899.

50   M. Li, J. Lu, K. Luo, Y. Li, K. Chang, K. Chen, J. Zhou, J. Rosen, L. Hultman, P. Eklund, P. O. Å. Persson, S. Du, Z. Chai, Z. Huang and Q. Huang, *J. Am. Chem. Soc.*, 2019, **141**, 4730–4737.

51   V. Kamysbayev, A. S. Filatov, H. Hu, X. Rui, F. Lagunas, D. Wang, R. F. Klie and D. V. Talapin, *Science*, 2020, **369**, 979–983.

52   Y. Bai, C. Liu, T. Chen, W. Li, S. Zheng, Y. Pi, Y. Luo and H. Pang, *Angew. Chem.*, 2021, **60**, 25318–25322.

53   S. Li, J. Zhu, W. Lu, Z. Liu, Z. Wang, L. Wang, Y. Tian and X. Cui, *J. Colloid Interface Sci.*, 2024, **663**, 801–809.

54   Q. Zhao, C. Zhang, R. Hu, Z. Du, J. Gu, Y. Cui, X. Chen, W. Xu, Z. Cheng, S. Li, B. Li, Y. Liu, W. Chen, C. Liu, J. Shang, L. Song and S. Yang, *ACS Nano*, 2021, **15**, 4927–4936.

55   L. Liu, M. Orbay, S. Luo, S. Duluard, H. Shao, J. Harmel, P. Rozier, P.-L. Taberna and P. Simon, *ACS Nano*, 2022, **16**, 111–118.

56   D. Wang, C. Zhou, A. S. Filatov, W. Cho, F. Lagunas, M. Wang, S. Vaikuntanathan, C. Liu, R. F. Klie and D. V. Talapin, *Science*, 2023, **379**, 1242–1247.

57   A. N. Enyashin and A. L. Ivanovskii, *J. Solid State Chem.*, 2013, **207**, 42–48.

58   K. Hantanasirisakul and Y. Gogotsi, *Adv. Mater.*, 2018, **30**, 1804779.

59   J. L. Hart, K. Hantanasirisakul, A. C. Lang, B. Anasori, D. Pinto, Y. Pivak, J. T. Van Omme, S. J. May, Y. Gogotsi and M. L. Taheri, *Nat. Commun.*, 2019, **10**, 522.

60   Q. Tang, Z. Zhou and P. Shen, *J. Am. Chem. Soc.*, 2012, **134**, 16909–16916.

61   M. Khazaei, M. Arai, T. Sasaki, A. Ranjbar, Y. Liang and S. Yunoki, *Phys. Rev. B*, 2015, **92**, 075411.

62   T. Schultz, N. C. Frey, K. Hantanasirisakul, S. Park, S. J. May, V. B. Shenoy, Y. Gogotsi and N. Koch, *Chem. Mater.*, 2019, **31**, 6590–6597.

63   W. Cao, J. Nie, Y. Cao, C. Gao, M. Wang, W. Wang, X. Lu, X. Ma and P. Zhong, *Chem. Eng. J.*, 2024, **496**, 154097.

64   H. Song and D. Jiang, *Nanoscale*, 2023, **15**, 16010–16015.

65   F. Xia, J. Lao, R. Yu, X. Sang, J. Luo, Y. Li and J. Wu, *Nanoscale*, 2019, **11**, 23330–23337.

66   C. J. Zhang, S. Pinilla, N. McEvoy, C. P. Cullen, B. Anasori, E. Long, S.-H. Park, A. Seral-Ascaso, A. Shmeliov, D. Krishnan, C. Morant, X. Liu, G. S. Duesberg, Y. Gogotsi and V. Nicolosi, *Chem. Mater.*, 2017, **29**, 4848–4856.

67   X. Wang, Z. Wang and J. Qiu, *Angew. Chem.,* 2021, **60**, 26587–26591.

68   S. Huang and V. N. Mochalin, *Inorg. Chem.*, 2019, **58**, 1958–1966.

69   V. Natu, J. L. Hart, M. Sokol, H. Chiang, M. L. Taheri and M. W. Barsoum, *Angew. Chem.*, 2019, **58**, 12655–12660.

70   X. Yang, Q. Wang, K. Zhu, K. Ye, G. Wang, D. Cao and J. Yan, *Adv. Funct. Mater.*, 2021, **31**, 2101087.

71   X. Zhao, A. Vashisth, E. Prehn, W. Sun, S. A. Shah, T. Habib, Y. Chen, Z. Tan, J. L. Lutkenhaus, M. Radovic and M. J. Green, *Matter*, 2019, **1**, 513–526.

72   A. Lee, M. Shekhirev, M. Anayee and Y. Gogotsi, *Graphene and 2D Mater.*, 2024, **9**, 77–85.

73   M. Naguib, J. Come, B. Dyatkin, V. Presser, P.-L. Taberna, P. Simon, M. W. Barsoum and Y. Gogotsi, *Electrochemistry Commun.*, 2012, **16**, 61–64.

74   X. Wang, S. Kajiyama, H. Iinuma, E. Hosono, S. Oro, I. Moriguchi, M. Okubo and A. Yamada, *Nat. Commun.*, 2015, **6**, 6544.

75   Y. Xie, M. Naguib, V. N. Mochalin, M. W. Barsoum, Y. Gogotsi, X. Yu, K.-W. Nam, X.-Q. Yang, A. I. Kolesnikov and P. R. C. Kent, *J. Am. Chem. Soc.*, 2014, **136**, 6385–6394.

76   M. Li, X. Li, G. Qin, K. Luo, J. Lu, Y. Li, G. Liang, Z. Huang, J. Zhou, L. Hultman, P. Eklund, P. O. Å. Persson, S. Du, Z. Chai, C. Zhi and Q. Huang, *ACS Nano*, 2021, **15**, 1077–1085.

77   J. Tang, X. Huang, T. Qiu, X. Peng, T. Wu, L. Wang, B. Luo and L. Wang, *Chem. Eur. J.*, 2021, **27**, 1921–1940.

78   C. Liang, Y. Meng, Y. Zhang, H. Zhang, W. Wang, M. Lu and G. Wang, *J. Energy Storage*, 2023, **65**, 107341.

79   X. Li, M. Li, Q. Yang, D. Wang, L. Ma, G. Liang, Z. Huang, B. Dong, Q. Huang and C. Zhi, *Adv. Energy Mater.*, 2020, **10**, 2001394.

80   T. Zhang, L. Chang, X. Zhang, H. Wan, N. Liu, L. Zhou and X. Xiao, *Nat. Commun.*, 2022, **13**, 6731.

81   S. Fleischmann, Y. Zhang, X. Wang, P. T. Cummings, J. Wu, P. Simon, Y. Gogotsi, V. Presser and V. Augustyn, *Nat. Energy*, 2022, **7**, 222–228.

82   X. Wang, T. S. Mathis, K. Li, Z. Lin, L. Vlcek, T. Torita, N. C. Osti, C. Hatter, P. Urbankowski, A. Sarycheva, M. Tyagi, E. Mamontov, P. Simon and Y. Gogotsi, *Nat. Energy*, 2019, **4**, 241–248.

83   Z. Bo, R. Wang, B. Wang, S. Sunny, Y. Zhao, K. Ge, K. Xu, Y. Song, E. Raymundo-Piñero, Z. Lin, H. Shao, Q. Yu, J. Yan, K. Cen, P.-L. Taberna and P. Simon, *Nat. Commun.*, 2025, **16**, 3813.

84   Z. Lin, P. Rozier, B. Duployer, P.-L. Taberna, B. Anasori, Y. Gogotsi and P. Simon, *Electrochem. Commun.*, 2016, **72**, 50–53.

85   G. Valurouthu, R. Panigrahi, M. Saraf, C. E. Shuck, B. S. Mallik, N. Kurra and Y. Gogotsi, *Batteries Supercaps*, 2023, **6**, e202300009.

86   X. Sun, Y. Li, Y. Wang, Z. Liu, K. Dong and S. Zhang, *Langmuir*, 2024, **40**, 2220–2229.

87   N. C. Osti, X. Lin, W. Zhao, X. Wang, C. Chen, Y. Gao, T. Torita, A. I. Kolesnikov, P. T. Cummings, Y. Gogotsi and E. Mamontov, *2D Mater.*, 2023, **10**, 014014.

88   M. R. Lukatskaya, S. Kota, Z. Lin, M.-Q. Zhao, N. Shpigel, M. D. Levi, J. Halim, P.-L. Taberna, M. W. Barsoum, P. Simon and Y. Gogotsi, *Nat. Energy*, 2017, **2**, 1–6.

89   M. Ghidiu, M. R. Lukatskaya, M.-Q. Zhao, Y. Gogotsi and M. W. Barsoum, *Nature*, 2014, **516**, 78–81.

90   G. Bergman, E. Ballas, Q. Gao, A. Nimkar, B. Gavriel, M. D. Levi, D. Sharon, F. Malchik, X. Wang, N. Shpigel, D. Mandler and D. Aurbach, *Adv. Energy Mater.*, 2023, **13**, 2203154.

91   X. Mu, D. Wang, F. Du, G. Chen, C. Wang, Y. Wei, Y. Gogotsi, Y. Gao and Y. Dall'Agnese, *Adv. Funct. Mater.*, 2019, **29**, 1902953.

92   M. Lounasvuori, Y. Sun, T. S. Mathis, L. Puskar, U. Schade, D. E. Jiang, Y. Gogotsi and T. Petit, *Nat. Commun.*, 2023, **14**, 1322.

93   D. Johnson, K. Hansen, R. Yoo and A. Djire, *ChemElectroChem*, 2022, **9**, e202200555.

94   H. Shao, K. Xu, Y. C. Wu, A. Iadecola, L. Liu, H. Ma, L. Qu, E. Raymundo-Piñero, J. Zhu, Z. Lin, P. L. Taberna and P. Simon, *ACS Energy Lett.*, 2020, **5**, 2873–2880.

95   M. R. Lukatskaya, *Adv. Energy Mater.*, 2015, **5**, 1500589.

96   D. Zhang, R. (John) Wang, X. Wang and Y. Gogotsi, *Nat. Energy*, 2023, **8**, 567–576.

97   C. Zhan, M. Naguib, M. Lukatskaya, P. R. C. Kent, Y. Gogotsi and D. Jiang, *J. Phys. Chem. Lett.*, 2018, **9**, 1223–1228.

98   Y. Sun, C. Zhan, P. R. C. Kent, M. Naguib, Y. Gogotsi and D. Jiang, *ACS Appl. Mater. Interfaces*, 2020, **12**, 763–770.

99   C. Zhan, W. Sun, P. R. C. Kent, M. Naguib, Y. Gogotsi and D. Jiang, *J. Phys. Chem. C*, 2019, **123**, 315–321.

100   M. R. Lukatskaya, O. Mashtalir, C. E. Ren, Y. Dall'Agnese, P. Rozier, P. L. Taberna, M. Naguib, P. Simon, M. W. Barsoum and Y. Gogotsi, *Science*, 2013, **341**, 1502–1505.

101   M. D. Levi, M. R. Lukatskaya, S. Sigalov, M. Beidaghi, N. Shpigel, L. Daikhin, D. Aurbach, M. W. Barsoum and Y. Gogotsi, *Adv. Energy Mater.*, 2015, **5**, 1400815.

102   Q. Gao, W. Sun, P. Ilani-Kashkouli, A. Tselev, P. R. C. Kent, N. Kabengi, M. Naguib, M. Alhabeb, W.-Y. Tsai, A. P. Baddorf, J. Huang, S. Jesse, Y. Gogotsi and N. Balke, *Energy Environ. Sci.*, 2020, **13**, 2549–2558.

103   Y. Ando, M. Okubo, A. Yamada and M. Otani, *Adv. Funct. Mater.*, 2020, **30**, 2000820.

104   A. Sugahara, Y. Ando, S. Kajiyama, K. Yazawa, K. Gotoh, M. Otani, M. Okubo and A. Yamada, *Nat. Commun.*, 2019, **10**, 850.

105   X. Wang, T. S. Mathis, Y. Sun, W.-Y. Tsai, N. Shpigel, H. Shao, D. Zhang, K. Hantanasirisakul, F. Malchik, N. Balke, D. Jiang, P. Simon and Y. Gogotsi, *ACS Nano*, 2021, **15**, 15274–15284.

106   X. Wang, S.-M. Bak, M. Han, C. E. Shuck, C. McHugh, K. Li, J. Li, J. Tang and Y. Gogotsi, *ACS Energy Lett.*, 2022, **7**, 30–35.

107   M. Saraf, B. Chacon, S. Ippolito, R. W. Lord, M. Anayee, R. (John) Wang, A. Inman, C. E. Shuck and Y. Gogotsi, *Adv. Funct. Mater.*, 2024, **34**, 2306815.

108   C. Chen, T. Wang, X. Zhao, A. Wu, S. Li, N. Zhang, X. Qu, L. Jiao and Y. Liu, *Adv. Funct. Mater.*, 2024, **34**, 2308508.

Introduction

2 Reversibly Electrochemical Intercalation of Ammonium and Tetraalkylammonium Cations in Ti$_3$C$_2$T$_x$ MXene

Reversibly Electrochemical Intercalation of Ammonium and Tetraalkylammonium Cations in Ti3C2Tx MXene

Abstract

The large and flexible interlayer spacing of MXenes, along with their hydrophilic and redox-active surface, make them promising for pseudocapacitive charge storage in aqueous electrolytes, including those with large non-metallic charge carriers. Despite the great diversity and potential sustainability benefits of non-metallic charge carriers, their intercalation process remains poorly understood, as the large ionic size has led to doubts about their ability to intercalate reversibly. In this work, we demonstrate reversible intercalation of ammonium ions (NH_4^+) and tetraalkylammonium cations (TMA^+, TEA^+, and TPA^+) in aqueous electrolytes and investigate the role of ion solvation in charge storage within flexible $Ti_3C_2T_x$ MXene interlayers. Interestingly, small, strongly solvated NH_4^+ ions intercalate at low solvation level and cause a rectangular-shaped CV with minimal structural change. In contrast, weakly solvated tetraalkylammonium cations, whose solvated sizes exceed MXene's interlayer spacing, intercalate into $Ti_3C_2T_x$ together with significant amount of water, resulting in distinct intercalative electrochemical signatures. This is accompanied by substantial interlayer spacing expansions (by 16.6 Å for TMA^+ and 20.7 Å for TEA^+) and viscoelastic softening. These findings reveal the unique behavior of non-metallic ion intercalation in 2D materials with flexible interlayer spacing and provide key insights into how ion solvation affect the interlayer structure and electrochemical performance.

2.1 Introduction

The intermittent output of renewables and the rising demand for electric vehicles, portable devices, and grid-scale storage highlight the need for efficient electrochemical energy storage (EES) systems[1]. Two-dimensional (2D) materials have emerged as promising candidates for EES due to their unique layered structures, offering large surface areas for ion adsorption and open interlayer channels for rapid ion transport, both crucial for achieving high energy and power densities simultaneously[2,3]. Among all 2D materials, 2D transition metal carbides and/or nitrides, or MXenes, are particularly attractive for EES applications, as their metallic conductivity enables rapid electron transfer, while their large interlayer spacing facilitates efficient ion transport[4–6]. Pseudocapacitive behavior has been observed in MXene electrodes in acidic and organic electrolytes, exhibiting high capacitance and great rate capability[7–11].

The typical EES charge storage process involves three steps: ion migration through the electrolyte, ion desolvation (or dehydration in aqueous media) at the electrode-electrolyte interface, and subsequent ion intercalation into the electrode[12,13]. In the electrolyte, ions are surrounded by solvent molecules, forming solvation shells that stabilize and facilitate their transport. At the electrode-electrolyte interfaces, ions typically undergo partial or complete desolvation, a process that introduces an energy barrier and contributes to increased interfacial resistance[14]. The degree of desolvation at this stage determines the solvation state of ions as they enter the electrode, which in turn affects their interactions within the host structure[15]. Ions intercalating with a lower solvation level generally experience charge screening induced by surrounding solvents, which weakens their interaction with the electrode and may limit charge storage. In contrast, ions retaining more solvation shell can move faster in the electrode, but their weaker coupling with the electrode may reduce overall charge storage capacity[12,16].

In bulk electrode materials with rigid crystal lattices or in microporous carbons, spatial constraints reinforces ion desolvation prior to intercalation or adsorption, as the confined space cannot accommodate solvated ions[17–19]. In 2D materials such as reduced graphene oxide (rGO), the relatively narrow interlayer spacing also imposes spatial restrictions that force ions to shed their solvation shells before intercalating[20–22]. In comparison, MXenes feature intrinsically large and highly flexible interlayer spacings due to weak van der Waals interactions between layers, which may allow the intercalation of different species and support dynamic structural change [23,24]. For example, a reversible interlayer expansion of 3.2 Å was observed in $Ti_3C_2T_x$ electrodes during cycling in a PEG-containing electrolyte, attributed to the co-insertion of Li^+ ions and PEG molecules[24]. This structural flexibility, combined with the presence of surface functional groups capable of interacting with intercalating species, enables ion intercalation at varying degrees of solvation that is not

typically observed in more rigid electrode materials. As a result, ion solvation becomes a key factor in determining the charge storage behavior of MXene-based EES systems.

Both the choice of the solvents and the identity of the ionic species influence the extent of solvation and, consequently, the charge storage processes. Some organic solvents (e.g. DMSO, ACN) may spontaneously intercalate into the MXene layers, thereby affecting the interlayer spacing at open-circuit potential. This alters the interlayer environment and can influence the extent of ion desolvation prior to electrochemical intercalation[25]. In neutral aqueous electrolytes, high polarity of H_2O typically results in incomplete ion desolvation. On the other hand, properties of the cations themselves also critically affect their desolvation behavior and how they interact with MXene layers. It has been revealed by a electrochemical quartz crystal microbalance study that ions with high charge-to-radius ratio, require more energy to desolvate and tend to co-intercalate with water molecules[26]. While weakly solvated ions like K^+ and Cs^+, are likely to intercalate in a less solvated form. The intercalation of these partially desolvated ions leads to d-spacing changes ranging from 0.2 Å to 0.5 Å in aqueous electrolytes, depending on ionic species used[27]. Meanwhile, this solvent co-intercalation process is accompanied by weak redox activity, as confirmed by *in-situ* Raman and Ultraviolet-visible (UV-Vis) spectroscopy[28,29]. Density functional theory (DFT) calculations suggested that the residue solvation shell may prevent direct interaction of intercalated metallic ions with MXenes' surface groups, resulting in charge storage process predominately governed by electric double-layer (EDL) formation[7].

Despite these insights, the role of solvation has so far only been explored in metallic ion-based systems. Non-metallic ions, which offer diverse chemistry, various sizes, and potential sustainability benefits, can also be intercalated into MXene interlayers[27,30]. A systematic understanding of how ion solvation impacts the charge storage behavior of these non-metallic ions, especially in cases where the solvated ion's size approaches or exceeds the host's interlayer spacing, is crucial for the development of novel energy storage solutions but is still lacking.

In this study, we investigate the electrochemical intercalation behavior of ammonium ions (NH_4^+) and tetraalkylammonium (TAA) cations ($[CH_3(CH_2)_n]_4N^+$, $n = 0$-2) of different sizes (TMA^+, TEA^+, TPA^+) in few-layered $Ti_3C_2T_x$ (f-$Ti_3C_2T_x$) MXene. NH_4^+ and TAA cations, which share similar tetrahedral symmetry, are selected as model charge carriers to systematically investigate the effects of ion solvation. Unlike strongly solvated NH_4^+ ions, TAA cations are weakly solvated by water molecules due to the hydrophobic methyl groups. Additionally, they usually have solvated ion sizes approach or exceed the intrinsic interlayer spacing of MXenes[31], mimicking a spatial confined environment for ion intercalation without altering the MXene structure. Moreover, the solvation structure of TAA cations can

be tuned by varying the alkyl chain length, enabling a controlled investigation of solvation effects.

To probe the ion intercalation process, we employed operando X-ray diffraction (XRD) to track dynamic interlayer spacing changes during electrochemical cycling, providing direct evidence of reversible intercalation of TAA cations. The gravimetric and viscoelastic property change during ion intercalation was further investigated using electrochemical quartz crystal microbalance with dissipation monitoring (EQCM-D). This study provides new insight into how ion solvation influences the intercalation mechanism and electrochemical behavior of flexible 2D MXenes for non-metallic ion storage.

2.2 Results and discussions

2.2.1 Electrochemical intercalation behavior of f-Ti$_3$C$_2$T$_x$ MXene in ammonium and tetraalkylammonium-based aqueous electrolytes

Few-layered Ti$_3$C$_2$T$_x$ was synthesized by selectively extracting the A-layer from a Ti$_3$AlC$_2$ precursor, followed by the sonication-assisted delamination. The resulting dispersion was vacuum-filtered into a film (f-Ti$_3$C$_2$T$_x$), which was subsequently employed as a self-freestanding electrode for this study. XRD results revealed that f-Ti$_3$C$_2$T$_x$ exhibited a d-spacing of 14.3 Å, corresponding to an interlayer spacing of ca. 5.1 Å (Ti$_3$C$_2$O$_2$ single layer thickness: 9.2 Å), suggesting the intercalation of two layers of water under ambient conditions (**Figure S2.1**)[8,32]. The interlayer spacing of f-Ti$_3$C$_2$T$_x$ was larger than the size of bare NH$_4^+$ (2.9 Å) and the solvated NH$_4^+$ (3.3 Å), whereas, smaller than TMA$^+$ (5.4 Å), TEA$^+$ (6.7 Å), TPA$^+$ (7.6 Å), as well as the solvated TAA cations (7.5 Å ~ 7.8 Å)[33–35]. FTIR spectroscopy was used to study the electrolyte by analyzing the hydrogen bonding of water. The broad stretching signal of -OH showed two maxima at ~3240 cm^{-1} (strong hydrogen bond) and ~3360 cm^{-1} (weak hydrogen bond)[36]. With increasing chain length, the relative intensity of strong hydrogen bonds raised, suggesting weaker interactions between larger TAA cations and water (**Figure S2.2**).

The electrochemical performance of f-Ti$_3$C$_2$T$_x$ in 1 M TMACl, 1 M TEACl, and 0.2 M TPACl electrolytes was evaluated using cyclic voltammetry and galvanostatic charge-discharge (GCD) techniques. In comparison, the charge storage behavior of f-Ti$_3$C$_2$T$_x$ in 1 M NH$_4$Cl was investigated, as NH$_4^+$ ions are more hydrophilic and feature smaller ionic radii. In NH$_4$Cl, f-Ti$_3$C$_2$T$_x$ displayed a rectangular cyclic voltammogram (CV) without noticeable peaks, characteristic of electric double-layer (EDL) behavior[37], within the potential window of -0.8 V ~ 0.2 V vs. Ag/AgCl (in 3.5 M KCl) (**Figure 2.1 a**). In contrast, box-like shaped CVs with a pair of well-separated redox peaks were observed in TAA-based electrolytes, indicative of possible intercalation (**Figure 2.1 b, c & d**). In TMACl, the cathodic and anodic peak

appeared at -0.7 V and -0.5 V (**Figure 2.1 b**), respectively, aligning well with the short plateaus in the GCD curves (**Figure S2.3**). This electrochemical intercalation contrasts with irreversible chemical intercalation, where intercalated TAA cations remain as structural pillars instead of charge carriers during electrochemical cycling[38–40]. Notably, the observed intercalation behavior also differs substantially from the previously reported adsorption behavior of TAA cations onto multi-layered $Ti_3C_2T_x$ powder, where rectangular CV shapes typical of EDL storage was shown[41]. This discrepancy between few-layered and multi-layered $Ti_3C_2T_x$ likely arises from the structural differences, as f-$Ti_3C_2T_x$ exhibits larger, more flexible interlayer spacing, which improves the ion accessibility.

The electrochemical intercalation phenomenon was universal across TAA-based aqueous electrolytes. In TEACl, redox peaks shifted toward more negative potentials (-0.82 V/-0.70 V) (**Figure 2.1 c**). Noteworthy, despite TEA$^+$ ions' bulkier size and more delocalized charge, which typically lead to weaker direct interactions, peak currents increased notably. Reduced capacitance at open circuit potential (OCP) suggested that this enhancement does not stem from the change in double-layer capacitance, but origins from the difference in ion intercalation. Interestingly, while TPA$^+$ is even larger than TEA$^+$, the redox-like peaks appeared at intermediate potential between those of TMA$^+$ and TEA$^+$. This non-monotonic trend in peak potential suggests that the intercalation behavior is governed not solely by ion size, but also strongly influenced by the solvation structure. Unlike TEA$^+$ cations, which maintain relatively open solvation shell, longer alkyl chains of TPA$^+$ enable a more compact solvation structure[42], which may reduce steric hindrance. The rate performance of f-$Ti_3C_2T_x$ in different electrolytes were evaluated based on the CV patterns collected at different scan rates (**Figure S2.4**). f-$Ti_3C_2T_x$ showed slightly higher capacitance in TEACl (58 ± 1 F g^{-1}) and TPACl (55 ± 3 F g^{-1}) compared to TMACl (51 ± 1 F g^{-1}), albeit lower rate retention. To understand the increasing capacitance with ion size, the EDL contribution (based on the capacitance at OCP) and the intercalative contribution to the overall charge was evaluated in different electrolytes at 5 mV s^{-1}. In TMACl, charge storage was predominantly capacitive, with an EDL contribution of 69.6% and an intercalative contribution of 30.4% (**Figure 2.1 e**). As the alkyl chain length increased, intercalative contribution became more dominant, reaching 63.9% in TEACl and further increasing to 75% in TPACl. This increasing intercalative contribution with longer chain length is likely due to weaker solvation of large TAA cation, which may reduce solvent-induced charge screening, thereby enhances charge storage.
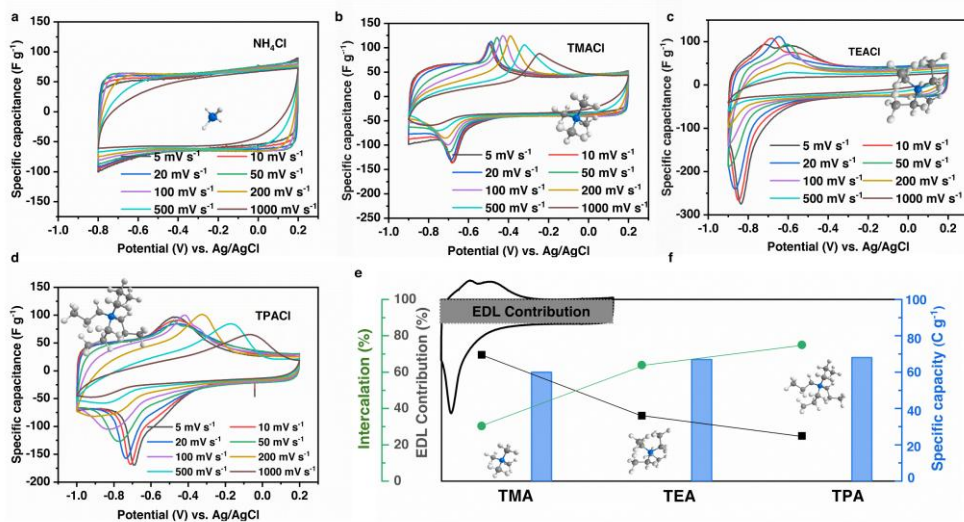
Figure 2.1 Cyclic voltammograms (CV) of f-Ti₃C₂Tₓ in NH₄Cl and tetraalkylammonium chloride electrolytes. CV of f-Ti₃C₂Tₓ in (a) NH₄Cl and (b) TMACl (c) TEACl (d) TPACl electrolyte at different scan rates. (e) EDL and intercalation contribution in tetraalkylammonium chloride electrolytes at 5 mV s⁻¹.

2.2.2 Boosted interlayer spacing by tetraalkylammonium cations intercalation

The dynamic ion intercalation behavior of f-Ti$_3$C$_2$T$_x$ was further investigated by tracking the *d*-spacing change of (0 0 2) plane using operando XRD. Depending on MXenes' functional groups and the electrolyte environment, solvated or bare ions can intercalate into the MXene interlayers, resulting in structural expansion or contraction[23,24,41,43]. During cycling in 1 M NH$_4$Cl electrolyte, no significant change in the interlayer spacing was observed (**Figure S2.5**). However, the absence of detectable peak shifts does not necessarily exclude NH$_4^+$ intercalation but suggests a balance between electrostatic attraction (which pulls layers together) and steric hindrance (which pushes layers apart) caused by solvated NH$_4^+$ ions[8]. In contrast, substantial d-spacing changes were seen in TMACl electrolyte. **Figure 2.2 a** shows the contour map of XRD patterns during the first three CV cycles in TMACl electrolyte, illustrating evolution of the (0 0 *l*) peaks of f-Ti$_3$C$_2$T$_x$. When f-Ti$_3$C$_2$T$_x$ was immersed in the TMACl electrolyte, a downshift to 5.8° was observed for the (0 0 2) peak, reflecting a d-spacing increase of 1 Å, likely due to the spontaneous intercalation of H$_2$O molecules. Upon the first cathodic sweep, at the onset peak potential (-0.7 V vs. Ag), the (0 0 2) peak showed an abrupt shift to a lower angle (4.7°). Simultaneously, new low-angle peaks appeared in the 3°- 4° range, along with a corresponding set of (004) reflection between 6° and 8°. This suggested the coexistence of MXene domains with different interlayer spacings during ion intercalation. Moreover, the occurrence of the (0 0 4) reflection suggested

37

improved stacking ordering of f-Ti$_3$C$_2$T$_x$. During the third cycle, the peak at 4.7° was no longer visible, implying pre-pillaring behavior. **Figure 2.2 b** and **2.2 c** illustrates the d-spacing change during the third CV scan. During charging (cathodic scan), d-spacing of the (0 0 2) plane remained nearly constant at 15.1 Å (interlayer spacing: 6.9 Å) from 0 V to -0.7 V, then expanded significantly at -0.7 V. Due to the limitation of the detector, low-angle measurement was not possible for our system. However, we can estimate the interlayer spacing change based on the (0 0 4) reflection, giving an overall expansion of 16.6 Å compared to the pristine MXene interlayer spacing. Considering the bare ion size of TMA$^+$ (~5.4 Å), this substantial structural expansion suggests that water molecules co-intercalate alongside TMA$^+$ ions, forming a multilayered stacking within the interlayer. During the discharging (anodic scan), the d-spacing of (0 0 2) plane continuously shrank from 31.7 to 23.1 Å from -0.9 V to -0.5 V, and then abruptly decreased to 15.1 Å at -0.5 V (anodic peak), suggesting a stepwise de-intercalation process. Subsequently, the d-spacing remained at 15.1 Å from -0.5 V to 0.1 V. After a full CV cycle, the d-spacing was recovered, indicating that the electrochemical intercalation of TMA$^+$ ions is reversible.

In TEACl electrolyte, f-Ti$_3$C$_2$T$_x$ also showed a notable d-spacing change, with (0 0 4) and (0 0 6) peaks emerging during charging, indicative of enhanced structural ordering by TEA$^+$ intercalation (**Figure 2.2 d**). Specifically, the d-spacing increased abruptly from 15.5 Å to 36.2 Å at -0.8 V, representing a drastic expansion by 20.7 Å (**Figure 2.2 e & f**). Despite this large structural change, f-Ti$_3$C$_2$T$_x$ demonstrated great cycling stability over 5,000 cycles, underscoring its stability against TAA cation intercalation (**Figure S2.6**). To the best of our knowledge, this is the first report of such a reversible and substantial interlayer spacing change upon electrochemical cycling for non-metallic cations, owing to the superior interlayer flexibility of f-Ti$_3$C$_2$T$_x$. Although the quantification of interlayer spacing change was challenging due to fewer detectable diffraction peaks, notable structural expansion also occurred during cycling in TPACl (**Figure S2.7**). The trend of interlayer spacing change revealed from XRD results aligned well with the peaks observed in the CVs, confirming the reversible electrochemical intercalation of TAA cations, irrespective of ionic radius. Given the smaller size of NH$_4^+$ ions compared to TAA cations, it is reasonable to infer that NH$_4^+$ ions can also electrochemically intercalate between the MXene layers during charging process. To confirm the possibility of proton co-intercalation in TAA-based electrolytes, TEACl was mixed with varying concentrations of HCl. As proton concentration increased, the cathodic peak shifted to more negative potentials, indicating that the competition with protons hindered the intercalation of TEA$^+$ (**Figure S2.8**). When the proton concentration reached 0.05 M, a distinct reduction peak at -0.5 V appeared, corresponding to proton intercalation (**Figure S2.8**). This observation implied that the charge storage in neutral tetraalkylammonium chloride electrolytes is primarily attributed to TAA cation intercalation,

ruling out the possibility of proton co-intercalation. Notably, TAA cation intercalation is irreversible in alkaline conditions, as evidenced by the absence of anodic peaks (**Figure S2.9**).
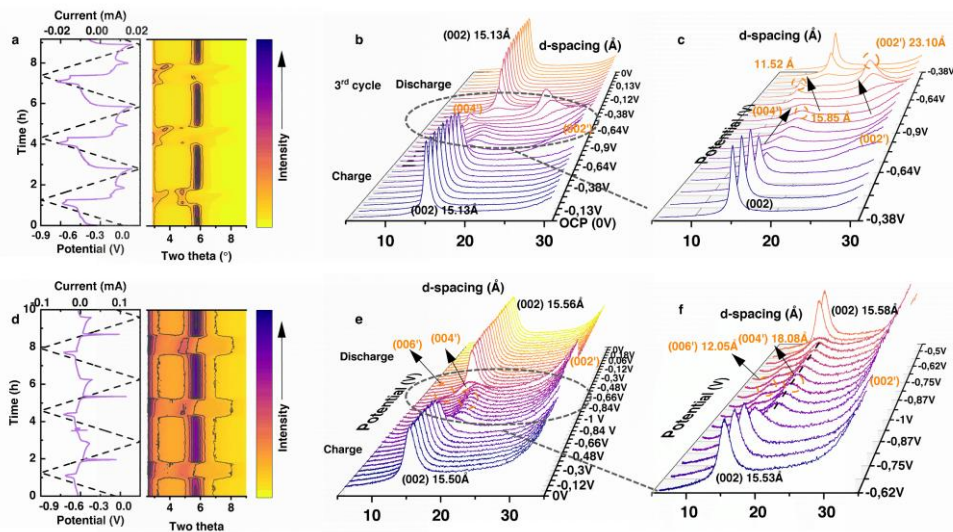

Figure 2.2 Operando X-ray diffraction measurements of Ti$_3$C$_2$T$_x$ in TMACl and TEACl electrolyte. (a) Current-voltage curve and corresponding XRD contour plots during first three electrochemical cycles in TEACl. (b) and (c) Change of d-spacing at different potential during the third cycle in 1 M TMACl. (d) Current-voltage curve and corresponding XRD contour plots during first three electrochemical cycles in TEACl. (e) and (f) Change of d-spacing at different potential during the third cycle in 1 M TEACl.

2.2.3 Significant water co-intercalation with tetraalkylammonium cations

Although XRD measurement provides valuable insights into ion intercalation, it does not directly reveal the water co-intercalation phenomenon. Therefore, electrochemical quartz crystal microbalance with dissipation (EQCM-D) was used to probe the potential-dependent gravimetric and viscoelastic response of f-Ti$_3$C$_2$T$_x$ during ion intercalation. EQCM-D enables simultaneously tracking frequency change (Δf) and dissipation change (ΔD) across multiple overtone orders (n). For rigid electrode, $\Delta D/n$ remains negligible and largely overtone-independent, while $\Delta f/n$ directly reflects gravimetric change according to the Sauerbrey relation $\Delta m = -C \cdot \Delta f/n$, where Δm is the area mass change upon cycling, C is the mass sensitivity constant (56.7 Hz μg^{-1} cm^{-2} for 5 MHz crystal). However, when the electrode exhibits viscoelastic property, due to significant water uptake, both $\Delta f/n$ and $\Delta D/n$ become overtone-dependent and ΔD can no longer be neglected[44]. Noteworthy, to enable the TAA ion intercalation, the EQCM measurement was conducted on a relatively thick film (~150 μg cm^{-2}). **Figure 2.3 a** shows frequency response and electrochemical current versus potential at a scan rate of 50 mV s^{-1} in 1 M NH$_4$Cl. Upon negative polarization, the frequency decreased

linearly, indicating continuous mass gaining due to NH_4^+ ion intercalation. The $\Delta f/n$ (**Figure 2.3 b**) and the $\Delta D/n$ (**Figure 2.3 c**) changes with different overtones, which is a typical feature for relatively thick MXene coating[44]. Despite slight deviations from rigid behavior, a rough estimation of the mass-to-charge ratio using Faraday's law and the Sauerbrey equation yielded a molar mass of ~33 g mol^{-1}, consistent with the co-insertion of one water molecule per NH_4^+ ion (see detailed discussion in the Supporting Information). In 1 M TMACl, obvious redox peaks centered around -0.7 V were observed (**Figure 2.3 d**). During the cathodic scan from -0.1 V to -0.6 V vs. Ag/AgCl, the frequency gradually decreased with relatively low dissipation, consistent with TMA$^+$ adsorption with slight viscoelastic change. However, from the cathodic peak onset (-0.6 V) to its offset (-0.7 V), a boosted ΔD (2×10^{-4}) was observed, reflecting a significant viscoelastic change[45] (**Figures 2.3 f**). Meanwhile, a sudden and substantial decrease in Δf was recorded (**Figures 2.3 d & e**), attributed to both gravimetric change and film softening due to water co-intercalation. This interpretation is supported by the large interlayer expansion captured by operando XRD at the cathodic peak. From -0.7 V to most negative potential (-1 V), no substantial change in Δf (**Figure 2.3 e**) and ΔD (**Figure 2.3 f**) was tracked, indicating saturation of the intercalation process. During the anodic sweep, frequency and dissipation gradually recovered, though with evident hysteresis, indicative of an asymmetric water intercalation/extraction mechanism accompanied with ion insertion/deinsertion. Importantly, the process was highly reversible, with no evidence of electrode delamination or signal degradation over multiple cycles (**Figure 2.3 e & f**). Similar trends were also shown in TEACl and TPACl electrolytes (**Figure S2.10,** see discussion in supplementary materials). These results suggested substantial water co-intercalation with TAA cations despite their weakly solvation nature.
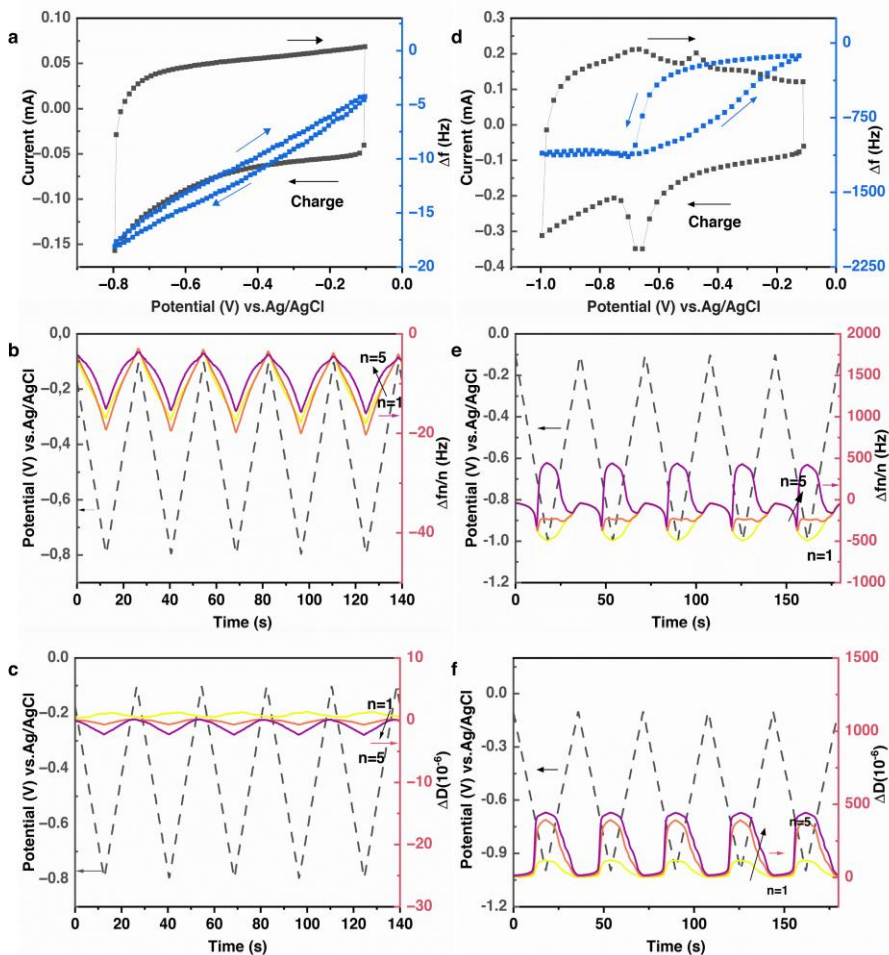
Figure 2.3 Operando EQCM-D measurements of Ti$_3$C$_2$T$_x$ in NH$_4$Cl and TMACl electrolyte. Current-voltage curve and corresponding frequency change at different potential in (a) NH$_4$Cl and (c) TMACl. Frequency change at different cycles in (b) NH$_4$Cl (e) TMACl. Dissipation changes at different cycles in (c) NH$_4$Cl (f) TMACl.

2.2.4 Intercalation dynamics of TAA cations upon cycling

To elucidate the kinetics of TAA cations intercalation, the logarithm of current at peak potential as a function of logarithm of scan rates was plotted and fitted with a linear model. The resulting slope ranged between 0.85 and 0.95 across all electrolytes (NH$_4$Cl, TMACl, TEACl, and TPACl), suggesting predominantly surface-controlled charge storage processes[46] (**Figure 2.4 a**). This is consistent with the nearly vertical slope observed in the

low-frequency region of the Nyquist plots (**Figure 2.4 b**). Moreover, the absence of high-frequency semi-circles reflected negligible charge transfer resistance (**Figure 2.4 b**). The Warburg factor (σ), determined as the slope of the linear fit of the real part of impedance (Z') versus the reciprocal of the square root of frequency ($\omega^{-1/2}$) in the Warburg region[47] (**Figure 2.4 c**), was calculated to assess diffusion kinetics of solvated TAA ion. Interestingly, despite its much larger size, TPA$^+$ exhibited a Warburg factor of 7.2 $\Omega\cdot cm^{-2}\cdot s^{1/2}$, comparable to TMA$^+$ (7.6 $\Omega\cdot cm^{-2}\cdot s^{1/2}$) and was lower than that of TEA$^+$ (σ =14.3 $\Omega\cdot cm^{-2}$ s$^{1/2}$). The large Warburg factor suggested the slowest ion diffusion of TEA$^+$ in Ti$_3$C$_2$T$_x$. Given the significant impact of interlayer water on ion diffusion between MXene layers[48], we hypothesized that the faster ion transport kinetic of TPA is due to the specific arrangement of water molecules in the hydration shell. These water molecules are positioned in the spaces between the alkyl chains of TPA$^+$, with the oxygen atom of the water maintaining a close distance of approximately 3.3 Å from the nitrogen atom[42]. This highlights the importance of solvation structure, beyond mere ionic radius, in determining intercalation kinetics. Impedance measurements at various potentials during the charging process after three cycles further revealed the reaction kinetics in TAA-based electrolytes. **Figure 2.4 d-f** illustrate the 3D bode plots of Ti$_3$C$_2$T$_x$ in TAA-based electrolytes, depicting the real capacitance (C') as functions of frequency and applied potential. A typical waterfall shape regardless of the applied potential was shown in TMACl electrolyte (**Figure 2.4 d**), in good agreement with minimal variation across different potential in the Nyquist plots (**Figure S2.11**). While a dip was observed at -0.9 V and -0.7 V in TEACl and TPACl, respectively, indicating an enhanced pseudocapacitive behavior (**Figure 2.4 e & f**)[49]. This may be attributed to effective charge transport facilitated by lower degree of solvation of TAA cations with longer chain length.
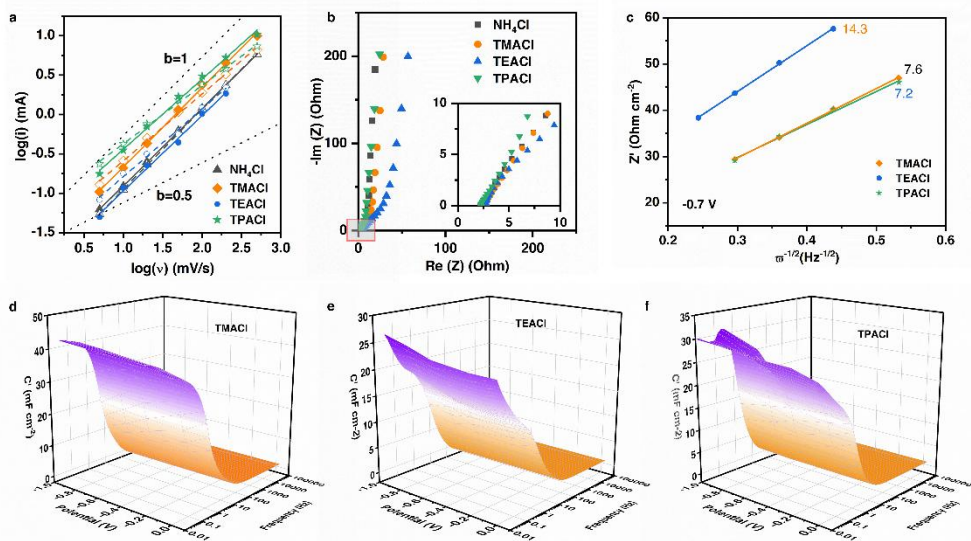
Figure 2.4 Kinetics evaluation of f-Ti$_3$C$_2$T$_x$ in NH$_4$Cl and tetraalkylammonium chloride electrolytes. (a) The relationship between cathodic (solid line) and anodic peak currents (dash line) and scan rates for f-Ti$_3$C$_2$T$_x$. (b) Nyquist plots of f-Ti$_3$C$_2$T$_x$ at open circuit voltage. (c) Linear fit showing the relationship between the real impedance (Z') and $\omega^{-1/2}$ in the Warburg frequency region. 3D Bode maps of real capacitance (C')-potential-frequency (f) of f-Ti$_3$C$_2$T$_x$ electrodes tested in (d) TMACl. (e) TEACl. (f) TPACl.

Interactions between intercalated non-metallic cations and f-Ti$_3$C$_2$T$_x$ were further explored. Hydrogen bonds may form between the positively charged hydrogen atoms of NH$_4^+$ and electronegative surface groups of the f-Ti$_3$C$_2$T$_x$. Evidence for this interaction was supported by X-ray photoelectron spectroscopy (XPS) analysis. For pristine Ti$_3$C$_2$T$_x$, the O 1s spectra were fitted to reveal contributions from Ti-O (529.6 eV), O-Ti-C (530.7 eV), C-Ti-OH (532.2 eV), C-O (533.6 eV), and H$_2$O (535.5 eV) species. After charging in NH$_4$Cl electrolytes, a slight increase in the C-Ti-OH/C-Ti-O ratio was observed, suggesting hydrogen bond formation (**Figure 2.5 c**). This is further corroborated by a downshift of approximately 0.5 eV in the O-Ti-C peak of the C 1s XPS spectra (**Figure 2.5 b**). Additionally, the A$_{1g}$ peak of f-Ti$_3$C$_2$T$_x$ located at 721 cm^{-1} in the Raman spectrum showed a slight redshift to 715 cm^{-1} after charging, which indicates the transformation from Ti=O to Ti-OH[28] (**Figure 2.5 a**). In comparison, much weaker spectral change was observed following intercalation of TAA cations, suggesting weaker interaction with the f-Ti$_3$C$_2$T$_x$.
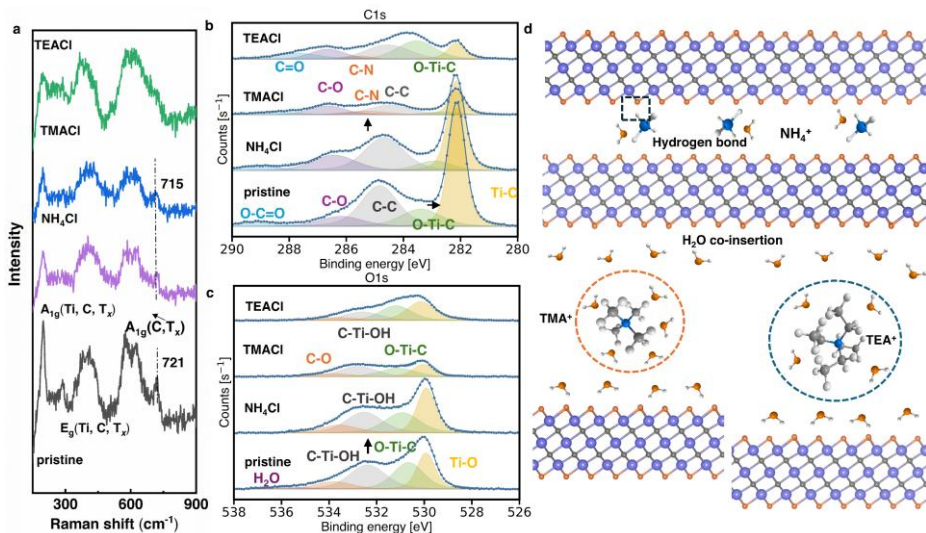
Figure 2.5 Interactions between intercalated ions and f-Ti$_3$C$_2$T$_x$ MXene. (a) Raman Spectroscopy of pristine f-Ti$_3$C$_2$T$_x$ MXene film and charged f-Ti$_3$C$_2$T$_x$ in different electrolytes. **(b)** High-resolution C1s and **(c)** High-resolution O1s X-ray photoelectron spectroscopy (XPS) of pristine f-Ti$_3$C$_2$T$_x$ film and charged f-Ti$_3$C$_2$T$_x$ in different electrolytes. **(d)** Schematics of ammonium and tetraalkylammonium ion storage behavior of f-Ti$_3$C$_2$T$_x$.

In summary, MXene exhibits an adaptive ion intercalation behavior governed significantly by ion solvation structure. The small, strongly solvated NH$_4^+$ ions insert into MXene's spacing with lower solvation level and form hydrogen bonds with MXene's surface groups (**Figure 2.5 d**), resulting in a rectangular shaped CV with minimal structural change. In contrast, the intercalation of large, weakly solvated TAA cations, which exceed the pristine interlayer spacing of MXene, is accompanied by substantial water co-insertion (**Figure 2.5 d**). This reversible water co-intercalation behavior induces pronounced interlayer spacing expansion and mechanical softening, leading to distinct intercalative peaks observed in CV. This finding confirms that the intercalation behavior for non-metallic ions differs fundamentally from that observed for metallic ions, where weaker solvation typically promotes ion desolvation prior to insertion. Instead, our results suggest that water co-intercalation not only persists but may be essential to enable the intercalation of hydrophobic TAA$^+$ cations, possibly by reducing unfavorable interactions with the hydrophilic MXene surface or by stabilizing the expanded interlayer environment.

2.3 Conclusion

In summary, we demonstrate that both ammonium and tetraalkylammonium cations can reversibly intercalate into $Ti_3C_2T_x$ MXene in aqueous electrolytes. While NH_4^+ intercalates in a partially desolvated state, causing minimal structural change, the reversible intercalation of bulkier TAA^+ cations occur with significant water co-insertion, leading to pronounced interlayer expansion. Altogether, this study advances the mechanistic understanding of intercalation phenomena of non-metallic ions in soft, layered materials, and highlights MXene's potential as a platform for probing ion intercalation behavior under nanoconfinement.

2.4 Supplementary information

Methods

Synthesis of Ti₃C₂Tₓ: To synthesize $Ti_3C_2T_x$, 1 g Ti_3AlC_2 was gradually added into a solution of 1.6 g LiF and 20 ml of 9 M HCl. This mixture was kept at 35°C and stirred for 24 hours for etching. Subsequently, the etched material was washed several times with deionized water through centrifugation at 8000 rpm until the pH of the supernatant was neutralized to 6. The remaining sediment was re-dispersed in 40 ml of deionized water and subjected to 1 hour of sonication under an argon atmosphere to facilitate the delamination of the multilayers. The suspension was then centrifuged at 3500 rpm for 1 hour, and the clear supernatant was collected, yielding a few-layered $Ti_3C_2T_x$ colloidal solution. The f-$Ti_3C_2T_x$ film was then obtained through vacuum-assisted filtration and utilized as an electrode for subsequent characterization.

Electrochemical measurements: Electrochemical performance was evaluated using Swagelok cells configured in a three-electrode setup with a Biologic VSP-300 potentiostat. In this configuration, the free-standing $Ti_3C_2T_x$ films served as the working electrode, Ag/AgCl (3.5 M KCl) and activated carbon were used as the reference and counter electrodes, respectively. The electrolytes consisted of 1 M aqueous solutions of NH_4Cl, TMACl, and TEACl, and 0.2 M TPACl respectively, while Whatman GF-A films served as separators. Cyclic voltammetry was conducted over scan rates ranging from 5 mV s^{-1} to 1 V s^{-1}. For galvanostatic charge and discharge (GCD) tests, current densities varied from 0.2 A g^{-1} to 10 A g^{-1}. Electrochemical impedance spectroscopy was performed with a 10 mV amplitude across a frequency range of 10 mHz to 200 kHz. The gravimetric specific capacitance derived from cyclic voltammetry is calculated using the formula:

$$C(\text{F g}^{-1}) = \frac{\int i \mathrm{d}v}{m\, s\, \Delta V}$$

where *i* represents the current (A), *s* is the scan rate (V s^{-1}), *m* is the mass of the working electrode (g), and ΔV is the applied voltage window (V).

The real capacitance (C′) was calculated using the following equations:

$$C' = \frac{-Z''}{2\,\pi f\,|Z|^2}$$

Where |Z| represents the absolute value of impedance (Ω), f stands for frequency (Hz), Z″ is the imaginary component of impedance(Ω), respectively.

Material characterization: X-ray diffraction (XRD) analyses were performed using a PANalytical X'Pert Pro X-ray diffractometer, equipped with Cu Kα radiation ($\lambda = 0.1542$ nm) at 45 kV and 40 mA, over a 2θ range of 5° to 65°. *In-situ* XRD patterns were collected over a 2θ range of 2.5° to 15°, with 0.02° increments and at a scan rate of 2.5° per minute, simultaneously with CV measurements at a scan rate of 0.2 mV s^{-1}, using a Biologic VSP-300 potentiostat. FTIR measurements were conducted to characterize the electrolytes using a Thermo Scientific Nicolet iS50 FTIR spectrometer equipped with iS50 ATR module. Raman spectroscopy was conducted using the Renishaw instrument with a 514 nm laser (1800 lines/mm grating). X-ray photoemission spectroscopy (XPS) was conducted using a Thermo Fisher K-Alpha surface spectrometer, which utilized monochromatic Al Kα radiation (1486.6 eV) as the X-ray source. The instrument was operated at 36 W (12 kV, 3 mA), with a flood gun set to 1 V and 100 μA, and a spot size of approximately 800 x 400 μm. The spectra were calibrated by hydrocarbon C1s peak at 284.8 eV. EQCM-D experiments were performed using an AWSensors X1 QCM-D equipped with temperature control unit. The frequency and dissipation change at different states of charge was recorded by applying cyclic voltammetry at 50 mV s^{-1} with a Biologic potentiostat in a three-electrode in-batch cell setup. Ti$_3$C$_2$T$_x$ dispersion (2 mg ml^{-1}) was spray-coated on 5 MHz Ti/Au quartz sensors (AWSensors) at 60-degree Celsius with a mass loading around 150 μg/cm^2 and used as the working electrode. The Ti wire served as counter electrode and the reference electrode was Ag/AgCl in 3.5 M KCl.
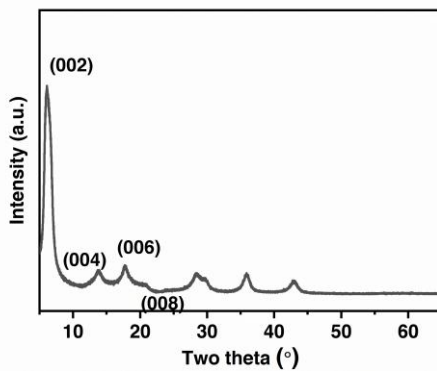
Figure S 2.1 Bragg-Brentano X-ray diffraction of f-Ti$_3$C$_2$T$_x$ film.
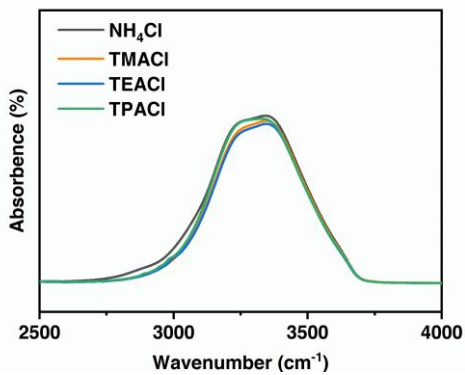
Figure S 2.2 Fourier transform infrared (FTIR) spectroscopy of different electrolytes.

47
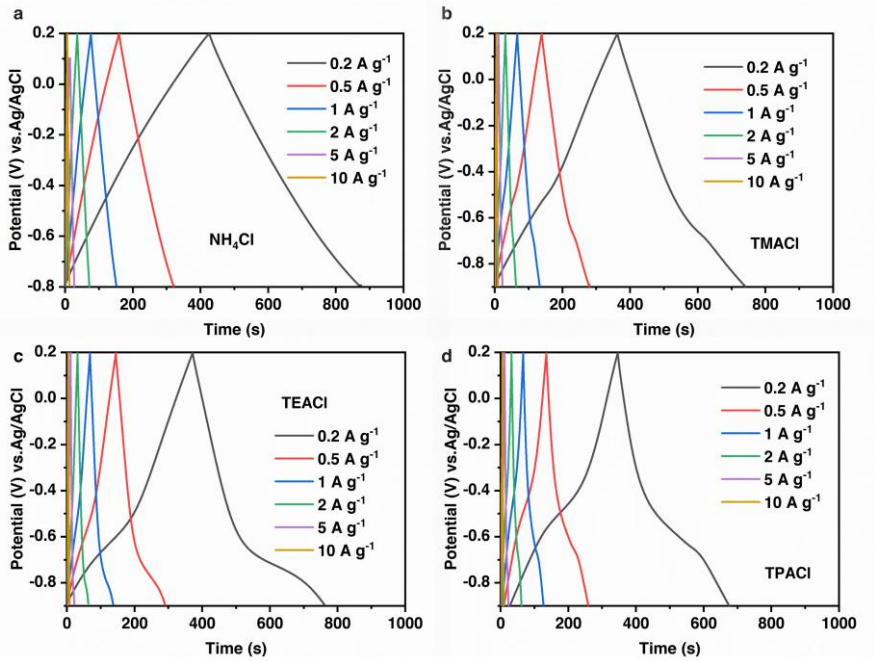
Figure S 2.3 Electrochemical performance of f-Ti$_3$C$_2$T$_x$. Galvanostatic charge-discharge (GCD) curves of f-Ti$_3$C$_2$T$_x$ in (a) NH$_4$Cl (b) TMACl (c) TEACl. (d) TPACl electrolyte at different current densities.
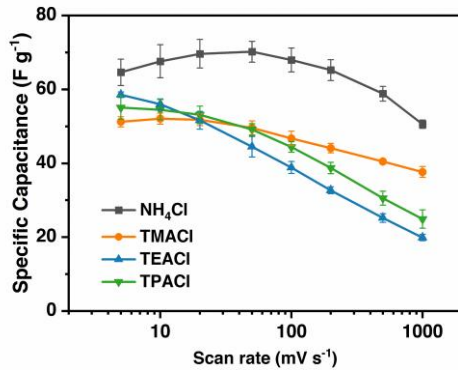

Figure S 2.4 Rate performance of f-Ti$_3$C$_2$T$_x$.
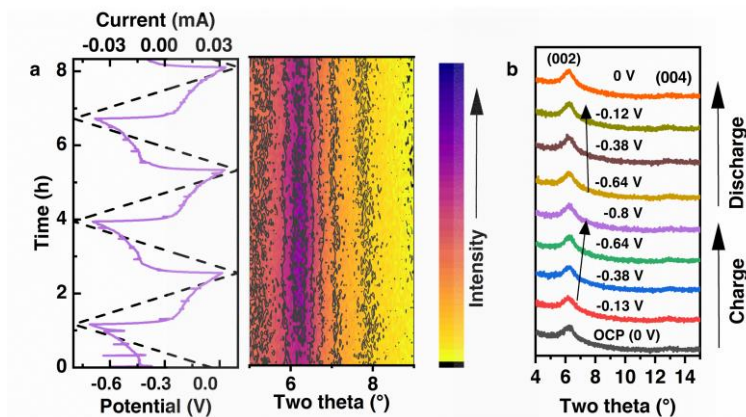
Figure S 2.5 Operando X-ray diffraction measurements of f-Ti$_3$C$_2$T$_x$ in NH$_4$Cl. (a) Current-voltage curve and corresponding XRD Contour plots during first three electrochemical cycles. (b) XRD pattern showing (0 0 2) peak at different potential during the third CV cycle in 1 M NH$_4$Cl.
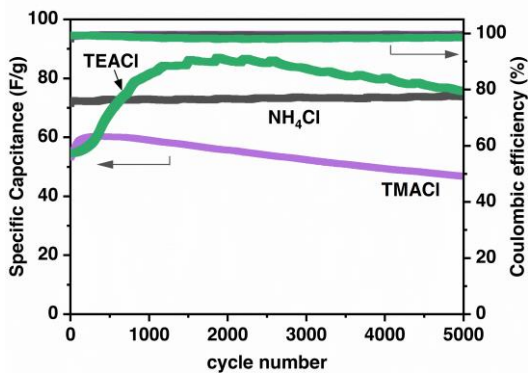
Figure S 2.6 Cycling performance of f-Ti$_3$C$_2$T$_x$ in 1 M NH$_4$Cl, TMACl and TEACl electrolyte at 1 A g^{-1}.
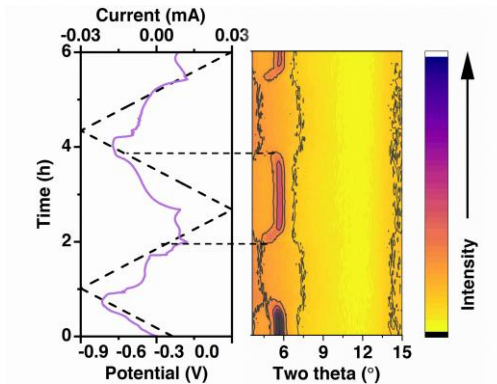
Figure S 2.7 Operando XRD measurement of f-Ti$_3$C$_2$T$_x$ in 0.2 M TPACl.
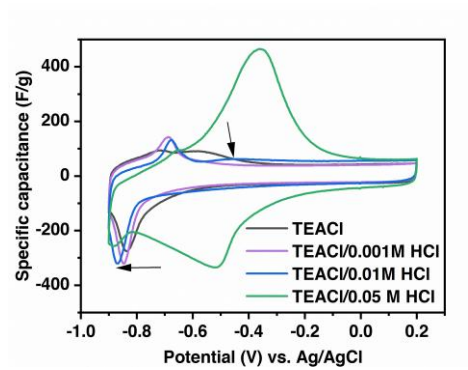
Figure S 2.8 CVs of f-Ti$_3$C$_2$T$_x$ collected at 5 mV s^{-1} in TEACl-HCl hybrid electrolytes.
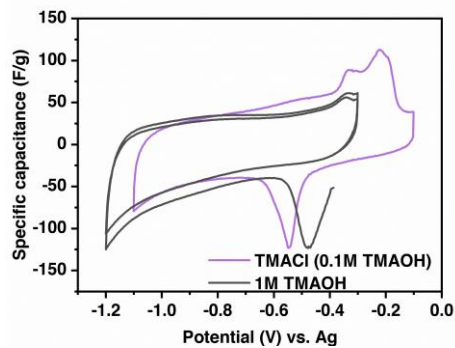
Figure S 2.9 CVs of f-Ti$_3$C$_2$T$_x$ collected at 5 mV s^{-1} in TMACl-TMAOH hybrid electrolytes.

50

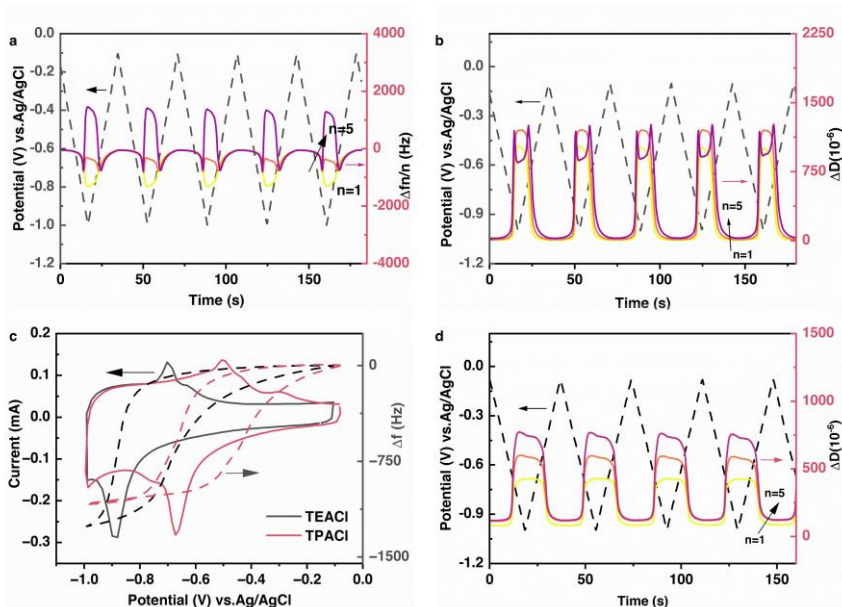**Reversibly Electrochemical Intercalation of Ammonium and Tetraalkylammonium Cations in Ti3C2Tx MXene**

Figure S 2.8 Operando EQCM-D measurements of $Ti_3C_2T_x$ in 1 M TEACl and 0.2 M TPACl electrolyte. (a) Frequency and (b) Dissipation change at different cycles in TEACl. (c) Current-voltage curve and corresponding frequency change at different potential in TEACl and TPACl. (d) Dissipation changes at different cycles in TPACl.

Supplementary discussion:

An approximate molecular weight of charge carrier in NH_4Cl was calculated based on following equation while assuming a rigid coating during cycling considering relatively small dissipation change: $M = n F \Delta f_1 / A q C_f$, where M is the atomic mass of the charge species (g mol^{-1}), n is the electron transfer number per unit (assume n=1), F is the Faraday constant (96485 C mol^{-1}), Δf_1 is the frequency change (Hz) at fundamental frequency, q is accumulated charge (C), C_f is mass sensitivity constant (56.6 Hz μg^{-1} cm^{-2}), A is the area of coating (cm^2). Therefore, the atomic mass of charge carrier can be estimated by fitting the Δf_1-q curve (the slope gives a value of M= 33 g mol^{-1}). In 1 M TEACl, the cathodic/anodic peak located at -0.9 V/-0.8 V, respectively, at a scan rate of 50 mV s^{-1} (**Figure S2.10 c**). During the cathodic scan, a gradual decrease in frequency was observed from -0.1 V to -0.8 V with relatively low dissipation (**Figure S2.10 a-b**), indicative of mass uptake with limited mechanical softening. A pronounced transition occurred between -0.8 V and -1.0 V, where the frequency dropped sharply by 10^3 Hz, and the dissipation factor increased to 9×10^{-4} (**Figure S2.10 b**), suggesting a significant viscoelastic response due to substantial water co-intercalation along with TEA^+. During the anodic scan, a gradual increase in frequency and a concurrent decrease in

dissipation were observed between -1.0 V and -0.8 V. A more abrupt increase in frequency and a marked decrease in dissipation followed from -0.8 V to -0.5 V, consistent with de-intercalation of both TEA$^+$ and H$_2$O. The dissipation eventually returned to baseline values (~6 ×10^{-6}), indicating the recovery of rigidity.

To enable a fair comparison with TPACl under the same film thickness, the TEACl-cycled electrode was thoroughly rinsed with deionized water and reused in 1 M TPACl. After 20 conditioning cycles to stabilize the electrochemical response, the changes in frequency and dissipation were recorded (**Figure S2.10 c**). As shown in **Figure S2.10 c-d**, the frequency/dissipation change in TPACl follows similar trends as TEACl, with a more positive turning point at -0.6 V. Moreover, both the Δf and ΔD were considerably smaller in TPACl. Given that the charge storage capacities in TEACl and TPACl are similar, one would expect a larger frequency shift in TPACl due to the higher molar mass of TPA$^+$, if the extent of water co-intercalation were comparable. However, the experimentally observed lower Δf and ΔD suggest reduced water uptake in the TPACl system compared to TEACl. Different degrees of water co-intercalation may result from the interplay between solvation energy, steric hindrance from alkyl chains, and ion accessibility within the MXene interlayers.
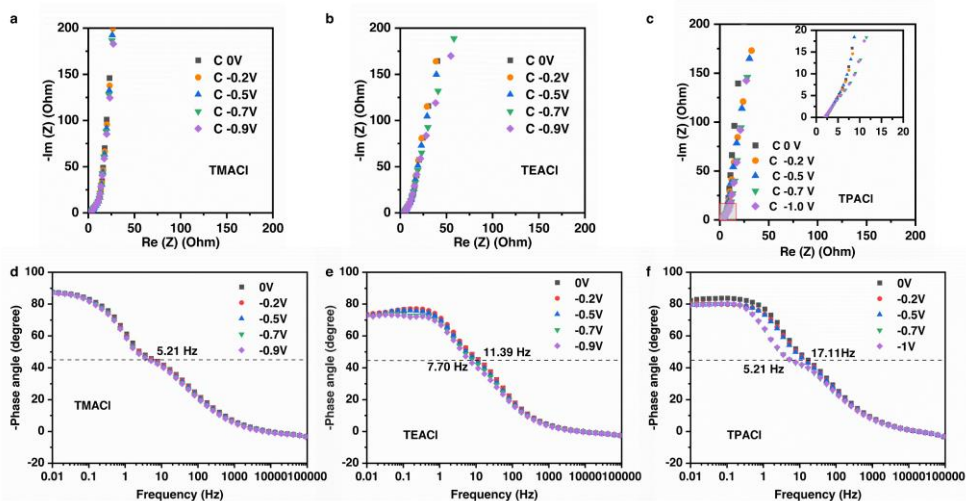

Figure S 2.9 Impedance analysis. Nyquist plots of f-Ti$_3$C$_2$T$_x$ at different potentials during charging process in (a) TMACl, (b) TEACl and (c) TPACl after three CV cycles. Bode plots of f-Ti$_3$C$_2$T$_x$ at different potentials during charging process in (d) TMACl, (e) TEACl and (f) TPACl after three CV cycles.

2.5 Reference

[1]   N. Kittner, F. Lill, D. Kammen, *Nat. Energy* **2017**, *2*.

[2]   E. Pomerantseva, Y. Gogotsi, *Nat. Energy* **2017**, *2*.

[3]   B. Mendoza-Sánchez, Y. Gogotsi, *Adv. Mater.* **2016**, *28*, 6104.

[4]   X. Li, Z. Huang, C. E. Shuck, G. Liang, Y. Gogotsi, C. Zhi, *Nat. Rev. Chem*. **2022**, *6*, 389.

[5]   B. Anasori, M. R. Lukatskaya, Y. Gogotsi, *Nat. Rev. Mater.* **2017**, *2*, 16098.

[6]   M. R. Lukatskaya, S. Kota, Z. Lin, M.-Q. Zhao, N. Shpigel, M. D. Levi, J. Halim, P.-L. Taberna, M. W. Barsoum, P. Simon, Y. Gogotsi, *Nat. Energy* **2017**, *2*, 1.

[7]   Y. Ando, M. Okubo, A. Yamada, M. Otani, *Adv. Funct. Mater.* **2020**, *30*, 2000820.

[8]   X. Mu, D. Wang, F. Du, G. Chen, C. Wang, Y. Wei, Y. Gogotsi, Y. Gao, Y. Dall'Agnese, *Adv. Funct. Mater.* **2019**, *29*, 1902953.

[10]   L. Liu, E. Raymundo-Piñero, S. Sunny, P.-L. Taberna, P. Simon, *Angew. Chem.* **2024**, *63*, e202319238.

[11]   M. R. Lukatskaya, *Adv. Energy Mater.* **2015**, *5*, 1500589.

[12]   S. Fleischmann, Y. Zhang, X. Wang, P. T. Cummings, J. Wu, P. Simon, Y. Gogotsi, V. Presser, V. Augustyn, *Nat. Energy* **2022**, *7*, 222.

[13]   H. Guo, M. Elmanzalawy, P. Sivakumar, S. Fleischmann, *Energy Environ. Sci.* **2024**, *17*, 2100.

[14]   X. Chen, Q. Zhang, *Acc. Chem. Res.* **2020**, *53*, 1992.

[15]   D. Kundu, S. Hosseini Vajargah, L. Wan, B. Adams, D. Prendergast, L. F. Nazar, *Energy Environ. Sci.* **2018**, *11*, 881.

[16]   K. Woo Nam, H. Kim, J. Hyeok Choi, J. Wook Choi, *Energy Environ. Sci.* **2019**, *12*, 1999.

[17]   J. Chmiola, G. Yushin, Y. Gogotsi, C. Portet, P. Simon, P. L. Taberna, *Science* **2006**, *313*, 1760.

[18]   C. Largeot, C. Portet, J. Chmiola, P.-L. Taberna, Y. Gogotsi, P. Simon, *J. Am. Chem. Soc.* **2008**, *130*, 2730.

[19]   Y. Liu, Y. Zhu, Y. Cui, *Nat. Energy* **2019**, *4*.

[20]   X. Zhang, S. Yang, X. Shan, S. Li, S. Tang, *Phys. Chem. Chem. Phys.* **2019**, *21*, 23697.

[21]   Y. Guo, X. Hong, Y. Su, W. Luo, R. Yu, J. Wu, E. J. M. Hensen, L. Mai, Y. Cao, *Small* **2021**, *17*, 2104649.

[22]   K. Ge, H. Shao, E. Raymundo-Piñero, P.-L. Taberna, P. Simon, *Nat. Commun.* **2024**, *15*, 1935.

[23]   X. Wang, T. S. Mathis, Y. Sun, W.-Y. Tsai, N. Shpigel, H. Shao, D. Zhang, K. Hantanasirisakul, F. Malchik, N. Balke, D. Jiang, P. Simon, Y. Gogotsi, *ACS Nano* **2021**, *15*, 15274.

[24]   C. Chen, A. de Kogel, M. Weijers, L. J. Bannenberg, X. Wang, *2D Mater.* **2023**, *11*, 015001.

[29]   X. Wang, T. S. Mathis, K. Li, Z. Lin, L. Vlcek, T. Torita, N. C. Osti, C. Hatter, P. Urbankowski, A. Sarycheva, M. Tyagi, E. Mamontov, P. Simon, Y. Gogotsi, *Nat. Energy* **2019**, *4*, 241.

[26]   M. R. Lukatskaya, O. Mashtalir, C. E. Ren, Y. Dall'Agnese, P. Rozier, P. L. Taberna, M. Naguib, P. Simon, M. W. Barsoum, Y. Gogotsi, *Science* **2013**, *341*, 1502.

[27]   N. Shpigel, M. D. Levi, S. Sigalov, T. S. Mathis, Y. Gogotsi, D. Aurbach, *J. Am. Chem. Soc.* **2018**, *140*, 8910.

[27]   D. Zhang, R. (John) Wang, X. Wang, Y. Gogotsi, *Nat. Energy* **2023**, *8*, 567.

[29]   D. Johnson, K. Hansen, R. Yoo, A. Djire, *ChemElectroChem* **2022**, *9*, e202200555.

[30]   G. Liang, F. Mo, X. Ji, C. Zhi, *Nat. Rev. Mater.* **2021**, *6*, 109.

[31]   M. Lu, W. Han, H. Li, W. Zhang, B. Zhang, *J. Energy Chem.* **2020**, *48*, 344.

[32]   Y. Sun, C. Zhan, P. R. C. Kent, M. Naguib, Y. Gogotsi, D. Jiang, *ACS Appl. Mater. Interfaces* **2020**, *12*, 763.

[33]   R. Zheng, Y. Li, H. Yu, X. Zhang, D. Yang, L. Yan, Y. Li, J. Shu, B.-L. Su, *Angew. Chem.* **2023**, *62*, e202301629.

[34]   Y. Marcus, *J. Solution Chem.* **2008**, *37*, 1071.

[35]   Y. Nagano, M. Sakiyama, T. Fujiwara, Y. Kondo, *J. Phys. Chem.* **1988**, *92*, 5823.

54

[36]   S. Strazdaite, J. Versluis, H. J. Bakker, *J. Phys. Chem. C* **2016**, *120*, 17290.

[37]   S. Fleischmann, J. B. Mitchell, R. Wang, C. Zhan, D. Jiang, V. Presser, V. Augustyn, *Chem. Rev.* **2020**, *120*, 6738.

[38]   M. Ghidiu, S. Kota, J. Halim, A. W. Sherwood, N. Nedfors, J. Rosen, V. N. Mochalin, M. W. Barsoum, *Chem. Mater.* **2017**, *29*, 1099.

[39]   H. Wang, M. Yoshio, *J. Power Sources* **2012**, *200*, 108.

[40]   R. Zhao, L. Zhang, C. Wang, L. Yin, *J. Power Sources* **2017**, *353*, 77.

[41]   M. D. Levi, M. R. Lukatskaya, S. Sigalov, M. Beidaghi, N. Shpigel, L. Daikhin, D. Aurbach, M. W. Barsoum, Y. Gogotsi, *Adv. Energy Mater.* **2015**, *5*, 1400815.

[42]   J. T. Slusher, P. T. Cummings, *J. Phys. Chem. B* **1997**, *101*, 3818.

[43]   Y. Li, H. Shao, Z. Lin, J. Lu, L. Liu, B. Duployer, P. O. Å. Persson, P. Eklund, L. Hultman, M. Li, K. Chen, X.-H. Zha, S. Du, P. Rozier, Z. Chai, E. Raymundo-Piñero, P.-L. Taberna, P. Simon, Q. Huang, *Nat. Mater.* **2020**, *19*, 894.

[44]   N. Shpigel, M. R. Lukatskaya, S. Sigalov, C. E. Ren, P. Nayak, M. D. Levi, L. Daikhin, D. Aurbach, Y. Gogotsi, *ACS Energy Lett.* **2017**, *2*, 1407.

[45]   K. M. Persson, R. Gabrielsson, A. Sawatdee, D. Nilsson, P. Konradsson, M. Berggren, *Langmuir* **2014**, *30*, 6257.

[46]   T. S. Mathis, N. Kurra, X. Wang, D. Pinto, P. Simon, Y. Gogotsi, *Adv. Energy Mater.* **2019**, *9*, 1902007.

[47]   S. Yadav, N. Kurra, *Energy Storage Mater.* **2024**, *65*, 103094.

[48]   J. Wen, Q. Fu, W. Wu, H. Gao, X. Zhang, B. Wang, *ACS Appl. Mater. Interfaces* **2019**, *11*, 7087.

[49]   N. Kurra, S. Uzun, G. Valurouthu, Y. Gogotsi, *Energy Storage Mater.* **2021**, *39*, 347.

3 High-rate Polymeric Redox in MXene-based Superlattice-like Heterostructure for Ammonium Ion Storage

Abstract:

Achieving both high redox activity and rapid ion transport is a critical and pervasive challenge in electrochemical energy storage applications. This challenge is significantly magnified when using large-sized charge carriers, such as the sustainable ammonium ion (NH_4^+). We report a self-assembled MXene/n-type conjugated polyelectrolyte (CPE) superlattice-like heterostructure that enables redox-active, fast, and reversible ammonium storage. The superlattice-like structure persists as the CPE:MXene ratio increases, accompanied by a linear increase in the interlayer spacing of MXene flakes and a greater overlap of CPE units. Concurrently, the redox activity per unit of CPE unexpectedly intensifies, a phenomenon that can be explained by the enhanced de-solvation of ammonium due to the increased volume of 3 Å-sized pores, as indicated by molecular dynamic simulations. At the maximum CPE mass loading (MXene:CPE ratio=2:1), the heterostructure demonstrates the strongest polymeric redox activity with a high ammonium storage capacity of 126.1 C g^{-1} and a superior rate capability at 10 A g^{-1}. This work unveils an effective strategy for designing tunable superlattice-like heterostructures to enhance redox activity and achieve rapid charge transfer for ions beyond lithium.

3.1 Introduction

Electrochemical energy storage (EES) devices, including rechargeable batteries and capacitors, are in increasing demand due to integrating more renewable energy sources into the grid and the growing adoption of electric vehicles[1,2]. Consequently, besides the imperative of enhancing performance, the significance of employing sustainable materials and green processes in the battery industry has escalated with the perspective of mitigating ecological implications[3]. Lithium-ion batteries dominate the EES industry due to their high energy density and relatively long cycling life. Sustainability concerns, however, have arisen due to the substantial consumption of lithium and specific transition metals, leading to resource depletion and increased raw materials costs[4]. Furthermore, the reliance on organic solvents in electrolytes and during electrode fabrication processes leads to safety hazards and environmental risks[5]. Aqueous ammonium ion (NH_4^+) storage is an emerging sustainable EES option, given that its electrolyte comprises earth-abundant elements that are theoretically unlimited[6]. However, NH_4^+ as a charge carrier exhibits distinct EES characteristics compared to metal ions due to its nestled charge and tetrahedral structure. It interacts with electrodes through hydrogen bonds and exhibits preferred orientations[7]. Hydrogen bond formation may lead to smaller electrochemical polarization and faster kinetics when NH_4^+ ions are used as charge carriers in some transition metal-based layered materials (V_2O_5 and Cobalt-nickel double hydroxide), compared to Na^+ or K^+ charge carriers[8,9].

Typical cathode materials for NH_4^+ storage include Prussian blue analogues (PBAs), vanadium-based oxides and manganese-based compounds[8,10,11], which typically possess flexible structures with spacious and adjustable internal voids. For instance, copper hexacyanoferrate (CuHCF), with its open framework, can undergo reversible NH_4^+ intercalation at 1.02 V (vs. S.H.E.), accompanied by the conversion between Cu^{2+} and Cu^+, resulting in a specific capacity of 60 mAh g^{-1} at 50 mA g^{-1}[10]. The selection of anode materials is constrained by the need for low intercalation potential, with transition metal sulfides and organic materials being the typical choices for anode materials[12–14]. Organic materials undergo reversible volumetric redox reactions concomitant with ammonium adsorption/desorption, thereby enabling a high NH_4^+ storage capacity[7,13,15]. For example, 3,4,9,10-perylenetetracarboxylic diimide demonstrated a capacity of 119 mAh g^{-1} and a good cycling stability at low rates[16]. However, organic electrodes typically encounter diffusion-limited redox activities and structural degradation at high charging rates, further exacerbated when large-sized NH_4^+ charge carriers are used. Developing materials capable of sustaining robust redox activity and structural integrity at elevated rates with NH_4^+ is particularly important for aqueous systems.

A promising candidate for high-rate EES is the family of two-dimensional early transition metal carbides and/or nitrides, known as MXenes. MXenes are characterized by a general formula of $M_{n+1}X_nT_x$ (n=1-4), where M, X, and T_x represent the transition metal, carbon/nitrogen, and surface groups, respectively[17]. They stand out for their excellent high-rate performance and long cycling life in various electrolytes, attributed to their superior electronic conductivity and flexible interlayer spacing[18–20]. Additionally, the abundant surface groups of MXenes can facilitate rapid surface redox reactions with various intercalated ions, contributing to pseudocapacitive behavior[21,22]. MXene as an NH_4^+ host, demonstrates highly reversible NH_4^+ storage capability, albeit yielding a moderate capacitance of ~ 50 F g^{-1}. This moderate capacitance is attributed to its weak surface interaction with NH_4^+ and a reduced ion accessibility caused by the restacking of 2D MXene layers[23]. Constructing MXene/conductive polymer heterostructures represents an efficient strategy to enhance redox activity and alleviate restacking issues of MXenes. Simultaneously, MXene offers a conductive framework and confinement for polymer chains, thereby enhancing charge transfer and prolonging cycling life. This synergistic effect between MXene and a polymer has been successfully utilized to enhance proton storage capacity in sulfuric acid electrolytes.[24,25] For example, $Ti_3C_2T_x$ MXene/polypyrrole (PPy) composite, which was prepared by *in-situ* polymerization of PPy in-between $Ti_3C_2T_x$ layers, showed a high capacitance and an excellent cycling stability, up to 25000 cycles[25].

Evenly-spaced and interconnected MXene-based heterostructure with ordered 2D stacking can maximize the heterogeneous interface between MXenes and polymers, which is crucial for leveraging the synergistic effect. Such an ordered structure has demonstrated great promise in significantly enhancement in the mechanical properties[26]. However, the formation of MXene-polymer composites often disrupts the ordered stacking of 2D MXenes, preventing the full exploitation of the benefits inherent in the heterogeneous structure. Moreover, MXene has been primarily composited with various p-type polymers, including, PPy, polyaniline,[27] and poly(3,4-ethylenedioxythiophene),[28] which require positive potentials to fully utilize their redox properties. On the other hand, MXene is susceptible to irreversible oxidation at positive potentials (ca. ~ 0.2 V vs. Ag) and is predominantly redox-active in the negative potential range ($\sim$ -1.2 V to 0 V vs. Ag in neutral aqueous electrolytes)[23,29]. This limits the application of MXene/p-type polymer composites to the negative potential range, where the redox activity and pseudocapacitance contribution of p-type polymers are not fully accessible. This motivates the design of a novel MXene-polymer heterostructure with an ordered structure, and a matched redox-active working window.

This work reports a superlattice-like MXene@conjugated polyelectrolyte (CPE) heterostructure, enabling high-rate and redox-active ammonium ion storage. CPEs are characterized by conjugated polymer backbones appended with ionic side chains and have

60

recently demonstrated high-rate pseudocapacitive performance for alkali ions[30,31]. For instance, a p-type CPE-K film can deliver a high rate performance of 67 F g^{-1} at 100 A g^{-1} as a positive electrode for K$^+$ storage, due to the presence of an ionic lattice in its ordered structure[30]. As an n-type CPE, p(cNDI-gT2) comprises alternating naphthalene-1,4,5,8-tetracarboxylic diimide (NDI) and 3,3'-dialkoxybithiophene structural units. The ammonium cationic functionalities on the side chain endow p(cNDI-gT2) with water solubility. Leveraging the excellent water solubility of Ti$_3$C$_2$T$_x$ and p(cNDI-gT2) CPE and their oppositely charged surfaces, we synthesized the Ti$_3$C$_2$@CPE heterostructures via a facile and green self-assembly process in water. In Ti$_3$C$_2$@CPE composites, CPE is confined and realigned in the interlayer of Ti$_3$C$_2$T$_x$, increasing the interlayer spacing of MXene. The resulting Ti$_3$C$_2$@CPE composites showed a periodic layered stacking pattern perpendicular to the base plane of MXene, resembling a superlattice structure. Notably, with increased CPE:MXene ratio, the ordered layered structure was maintained with a linear expansion in the interlayer spacing, attributed to the gradual overlay of CPE between MXene layers. Such a superlattice-like configuration enables heterostructures with effective charge transfer and improved structural stability. Unexpectedly, a higher CPE loading in the heterostructure enhances the polymeric redox (or polymer utilization) per unit of polymer. Hereby the Ti$_3$C$_2$@CPE 2:1 electrode with the highest CPE loading delivered a high specific charge of 126.1 C g^{-1} at 0.1 A g^{-1} (1.5 times higher than that of Ti$_3$C$_2$T$_x$), and a superior rate capability (102.8 C g^{-1} at 10 A g^{-1}) in combination with a long cycling life (10 000 cycles) for NH$_4^+$ ion storage.

3.2 Results and discussions

3.2.1 Highly ordered Ti$_3$C$_2$@CPE heterostructure

Figure 3.1 a illustrates the preparation of p(cNDI-gT2) CPE and Ti$_3$C$_2$T$_x$ MXene, as well as the self-assembly process between the two components in water. CPEs are polymers characterized by conjugated backbones bearing ionic functionalities that enable synthetically tunable physico-electrochemical property[31,32]. We chose p(cNDI-gT2) due to the following key structural features: 1) electron-accepting naphthalene diimide (NDI) units in the conjugated backbone confer the CPE a negative redox potential window (-0.9 ~ 0.3 V vs. Ag/AgCl) matching that of the MXene; 2) cationic quaternary ammonium groups on the side chains facilitates water-processability and electrostatic-driven self-assembly with negatively-charged MXene flakes; and 3) oligo(ethylene glycol) side chains further enhance water-processability and ionic transport[33]. p(cNDI-gT2) was synthesized via direct arylation polymerization (DAP), followed by a post-functionalization step to install cationic groups on the side chains of the NDI unit[33]. Due to polar side chains, p(cNDI-gT2) can be well dispersed in water with a positive zeta potential of +61 mV (**Figure S3.1**). Ti$_3$C$_2$T$_x$ was

prepared by *in-situ* HF etching from the Ti_3AlC_2 precursor, followed by sonication-assisted delamination (**Figure 3.1 a**)[17]. Due to the existence of the hydrophilic surface groups, MXene usually shows a zeta potential from -80 to -30 mV in water,[34] enabling it to be assembled with positive charged p(cNDI-gT2) CPE through complementary electrostatic interactions. The facile self-assembly of $Ti_3C_2T_x$ and CPE was performed by mixing $Ti_3C_2T_x$ and the p(cNDI-gT2) water solution in various weight ratios (10:1, 5:1, and 2:1 of $Ti_3C_2T_x$-to-p(cNDI-gT2)). The resulting composites are denoted as Ti_3C_2@CPE r:1, where 'r' signifies the weight ratio of $Ti_3C_2T_x$-to-p(cNDI-gT2). Upon the addition of CPE to the MXene solution, self-assembly takes place immediately (depicted in **Figure 3.1 a**), as agglomeration was observed within a few seconds, yielding precipitates (**Figure S3.2**). The maximum CPE loading that can be assembled with MXene is observed at an $Ti_3C_2T_x$:CPE ratio of 2:1. The agglomerates were obtained as flexible and self-freestanding films (**Figure S3.3**) by vacuum-assisted filtration, followed by drying at room temperature in a desiccator, while excessive CPE remained in the filtrate (as illustrated in **Figure 3.1 a**).

Bragg-Brentano X-ray diffraction (XRD) was employed to gain insights into the structure of Ti_3C_2@CPE films. The XRD pattern of p(cNDI-gT2) in the powder form displays a diffraction peak at $2\theta = 5°$ (**Figure S3.4**) that indicates interchain lamellar stacking, and a broad peak at $2\theta = 23°$ that corresponds to π-stacking of the conjugated backbones[35]. In contrast, the Ti_3C_2@CPE films only showed the signal of (0 0 *l*) diffraction peaks characteristic of $Ti_3C_2T_x$, indicating a preferential horizontal stacking. Compared to the pristine $Ti_3C_2T_x$ MXene, an obvious downshift of the (0 0 2) diffraction peak is observed for all three Ti_3C_2@CPE films, corresponding to increased *d*-spacings (**Figure 3.1 b**). Specifically, the *d*-spacing of Ti_3C_2@CPE 10:1 and Ti_3C_2@CPE 5:1 film increased to 1.55 nm and 1.94 nm, respectively, while the Ti_3C_2@CPE 2:1 film showed an even larger *d*-spacing of 2.36 nm, which is nearly twice that of $Ti_3C_2T_x$ (1.21 nm). We attribute the increase in interlayer spacing to CPE pillared between $Ti_3C_2T_x$ sheets. Energy dispersive X-ray spectroscopy measurements (**Figure S3.5**) reveal a homogeneous distribution of Ti, S and N elements within the lamella Ti_3C_2@CPE structure, indicating that CPE is uniformly sandwiched between adjacent $Ti_3C_2T_x$ layers.
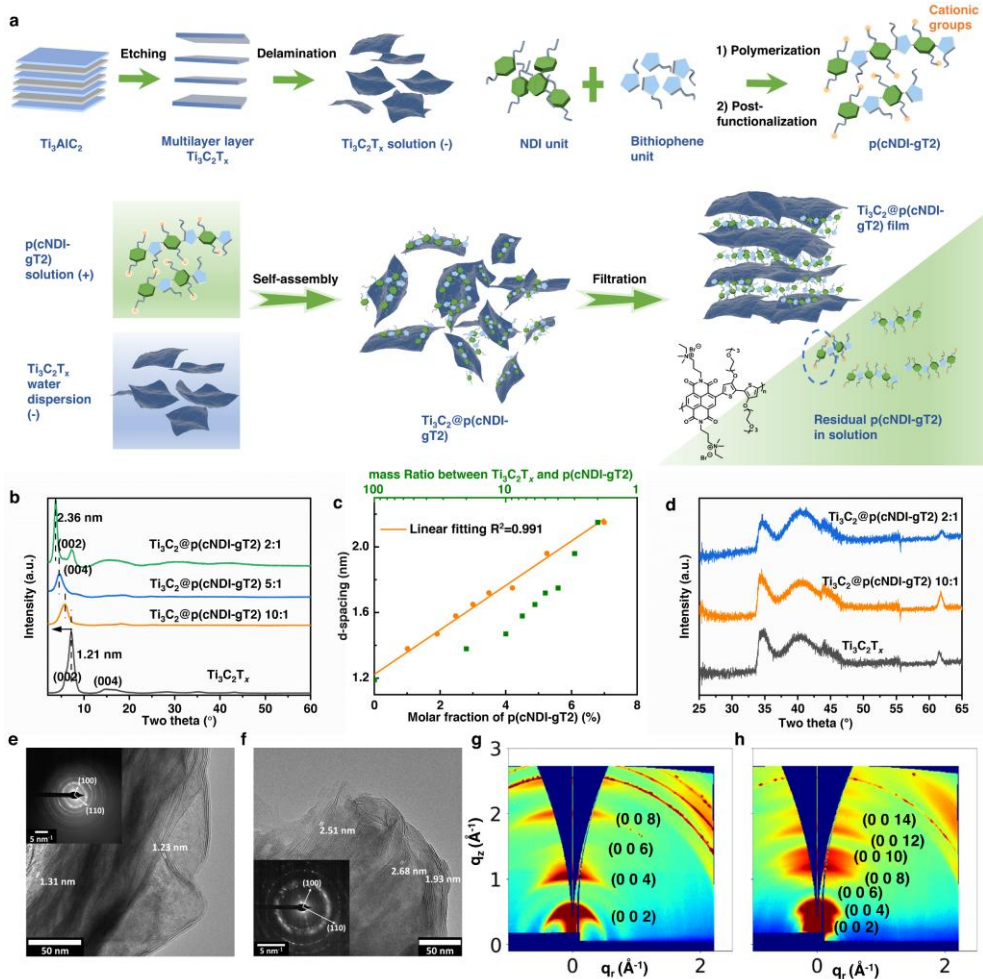
Figure 3.1 (a) Schematic illustration of the synthesis process and self-assembly process of Ti$_3$C$_2$T$_x$ and p(cNDI-gT2) CPE. (b) Bragg-Brentano XRD patterns of Ti$_3$C$_2$T$_x$ film and self-assembled Ti$_3$C$_2$@CPE film with different mass ratio (10:1, 5:1 and 2:1). (c) The d-spacing change of Ti$_3$C$_2$@CPE with different MXene:CPE ratio. The orange dots represent the d-spacing of Ti$_3$C$_2$T$_x$ with different molar fraction of CPE, while the green dots show the corresponding mass ratio between Ti$_3$C$_2$T$_x$ and CPE. (d) Transmission XRD patterns of Ti$_3$C$_2$T$_x$ and Ti$_3$C$_2$@CPE films. High-resolution transmission electron microscopy imaging of (e) Ti$_3$C$_2$T$_x$ and (f) Ti$_3$C$_2$@CPE 2:1, including selected area diffraction patterns as insets. Grazing incidence wide angle X-ray scattering of (g) Ti$_3$C$_2$T$_x$ film and (h) Ti$_3$C$_2$@CPE 2:1.

The influence of the relative ratio of MXene-to-CPE in the composites on the interlayer spacing was systematically investigated by varying the mass ratios from 20:1 to 2:1 (**Figure S3.6**). All films were dried at 150 °C under vacuum for 12 h before XRD inspection to remove the adsorbed water molecules between the layers as much as possible. Interestingly, the

63

increase in d-spacing follows a linear correlation with the molar fraction of CPE in the MXene-polymer composites (**Figure 3.1 c**, **Table S3.1**). This enables the precise tuning of interlayer spacings, while maintaining the regular layered patterns of MXene. Broadening of the (0 0 2) diffraction peak was observed in all Ti_3C_2@CPE films with ratios ranging from 20:1 to 3:1 (see **Table S3.1**) relative to the pristine MXene, indicating less uniform interlayer spacings. Surprisingly, a further increase in the loading of CPE in a 2:1 composite resulted in the appearance of a sharp diffraction peak (**Figure 3.1 b**), suggesting a highly uniform interlayer spacing.

Transmission XRD with the beam perpendicular to the film was employed on $Ti_3C_2T_x$, Ti_3C_2@CPE 10:1 and Ti_3C_2@CPE 2:1 to reveal possible structural features that may be buried under the intense (0 0 l) peaks or not shown in the Bragg-Brentano XRD patterns due to the significant preferential orientation of 2D MXene nanosheets (**Figure 3.1 d**). For each film, there were low-intensity humps between $2\theta = 34°$- $48°$, which are attributed to the expected (0 1 l) diffractions of $Ti_3C_2T_x$ MXene[36]. No obvious difference between Ti_3C_2@CPE films and MXene has been observed. Analysis of the morphology and crystal structure of $Ti_3C_2T_x$ and Ti_3C_2@CPE was performed by transmission electron microscopy (TEM) (**Figure 3.1 e-f, Figure S3.7**). The two-dimensional, flake-like morphology of $Ti_3C_2T_x$ is maintained after self-assembly with CPE for all ratios, as highlighted by the high-resolution TEM images. The interlayer spacing of each sample can be derived locally from HRTEM, showing consistency with XRD results by doubling from ca. 1.2-1.3 nm for pure $Ti_3C_2T_x$ (**Figure 3.1 e**) to 1.9-2.7 nm for Ti_3C_2@CPE 2:1 (**Figure 3.1 f**, **Figure S3.8**). It should be noted that slight local variations in the interlayer spacings derived from HRTEM analysis, especially for polymer-functionalized samples, can be a consequence of the small crystalline domain sizes, i.e., few-layer character of the samples and potential electron beam damages during analysis. The crystal structure of the $Ti_3C_2T_x$ MXene sheets can further be locally analyzed using selected area electron diffraction (SAED). Strong diffraction rings can be observed at d-spacings of ca. 2.6 and 1.5 Å, corresponding to the (100) and (110) sets of planes of pristine $Ti_3C_2T_x$ MXene, respectively[37]. Furthermore, the absence of changes in diffraction ring position after polymer functionalization strongly indicates the absence of intralyer modification of MXene sheets by the self-assembly process, suggesting that CPE occupies exclusively interlayer space and does not incorporate into the $Ti_3C_2T_x$ crystal structure, for example, by forming covalent bonds.

More information on the orientational structure of the MXene@CPE films was obtained by performing 2D grazing incidence wide angle X-ray scattering (GIWAXS) measurements. Generally, the shape of the Debye-Scherrer diffraction rings in GIWAXS data can provide insights into the overall crystallinity and texture. The width of the rings is associated with the size and distribution of crystallites, with peak broadening reflecting smaller crystallites,

64

structural defects, or disorder. Additionally, the azimuthal angular distribution (χ) along the Debye-Scherrer rings sheds light on the orientation and ordering of crystallites, with anisotropic features indicating preferential alignment[38]. Consistent with the Bragg-Brentano XRD measurements and SAED, a preferred stacking of the MXene flakes along the c direction was observed for all Ti_3C_2@CPE. In $Ti_3C_2T_x$, four orders of the (0 0 l) direction were registered, corresponding to (0 0 2), (0 0 4), (0 0 6) and (0 0 8) planes, as shown in **Figure 3.1 g**. Ti_3C_2@CPE 10:1 and Ti_3C_2@CPE 5:1 exhibited the same level of peak registration as $Ti_3C_2T_x$. However, much broader diffraction rings were observed in both Ti_3C_2@CPE 10:1 and Ti_3C_2@CPE 5:1 (**Figure S3.9**). In the Ti_3C_2@CPE 2:1 film, six orders of the scattering peaks in (0 0 l) series were registered up to (0 0 14) reflection (**Figure 3.1 h**). The missing (006) scattering is due to the minimum of the form factor of the materials. The scattering peaks of Ti_3C_2@CPE 2:1 film show narrower features in both q_z and azimuthal directions, compared to the 5:1, 10:1 and pristine $Ti_3C_2T_x$ films, suggesting a higher stacking order in the in-plane and out-of-plane directions[26,39]. This enhancement in stacking order indicates a superlattice-like structure where CPE is uniformly situated between $Ti_3C_2T_x$ layer, providing a periodic pattern.

Molecular dynamic (MD) simulations were carried out to reveal the structures of Ti_3C_2@CPE heterostructures at the atomistic level. As shown in **Figure 3.2 a**, the simulated *d*-spacing displays a linear increase with the polymer concentration in the composite and is in reasonable agreement with the experimental values. To reveal the composite structure behind the increasing spacing with the polymer concentration, we analyzed typical snapshots from the MD simulations for the 10:1, 5:1, and 2:1 structures of the Ti_3C_2@CPE composites. As shown in **Figure 3.2 d** for the 10:1 structure, the CPE units lie parallel between the MXene layers, forming a neat monolayer with interlocking side chains (see **Figure S3.10** for a large top view). As the CPE loading increases to MXene:CPE=5:1 (**Figure 3.2 e**), the CPE units are slightly inclined with noticeable crowding and overlapping (**Figure S3.10**), increasing the d-spacing to 1.91 nm. Meanwhile, the enlarged interlayer spacing may allow the side chains of CPE moving more freely when they are not densely packed. Hence, we can observe the increased (0 0 2) peak width when the mass ratio of Ti_3C_2-to-CPE increases from 20:1 to 3:1 (**Figure S3.6**). In contrast, the Ti_3C_2@CPE 2:1 heterostructure shows a pseudo-bilayer stacking pattern (**Figure 3.2 f**), where the crowding CPE units are slantingly aligned in two layers but with significant overlapping (**Figure S3.10**). This leads to a narrower (0 0 2) peak width, indicating a narrow distribution of the interlayer space.

The successful assembly between $Ti_3C_2T_x$ and CPE was further confirmed by X-ray photoelectron spectroscopy (XPS). As illustrated in **Figure 3.2 b** and **Figure 3.2 c**, no sulfur was detected in $Ti_3C_2T_x$, while the intensity of sulfur peak gradually increased with more CPE presenting in Ti_3C_2@CPE heterostructures. The interaction between polymers and

MXenes may involve electrostatic attraction, hydrogen bonding, Van der Waals interaction, π-π interaction and/or covalent bonding, depending on the structure of the polymers[24,40,41]. As mentioned above, $Ti_3C_2T_x$ nanosheets show negative surface charge due to the strong electronegative functional groups. Meanwhile, the side chains of p(cNDI-gT2) CPE contain positively charged ammonium groups, which is balanced by bromide ions (Br⁻) to obtain charge neutrality. After self-assembly, particularly relevant change in the XPS spectra is the absence of a Br signal for the Ti_3C_2@CPE composites, in contrast to pure p(cNDI-gT2) CPE (**Figure 3.2 c**). Due to the robust electrostatic attraction between the cationic ammonium groups of CPE and the negatively charged surface of $Ti_3C_2T_x$, the removal of Br⁻ ions is necessary to maintain charge neutrality, aligning well with findings reported previously[40]. Hence, the depletion of bromide ions (Br⁻) in the heterostructures confirms that the electrostatic interactions contribute to the self-assembly process. More information about the chemical environment and the possible interaction in Ti_3C_2@CPE heterostructures were obtained by analyzing the high-resolution scans of Ti2p, N1s, S2p, O1s, C1s, Cl2p and F1s spectra (**Figure 3.2 g-i** & **Figure S3.11**). Importantly, no covalent bonds were formed between $Ti_3C_2T_x$ and CPE, as shown by the high-resolution Ti2p XPS spectra. The Ti2p XPS spectrum of $Ti_3C_2T_x$ was fitted into four peaks at 454.9/460.6 eV, 455.6/461.5 eV, 456.7/462.6 eV, and 458.2/463.6 eV (Ti2p3/2 / Ti2p1/2) corresponding to Ti-C, Ti(II), Ti(III), and Ti-O (Ti(IV)), respectively (**Figure 3.2 g**)[42,43]. No noticeable change in the Ti2p spectra can be seen after self-assembly, indicating the absence of covalent bonds between CPE and surface Ti atoms. Interestingly, all fitted XPS peaks that belong to CPE irrespective of elements showed significant blueshift (~1.5 eV) in binding energy (BE) after self-assembly (**Figure 3.2 h-i**, **Figure S3.11**), even after we correct for the shift of the hydrocarbon peak at 284.8 eV in the C1s spectra (at max 0.2 eV shift). Such a shift in binding energy could arise from local sample charging and/or the presence of an electric field due to aligned dipole moments (More discussion see **Figure S3.11**).
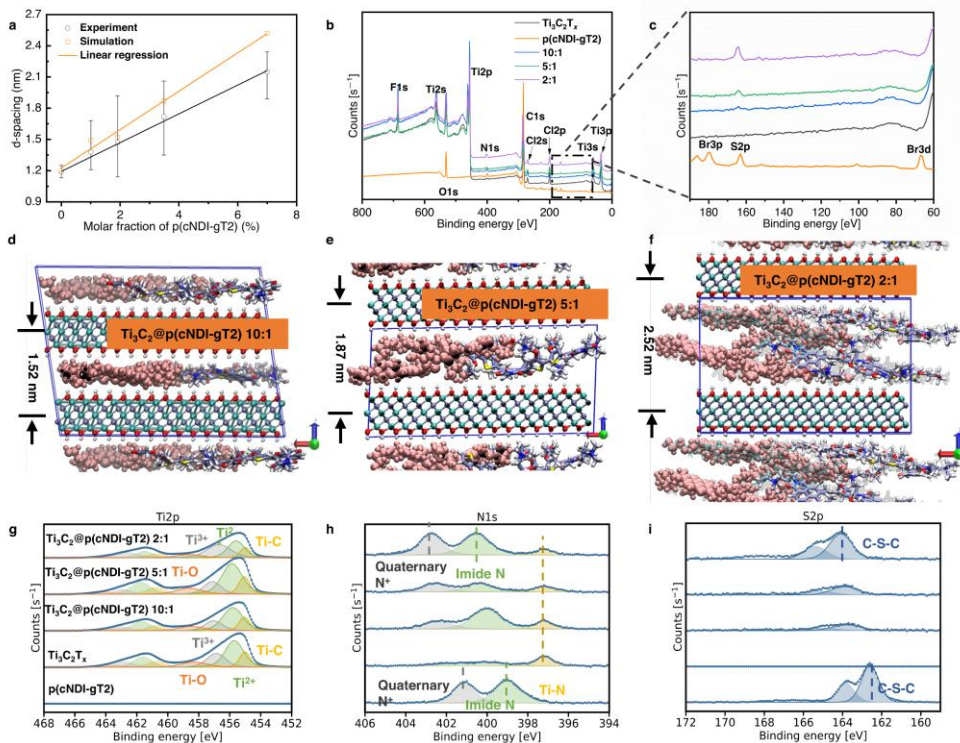
Figure 3.2 (a) Comparison of d-spacings at different MXene:CPE molar fractions between experiments and molecular dynamics (MD) simulations. The error bar represents the d-spacing within the Full Width at Half Maximum (FWHM) region of the experimental result. (b) XPS survey spectra of p(cNDI-gT2) CPE, $Ti_3C_2T_x$, Ti_3C_2@CPE. (c) A magnification of the XPS survey spectra of p(cNDI-gT2), $Ti_3C_2T_x$, Ti_3C_2@CPE in selected binding energy region from 190 eV to 60 eV. (d) Simulation snapshot of Ti_3C_2@CPE 10:1 showing the horizontal alignment of CPE between adjacent $Ti_3C_2T_x$ layers (the two different polymer units are contrasted with the CPK model on the left and the stick model on the right). (e) Simulation snapshot of Ti_3C_2@CPE 5:1 showing slightly inclined CPE units and their partial overlay in the middle of the unit cell, indicating an incipient bilayer. (f) Simulation snapshot of Ti_3C_2@CPE 2:1 showing a bilayer stacking of slantly aligned CPE with significant multilayer overlapping. (g) High-resolution Ti2p X-ray photoelectron spectroscopy. (h) High-resolution N1s X-ray photoelectron spectroscopy. (i) High-resolution S2p X-ray photoelectron spectroscopy.

Fourier transform infrared spectroscopy (FTIR) was also performed (**Figure S3.12**), revealing a featureless FTIR spectrum for the $Ti_3C_2T_x$ film, consistent with previous reports[40]. Weak signals belonging to CPE were observed in Ti_3C_2@CPE 2:1, validating the existence of the polymer in the heterostructure.

3.2.2 Electrochemical performance of Ti_3C_2@CPE heterostructure

To understand the relationship between the tunable structure of Ti_3C_2@CPE and its electrochemical NH_4^+ storage behavior, we performed electrochemical characterizations on

10:1, 5:1 and 2:1 Ti$_3$C$_2$@CPE electrodes using three-electrode cells with 1 M NH$_4$Cl aqueous electrolyte. **Figure 3.3 a** illustrates the cyclic voltammograms (CV) of the Ti$_3$C$_2$T$_x$ MXene, p(cNDI-gT2) CPE, and Ti$_3$C$_2$@CPE electrodes. Rectangular CVs (**Figure S3.14 b**) with no visible redox peaks were observed for Ti$_3$C$_2$T$_x$ in 1 M NH$_4$Cl aqueous electrolyte, indicating pseudocapacitive behavior. The galvanostatic charge and discharge (GCD) curve of Ti$_3$C$_2$T$_x$ shows a sloping feature, in good agreement with the CV (**Figure S3.17 b**). This behavior is consistent with the previous report of NH$_4^+$ storage in Ti$_3$C$_2$T$_x$ MXene, which can be attributed to the NH$_4^+$ (de-)intercalation[23]. A capacitance of 81.5 F g^{-1} was obtained at 0.1 A g^{-1} based on the discharge curve of MXene. Meanwhile, the CVs of p(cNDI-gT2) (**Figure S3.14 a**) feature two reduction peaks at -0.52 V (peak 1) and -0.80 V (peak 2) vs. Ag/AgCl (3.5 M KCl). When naphthalene diimide (NDI) units interacts with cations, per NDI unit experiences two sequential one-electron reduction process, forming a radical anion and a dianion, respectively (**Figure S3.15**)[32,44]. During anodic scan, the two oxidation peaks merge and form a broad oxidation peak at -0.1 V, indicative of a large overpotential for the radical dianion formation/elimination. This two-electron transfer process of p(cNDI-gT2) CPE during charge and discharge leads to a high capacity of 211 C g^{-1} (~ 192.0 F g^{-1}) at 0.1 A g^{-1} (**Figure 3.3 c**). However, with increasing scan rates, the intensity of redox peaks (or peak currents) decreased, and polarization became more severe (a peak separation above 1 V at 20 mV s^{-1}), indicative of sluggish kinetics (**Figure S3.14 a**).
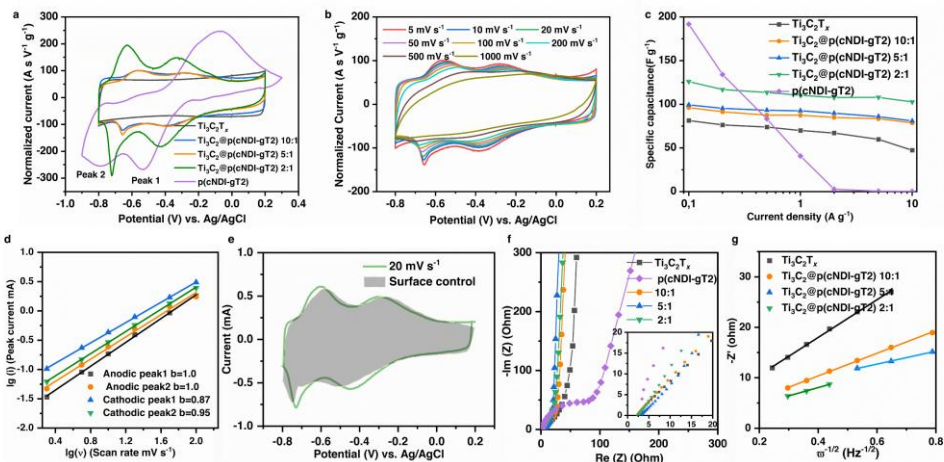

Figure 3.3 Electrochemical performance of Ti$_3$C$_2$T$_x$, p(cNDI-gT2) CPE and Ti$_3$C$_2$@CPE 2:1. CV curves of (a) Comparison of CVs at 5 mV s^{-1}. (b) CVs of Ti$_3$C$_2$@CPE 2:1 at different scan rates ranging from 5 mV s^{-1} to 1 V s^{-1}. (c) Rate performance of Ti$_3$C$_2$T$_x$, p(cNDI-gT2) CPE and Ti$_3$C$_2$@CPE in 1 M NH$_4$Cl based on GCD. (d) The relationship between cathodic and anodic peak currents and scan rates for Ti$_3$C$_2$@CPE 2:1. (e) Pseudocapacitive contribution of Ti$_3$C$_2$@CPE 2:1 at 20 mV s^{-1}. (f) Nyquist plots of Ti$_3$C$_2$T$_x$, p(cNDI-gT2), and

Ti$_3$C$_2$@CPE films, where the inset shows a magnification of the high-frequency range. (g) Linear fit showing the relationship between the real impedance (Z') and $\omega^{-1/2}$ of Ti$_3$C$_2$T$_x$ and Ti$_3$C$_2$@CPE in the Warburg frequency region.

In comparison, the CVs of Ti$_3$C$_2$@CPE films show characteristic pseudocapacitive features: quasi-rectangular with two redox peaks with a small peak separation (**Figure 3.3 a**). Notably, the second pair of reductive/oxidative peaks (peak 2) for Ti$_3$C$_2$@CPE 10:1, 5:1 and 2:1 are located at -0.57 V/-0.66 V, -0.57 V/-0.66 V and -0.63 V/-0.71 V vs. Ag/AgCl, respectively. These redox peaks inherited from p(cNDI-gT2) further confirm that the structure of CPE remains unaltered after the assembly process. Compared to CPE, much smaller peak separations of ~ 0.1 V were observed for all Ti$_3$C$_2$@CPE films. The redox peaks are more pronounced for Ti$_3$C$_2$@CPE 2:1 as compared to 10:1 and 5:1, owing to the higher mass loading of CPE in the heterostructure (**Figure 3.3 a**). Importantly, the redox peaks were clearly observed even at high scan rates of 500 mV s^{-1}, reflecting fast charge storage kinetics (**Figure 3.3 b**). Cyclic voltammetry was also conducted in 1 M NH$_4$NO$_3$ (**Figure S3.16**), showing CVs with redox peaks located at the same potential as those observed in NH$_4$Cl. This consistency suggests that the redox reactions are due to the interaction between NH$_4^+$ and the heterostructure, with minimal influence from the anions on electrochemical behavior. The redox peaks shown in the CVs collected in 1 M NH$_4$Cl correlate well with the GCD curves, in which two short plateaus at ca. -0.4 V and ca. -0.7 V can be observed (**Figure S3.17**). The calculated specific capacitance at different current densities is plotted in **Figure 3.3 c**. Ti$_3$C$_2$@CPE 10:1, 5:1 and 2:1 show specific capacitances of 96.3 C g^{-1} (96.3 F g^{-1}), 99.4 C g^{-1} (99.4 F g^{-1}), and 126.1 C g^{-1} (126.1 F g^{-1}) at 0.1 A g^{-1}, respectively. These values are higher than that of MXene and can be attributed to additional capacity contributions from the redox-active CPE. Although p(cNDI-gT2) CPE alone showed the highest specific capacity at a low rate (0.1 A g^{-1}), its performance dropped drastically to 45.1 C g^{-1} (~ 40.7 F g^{-1}) at 1 A g^{-1} and almost no capacity was delivered at 10 A g^{-1} (**Figure S3.17**). On the other hand, Ti$_3$C$_2$T$_x$ demonstrates good rate capability, exhibiting a capacitance of 47.4 C g^{-1} (47.4 F g^{-1}, 58% retention) at 10 A g^{-1}. Remarkably, Ti$_3$C$_2$@CPE heterostructures delivered significantly improved rate performance over the individual components on their own, demonstrating a synergistic effect. This can be seen from the GCD curves at the high current density of 10 A g^{-1}, where Ti$_3$C$_2$@CPE 2:1 delivered the longest discharge time among all the electrodes. Moreover, high capacitance retentions of 81.9 % (78.9 F g^{-1}), 81.3% (80.9 F g^{-1}) and 81.5% (102.8 F g^{-1}) at 10 A g^{-1} was obtained for Ti$_3$C$_2$@CPE 10:1, 5:1 and 2:1, respectively. To gain a comprehensive understanding of the superior rate performance of Ti$_3$C$_2$@CPE for NH$_4^+$ storage, their charge storage kinetics are investigated. CVs collected at different scan rates were analyzed to determine the rate-limiting factor. The peak currents of CV curves and scan rates follow the power-law relationship:

$$i(V) = av^b$$

where i stands for the peak current, v represents the scan rate, a is a variable, and b is a parameter that determines the kinetics, ranging from 0.5 to 1.0. Typically, a diffusion-controlled process has a b value equals to 0.5, while an electrochemical process with $b = 1$ is dominated by surface-controlled behavior[45]. The b values for CPE were determined to be 0.75 for the first cathodic peak and 0.53 for the second cathodic peak (**Figure S3.18**). Apparently, the NH_4^+ storage on CPE is dominated by sluggish diffusion-controlled processes. In contrast, b values close to 1.0 were obtained for all Ti_3C_2@CPE electrodes (**Figure 3.3 d**, **Figure S3.19**), indicative of charge storage processes that are dominated by surface redox reactions. For instance, Ti_3C_2@CPE 2:1 electrode showed b values of 1.0 for both anodic peaks, and b values of 0.87 and 0.95 for the first and the second cathodic peaks, respectively (**Figure 3.3 d**). The contribution of surface-controlled capacitance of Ti_3C_2@CPE 2:1 was further evaluated using following equation:

$$i = k_1 v + k_2 v^{1/2}$$

where v represents the scan rate, and k_1 and k_2 stands for the contribution of surface-controlled current and diffusion-controlled current, respectively[46]. Interestingly, 99% of the charge storage capacity for Ti_3C_2@CPE 2:1 is controlled by surface redox reaction (**Figure 3.3 e**). This all-pseudocapacitive behavior indicates fast charge storage kinetics in the Ti_3C_2@CPE films.

Electrochemical impedance spectroscopy (EIS) measurements were carried out to further examine the kinetics of Ti_3C_2@CPE electrodes (**Figure 3.3 f**) and fitted using the equivalent electric circuit (**Figure S3.20, Table S3.2**). The Nyquist plot of CPE shows a large semi-circle at high frequency, representing a large charge transfer resistance (64.89 Ω) for NH_4^+ storage. Compared to CPE, no evident semi-circles were observed for Ti_3C_2@CPE electrodes at high frequency, indicating negligible interfacial charge transfer resistance (lower than 1 Ω). This can be attributed to the reduced electron transfer resistance in the heterostructure. Additionally, the charge transfer process must overcome an activation barrier for ions to enter the hosting material[47]. Hence, the minimal charge transfer resistance also implies that solvated NH_4^+ ions are capable of being stored within the heterostructure. Besides, all Ti_3C_2@CPE electrodes exhibited a slope close to 90° at the low-frequency range, indicating typical capacitive behavior. Moreover, the Warburg factor (σ), or the slope of the linear fit of the real part of impedance versus $\omega^{-1/2}$ within the Warburg region (**Figure S3.21**), was calculated to evaluate the kinetics of ion diffusion (**Figure 3.3 g**). Ti_3C_2@CPE 5:1 shows the lowest slope ($\sigma = 12$) among all electrodes, which is then followed by Ti_3C_2@CPE 2:1 ($\sigma = 16$) and Ti_3C_2@CPE 10:1 ($\sigma = 21$) and $Ti_3C_2T_x$ ($\sigma = 37$). As the diffusion coefficient of ions

is inversely proportional to the Warburg factor, a lower slope indicates faster ion diffusion in Ti_3C_2@CPE heterostructures, in contrast to the pristine $Ti_3C_2T_x$ electrode, due to the enlarged interlayer spacing. Importantly, the ionic diffusion coefficient of Ti_3C_2@CPE 2:1 is comparable to that of Ti_3C_2@CPE 5:1 structure. It implies that Ti_3C_2@CPE 2:1 film is capable of effective ion transport even with the close pseudo-bilayer stacking of CPE.
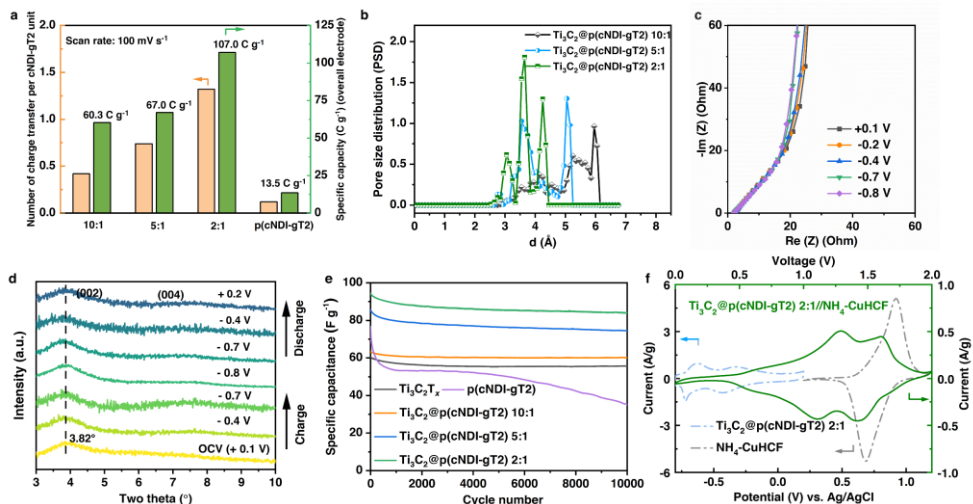

Figure 3.4 (a) Charge transfer number of p(cNDI-gT2) CPE in different Ti_3C_2@CPE electrodes at 100 mV s^{-1}. (b) Simulated pore size distribution of Ti_3C_2@CPE. (c) Nyquist plots of Ti_3C_2@CPE 2:1 upon cathodic scan. (d) Ex-situ XRD patterns of Ti_3C_2@CPE 2:1 electrode at different potentials. (e) Cycling performance of $Ti_3C_2T_x$, p(cNDI-gT2) and Ti_3C_2@CPE at 1 A g^{-1}. (f) CV curves of Ti_3C_2@CPE 2:1// NH$_4$-CuHCF hybrid capacitor.

3.2.3 Enhanced redox contribution from structure induced desolvation

To understand the contribution of polymeric redox to the overall charge storage capacity, we evaluated the utilization of CPE (or electron transfer per structural unit) at different scan rates (from 5 mV s^{-1} to 100 mV s^{-1}) by analyzing CV curves (**Table S3.3**). At high scan rates, all composites showed improved utilization of the CPE for charge storage relative to p(cNDI-gT2) CPE on its own, demonstrating the advantage of the self-assembled heterostructures for rapid charge storage kinetics. At 100 mV s^{-1}, the electron transfer number delivered per CPE unit of pristine CPE is only 0.12 (6% utilization). The number increases to 0.42 (21% utilization) and 0.74 (37% utilization) for Ti_3C_2@CPE 10:1 and 5:1, respectively. Interestingly, Ti_3C_2@CPE 2:1 exhibits the highest utilization of the CPE among all Ti_3C_2@CPE at all scan rates, with a charge transfer number of 1.32 (66% utilization) at 100 mVs^{-1}(**Figure 3.4 a** & **Table S3.3**). However, the crowded pseudo-bilayer stacking of CPE in the interlayer spacing of $Ti_3C_2T_x$ in Ti_3C_2@CPE 2:1 may lead to reduced NH$_4^+$ accessibility.

Additionally, Ti_3C_2@CPE 2:1 slows slightly lower kinetics than Ti_3C_2@CPE 5:1, as previously discussed. However, Ti_3C_2@CPE 2:1 structure, which was expected to exhibit a lower electron transfer number (or utilization) compared to Ti_3C_2@CPE 5:1, actually demonstrates a higher electron transfer number. Such an anomalous increase in the polymer utilization in Ti_3C_2@CPE 2:1 structure is probably attributed to more effective charge transfer induced by NH_4^+ de-solvation[48]. To confirm our assumption, the pore size distribution of each Ti_3C_2@CPE structure was evaluated based on the configurations from the MD simulations (**Figure 3.4 b**). One can see that Ti_3C_2@CPE 2:1 shows a much higher distribution of smaller pores whose radius are comparable to bare NH_4^+ ions (~3.0 Å in diameter, **Figure 3.4 b**), which can enforce the striping of solvents due to the porous confinement effect[49,50]. The reinforced de-solvation can improve the interaction between NH_4^+ and CPE, and thereby results in more effective charge transfer.

Since Ti_3C_2@CPE 2:1 outperformed all other electrodes, its structural evolution and reaction kinetics during the charging process were further analyzed. A nearly vertical slope was observed in the low-frequency region of Nyquist plots at all applied potentials during the intercalation of NH_4^+ for Ti_3C_2@CPE 2:1 (**Figure 3.4 c**), which also confirmed the fast surface redox reaction upon NH_4^+ intercalation[51]. Ex-situ XRD was conducted to monitor the structural evolution of Ti_3C_2@CPE 2:1 electrode upon NH_4^+ intercalation at different potentials. The (0 0 2) peak of Ti_3C_2@CPE 2:1 is maintained at 3.82° for all states of charge, indicating a constant d-spacing with NH_4^+ intercalation (**Figure 3.4 d**). This negligible volume change of the electrode is beneficial for maintaining the structural integrity of the electrode, enabling high cycling stability. Remarkably, over 89% of the capacitance was retained after 10 000 cycles at a current density of 1 A g^{-1} for Ti_3C_2@CPE 2:1 (**Figure 3.4 e**). Meanwhile, CPE on its own showed a lower capacitance retention of 46%, presumably due to its gradual dissolution into the aqueous electrolyte. As shown in **Figure S3.22**, after cycling p(cNDI-gT2) CPE in the NH_4Cl electrolyte, the glass fiber separator turned green, which indicates the dissolution of CPE in the electrolyte. In contrast, no color change of separator was observed with Ti_3C_2@CPE 2:1 electrode, highlighting the superior structural stability of the Ti_3C_2@CPE heterostructure. The electrochemical test was also conducted in 1 M KCl electrolyte to showcase the benefits of Ti_3C_2@CPE 2:1 heterostructure (**Figure S3. 23**). A high capacitance of 123 F g^{-1} at 0.1 A g^{-1} and an impressive capacitance retention of 105 F g^{-1} at 10 A g^{-1} were achieved with 1 M KCl electrolytes, demonstrating the versatility of our superlattice-like structure for high-rate energy storage.

To demonstrate the potential of Ti_3C_2@CPE 2:1 electrode in a full cell, we fabricated an asymmetric hybrid capacitor based on a Ti_3C_2@CPE 2:1 negative electrode and a $NH_4CuFe(CN)_6$ (NH4-CuHCF) positive electrode. XRD and electrochemical performance of NH4-CuHCF positive electrode are presented in **Figure S3.24** & **S3.25**. As shown in **Figure**

3.4 f & **Figure S3.26**, Ti_3C_2@CPE 2:1//NH$_4$-CuHCF hybrid capacitor could be operated within a wide voltage window of 2.0 V in 1 M NH$_4$Cl. Two separate redox couples located at 1.1 V/1.3 V and 1.4 V/1.6 V were featured in CV and GCD, which is consistent with the two-step charging/discharging behavior of Ti_3C_2@CPE 2:1. **Figure S3.27** illustrates the Ragone plots of the Ti_3C_2@CPE 2:1//NH$_4$-CuHCF hybrid capacitor and other state-of-the-art NH$_4^+$ storage devices based on polymer electrodes. An energy density of 14 Wh kg^{-1} at a power density of 2.2 kW kg^{-1} was achieved due to the outstanding rate performance of Ti_3C_2@CPE 2:1.

The Ti_3C_2@CPE superlattice structure constructed by self-assembly exhibited improved ammonium EES performance due to the maximized synergistic effect. Firstly, the unique structure of Ti_3C_2@CPE enables polymeric redox contribution of the CPE, contributing to higher capacity. Secondly, the uniform stacking can maximize the heterogeneous interface between the highly conductive MXene and p(cNDI-gT2), ensuring fast electron transfer. Thirdly, the p(cNDI-gT2) is situated between the MXene layer, expanding the interlayer spacing of MXene and suppressing tight self-restacking. This structure allows better NH$_4^+$ accessibility and fast ion diffusion, which leads to superior rate performance. Finally, the strong interfacial electrostatic interaction between MXene and the CPE helps improve the structural integrity of the electrode for maintaining long-term cycling stability. Importantly, the flexibility of fine tuning this superlattice structure offers the chance to modify the microscopic structure of CPE within the interlayer of MXene while retaining the superlattice-like structure. Consequently, the polymeric redox activity was unexpectedly enhanced due to the increased volume of 3 Å-sized pores, which demonstrates the uniqueness of our Ti_3C_2@CPE heterostructure.

3.3 Conclusion

In this work, an n-type p(cNDI-gT2) CPE was self-assembled with $Ti_3C_2T_x$ MXene in water to construct Ti_3C_2@CPE superlattice-like structures for aqueous NH$_4^+$ storage. The green and facile self-assembly process is facilitated by cooperative interfacial electrostatic interactions between CPE and MXene flakes. In the Ti_3C_2@CPE heterostructure, CPE is sandwiched between adjacent MXene layers while MXene is able to maintain its ordered layered structure. The superlattice-like structure maximized the synergistic effects between CPE and MXene for NH$_4^+$ storage. The MXene component acts as an active material for NH$_4^+$ storage, provides a high electronic conductivity framework, and prevents CPE dissolution, and constrains volume changes during cycling. The redox-active n-type CPE enhances NH$_4^+$ storage ability, while acting as a spacer to enlarge interlayer spacing, preventing MXene restacking. Notably, the *d*-spacing of the MXene in the heterostructure could be adjusted by varying the amounts of CPE, while preserving the superlattice-like structure. With the highest

polymer loading, Ti_3C_2@CPE 2:1 exhibited a significantly increased d-spacing of 2.36 nm compared to 1.15 nm in pristine $Ti_3C_2T_x$. The Ti_3C_2@CPE 2:1 sample also exhibited the highest utilization of CPE or the strongest polymeric redox of CPE. MD simulations suggest that the increased pore volume, particularly in ~3 Å-sized pores within Ti_3C_2@CPE 2:1, may facilitate the de-solvation of NH_4^+ ions and enhance redox activity. Consequently, Ti_3C_2@CPE 2:1 delivered a high specific charge storage capacity of 126.1 C g^{-1} at 0.1 A g^{-1} (1.5 times higher than that of $Ti_3C_2T_x$), superior rate capability of 81.5% retention at 10 A g^{-1} and high capacitance retention of 89% over 10 000 cycles for NH_4^+ storage. Further improvements in the capacitance of our heterostructure can be achieved by reducing the molecular weight of CPE and/or introducing additional redox-active sites, while maintaining the superlattice-like structure is essential to maximize the utilization of the new CPEs. Our results provide an efficient strategy for designing tunable superlattice-like structures and highlights the importance of fine-tuning the heterostructures to maximize the synergistic effects in the heterostructure for high-performance energy storage. This study also demonstrates a rational design routine for simultaneously facilitating redox activity and ion transport in the heterostructures, opening up new opportunities for a wide range of applications in energy conversion, harvesting, and storage.

3.4 Supplementary information

Methods:

Synthesis of $Ti_3C_2T_x$: $Ti_3C_2T_x$ was prepared using conventional *in-situ* HF etching method.[2] In general, 1g of Ti_3AlC_2 was slowly added into the mixing etchant solution of 1.6 g LiF and 20 ml 9 M HCl and stirred at 35°C for 24 h in oil bath. The etched product was repeatedly washed with DI Water by centrifugation at 8000 rpm until the PH of supernatant reached 6. Then, the sediment was re-dispersed in 40 ml DI water and sonicated for 1 h under argon to delaminate the multilayer. After that, the suspension was centrifuged at 3500 rpm for 1 h and the supernatant was collected as few-layered $Ti_3C_2T_x$ colloidal solution. The concentration (~ 8 mg ml^{-1}) of delaminated MXene solution was determined by vacuum assisted filtration. Synthesis of p(cNDI-gT2): p(cNDI-gT2) was synthesized according to a previous report – briefly, the neutral polymer p(NDI-gT2) was first prepared, followed by a post-functionalization step to install the cationic quaternary ammonium groups on the side chains.[33]

Self-assembly of p(cNDI-gT2): The self-assembly of $Ti_3C_2T_x$ and p(cNDI-gT2) was manufactured by mixing $Ti_3C_2T_x$ MXene suspension (0.02 mg ml^{-1}) with (0.01 mg ml^{-1}) p(cNDI-gT2) solution in different weight ratio (10:1, 5:1 and 2:1) under vigorously stirring. The mixtures were then filtered with the assistant of vacuum. The excessive p(cNDI-gT2)

was filtrated into the solution, while the assembled $Ti_3C_2@p(cNDI-gT2)$ was washed with DI-water and formed a self-freestanding film after drying at RT.

Synthesis of NH_4-CuHCF: The NH_4-CuHCF was synthesized by a co-precipitation method as previously reported in the literature[16]. In general, 0.1 M $Cu(NO_3)_2$ (40 ml) was dropwise added into 40 ml 0.1 M $Na_4Fe(CN)_6$ solution under vigorous stirring. The $Na_2Cu[Fe(CN)_6]$ (Cu-HCF) precipitation was then collected and dried in the oven at 60 °C overnight. NH_4-CuHCF was prepared by a following ion-exchange method. Briefly, 1 g Cu-HCF was added into 40 mL of 1 M $(NH_4)_2SO_4$ solution and stirred for 6 h. After the exchange, the sediment was washed with DI water and dried in the oven for further characterization. The X-ray diffraction analyses were conducted on an X'Pert Pro X-ray diffractometer (PANalytical) using Cu Kα radiation (0.1542 nm at 45 kV and 40 mA with 2θ range= 3°- 60°).

GIWAXS measurements were performed at 11-BM CMS beamline at National Synchrotron Light Source II (NSLS II), Brookhaven National Lab. The X-ray beam with the energy of 13.5 keV shone on the thin film samples in the grazing incident geometry. A Pilatus800k area detector was placed 260 mm away from samples to collect scattering patterns. The typical incident angle was 0.1° and exposure time was 10 s.

2D transmission XRD measurements were performed with a Bruker D8 Discover diffractometer (Bruker AXS GmbH, Karlsruhe, Germany). This diffractometer is equipped with a IμS micro-focus X-ray source (Cu k_α, λ = 0.1542 nm, operating at 50 kV, 1.0 mA) and a 2048-pixel Vantec 500 Mikrogap 2D X-ray. The detector was placed 300 mm from the sample allowing a simultaneous covering of a 2θ range of 23°. Measurements were performed by stepwise changing the central diffraction angle of the detector from 2θ = 15 to 55° in steps of 10° to ensure enough overlap between the different diffraction patterns. At each detector angle, a pattern was collected for 1 h. Subsequently, the patterns were stitched together using the Bruker EVA V4.1.1 software and radial averaging was performed to create the 1D XRD patterns.

Transmission electron microscopy was conducted using a Talos F200i microscope (Thermo Fisher Scientific) operating at an accelerating voltage of 200 kV. Selected area electron diffraction (SAED) patterns were captured using a 10 μm diameter selected-area aperture. Before TEM analysis, the samples were prepared by gently rubbing the powders onto a carbon coated Formvar film on a copper TEM grid. The obtained TEM images and SAED patterns were further analyzed via Velox software.

Cross-sectional scanning electron microscopy (SEM) was performed with JEOL JSM-6010LA equipment using an accelerating voltage of 10 kV. The composition of the films was

analyzed by examining energy dispersive X-ray (EDX) elemental maps to determine the specific distribution of elements present.

Inductively coupled plasma optical emission spectroscopy (ICP-OES) was measured using Perkin Elmer Optima 8000 DV. The mass ratio between Ti and S was calculated to determine the mass ratio between MXene and p(cNDI-gT2). To dissolve the sample, approximately 30 mg of sample was destructed in 4.5 ml 30% HCl + 1.5 ml 65% HNO_3 + 0.2 ml 40% HF mixture using the microwave. The destruction time in the microwave was 60 min at max power. After destruction, the samples were diluted to 50 ml with MQ.

X-ray photoemission spectroscopy (XPS) was measured using a Thermo Fisher K-Alpha surface spectrometer with a monochromatic Al Kα (1486.6 eV) as the X-ray source that was operated at 36 W (12 kV, 3 mA), a flood gun operating at 1 V, 100 µA, and a spot size of approximately 800 x 400 µm. The base pressure in the analysis chamber was approximately $2 \cdot 10^{-9}$ mbar. For the survey scans, the pass energy was set to 200 eV. High-resolution scans of the Ti2p, N1s, S2p, O1s, and C1s region were collected across corresponding binding energy ranges with the analyser set to a pass energy of 50 eV. In the analysis, the binding energy was corrected for the charge shift using the primary C1s hydrocarbon peak at BE = 284.8 eV as a reference. Peak fitting of the high-resolution XPS spectra was performed with ThermoFisher Avantage software using symmetric Gaussian-Lorentzian curves and Shirley background. For Ti2p fitting, the relative position/spectral component splitting was constrained as: Ti (C) = 6.1 +/- 0.2 eV, Ti(II) = 5.7 +/- 0.2 eV, Ti(III) 5.7 +/- 0.2 eV and Ti(O) = 5.7 +/- 0.2 eV. We also constrained the FWHM of the Ti 3/2 peak (< 3 eV). A limit of 1.5 eV for FWHM of peaks was used for fitting C1s, O1s and S2p spectra.

FTIR measurements were conducted using a Nicolet 6700 FT-IR Spectrometer, equipped with a Deuterated Triglycine Sulfate (DTGS) detector and an internal Globar light source. The spectral resolution was set to 4 cm^{-1}, and measurements were conducted in the transmission mode to capture the material's infrared absorption characteristics. A solution of the material under investigation was carefully drop-casted onto one side of a double-side polished native Ge substrate, ensuring uniform distribution across the surface. The Ge wafer was then annealed at approximately 100°C to facilitate the evaporation of the solvent, resulting in the formation of thin films of the tested materials. The Ge substrate, bearing the thin film, was positioned within the spectrometer's sample compartment, which was purged with nitrogen gas. A background correction was made to minimize the influence of background water vapor and the Ge substrate.

Solid-state (SS) NMR spectroscopy was performed to quantify the ratio between -OH and -F surface terminations. A quantitative spin counting experiment reported elsewhere[52] was

done using a Bruker Avance III spectrometer operated at a magnetic field strength of 11.7 T with a Bruker 1.9 mm resonance probe (MAS = 32 kHz). A recycle delay of 15 s was used for the ^{1}H spectra and 120 s for the ^{19}F spectra.

Electrochemical measurements:

The electrochemical performance of the Ti$_3$C$_2$T$_x$@CPE in 1 M NH$_4$Cl were tested with a three-electrode configuration using Swagelok cells. Free-standing Ti$_3$C$_2$T$_x$@CPE films were employed as the working electrode while Ag/AgCl (3.5 M) and activated carbon served as reference and counter electrode, respectively. The p(cNDI-gT2) electrode was obtained by coating the slurry of p(cNDI-gT2) powder, conductive acetylene black and PVDF binder on the titanium foil current collector with a mass ratio of 8:1:1. The NH$_4$-CuHCF electrode was prepared by coating the slurry of NH$_4$-CuHCF powder, conductive acetylene black and PVDF binder on the aluminum foil in a mass ratio of 7:2:1.

All electrochemical measurements were performed using a Biologic VSP-300 potentiostat. Cyclic voltammetry was measured from 5 mV s^{-1} to 1 V s^{-1}. The current densities applied for galvanostatic charge and discharge (GCD) ranged from 0.1 A g^{-1} to 10 A g^{-1}. Electrochemical impedance spectroscopy was recorded using a 10 mV amplitude with frequencies ranging from 10 mHz to 200 kHz.

The theoretical specific capacity of p(cNDI-gT2) is calculated according to:

$$q(\text{C g}^{-1}) = \frac{nF}{M}$$

Where n is the number of charge transfer, F is Faraday constant (96485 C/mol) and M is the molecular weight of polymer (g mol^{-1}).

The capacitance determined from CV is calculated according to:

$$C(\text{F}) = \frac{\int i \, dv}{s \, \Delta V}$$

Where i is the Current (A), s (V s^{-1}) represents the scan rate, ΔV (V) is the applied voltage window.

The capacitance calculated from GCD (discharge branch) follows:

$$C(\text{F}) = \int \frac{i \, dt}{dV}$$

In which V is the potential (V), i is the Current (A), t represents the discharge time (s).

Gravimetric specific capacitance C (F g^{-1}) is normalized by the mass of the working electrode.

For the full cell, the energy density is calculated by:

$$E \text{ (Wh kg}^{-1}) = \frac{\int V \, dq}{3.6 \, m}$$

In which V is the potential (V), q is the charge (C), m is the total mass of positive and negative electrode (g).

The power density is calculated by:

$$P \text{ (W kg}^{-1}) = \frac{3.6 \, E}{\Delta t}$$

Where E is the energy (Wh kg^{-1}), Δt represents the discharge time (s).

MD simulation:

MD simulations were performed in BIOVIA Materials Studio suite. Mole ratio of surface termination groups was taken as F:O:OH=1:1:1, according to the experimental value. Symmetric surface groups locate right above the central Ti in the FCC configuration. A Ti$_3$C$_2$T$_2$ orthorhombic supercell 4 × 3 × 1 (a × b × c) with 12 formula units initially taken from a previous DFT calculation[53] was used as a building block for Ti$_3$C$_2$@p(cNDI-gT2) heterostructures. The number of polyelectrolytes assembled into the interlayer of MXene was predetermined by specific mole ratio. Mass ratios between MXene and p(cNDI-gT2) of 10:1, 5:1 and 2:1 correspond to mole ratios of Ti$_3$C$_2$T$_2$ unit formula and monomer of 48:1, 24:1 and 12:1, respectively. A 16×12×1 supercell was used for Ti$_3$C$_2$T$_2$. The experimental d-spacings were taken as initial c lattice values, where nothing was between the interlayer of pristine Ti$_3$C$_2$T$_2$. The mole ratio of Ti$_3$C$_2$T$_2$: Li$^+$3H$_2$O was taken to model the structure without p(cNDI-gT2). The Universal Force Field was used for both MXene Ti$_3$C$_2$T$_2$ and polyelectrolyte p(cNDI-gT2) with two monomers[54]. Partial Charges were calculated using the QEq method. The deprotonation of surface OH groups was applied to balance positive charge of polyelectrolyte. The supercells of heterostructures, subjected to isostatic external pressure of 1 atm, were geometrically optimized with atom positions and cell parameters following a previous study[55]. The resulting structures were used as initial configurations in subsequent MD runs. NPT MD simulations were run at 298 K and 1 atm for 1 ns for equilibration and another 500 ps for production. The equilibrated trajectories were used for structural analysis. Pore size distribution with N$_2$ as the probe was calculated using PoreBlazer v4.0[56].
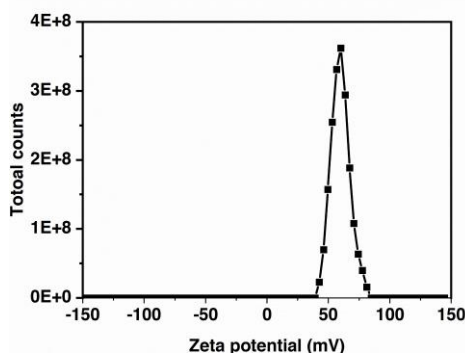
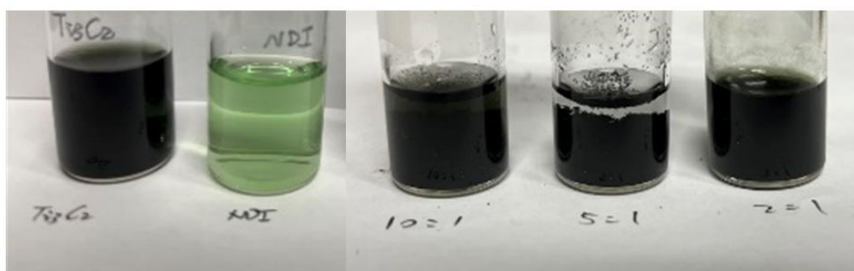Figure S 3.1 Zeta potential analysis of p(cNDI-gT2) CPE.

Figure S 3.2 Digital photograph of the self-assembly process.

Supplementary discussion: A light-green supernatant was obtained in Ti_3C_2@CPE 2:1, in contrast to Ti_3C_2@CPE 5:1 and Ti_3C_2@CPE 10:1, which can be attributed to the excessive p(cNDI-gT2) remaining in the solution. The actual weight percentage of p(cNDI-gT2) in Ti_3C_2@CPE 2:1 is determined to be 29% using inductively coupled plasma optical emission spectroscopy (ICP-OES).
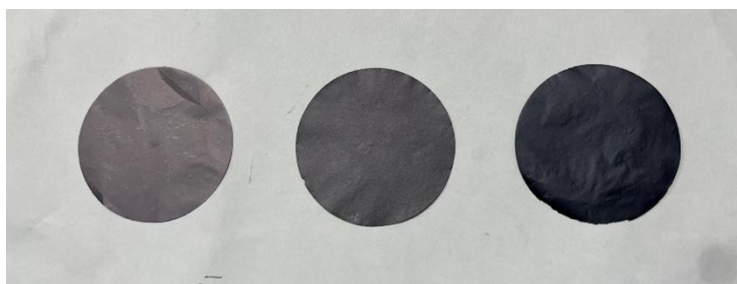
Figure S 3.3 Digital photograph of the $Ti_3C_2T_x$, Ti_3C_2@CPE 10:1 and Ti_3C_2@CPE 2:1 (From left to right).
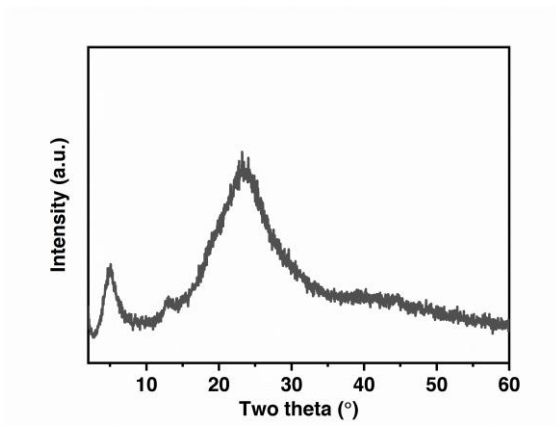
Figure S 3.4 Bragg-Brentano X-ray diffraction pattern of p(cNDI-gT2) powder.
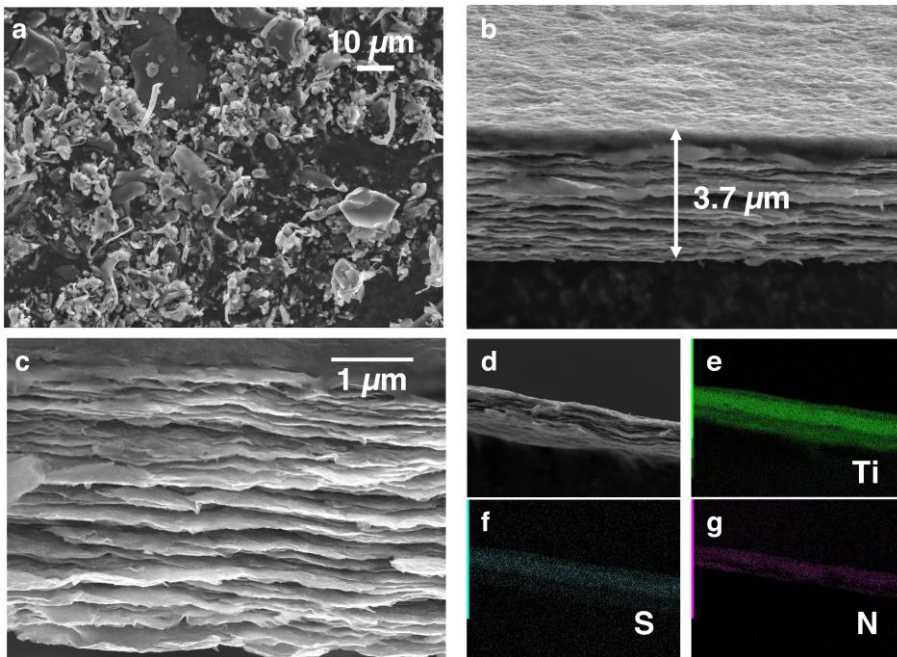
Figure S 3.5 Morphology of p(cNDI-gT2) and Ti$_3$C$_2$@CPE 2:1. (a) SEM image of p(cNDI-gT2). (b) and (c) cross-sectional image of Ti$_3$C$_2$@CPE 2:1. (d)-(g) Energy dispersive X-ray (EDX) spectroscopy of Ti$_3$C$_2$@CPE 2:1.
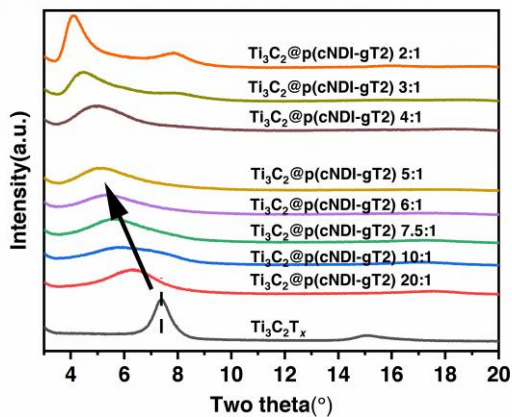
Figure S 3.6 Bragg-Brentano XRD patterns of Ti$_3$C$_2$T$_x$ and Ti$_3$C$_2$@CPE.

3
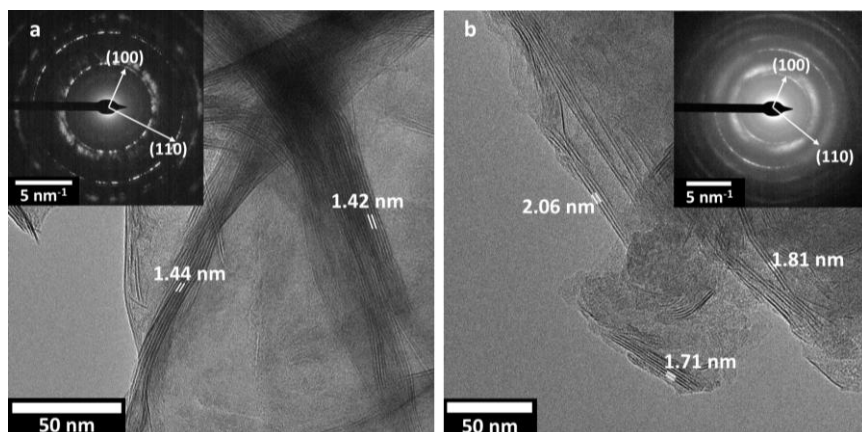
Figure S 3.7 HRTEM of (a) Ti$_3$C$_2$@CPE 10:1 and (b) Ti$_3$C$_2$@CPE 5:1, including SAED pattern as insets, identifying diffraction rings corresponding to the (100) and (110) sets of planes of Ti$_3$C$_2$T$_x$ with d-spacings of 2.6 Å and 1.5 Å, respectively.[2]
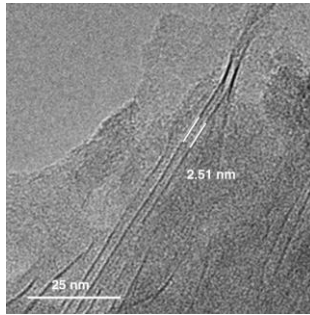
Figure S 3.8 HRTEM of Ti$_3$C$_2$@CPE 2:1.
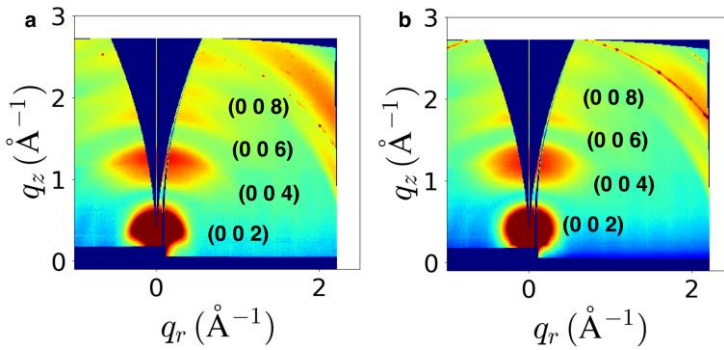
Figure S 3.9 GIWAXS patterns of (a) Ti$_3$C$_2$@CPE 10:1. (b) Ti$_3$C$_2$@CPE 5:1.
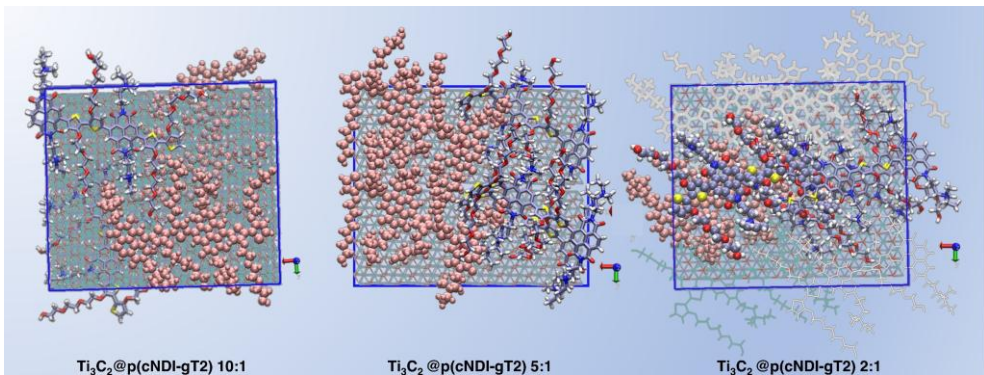
Figure S 3.10 MD simulation snapshots showing the top view of Ti$_3$C$_2$@CPE structure. Legend: cyan, Ti; ice blue, C; red, O; Brown, F; White, H; Yellow, S; Blue, N. Individual polymers were illustrated with different renderings for clarity.

Supplementary discussion: In the pristine MXene, the simulated d-spacing is 1.02 nm consistent with DFT value of 0.97 nm that indicates the applicability of the UFF for MXene system[57]. MXene intercalating with 48:1 Li^+3H_2O shows a d-spacing of 1.2 nm, in accord with $d_{experiment} = 1.19$ nm for self-assembled MXene structure without p(cNDI-gT2). This observation suggests that there is still intercalated Li^+ and water left between MXene even with the experimental procedure of vacuum and high temperature drying. In the 96:1 case, the simulated d-spacing is 1.49 nm vs. $d_{experiment} = 1.38$ nm. In this low polyelectrolyte concentration, p(cNDI-gT2) conformation is perfectly parallel to the MXene base layer. Increasing polyelectrolyte mole ratio to 48:1, the simulated d-spacing only increases slightly to 1.52 nm with parallel p(cNDI-gT2) alignment and interlocking side chains. At 24:1 mole ratio, parallel alignment cannot be maintained and slightly inclined conformation with noticeable overlapping in the c direction was observed. In the 12:1 case, bilayer stacking with two slanted p(cNDI-gT2) monolayers is evident. Significant overlaying can be seen in each monolayer.
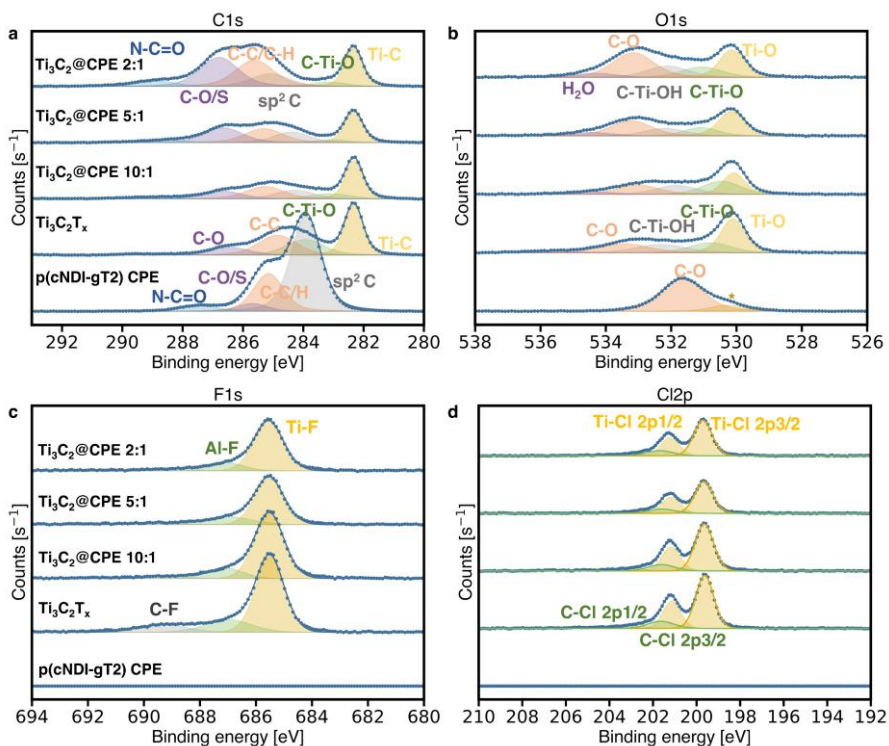
3

Figure S 3.11 (a) C1s and (b) O1s XPS spectra (c) F1s and (d) Cl2p of p(cNDI-gT2) CPE, $Ti_3C_2T_x$, and Ti_3C_2@CPE.

Supplementary discussion: Notably, the N1s peak located at 397.3 eV of the pristine $Ti_3C_2T_x$ sample (**Figure 3.2 h**) is attributed to the interaction of the surface Ti atom with adsorbed N pollutants. This peak remains present for the Ti_3C_2@CPE. The N1s spectrum for p(cNDI-gT2) was assigned into two peaks centered at 399.0 eV and 401.2 eV, corresponding to the imide N in the conjugated backbone and quaternary N^+ group in the pendant side chains, respectively. When p(cNDI-gT2) was assembled with MXene, the quaternary N^+ of p(cNDI-gT2) showed an increasing BE from 401.5 eV to 402.2 eV for both Ti_3C_2@CPE 10:1 and Ti_3C_2@CPE 5:1, and to 402.7 eV for Ti_3C_2@CPE 2:1. This substantial increase in BE cannot be explained by electrostatic interaction, as the anticipated electrostatic attraction between MXene and p(cNDI-gT2) would result in a higher electron density around quaternary N^+ and thus cause a downshift to a lower BE, a trend opposite to the observed increase in BE. Additionally, the imide N peak also shifted upwards in BE for all Ti_3C_2@CPE films (400.2 eV, 400.5 eV and 400.7 eV for Ti_3C_2@CPE 10:1, Ti_3C_2@CPE 5:1, Ti_3C_2@CPE 2:1, respectively). Similar increase in BE by 1.5 eV of C-S was observed in the S2p spectra after self-assembly (**Figure 3.2 i**). O1s and C1s signals are also analyzed to reveal the change of p(cNDI-gT2) after self-assembly. For instance, a significant blueshift of C-O signal associated with the p(cNDI-gT2) has been observed in both C1s and O1s spectra, which is possibly attributed to the surface charging or the dipole moment formed between $Ti_3C_2T_x$ MXene and p(cNDI-gT2). The surface terminations of $Ti_3C_2T_x$ MXene were further analyzed through the O1s, F1s, Cl2p spectra of $Ti_3C_2T_x$ and Ti_3C_2@CPE. No significant difference between original $Ti_3C_2T_x$ and Ti_3C_2@CPE was seen, also suggesting the self-assembly of $Ti_3C_2T_x$ and p(cNDI-gT2) is mainly driven by the electrostatic force, rather than the formation of covalent bond. Moreover, we analyze the O1s signal quantitively to estimate the ratio between -OH and =O of MXene, in order to reveal the chemical formula of $Ti_3C_2T_x$ for MD simulation. Since the intensity between C-Ti-O and C-Ti-OH is calculated to be 1:1, the molar ratio between -OH and =O of $Ti_3C_2T_x$ is determined to be 1-to-1.
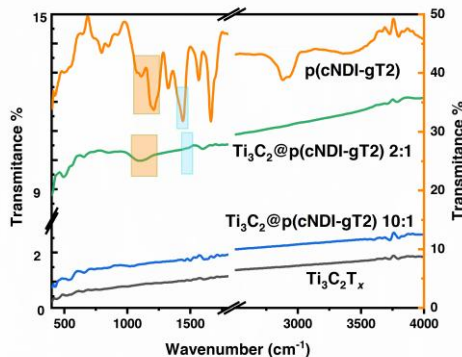
Figure S 3.12 FTIR spectra of p(cNDI-gT2), Ti$_3$C$_2$T$_x$, Ti$_3$C$_2$@CPE 10:1 and Ti$_3$C$_2$@ CPE 2:1 within the wavenumber range from 400 - 4000 cm^{-1}.
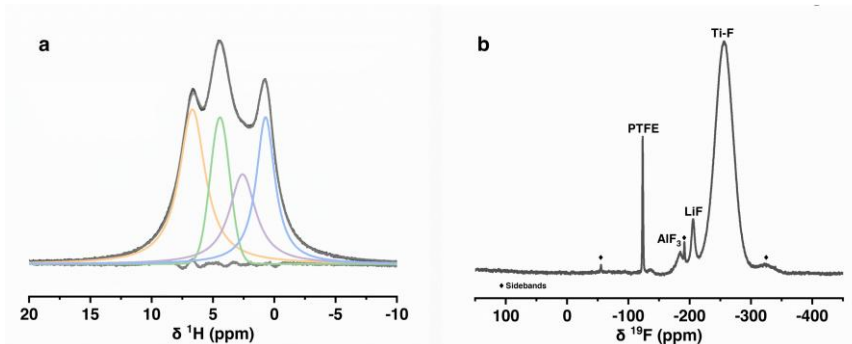

Figure S 3.13 (a) ^{1}H and (b) ^{19}F NMR spectra (11.7 T) of Ti$_3$C$_2$T$_x$ recorded at 32 kHz MAS.

Supplementary discussion: In general, the spin counting experiments are conducted on three samples of different known masses of adamantane, Ti$_3$C$_2$T$_x$ and PTFE, respectively. The mass of H$_2$O, and AlF$_3$, LiF impurities can be calculated from the relative ^{1}H and ^{19}F intensity compared to adamantane and PTFE, respectively. (^{1}H spectra were referenced relative to adamantane at 1.81 ppm, and ^{19}F spectra were referenced relative to PTFE at -122 ppm.) The mass of Ti$_3$C$_2$T$_x$ is then determined by subtracting the mass of impurities from the total sample mass. The ^{1}H spectrum was fitted into four peaks: 0.68 ppm, 2.54 ppm, both of which correspond to the surface -OH groups, and 4.42 ppm and 6.64 ppm that correspond to the absorbed H$_2$O[58]. The ^{19}F spectrum of Ti$_3$C$_2$T$_x$ sample was assigned to LiF (-205.9 ppm), AlF$_3$(-183.7 ppm) and Ti-F(-256.3 ppm)[52]. The estimated molar ratio between -F and -OH surface groups is found to be 1:1. Therefore, the surface chemistry of original Ti$_3$C$_2$T$_x$ is estimated to be : -OH: =O: -F =1:1:1.
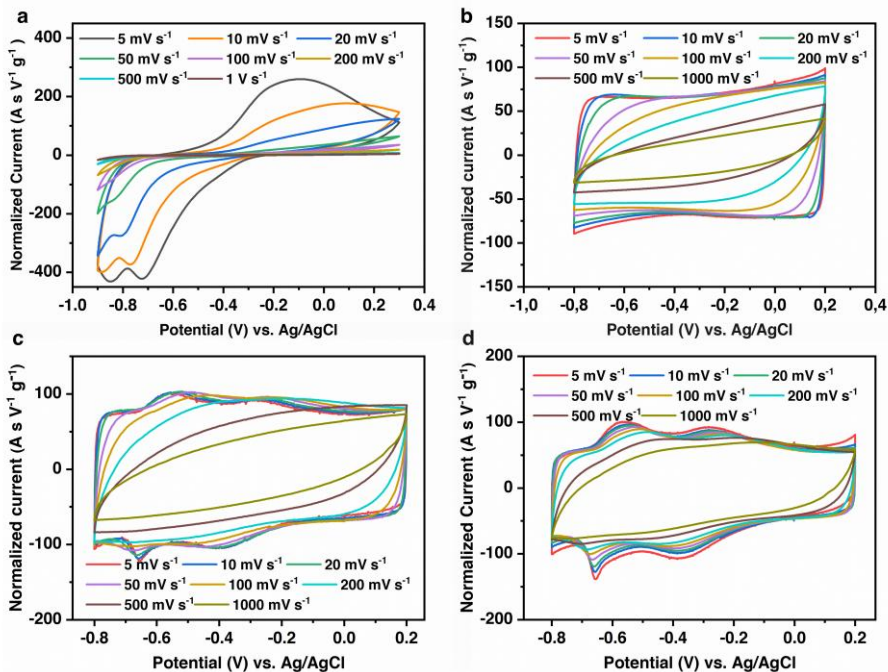
Figure S 3.14 Cyclic voltammograms (CV) of (a) p(cNDI-gT2). (b)Ti$_3$C$_2$T$_x$. (c) Ti$_3$C$_2$@CPE 10:1. and (d) Ti$_3$C$_2$@CPE 5:1 in 1 M NH$_4$Cl at different scan rates from 5 mV s^{-1} and 1 V s^{-1}.
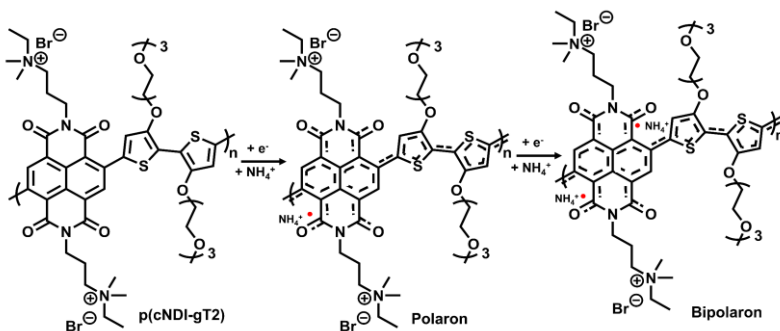

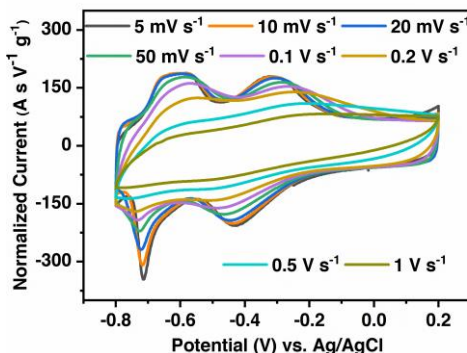**Figure S 3.15 The two-electron charge transfer process of p(cNDI-gT2) for NH$_4^+$ storage.**

Figure S 3.16 Cyclic voltammograms (CV) of Ti$_3$C$_2$@CPE 2:1 in 1 M NH$_4$NO$_3$ at different scan rates from 5 mV s^{-1} and 1 V s^{-1}.
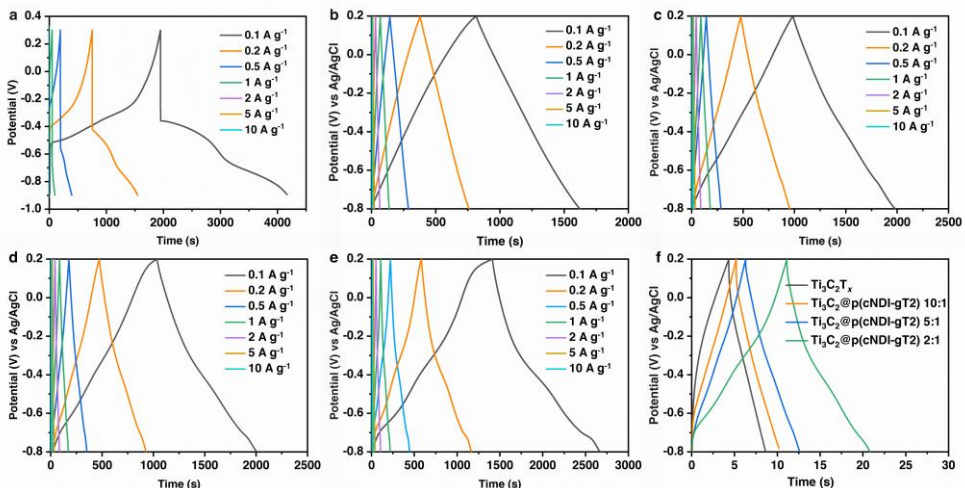

Figure S 3.17 Electrochemical performance of Ti$_3$C$_2$T$_x$, p(cNDI-gT2) and Ti$_3$C$_2$@CPE in 1 M NH$_4$Cl. Galvanostatic charge and discharge (GCD) curves of (a) p(cNDI-gT2). (b)Ti$_3$C$_2$T$_x$. (c) Ti$_3$C$_2$@CPE 10:1. (d) Ti$_3$C$_2$@CPE 5:1 and (e) Ti$_3$C$_2$@CPE 2:1 at current densities ranging from 0.1 to 10 A g^{-1}. (f) GCD curves of Ti$_3$C$_2$T$_x$ and Ti$_3$C$_2$@CPE at 10 A g^{-1}.
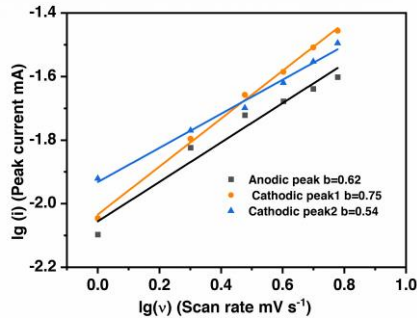
Figure S 3.18 The relationship between cathodic and anodic peak currents and scan rates for p(cNDI-gT2).

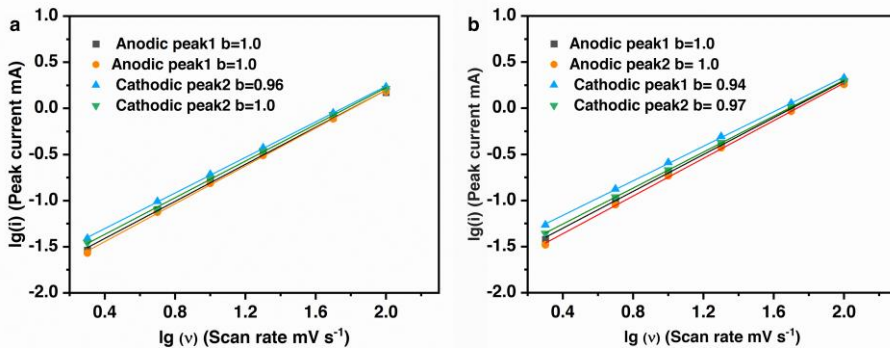**Figure S 3.19** The relationship between cathodic and anodic peak currents and scan rates for (a) Ti_3C_2@CPE 10:1 and (b) Ti_3C_2@CPE 5:1.
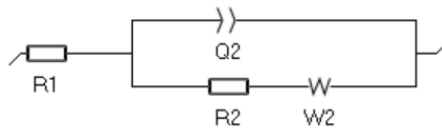

Figure S 3.20 equivalent electrical circuit used for impedance fitting. Where R_1 stands for series ohmic resistance (R_s), R_2 represents the charge transfer resistance (R_{ct}) , w is the warburg resistance and Q_2 is the Constant phase element.
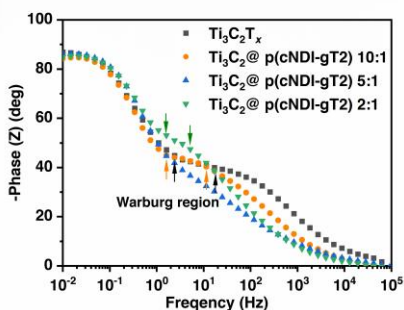
Figure S 3.21 Bode plots of $Ti_3C_2T_x$ and Ti_3C_2@CPE films showing the Warburg region.

Supplementary discussion: At a low frequency of 10 mHz, all Ti_3C_2@CPE films show a phase angle close to $-90°$ in 1 M NH_4Cl electrolyte, demonstrating capacitive behavior. Frequencies corresponding to a phase angle of $-45°$ are considered as the Warburg region, which is marked with arrows.

Figure S 3.22 Images of GF-A separators after cycling with p(cNDI-gT2) (left) and Ti_3C_2@CPE 2:1 electrode in 1M NH_4Cl electrolytes.
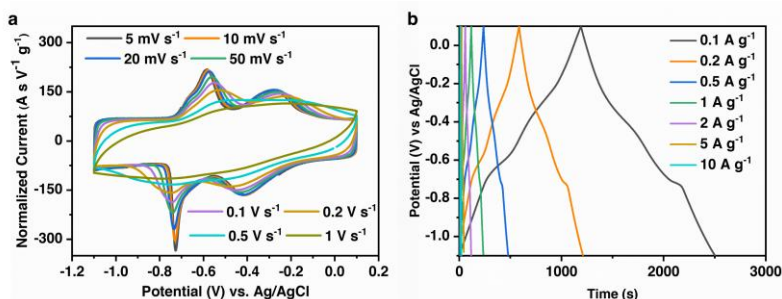
Figure S 3.23 Electrochemical performance of Ti_3C_2@CPE 2:1 in 1 M KCl. (a) CVs of Ti_3C_2@CPE 2:1 at different scan rates from 5 mV s^{-1} and 1 V s^{-1}. and (b) Galvanostatic charge and discharge (GCD) curves at current densities ranging from 0.1 to 10 A g^{-1}.
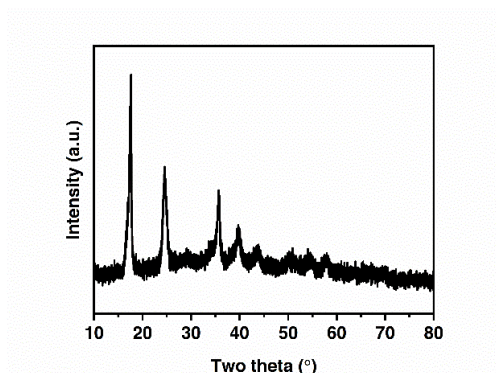
Figure S 3.24 XRD pattern of $(NH_4)_2CuFe(CN)_6$ (NH$_4$-CuHCF).
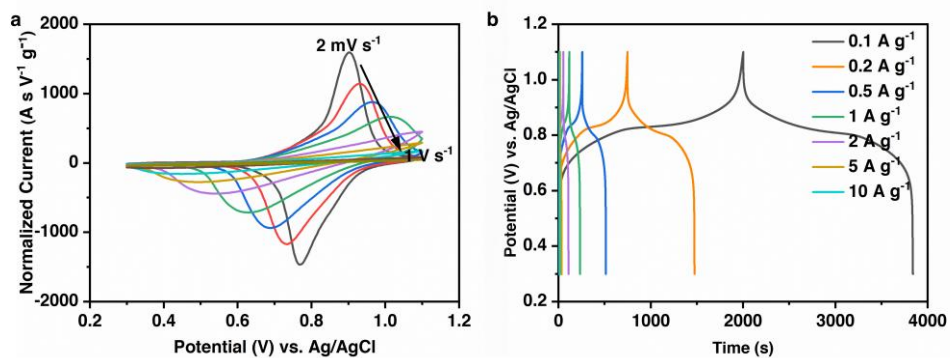
Figure S 3.25 (a) CV curves of NH$_4$-CuHCF at different scan rates (ranging from 2 mV s^{-1} to 1V s^{-1}). (b) The GCD curves of NH$_4$-CuHCF at different current densities.

Supplementary discussion: The electrochemical performance of NH$_4$-CuHCF was evaluated by cyclic voltammetry and galvanostatic charge and discharge within a potential window from 0.3 V to 1.1 V vs. Ag/AgCl (3.5 M). The CV curves feature a widely spread cathodic/anodic current peak at 0.72/0.87 V vs. Ag/AgCl, which is possibly attributed to the $[Fe(CN)_6]^{3-}/[Fe(CN)_6]^{4-}$ couple upon NH$_4^+$ (de)intercalation. The specific capacity of NH$_4$-CuHCF was calculated to be 199.8 C g^{-1} at 0.1 A g^{-1}.
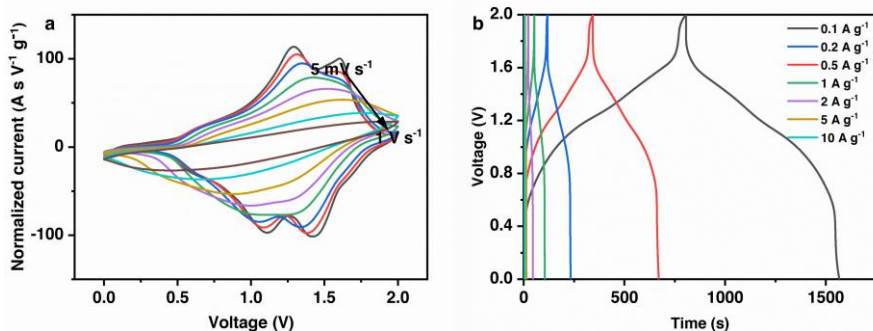
Figure S 3.26 (a) CV curves at different scan rates ranging from 5 mV s^{-1} to 1 V s^{-1} and **(b)** GCD curves at different current densities of the Ti$_3$C$_2$@CPE 2:1//NH$_4$-CuHCF.

Supplementary discussion: For full-cells, the Ti$_3$C$_2$@CPE 2:1 negative electrode was paired with the NH$_4$-CuHCF positive electrode in a weight ratio ≈2:1. Ti$_3$C$_2$@CPE 2:1//NH$_4$-CuHCF hybrid capacitor could be operated within a wide voltage window of 2.0 V in 1 M NH$_4$Cl electrolyte.
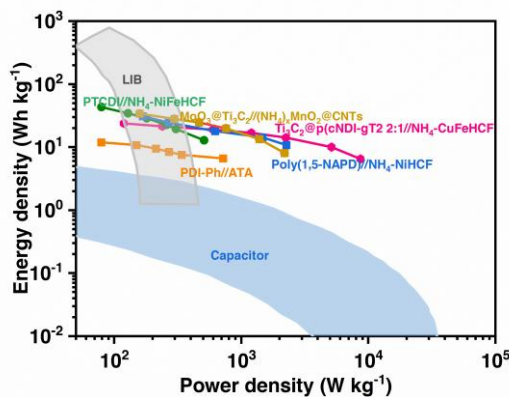
Figure S 3.27 Ragone plot of Ti$_3$C$_2$@CPE 2:1//NH$_4$-CuHCF full cell and the comparison with other ammonium-ion storage systems [16,59–61].

Supplementary Tables

Table S 3.1 d-spacing and FWHM of the (0 0 2) diffraction peak of different $Ti_3C_2T_x$@CPE composites.

Mass ratio between $Ti_3C_2T_x$ and p(cNDI-gT2)	Molar fraction of p(cNDI-gT2) in the composite (%)	d-spacing after drying at 150°C over night (nm)	Increase in d-spacing (nm)	FWHM of (0 0 2) peak (°)
$Ti_3C_2T_x$	-	1.19	-	0.75
20:1	1.04	1.38	0.19	0.996
10:1	2.04	1.47	0.28	1.012
7.5:1	3.03	1.58	0.39	1.009
6:1	3.45	1.65	0.46	0.977
5:1	4.00	1.72	0.53	0.957
4:1	5.00	1.75	0.56	1.005
3:1	6.67	1.96	0.77	1.109
2:1	7.7	2.15	0.96	0.761

Table S 3.2 EIS fitting results of $Ti_3C_2T_x$,p(cNDI-gT2) CPE and Ti_3C_2@CPE in 1 M NH_4Cl.

	R_s (Ω)	R_{ct} (Ω)
$Ti_3C_2T_x$	2.40	0.2
Ti_3C_2@CPE 10:1	2.30	0.55
Ti_3C_2@CPE 5:1	3.03	0.99
Ti_3C_2@CPE 2:1	2.51	1.04
p(cNDI-gT2) CPE	3.55	64.89

Table S 3.3 Calculated utilization of p(cNDI-gT2) in Ti$_3$C$_2$@CPE.

Scan rate (mV s^{-1})	Specific Capacity based on the mass of individual component (C g^{-1})	Ti$_3$C$_2$T$_x$	Ti$_3$C$_2$@CPE 10:1	Ti$_3$C$_2$@CPE 5:1	Ti$_3$C$_2$@CPE 2:1	p(cNDI-gT2)
5	Ti$_3$C$_2$T$_x$	66.1 C g^{-1}	64.7 C g^{-1}	73.7 C g	93.7 C g^{-1}	-
	p(cNDI-gT2)	-	97.8 C g^{-1}	94.3 C g^{-1}	180 C g^{-1}	48.0 C g^{-1}
	Electron transfer number per p(cNDI-gT2) unit	-	0.96 (48% utilization)	0.92 (56%)	1.78 (89%)	0.97 (48%)
10	Ti$_3$C$_2$T$_x$	63.8 C g^{-1}	62.3 C g^{-1}	70.3 C g^{-1}	93.7 C g^{-1}	-
	p(cNDI-gT2)	-	97.8 C g^{-1}	94.3 C g^{-1}	172.5 C g^{-1}	35.6 C g^{-1}
	Electron transfer number per p(cNDI-gT2) unit	-	0.96 (48% utilization)	0.92 (56%)	1.70 (85%)	0.72 (36%)
20	Ti$_3$C$_2$T$_x$	61.5 C g^{-1}	62.3 C g^{-1}	69.0 C g^{-1}	93.7 C g^{-1}	-
	p(cNDI-gT2)	-	88.6 C g^{-1}	87.8 C g^{-1}	159.3 C g^{-1}	25.5 C g^{-1}
	Electron transfer number per p(cNDI-gT2) unit	-	0.88 (44%)	0.86 (43%)	1.56 (78%)	0.24 (12%)
50	Ti$_3$C$_2$T$_x$	57.6 C g^{-1}	62.3 C g^{-1}	66.8 F g^{-1}	93.7 C g^{-1}	-
	p(cNDI-gT2)	-	67.2 C g^{-1}	81.4 C g^{-1}	148.1 C g^{-1}	18.4 C g^{-1}
	Electron transfer number per	-	0.66 (33%)	0.8 (40%)	1.46 (73%)	0.18 (9%)

3

	p(cNDI-gT2) unit					
100	$Ti_3C_2T_x$	53.1 C g^{-1}	62.0 C g^{-1}	65.5 C g^{-1}	93.7 C g^{-1}	-
	p(cNDI-gT2)	-	42.8 C g^{-1}	75.0 C g^{-1}	133.0 C g^{-1}	13.5 C g^{-1}
	Electron transfer number per p(cNDI-gT2) unit	-	0.42 (21%)	0.74 (37%)	1.32 (67%)	0.12 (6%)

Supplementary discussion: The current contribution from MXene at different scan rate (5 - 100 mV s^{-1}) in Ti_3C_2@CPE heterostructures are estimated as the value at the OCV on each CV curve. The capacity contribution of $Ti_3C_2T_x$ is calculated by integrating the current over time. The redox contribution from p(cNDI-gT2) is calculated by extracting the contribution of MXene from Ti_3C_2@CPE 10:1, 5:1 and 2:1 sample, respectively. The specific capacity of MXene and p(cNDI-gT2) is calculated based on the mass of individual component in the corresponding sample. Taking the theorical specific capacity of p(cNDI-gT2) (203 C g^{-1}) into consideration, the electron transfer number per p(cNDI-gT2) unit and the utilization in Ti_3C_2@CPE at different rates can be estimated accordingly.

3.5 Reference

1   P. Simon and Y. Gogotsi, *Nat. Mater.*, 2020, **19**, 1151–1163.

2   M. Li, J. Lu, Z. Chen and K. Amine, *Adv.Mater.*, 2018, **30**, 1800561.

3   J. Li, J. Fleetwood, W. B. Hawley and W. Kays, *Chem. Rev.*, 2022, **122**, 903–956.

4   R. Schmuch, R. Wagner, G. Hörpel, T. Placke and M. Winter, *Nat. Energy*, 2018, **3**, 267–278.

5   A. Kwade, W. Haselrieder, R. Leithoff, A. Modlinger, F. Dietrich and K. Droeder, *Nat. Energy*, 2018, **3**, 290–300.

6   J. Han, A. Varzi and S. Passerini, *Angew. Chem. Int. Ed*. 2022, **61**, e202115046.

7   Y. Sun, B. Yin, J. Yang, Y. Ding, M. Li, H. Li, J. Li, B. Jia, S. Zhang and T. Ma, *Energy Environ. Sci.*, 2023, **16**, 5568–5604.

8   C. Liu, M. Li, J. Meng, P. Hei, J. Wang, Y. Song and X.-X. Liu, *Adv. Funct. Mater.*, 2024, **34**, 2310437.

9   S. Dong, W. Shin, H. Jiang, X. Wu, Z. Li, J. Holoubek, W. F. Stickle, B. Key, C. Liu, J. Lu, P. Alex. Greaney, X. Zhang and X. Ji, *Chem.*, 2019, **5**, 1537–1551.

10   C. D. Wessells, S. V. Peddada, M. T. McDowell, R. A. Huggins and Y. Cui, *J. Electrochem. Soc.*, 2011, **159**, A98.

11   Q. Chen, M. Song, X. Zhang, J. Zhang, G. Hou and Y. Tang, *J. Mater. Chem. A*, 2022, **10**, 15614–15622.

12   L. Han, J. Luo, R. Zhang, W. Gong, L. Chen, F. Liu, Y. Ling, Y. Dong, Z. Yong, Y. Zhang, L. Wei, X. Zhang, Q. Zhang and Q. Li, *ACS Nano*, 2022, **16**, 14951–14962.

13   S. Zhang, K. Zhu, Y. Gao and D. Cao, *ACS Energy Lett.*, 2023, **8**, 889–897.

14   R. Zheng, Y. Li, H. Yu, X. Zhang, D. Yang, L. Yan, Y. Li, J. Shu and B.-L. Su, *Angew. Chem. Int. Ed.* , 2023, **62**, e202301629.

15   Z. Tian, V. S. Kale, Y. Wang, S. Kandambeth, J. Czaban-Jóźwiak, O. Shekhah, M. Eddaoudi and H. N. Alshareef, *J. Am. Chem. Soc.*, 2021, **143**, 19178–19186.

16   X. Wu, Y. Qi, J. J. Hong, Z. Li, A. S. Hernandez and X. Ji*, Angew. Chem.* , 2017, **129**, 13206–13210.

17   M. Naguib, V. N. Mochalin, M. W. Barsoum and Y. Gogotsi, *Adv. Mater.*, 2014, **26**, 992–1005.

18   X. Li, Z. Huang, C. E. Shuck, G. Liang, Y. Gogotsi and C. Zhi, *Nat. Rev. Chem.*, 2022, **6**, 389–404.

19   X. Wang, T. S. Mathis, K. Li, Z. Lin, L. Vlcek, T. Torita, N. C. Osti, C. Hatter, P. Urbankowski, A. Sarycheva, M. Tyagi, E. Mamontov, P. Simon and Y. Gogotsi, *Nat. Energy*, 2019, **4**, 241–248.

20   M. Ghidiu, M. R. Lukatskaya, M.-Q. Zhao, Y. Gogotsi and M. W. Barsoum, *Nature*, 2014, **516**, 78–81.

21   Y. Li, H. Shao, Z. Lin, J. Lu, L. Liu, B. Duployer, P. O. Å. Persson, P. Eklund, L. Hultman, M. Li, K. Chen, X.-H. Zha, S. Du, P. Rozier, Z. Chai, E. Raymundo-Piñero, P.-L. Taberna, P. Simon and Q. Huang, *Nat. Mater.*, 2020, **19**, 894–899.

22   M. R. Lukatskaya, *Adv. Energy Mater.*, 2015, **5**, 1500589.

3

23   M. R. Lukatskaya, O. Mashtalir, C. E. Ren, Y. Dall'Agnese, P. Rozier, P. L. Taberna, M. Naguib, P. Simon, M. W. Barsoum and Y. Gogotsi, *Science*, 2013, **341**, 1502–1505.

24   W. Yang, B. Huang, L. Li, K. Zhang, Y. Li, J. Huang, X. Tang, T. Hu, K. Yuan and Y. Chen, *Small Methods*, 2020, **4**, 2000434.

25   M. Boota, B. Anasori, C. Voigt, M.-Q. Zhao, M. W. Barsoum and Y. Gogotsi, *Adv. Mater.*, 2016, **28**, 1517–1522.

26   K. A. S. Usman, J. Zhang, D. Y. Hegh, A. O. Rashed, D. Jiang, P. A. Lynch, P. Mota-Santiago, K. L. Jarvis, S. Qin, E. L. Prime, M. Naebe, L. C. Henderson and J. M. Razal, *Adv. Mater. Interfaces*, 2021, **8**, 2002043.

27   K. Li, X. Wang, S. Li, P. Urbankowski, J. Li, Y. Xu and Y. Gogotsi, *Small*, 2020, **16**, 1906851.

28   G. S. Gund, J. H. Park, R. Harpalsinh, M. Kota, J. H. Shin, T. Kim, Y. Gogotsi and H. S. Park, *Joule*, 2019, **3**, 164–176.

29   X. Wang, S.-M. Bak, M. Han, C. E. Shuck, C. McHugh, K. Li, J. Li, J. Tang and Y. Gogotsi, *ACS Energy Lett.*, 2022, **7**, 30–35.

30   B. R. P. Yip, R. Javier Vázquez, Y. Jiang, S. R. McCuskey, G. Quek, D. Ohayon, X. Wang and G. C. Bazan, *Adv. Mater.*, 2024, **36**, 2308631.

31   G. Quek, B. Roehrich, Y. Su, L. Sepunaru and G. C. Bazan, *Adv. Mater.*, 2022, **34**, 2104206.

32   D. Moia, A. Giovannitti, A. A. Szumska, I. P. Maria, E. Rezasoltani, M. Sachs, M. Schnurr, P. R. F. Barnes, I. McCulloch and J. Nelson, *Energy Environ. Sci.*, 2019, **12**, 1349–1357.

33   G. Quek, R. J. Vázquez, S. R. McCuskey, B. Kundukad and G. C. Bazan, *Adv. Mater.*, 2022, **34**, 2203480.

34   G. B. Tezel, K. Arole, D. E. Holta, M. Radovic and M. J. Green, *J.Colloid Interface Sci.*, 2022, **605**, 120–128.

35   S. Sharma, N. B. Kolhe, V. Gupta, V. Bharti, A. Sharma, R. Datt, S. Chand and S. K. Asha, *Macromolecules*, 2016, **49**, 8113–8125.

36   M. Ghidiu and M. W. Barsoum, *J. Am. Ceram. Soc.*, 2017, **100**, 5395–5399.

37   M. Volkov, E. Willinger, D. A. Kuznetsov, C. R. Müller, A. Fedorov and P. Baum, *ACS Nano*, 2021, **15**, 14071–14079.

38   J. A. Steele, E. Solano, D. Hardy, D. Dayton, D. Ladd, K. White, P. Chen, J. Hou, H. Huang, R. A. Saha, L. Wang, F. Gao, J. Hofkens, M. B. J. Roeffaers, D. Chernyshov and M. F. Toney, *Adv. Energy Mater.*, 2023, **13**, 2300760.

39   M. Boota, C. Chen, L. Yang, A. I. Kolesnikov, N. C. Osti, W. Porzio, L. Barba and J. Jiang, *Chem. Mater.*, 2020, **32**, 7884–7894.

40   M. Boota, M. Pasini, F. Galeotti, W. Porzio, M.-Q. Zhao, J. Halim and Y. Gogotsi, *Chem. Mater.*, 2017, **29**, 2731–2738.

41   X. Jin, W. Zhang, S. Liu, T. Zhang, Z. Song, W. Shao, R. Mao, M. Yao, X. Jian and F. Hu, *Chem. Eng. J.*, 2023, **451**, 138763.

42   P. H. Nguyen, D. H. Nguyen, D. Kim, M. K. Kim, J. Jang, W. H. Sim, H. M. Jeong, G. Namkoong and M. S. Jeong, *ACS Appl. Mater. Interfaces*, 2022, **14**, 51487–51495.

43   R. B. Rakhi, B. Ahmed, M. N. Hedhili, D. H. Anjum and H. N. Alshareef, *Chem. Mater.*, 2015, **27**, 5314–5323.

44   C. R. DeBlase, K. Hernández-Burgos, J. M. Rotter, D. J. Fortman, D. dos S. Abreu, R. A. Timm, I. C. N. Diógenes, L. T. Kubota, H. D. Abruña and W. R. Dichtel, *Angew. Chem. Int. Ed.*, 2015, **54**, 13225–13229.

45   T. S. Mathis, N. Kurra, X. Wang, D. Pinto, P. Simon and Y. Gogotsi, *Adv. Energy Mat.*, 2019, **9**, 1902007.

46   T. Brezesinski, J. Wang, J. Polleux, B. Dunn and S. H. Tolbert, *J. Am. Chem. Soc.*, 2009, **131**, 1802–1809.

47   S. Fleischmann, J. B. Mitchell, R. Wang, C. Zhan, D. Jiang, V. Presser and V. Augustyn, *Chem. Rev.*, 2020, **120**, 6738–6782.

48   K. Ge, H. Shao, E. Raymundo-Piñero, P.-L. Taberna and P. Simon, *Nat. Commun.*, 2024, **15**, 1935.

49   J. Chmiola, G. Yushin, Y. Gogotsi, C. Portet, P. Simon and P. L. Taberna, *Science*, 2006, **313**, 1760–1763.

50   S. Fleischmann, Y. Zhang, X. Wang, P. T. Cummings, J. Wu, P. Simon, Y. Gogotsi, V. Presser and V. Augustyn, *Nat. Energy*, 2022, **7**, 222–228.

3

51   X. Wang, T. S. Mathis, Y. Sun, W.-Y. Tsai, N. Shpigel, H. Shao, D. Zhang, K. Hantanasirisakul, F. Malchik, N. Balke, D. Jiang, P. Simon and Y. Gogotsi, *ACS Nano*, 2021, **15**, 15274–15284.

52   M. A. Hope, A. C. Forse, K. J. Griffith, M. R. Lukatskaya, M. Ghidiu, Y. Gogotsi and C. P. Grey, *Physical Chemistry Chemical Physics*, 2016, **18**, 5099–5102.

53   R. Peng, K. Han and K. Tang, *Journal of The Electrochemical Society*, 2022, **169**, 060523.

54   A. K. Rappe, C. J. Casewit, K. S. Colwell, W. A. Goddard and W. M. Skiff, *J. Am. Chem. Soc.*, 1992, **114**, 10024–10035.

55   O. Mashtalir, M. Naguib, V. N. Mochalin, Y. Dall'Agnese, M. Heon, M. W. Barsoum and Y. Gogotsi, *Nat. Commun.*, 2013, **4**, 1716.

56   L. Sarkisov, R. Bueno-Perez, M. Sutharson and D. Fairen-Jimenez, *Chem. Mater.*, 2020, **32**, 9849–9867.

57   M. Naguib, M. Kurtoglu, V. Presser, J. Lu, J. Niu, M. Heon, L. Hultman, Y. Gogotsi and M. W. Barsoum, in *MXenes*, *Adv. Mater.*, 2021, **23**, 4248-4253.

58   T. Kobayashi, Y. Sun, K. Prenger, D. Jiang, M. Naguib and M. Pruski, *J. Phys. Chem. C*, 2020, **124**, 13649–13655.

59   K. C. S. Lakshmi, X. Ji, T.-Y. Chen, B. Vedhanarayanan and T.-W. Lin, *J. Power Sources*, 2021, **511**, 230434.

60   L. Yang, W. Zheng, J. Halim, J. Rosen, Z. Sun and M. W. Barsoum, *Batteries Supercaps*, 2023, **6**, e202200432.

61   L. Yan, Y. Qi, X. Dong, Y. Wang and Y. Xia, *eScience*, 2021, **1**, 212–218.

3

4 Enhancing pseudocapacitive Intercalation in Ti$_3$C$_2$T$_x$ MXene with Molecular Crowding Electrolytes

Abstract

The growing demand for safe, cost-efficient, high-energy and high-power electrochemical energy storage devices has stimulated the development of aqueous-based supercapacitors with high capacitance, high rate capability, and high voltage. 2D titanium carbide MXene-based electrodes have shown excellent rate capability in various dilute aqueous electrolytes, yet their potential window is usually narrower than 1.2 V. In this study, we show that the potential window of $Ti_3C_2T_x$ MXene can be efficiently widened to 1.5 V in a cost-effective and environmentally benign polyethylene glycol (PEG) containing molecular crowding electrolyte. Additionally, a pair of redox peaks at -0.25 V/-0.05 V vs. Ag (cathodic/anodic) emerged in cyclic voltammogram after the addition of PEG, yielding an additional 25% capacitance. Interestingly, we observed the co-insertion of the molecular crowding agent PEG-400 during the Li^+ intercalation process based on *in-situ* X-ray diffraction analysis. As a result, $Ti_3C_2T_x$ electrodes presented an interlayer space change of 4.7 Å during a complete charge/discharge process, which is the largest reversible interlayer space change reported so far for MXene-based electrodes. This work demonstrates the potential of adding molecular crowding agents to improve the performance of MXene electrodes in aqueous electrolytes and to enlarge the change of the interlayer spacing.

4

4.1 Introduction

There is an increasing need for safe, low-cost, high-energy and high-power electrochemical energy storage (EES) devices due to the rapidly growing market for electric vehicles and renewable energy. Capacitive/pseudocapacitive energy storage, which involves the formation of electrochemical double layer (EDL) and/or surface-controlled redox reactions, shows a high power density and superior cycling stability, but a lower energy density compared to Li-ion batteries[1,2]. Commercial EDL capacitors with activated carbon electrodes and traditional organic electrolytes can achieve an energy density of 10 Wh kg^{-1} at a superior power density of 30 kW kg^{-1} [3]. However, the inherent flammability and toxicity of organic electrolytes raise significant safety concerns. Aqueous electrolytes are considered reliable alternatives to organic electrolytes because they are much safer, more cost-effective, and eco-friendly. The main issue with dilute aqueous electrolytes is that their electrochemical stability windows (ESW) are limited by the water electrolysis reaction (~1.23 V). The narrow ESW not only restricts the options of promising electrodes but also limits the energy and power density of aqueous energy storage devices[4]. Increasing the salt concentration in water has been found to extend the ESW of aqueous electrolytes by suppressing water decomposition. For example, the use of "water-in-salt" (WIS) 21 m Lithium bis(trifluoromethanesulfonyl)imide (LiTFSI) electrolyte leads to a wide ESW of up to 3 V[5]. Meanwhile, the high cost of the WIS electrolytes with fluorinated lithium salts impedes their practical application. One promising approach to widen the ESW without increasing the cost is to use the molecular crowding aqueous electrolyte (MCE). By introducing polyethylene glycol (PEG) as the crowding agent, a wide ESW of 3.2 V has been reached with only 2 m LiTFSI concentration. In MCE, the ethereal oxygen atom in PEG has a higher negative charge density than the oxygen atom in water, leading to weaker hydrogen bonding between H$_2$O–PEG compared to H$_2$O–H$_2$O. Thus, the H–O covalent bond in water is strengthened, and hence, a higher overpotential is needed to electrochemically decompose water[6].

MXene (M$_{n+1}$X$_n$T$_x$) is an emerging family of two-dimensional transition metal carbides and/or nitrides, in which M is an early transition metal, X represents C and/or N, and T$_x$ stands for surface groups such as =O, -OH, -Cl or -F. MXenes exhibit good mechanical stability, great hydrophilicity, superior electronic conductivity, and flexible interlayer spacing, which makes them promising electrode materials for EES[7–9]. A variety of cations, solvent molecules, and large organic molecules have been observed to intercalate spontaneously or electrochemically into MXene interlayers, resulting in changes in interlayer spacing[10–12]. The electrochemical intercalation processes of ions and molecules are highly dependent on the surface chemistry of MXene and the electrolyte composition. For example, strong surface

redox reactions have been observed with the proton intercalation process in $Ti_3C_2T_x$ electrode with acidic aqueous electrolytes. The surface redox reaction occurs due to the transformation between the oxygen surface groups (=O) and hydroxyl (-OH) groups, accompanied by the change of Ti oxidation state[13–17]. Meanwhile, $Ti_3C_2T_x$ displays EDL capacitive-dominating charge storage in neutral aqueous electrolytes due to the weaker interactions between the intercalated cations and MXene surface groups[18,19]. Though the potential window of MXene in the neutral aqueous electrolyte is slightly wider than that in the acidic electrolyte, it is still < 1.2 V, limited by the hydrogen evolution reaction (HER) and MXene oxidation. With the WIS electrolytes, the MXene oxidation can be suppressed, which widens the potential window of $Ti_3C_2T_x$ up to 1.6 V. Moreover, a unique desolvation-free Li^+ ion intercalation process has been observed at the positive potential in the $Ti_3C_2T_x$ electrode with WIS electrolytes, contributing to extra capacitance[20].

This study investigated the electrochemical behavior of $Ti_3C_2T_x$ in a low-cost and environmentally benign aqueous MCE (2 m LiTFSI-PEG:H_2O) for the first time. Interestingly, MXene with MCEs showed an extra pair of redox peaks on the cyclic voltammogram (CV) compared to 2 m LiTFSI aqueous electrolyte, contributing 25% capacitance increase. To reveal the electrolyte intercalation process of MXene with MCEs, we performed the X-ray diffraction (XRD) to monitor the $Ti_3C_2T_x$ interlayer spacing change during cycling. The results indicate that the extra redox peak is due to the intercalation of solvated Li^+. We also observed the co-insertion of PEG-400, which leads to a large reversible interlayer space change of MXene during the charge and discharge process.

4.2 Results and discussions

4.2.1 Electrochemical behavior of $Ti_3C_2T_x$ in PEG-based Molecular crowding electrolyte

MCEs were made by adding PEG-400 or PEG-8000 to 2 m LiTFSI aqueous electrolyte, and the electrolyte compositions are listed as follows: 2 m LiTFSI-7:3 PEG-400:H_2O (or 7:3 PEG-400), 2 m LiTFSI-8:2 PEG-400:H_2O (or 8:2 PEG-400), and 2 m LiTFSI-7:3 PEG-8000:H_2O (or 7:3 PEG-8000). The electrolyte properties, including stability window, viscosity, and ionic conductivity, are summarized in Table S4.1. The addition of PEG-400 and PEG-8000 to 2 m LiTFSI with a PEG:H_2O mass ratio of 7:3 lowered the ionic conductivity from 20.8 mS cm^{-1} of 2 m LiTFSI to 4.15 mS cm^{-1} and 4.25 mS cm^{-1}, respectively. Further increasing the PEG-400:H_2O ratio to 8:2 increased the viscosity and reduced the ionic conductivity of the electrolyte to 1.06 mS cm^{-1}, which agrees with previous research[6,21].

Ti$_3$C$_2$T$_x$ MXene used in this study was obtained by selectively removing the A layer from the high-Al MAX precursor using LiF-HCl etching[22]. As shown in **Figure S4.1**, the characteristic peaks of precursor Ti$_3$AlC$_2$ vanished after etching and the (002) peak shifted to 6.96°, corresponding to a d-spacing of 12.7 Å, indicating the successful synthesis of Ti$_3$C$_2$T$_x$. The complete removal of the Al layer was also confirmed by X-ray photoelectron spectroscopy, as no Al was detected (**Figure S4.2**). The high-resolution Ti2p and C1s peaks were fitted, showing the typical pattern reported in the literature (**Figure S4.3**)[22]. When Ti$_3$C$_2$T$_x$ was immersed in the electrolytes, the interlayer spacing increased to 17.1 Å, 19.2 Å, 17.4 Å and 16.1 Å in LiTFSI-H$_2$O, 7:3 PEG-400, 8:2 PEG-400 and 7:3 PEG-8000, respectively (**Figure 4.1 a**). The d-spacing increase in the LiTFSI-H$_2$O electrolyte can be explained by the spontaneous intercalation of Li$^+$ and H$_2$O molecules[23]. Compared to the LiTFSI-H$_2$O electrolyte, the d-spacing change in both PEG-400 electrolytes is larger, which is likely due to the insertion of PEG-400 molecules. The spontaneous PEG-400 insertion could be facilitated by the strong hydrogen bonding between the functional group of MXene and PEG[24]. The d-spacing increase is the smallest for 7:3 PEG-8000 among all electrolytes, suggesting that PEG-8000 does not intercalate spontaneously. This is probably because the PEG-8000 molecules are larger than the original interlayer spacing of MXene[25].
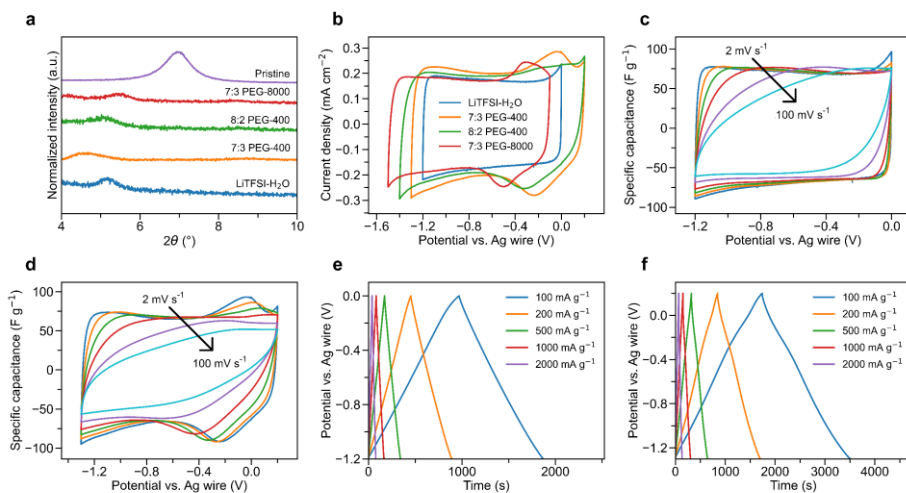

Figure 4.1 XRD patterns and electrochemical performance of Ti$_3$C$_2$T$_x$ electrodes in four electrolytes: LiTFSI-H$_2$O, 7:3 PEG-400, 8:2 PEG-400, and 7:3 PEG-8000. (a) XRD patterns of Ti$_3$C$_2$T$_x$ before and after immersing in different electrolytes. (b) Comparison of cyclic voltammogram curves at 2 mV s^{-1} of Ti$_3$C$_2$T$_x$. (c) Cyclic voltammogram curves of Ti$_3$C$_2$T$_x$ in LiTFSI-H$_2$O at different scan rates. The scan rates from the outer to the inner cycle are 2, 5, 10, 20, 50, and 100 mV s^{-1}. (d) Cyclic voltammogram curves of Ti$_3$C$_2$T$_x$ in 7:3 PEG-400 at

different scan rates. (e) Galvanostatic charge-discharge curves of $Ti_3C_2T_x$ in LiTFSI-H$_2$O. (f) Galvanostatic charge-discharge curves of $Ti_3C_2T_x$ in 7:3 PEG-400.

The ESW of the electrolytes was evaluated on glassy carbon (GC) electrodes using linear sweep voltammetry (LSV) at a scan rate of 2 mV s^{-1}. As shown in **Figure S4.4**, the introduction of PEG did not significantly widen the ESW of 2 m LiTFSI electrolyte on the GC electrode. In comparison, using MCEs expanded the potential window of MXene electrodes obviously (**Figure S4.5**). As a higher overpotential is needed to break the stronger covalent O-H bonds of water due to the introduction of PEG, the MCE electrolytes could be operated at a more negative potential range. Additionally, the decreased fraction of free water molecules in PEG-based MCE can suppress the oxidation of MXene and expand the positive potential range. Therefore, a voltage window expansion of 0.3, 0.4, and 0.2 V compared to the 2 m LiTFSI was achieved in 7:3 PEG-400, 8:2 PEG-400, and 7:3 PEG-8000, respectively. It is clear that the mass fraction of PEG influences the width of the stability window, which was also observed in other studies[6,26].

The electrochemical performance of $Ti_3C_2T_x$ in MCE was evaluated using cyclic voltammetry at 2 mV s^{-1} in three-electrode devices. The cyclic voltammogram (CV) curves for LiTFSI-H$_2$O (**Figure 4.1 b**) were rectangular in shape, which is a characteristic of the EDL capacitive charge storage mechanism[2]. Meanwhile, the CVs with MCEs all showed a pair of redox peaks at a less negative potential, which were absent for the 2 m LiTFSI electrolyte (**Figure 4.1 b**). The emerged redox peaks in MCEs contribute ~25% additional capacitance to the MXene electrodes. Similar redox peaks were also observed on $Ti_3C_2T_x$ with 19.8 m LiCl WIS electrolytes, corresponding to the intercalation of desolvation-free Li$^+$ ions in MXene sheets [20]. The difference is that the peak separations in all three MCEs were ~0.2 V, which is much smaller than that of 0.76 V in the WIS electrolyte. The cathodic and anodic redox peaks of the 7:3 PEG-400 were located at -0.25 and -0.05 V, respectively. Increasing the PEG:H$_2$O ratio to 8:2 leads to a slight shift of redox peaks to -0.3 and -0.1 V. By using PEG-8000 in the MCEs, a shift of the voltage window and the position of the redox peaks (-0.5 and -0.3 V) was observed.

To assess the high-rate performance of $Ti_3C_2T_x$ in MCEs, we conducted the CV test at different scan rates and Galvanostatic charge and discharge (GCDs) at different current densities (**Figure 4.1 c-f**, **Figure S4.6**). The GCD curves of $Ti_3C_2T_x$ in LiTFSI-H$_2$O (**Figure 4.1 e**) display a sloping feature with no observable voltage plateaus, indicating EDL capacitive mechanism (**Figure 4.1 c**). In the 7:3 PEG-400 electrolyte, the redox peak separation increased at higher scan rates. Additionally, the redox peak intensity decreased, such that the peaks are no longer visible at 100 mV s^{-1} (**Figure 4.1 d**). Correspondingly,

bumps can be observed in the GCD curve in 7:3 PEG-400 (**Figure 4.1 f**) at the potential of the redox reactions, which then flatten out at higher current densities. Similar trends were observed for the 8:2 PEG-400 and 7:3 PEG-8000 electrolytes (**Figure S4.6**).

Figure 4.2 a displays the capacitance retention of $Ti_3C_2T_x$ in MCE at different scan rates. In LiTFSI-H_2O electrolyte, $Ti_3C_2T_x$ exhibited a capacitance of 80.2 F g^{-1} at 2 mV s^{-1} and a capacitance retention of 72% at 100 mV s^{-1}. An increased capacitance of 100.8 F g^{-1} and 98.2 F g^{-1} was obtained in 7:3 PEG-400, 8:2 PEG-400 electrolytes at 2 mV s^{-1}, respectively. However, they showed a lower capacitance retention of 52% and 29% at 100 mV s^{-1}, respectively, caused by the reduced ionic conductivity of the electrolyte. Despite the similar ionic conductivity, 7:3 PEG-8000 exhibited a worse rate performance than 7:3 PEG-400 due to its high electrolyte viscosity, retaining only 34% of the initial capacitance (96.0 F g^{-1}) at 100 mV s^{-1}.
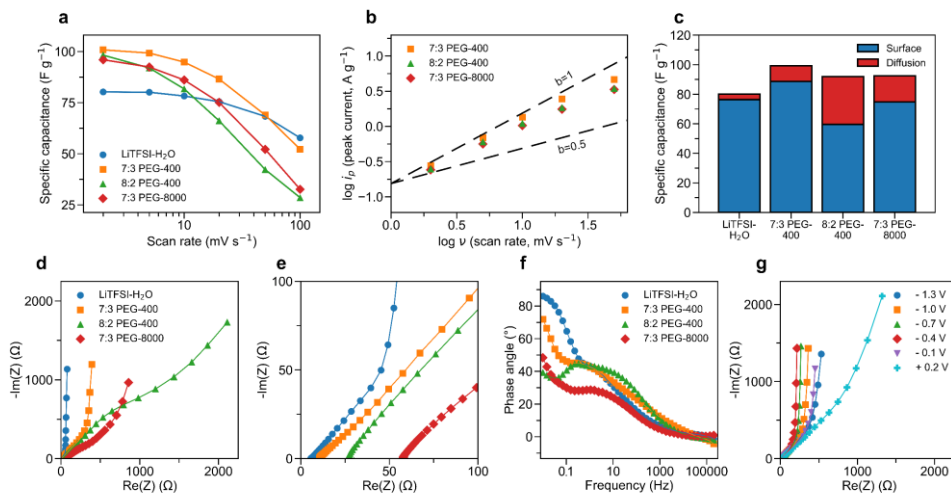

4

Figure 4.2 Electrochemical characterization of $Ti_3C_2T_x$ electrodes in 2 m LiTFSI, 7:3 PEG-400, 8:2 PEG-400 and 7:3 PEG-8000 electrolytes. (a) Capacitance retention of $Ti_3C_2T_x$ from 2 mV s^{-1} to 100 mV s^{-1}. (b) Determination of the b value by taking the slope of the logarithm of the anodic peak current (i_p) versus the logarithm of the scan rate (υ) from 2 mV s^{-1} to 50 mV s^{-1}. Only electrolytes containing PEG are shown. (c) Bar chart displaying the capacitances contributed by either surface-controlled or diffusion-controlled process at 5 mV s^{-1}. (d) and (e) Nyquist impedance and (f) Bode plot of $Ti_3C_2T_x$ at the open circuit potential. (g) 7:3 PEG-8000 at different applied potentials during the discharge process.

To evaluate the reaction kinetics of the electrochemical process, the CVs recorded at different scan rates were used to obtain the *b* value in each MCE (**Figure 4.2 b**). Typically, a *b* value equal to 0.5 stands for semi-infinite diffusive behavior, whereas a b value of 1 represents

surface-controlled behavior[27,28]. The obtained b values were 0.88, 0.82, and 0.82 for 7:3 PEG-400, 8:2 PEG-400, and 7:3 PEG-8000, respectively, indicating that the electrochemical processes all involve combined diffusion-controlled and surface-controlled kinetics. A deconvolution analysis[29] was then performed to determine the contribution of surface-controlled and diffusion-controlled capacitance at 5 mV s^{-1} (**Figure 4.2 c**). Among all electrolytes, 8:2 PEG-400 showed the most sluggish kinetics, with 64.7% of its capacitance being surface-controlled. This value is followed by 81.0% of 7:3 PEG-8000, 89.4% of 7:3 PEG-400, and 95.4% of LiTFSI-H$_2$O. The slower kinetics in MCE can also explain the worse rate performance compared to LiTFSI-H$_2$O.

Electrochemical impedance spectroscopy (EIS) was recorded at the open circuit potential to further unravel the kinetics of Ti$_3$C$_2$T$_x$ in MCEs. As shown in the Nyquist plot in **Figure 4.2 e**, the serial resistance increased when PEG was introduced into 2 m LiTFSI, which was attributed to the decreased ionic conductivity and increased viscosity of the MCEs. No obvious semicircles have been observed at high frequencies for all electrolytes, suggesting negligible charge transfer resistances. In LiTFSI-H$_2$O, a near vertical slope was observed in the low-frequency region in the Nyquist plot (**Figure 4.2 d**), and a phase angle response of -86° was recorded at a low frequency of 10 mHz in the bode plot (**Figure 4.2 f**). Both observations suggest the capacitive charge storage mechanism. Differently, in the case of 7:3 PEG-400 and 7:3 PEG-8000, the phase angles of Ti$_3$C$_2$T$_x$ electrode reached -72° and -49° at low frequency, respectively. The lower phase angles imply more sluggish diffusion kinetics in the MCEs than in LiTFSI-H$_2$O[30]. Notably, a new arc emerged at the low-frequency region in the Nyquist plot in 8:2 PEG-400, which may indicate another charge transport process at low frequency[31]. The Nyquist plots of Ti$_3$C$_2$T$_x$ in 7:3 PEG-400 electrolyte were recorded at different applied potentials during discharging process (**Figure 4.2 g**). Capacitive behavior dominated at almost all applied potentials, except for +0.2 V. The more sluggish kinetics indicate a different electrochemical process at the most positive potential. The cycling stability of Ti$_3$C$_2$T$_x$ electrode in 7:3 PEG-400 electrolyte was evaluated using GCD at a current density of 1 A g^{-1}. A capacitance retention of ~80% was obtained after 10 000 cycles, indicating great reversibility (**Figure S4.7**).

4.2.2 The role of PEG on Li$^+$ ion intercalation of Ti$_3$C$_2$T$_x$

In-situ XRD was used to investigate the interlayer spacing changes of Ti$_3$C$_2$T$_x$ during the first three CV cycles. The interlayer space changes of MXenes during the charge and discharge process are determined by both the steric effect and the electrostatic interaction. In general, the insertion of cations that have large solvated ionic radius may lead to an expansion of d-spacing, whereas the intercalation of small cations may lead to a d-spacing shrinkage.

Therefore, the evolution of the interlayer spacing during cycling provides important information about the intercalated species. As mentioned above, significant increases in *d*-spacing were observed when $Ti_3C_2T_x$ was immersed in all electrolytes, due to the spontaneous intercalation of solvated Li^+ or PEG-400 (**Figure 4.1 a**). During the first CV cycle, the continuous increase of both the d-spacing and the intensity of (002) peak was observed during charging, which may be attributed to the gradual wetting of $Ti_3C_2T_x$ in viscous MCEs. The *d*-spacing evolution of the second cycle was the same as the third cycle in each electrolyte, indicating that the charge/discharge process was stabilized and reversible from the second cycle onwards. As shown in **Figure 4.3 a** and **Figure S4.8 a**, when a negative potential was applied, the d-spacing of $Ti_3C_2T_x$ in LiTFSI-H$_2$O electrolyte decreased continuously from 16.9 Å to 16.4 Å during the Li^+ intercalation process. The slight shrinkage of the interlayer space should be correlated to the electrostatic attraction between the intercalated Li^+ and negatively charged MXene layers, which has been observed in other MXenes-dilute aqueous electrolyte systems[23]. During the discharge process, the de-intercalation of Li^+ happened, leading to an expansion of d-spacing back to 16.9 Å (**Figure 4.3 a**).

By introducing PEG-400 or PEG-8000 as the crowding agents, a different solvation structure is formed due to the hydrogen bonds between H$_2$O and PEG molecules, resulting in a significantly decreased amount of free water. As a result, a more complex d-spacing evolution of the MXene was observed in 7:3 PEG-400 electrolyte (**Figure 4.3 b**, **Figure S4.8 b**). During the charging process, an additional (002) diffraction peak with a large d-spacing of 20.1 Å suddenly appeared at -0.2 V vs. Ag. Simultaneously, a reduction of the intensity of pristine (002) peak (16.9 Å) was observed. These synchronous changes indicated that part of the MXene flakes underwent an interlayer space expansion of 3.2 Å at -0.2 V vs. Ag. A reduction peak can be observed on the corresponding CV curve, indicating an enhanced Li^+ intercalation occurs during this process with large interlayer space change. A similar abrupt increase of interlayer spacing by 1.9 Å was observed using *in-situ* XRD when fully solvated Li^+ ions (Li (H$_2$O)$_3^+$) intercalated MXene in a WIS electrolyte[20]. Compared to the WIS electrolyte, the larger d-spacing change of 3.2 Å in 7:3 PEG-400 electrolyte may be attributed to the co-insertion of PEG-400 molecules. As the potential decreased further to -1.3 V, the d-spacing continuously decreased to 15.4 Å, possibly due to the stronger interactions between the more negatively charged MXene surface and a larger number of the intercalated Li^+. Reversibly, the d-spacing increased from 15.4 Å at -1.3 V to 17.0 Å at +0.2 V during discharge due to the Li^+ de-intercalation. Again, an abrupt d-spacing increase can be observed during the cathodic scan, at the potential with oxidation peak on the CV curve (0 V). During the overall charge/discharge process, a reversible d-spacing change of 4.7 Å was observed, which, to our best knowledge, is the largest value ever reported for MXene electrodes. Such a large change in d-spacing may hold great potential for MXene-based electrochemical

4

actuators where the actuating behavior is driven by the deformation of electrode. By further increasing the ratio of PEG-400, the evolution process of the d-spacing in 8:2 PEG-400 was similar to that in 7:3 PEG-400 (**Figure 4.3 c**), except that less MXene flakes exhibited abrupt interlayer spacing change due to the increased viscosity of the electrolyte. The co-intercalation of PEG was also confirmed by XPS measurements. **Figure S4.9** illustrates the high-resolution C1s and O1s XPS pattern of charged $Ti_3C_2T_x$ (at −0.5 V). There was a notable rise in C-O content in the 7:3 PEG-400 compared to the LiTFSI-H_2O electrolyte, which is likely attributed to the intercalation of PEG.

To understand the impact of PEG insertion process on the d-spacing evolution, PEG-400 was replaced by PEG-8000 with a much larger size of 3 Å x 42 Å x 102 Å[25]. The insertion of the PEG-8000 was prevented as no sudden d-spacing change was observed in 7:3 PEG-8000 (**Figure 4.3 d**, **Figure S4.8 c**). Instead, a small and continuous d-spacing expansion from 16.2 Å to 16.4 Å can be observed from -0.1 V to -0.8 V during charging. This small expansion is different from both the PEG-400 MCE and the dilute system, where a significant increase and a slight continuous decrease in the d-spacing occurs, respectively This phenomenon can be explained by the intercalation of solvated Li^+. Further charging led to a continuous d-spacing shrinkage from 16.4 Å to 15.9 Å, which may be attributed to the strong electrostatic interaction between MXene and intercalated Li^+. Despite the lack of abrupt d-spacing changes in PEG-8000 electrolyte, redox peaks can still be seen in the CV (**Figure 4.1 b**). This suggests that the additional redox process is governed by the intercalation of solvated Li^+, rather than the co-insertion of the PEG molecules.

Based on the previous discussion, the charge storage process of $Ti_3C_2T_x$ in the MCEs differs from that in the 2 m LiTFSI aqueous electrolyte (**Figure 4.4 a-b**). In the 2 m LiTFSI aqueous electrolyte, the intercalation of Li^+ into MXene layers during the charging process leads to a continuous decrease of d-spacing (**Figure 4.4 a**). The continuous d-spacing shrinkage is caused by the increasing electrostatic attraction between the MXene surface and the intercalated ions. Meanwhile, the Li^+ intercalation process in the MCEs (both PEG-400 and PEG-8000) involves two steps, such that the interlayer spacing first increases and then decreases. The interlayer spacing increase in PEG-400 and PEG-8000 containing electrolytes should be correlated to the Li^+-water co-intercalation. The interlayer spacing shrinkage process at the more negative potential is similar to that in the 2 m LiTFSI, indicating that less or no co-inserted water accompanies the Li^+ intercalation. Compared to the dilute aqueous electrolyte, the additional redox peaks on CV in MCEs should be related to Li^+-water co-intercalation caused by the changed electrolyte environment in the bulk electrolyte with the addition of PEG. This extra solvated Li^+ intercalation process leads to an increase of capacitance by 25%, compared to the dilute electrolyte. Notably, a unique abrupt interlayer

spacing increase (up to 3.2 Å) was observed in PEG-400 containing MCE at the potential with redox peak on the CV curve. The abrupt interlayer spacing change can be explained by the co-insertion of PEG-400. As a result, the discharge process in 7:3 PEG-400 leads to a significant overall interlayer spacing change of 4.7 Å. DFT simulations and other in situ techniques, such as electrochemical quartz crystal microbalance, should be used to gain more insights on the co-intercalation process.
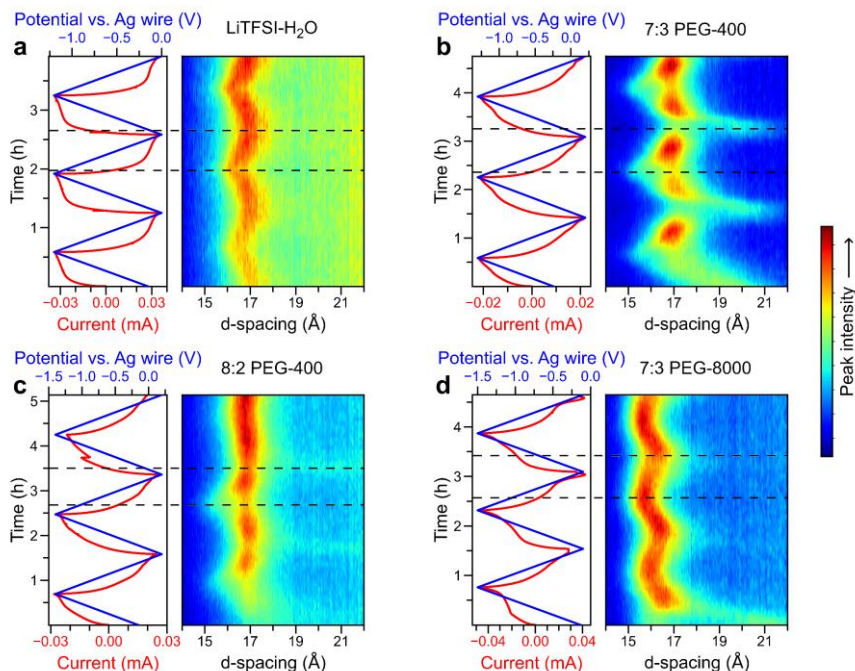

Figure 4.3 *In-situ* **XRD contour plots and current profile obtained while cycling Ti$_3$C$_2$T$_x$ at a constant scan rate of 0.5 mV s^{-1} in (a) LiTFSI-H$_2$O. (b) 7:3 PEG-400. (c) 8:2 PEG-400. (d) 7:3 PEG-8000. The x-axis of the contour plot is the d-spacing of Ti$_3$C$_2$T$_x$. The dashed lines indicate the position of the largest and smallest d-spacing.**
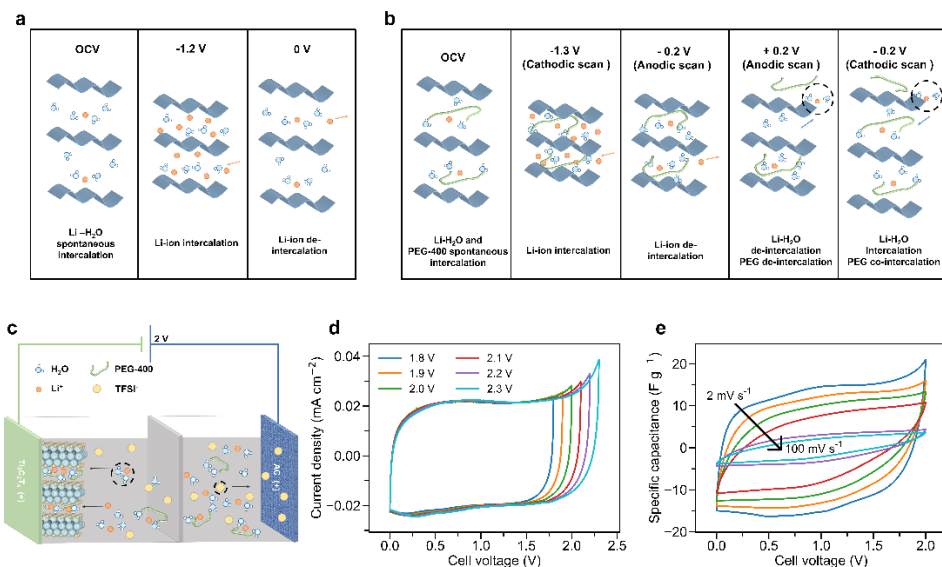
Figure 4.4 (a) Schematic illustration of the charge storage mechanism of $Ti_3C_2T_x$ in LiTFSI-H_2O. (b) Schematic illustration of the charge storage mechanism of $Ti_3C_2T_x$ in LiTFSI-PEG-400:H_2O. (c) Schematic illustration of a full cell with a $Ti_3C_2T_x$ negative electrode, an active carbon positive electrode, and a PEG-400:H_2O electrolyte. (d) Voltage window determination of an asymmetric $Ti_3C_2T_x$//AC full cell with a 7:3 PEG-400 electrolyte by cyclic voltammetry. (e) Cyclic voltammogram curves of an asymmetric $Ti_3C_2T_x$//AC full cell in 7:3 PEG-400. The scan rates from the outer to the inner cycle are 2, 5, 10, 20, 50, and 100 mV s^{-1}.

We assembled a full cell using $Ti_3C_2T_x$ as the negative electrode and 7:3 PEG-400 as the electrolyte to demonstrate the practical application of the electrolyte. An activated carbon-based positive electrode was paired with the MXene electrode with a mass ratio of 1:1, as illustrated in **Figure 4.4 c**. The optimal voltage window was determined to be 2.0 V using CV at 2 mV s^{-1}, reaching >95% Coulombic efficiency (**Figure 4.4 d**). **Figure 4.4 e** shows the rate performance of the full cell. A specific capacitance of 25.6 F g^{-1} was obtained at 2 mV s^{-1} based on the mass of both electrodes, and 55% of the capacitance was retained at 20 mV s^{-1}. The wide voltage window allowed the $Ti_3C_2T_x$//AC asymmetric capacitor to deliver a high energy density of 14.2 Wh kg^{-1} in 7:3 PEG-400 electrolyte with a power density of 52 W kg^{-1}, which is comparable to that of the WIS electrolyte (9.2 Wh kg^{-1} at 41 W kg^{-1}) [20].

4.3 Conclusion

In this study, the electrochemical behavior of $Ti_3C_2T_x$ was investigated in combination with safe and low-cost PEG-based molecular crowding electrolytes (MCEs). The introduction of PEG expanded the potential window of $Ti_3C_2T_x$ in 2 m LiTFSI from 1.2 V to ~1.5 V. More

interestingly, $Ti_3C_2T_x$ showed an additional pair of redox peaks (-0.25 V/-0.05 V) on the CV curve in all MCEs, which contributed 25% additional capacitance to the MXene electrode. Based on the *in-situ* XRD analysis, abrupt interlayer spacing expansion and shrinkage were observed at the potentials with redox peaks in the PEG-400 containing MCE, whereas no abrupt changes observed in the PEG-8000 containing MCE. This indicates that the PEG-400 can co-insert the MXene interlayer reversibly and the insertion of PEG-8000 is prevented. Also, the additional redox peaks on CV should be attributed to the changed solvation structure with the addition of PEG in the bulk electrolyte, rather than the co-insertion of PEG. The co-intercalation of PEG-400 with Li^+ at the peak potential and the following intercalation of Li^+ at the more negative potential in the discharge process lead to a significant MXene interlayer spacing change of 4.7 Å. The enhanced pseudocapacitive performance and the large reversible interlayer spacing change demonstrate the uniqueness of using MCEs with MXene electrode.

4.4 Supplementary information

Methods:

Material Synthesis: Synthesis of Ti_3AlC_2 MAX phase: TiC (Alfa Aesar, 99.5%, 2 μm powder), Ti (Alfa Aesar, 99.5%, 325 mesh) and Al (Alfa Aesar, 99.5%, 325 mesh) powders were mixed in a 2:1.25:2.2 molar ratio and sintered at 1380 °C in a tube furnace (TMAXCN, KTL1700) for 2 hours under an 80 sccm argon flow. The resulting sintered MAX phase was then milled into a powder, washed with 9 M HCl (Alfa Aesar, 36%), and subsequently neutralized with deionized water, after which it was dried overnight at 80 °C. Synthesis of $Ti_3C_2T_x$ MXene: 0.5 g of Ti_3AlC_2 MAX phase powder and 0.8 g of LiF powder (Alfa Aesar, 98.5%) were mixed in 10 mL of 9 M HCl. The etching was conducted for 24 h at 35 °C with a 500 rpm stirring speed. After etching, the sediment was washed with deionized water until the pH of the supernatant reached 6. Then, the supernatant was collected and sonicated for 30 min. $Ti_3C_2T_x$ dispersion was obtained by subsequent centrifuging for 30 min at 3500 rpm, after which it was filtered into a film over a membrane (Jinteng, 0.2 μm pore size).

Electrochemical setup: Swagelok cells with glassy carbon current collectors were used to assemble the three-electrode cell. $Ti_3C_2T_x$ film with a mass loading of 1.0 mg cm^{-2} was used as the working electrode. A mixture of activated carbon (Brunswich, YP-50F 6μ) and PTFE (Sigma-Aldrich, 60 wt% in H_2O) in a 95:5 mass ratio was used as an overcapacitive counter electrode. They were separated by a glass fiber membrane (Whatman, GF/A). Polished Ag wire (Alfa Aesar, 99.9%) was used as a reference electrode. A 3-electrode electrochemical cell was used for *in-situ* XRD, in which a $Ti_3C_2T_x$ working electrode was pressed against a

4

Kapton film by a glassy carbon current collector. Pt was used as the counter electrode and an Ag wire was used as reference electrode.

Electrochemical characterization: All electrochemical measurements were performed on a Biologic VSP-300 potentiostat. The scan rates used for cyclic voltammetry ranged from 2 mV s^{-1} to 100 mV s^{-1}. The current densities used for galvanostatic cycling ranged from 100 mA g^{-1} to 2000 mA g^{-1}. Electrochemical impedance spectroscopy was done with frequencies ranging from 10 mHz to 200 kHz with a 10 mV amplitude.

Table 4.1 Electrolyte properties obtained at 20 °C.

Electrolyte	Abbr. names of electrolyte	Potential window (V)	Viscosity (mPa s)	Ionic conductivity (mS cm^{-1})
2 m LiTFSI-H$_2$O	H$_2$O	3.3	11.5	20.8
2 m LiTFSI-7:3 PEG-400:H$_2$O	7:3 PEG-400:H$_2$O	3.3	112	4.15
2 m LiTFSI-8:2 PEG-400:H$_2$O	8:2 PEG-400:H$_2$O	3.4	229	1.06
2 m LiTFSI-7:3 PEG-8000:H$_2$O	7:3 PEG-8000:H$_2$O	3.6	2410	4.25

4

Supplementary Figures
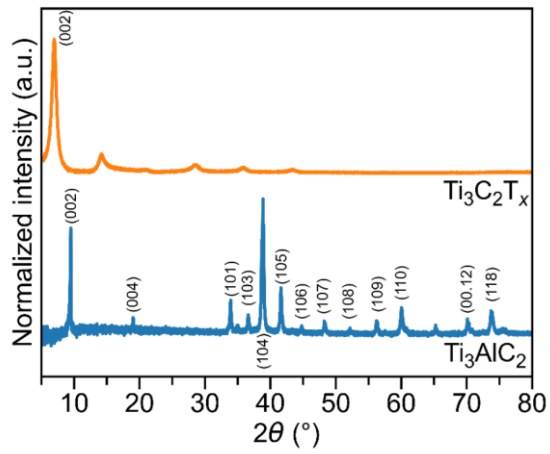
Figure S 4.1 XRD pattern of Ti$_3$AlC$_2$ and Ti$_3$C$_2$T$_x$.
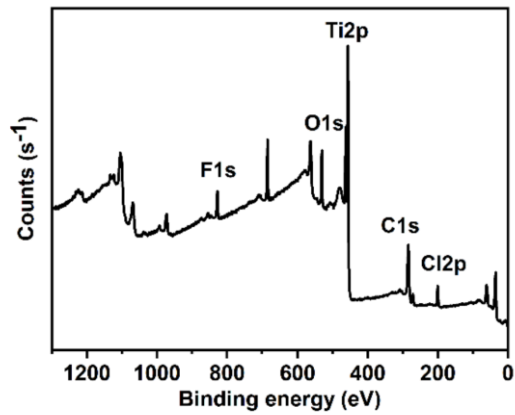
Figure S 4.2 XPS survey of Ti$_3$C$_2$T$_x$.

4
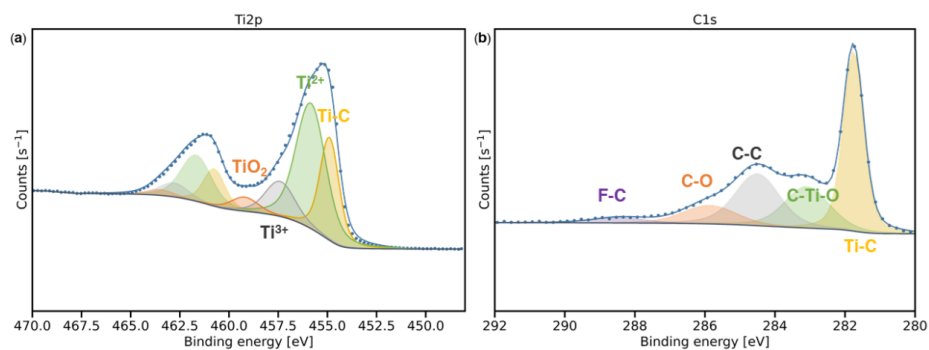
Figure S 4.3 (a) high-resolution Ti 2p spectrum, and (b) high-resolution C 1s spectrum of Ti$_3$C$_2$T$_x$.
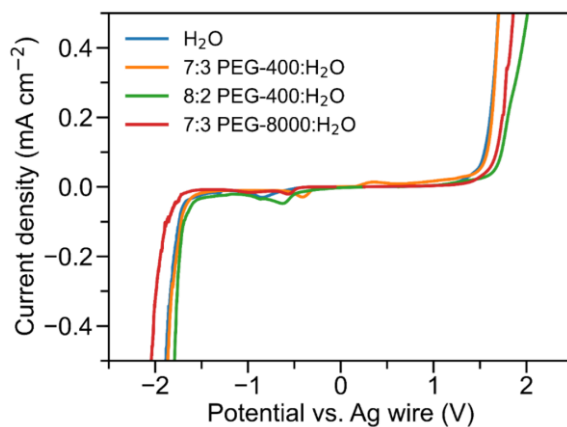
Figure S 4.4 Electrochemical stability windows determination of the molecular crowding electrolytes using linear sweep voltammetry at 2 mV s^{-1}.
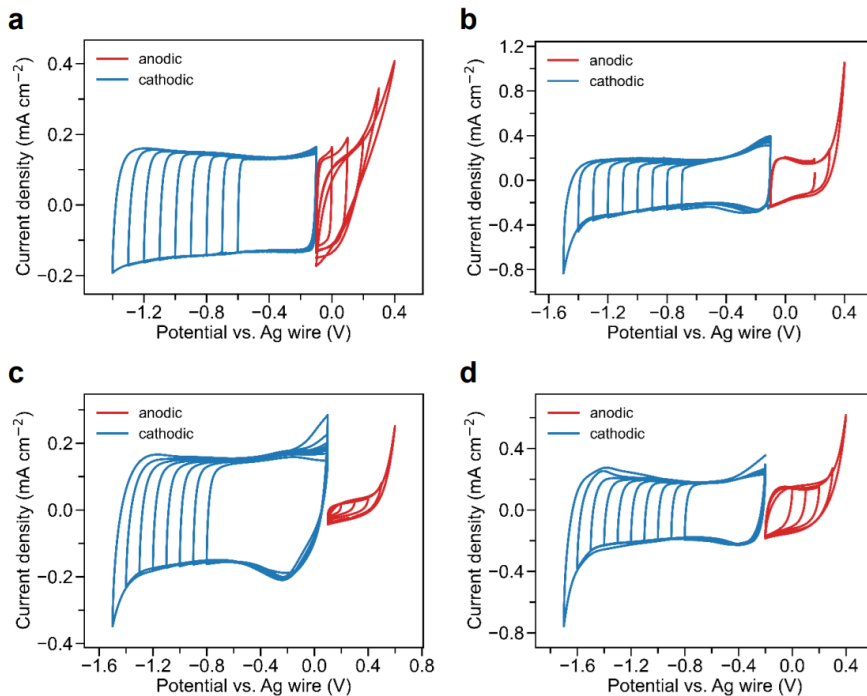
Figure S 4.5 Potential window determination of $Ti_3C_2T_x$ electrodes in molecular crowding electrolytes using CV at 2 mV s^{-1}. (a) LiTFSI-H$_2$O (b) 7:3 PEG-400 (c) 8:2 PEG-400 (d) 7:3 PEG8000.

4
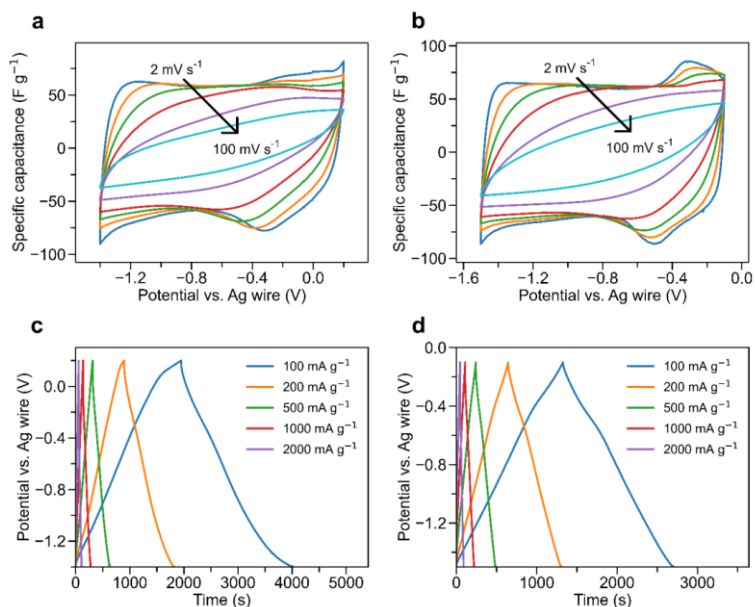
Figure S 4.6 Electrochemical performance of Ti$_3$C$_2$T$_x$ electrodes in 8:2 PEG-400 and 7:3 PEG-8000. (a) Cyclic voltammogram curves of Ti$_3$C$_2$T$_x$ in 8:2 PEG-400. The scan rates from the outer to the inner cycle are 2, 5, 10, 20, 50, and 100 mV s^{-1}. (b) Cyclic voltammogram curves of Ti$_3$C$_2$T$_x$ in 7:3 PEG-8000. The scan rates from the outer to the inner cycle are 2, 5, 10, 20, 50, and 100 mV s^{-1}. (c) Galvanostatic charge-discharge curves of Ti$_3$C$_2$T$_x$ in 8:2 PEG-400. (d) Galvanostatic charge/discharge curves of Ti$_3$C$_2$T$_x$ in 7:3 PEG-8000.

.
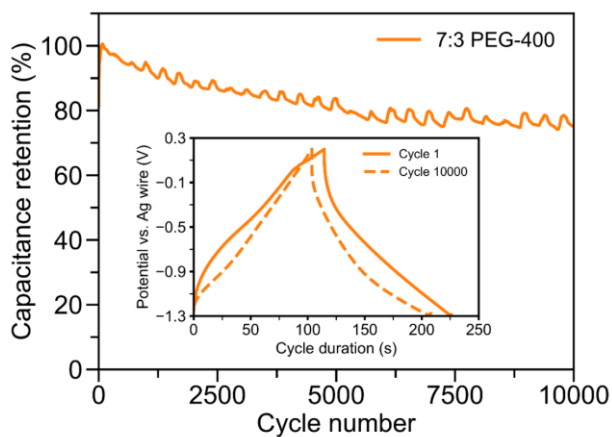
Figure S 4.7 Cycling performance of Ti$_3$C$_2$T$_x$ electrodes in 7:3 PEG-400.
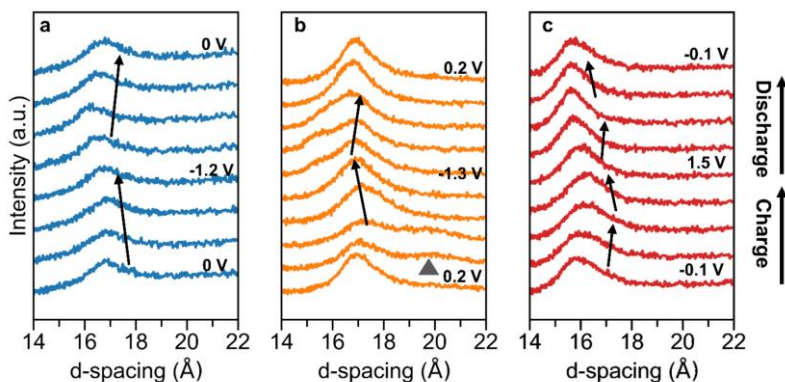
Figure S 4.8 In situ XRD patterns of Ti$_3$C$_2$T$_x$ electrodes in (a) LiTFSI-H$_2$O, (b) 7:3 PEG-400, (c) 7:3 PEG-8000. The 3rd cycle is shown for each case, starting with the charge scan.
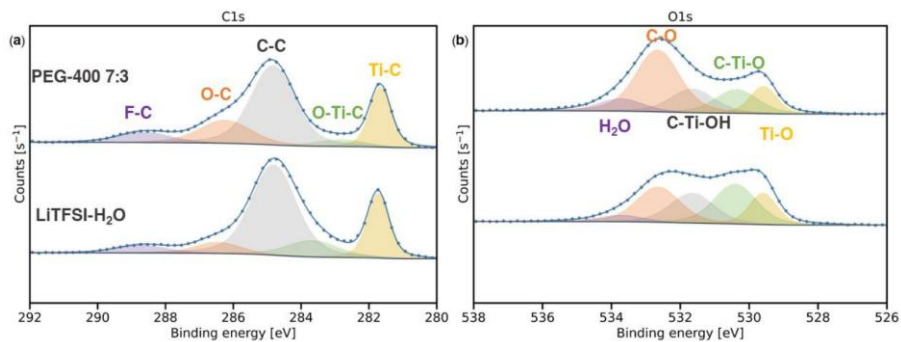

Figure S 4.9 (a) high-resolution C 1s spectrum, and (b) high-resolution O 1s spectrum of Ti$_3$C$_2$T$_x$ after charged at -0.5 V in LiTFSI-H$_2$O and 7:3 PEG-400.

4.5 Reference

1   P. Simon and Y. Gogotsi, *Nat. Mater.*, 2020, **19**, 1151–1163.

2   Y. Wang, Y. Song and Y. Xia, *Chem. Soc. Rev.*, 2016, **45**, 5925–5950.

3   L. Liu, P.-L. Taberna, B. Dunn and P. Simon, *ACS Energy Lett.*, 2021, **6**, 4311–4316.

4   M. Zhou, Z. Bo and Kostya (Ken) Ostrikov, *Phys. Chem. Chem. Phys.*, 2022, **24**, 20674–20688.

5   L. Suo, O. Borodin, T. Gao, M. Olguin, J. Ho, X. Fan, C. Luo, C. Wang and K. Xu, *Science*, 2015, **350**, 938–943.

6   J. Xie, Z. Liang and Y.-C. Lu, *Nat. Mater.*, 2020, **19**, 1006–1011.

7   X. Li, Z. Huang, C. E. Shuck, G. Liang, Y. Gogotsi and C. Zhi, *Nat. Rev. Chem.*, 2022, **6**, 389–404.

8   B. Anasori, M. R. Lukatskaya and Y. Gogotsi, *Nat. Rev. Mater.,* 2017, **2**, 16098.

9   M. R. Lukatskaya, S. Kota, Z. Lin, M.-Q. Zhao, N. Shpigel, M. D. Levi, J. Halim, P.-L. Taberna, M. W. Barsoum, P. Simon and Y. Gogotsi, *Nat. Energy*, 2017, **2**, 1–6.

10   M. Lu, W. Han, H. Li, W. Zhang and B. Zhang, *J. Energy Chem.*, 2020, **48**, 344–363.

11   N. Jäckel, B. Krüner, K. L. Van Aken, M. Alhabeb, B. Anasori, F. Kaasik, Y. Gogotsi and V. Presser, *ACS Appl. Mater. Interfaces*, 2016, **8**, 32089–32093.

12   Z. Lin, P. Rozier, B. Duployer, P.-L. Taberna, B. Anasori, Y. Gogotsi and P. Simon, *Electrochem. Commun.*, 2016, **72**, 50–53.

13   X. Mu, D. Wang, F. Du, G. Chen, C. Wang, Y. Wei, Y. Gogotsi, Y. Gao and Y. Dall'Agnese, *Adv. Funct. Mater.*, 2019, **29**, 1902953.

14   H. Shao, K. Xu, Y. C. Wu, A. Iadecola, L. Liu, H. Ma, L. Qu, E. Raymundo-Piñero, J. Zhu, Z. Lin, P. L. Taberna and P. Simon, *ACS Energy Lett.*, 2020, **5**, 2873–2880.

15   D. Johnson, K. Hansen, R. Yoo and A. Djire, *ChemElectroChem*, 2022, **9**, e202200555.

16   M. Brunet Cabré, D. Spurling, P. Martinuz, M. Longhi, C. Schröder, H. Nolan, V. Nicolosi, P. E. Colavita and K. McKelvey, *Nat. Commun.*, 2023, **14**, 374.

17   T. B. Sobyra, T. S. Mathis, Y. Gogotsi and P. Fenter, *ACS Appl. Mater. Interfaces*, 2021, **13**, 43597–43605.

18   Y. Ando, M. Okubo, A. Yamada and M. Otani, *Adv. Funct. Mater.*, 2020, **30**, 2000820.

19   X. Wang, S. Kajiyama, H. Iinuma, E. Hosono, S. Oro, I. Moriguchi, M. Okubo and A. Yamada, *Nat. Commun.*, 2015, **6**, 6544.

20   X. Wang, T. S. Mathis, Y. Sun, W.-Y. Tsai, N. Shpigel, H. Shao, D. Zhang, K. Hantanasirisakul, F. Malchik, N. Balke, D. Jiang, P. Simon and Y. Gogotsi, *ACS Nano*, 2021, **15**, 15274–15284.

21   A. Johansson, A. Lauenstein and J. Tegenfeldt, *J. Phys. Chem.*, 1995, **99**, 6163–6166.

22   T. S. Mathis, K. Maleski, A. Goad, A. Sarycheva, M. Anayee, A. C. Foucher, K. Hantanasirisakul, C. E. Shuck, E. A. Stach and Y. Gogotsi, *ACS Nano*, 2021, **15**, 6420–6429.

23   M. R. Lukatskaya, O. Mashtalir, C. E. Ren, Y. Dall'Agnese, P. Rozier, P. L. Taberna, M. Naguib, P. Simon, M. W. Barsoum and Y. Gogotsi, *Science*, 2013, **341**, 1502–1505.

24   M.Mao, K.-X. Yu, C.-F. Cao, L.-X. Gong, G.-D. Zhang, L. Zhao, P. Song, J.-F. Gaoand L.-C. Tang, *Chem. Eng. J.*, 2022, **427**, 131615.

25   K. A. Rubinson and S. Krueger, *Polymer*, 2009, **50**, 4852–4858.

26   D. Dong, J. Xie, Z. Liang and Y.-C. Lu, *ACS Energy Lett.*, 2022, **7**, 123–130.

27   T. S. Mathis, N. Kurra, X. Wang, D. Pinto, P. Simon and Y. Gogotsi, *Adv. Energy Mater.*, 2019, **9**, 1902007.

28   P. Simon, Y. Gogotsi and B. Dunn, *Science*, 2014, **343**, 1210–1211.

29   T.-C. Liu, W. G. Pell, B. E. Conway and S. L. Roberson, *J. Electrochem. Soc.*, 1998, **145**, 1882.

30   N. Kurra, S. Uzun, G. Valurouthu and Y. Gogotsi, *Energy Storage Mater.*, 2021, **39**, 347–353.

31   L. O'Neill, C. Johnston and P. S. Grant, *J. Power Sources*, 2015, **274**, 907–915.

4

4

5 Solvation Structure Engineering with Co-Solvents Enables Tunable Charge Storage Mechanisms in MXenes

Abstract

Modulating ion-solvent interactions offers a powerful approach to tune the desolvation process, which in turn influences both the capacity and kinetics of electrochemical charge storage. This influence is particularly complex in 2D MXenes due to their surface redox activity and flexible interlayer spacing and thus remains underexplored. In this study, we investigate how tuning the Na^+ solvation structure using acetonitrile (ACN) co-solvents affects charge storage mechanism of $Ti_3C_2T_x$ MXene. The addition of ACN enables a new intercalation process at relatively positive potential, which enhances the overall capacitance by ~30%. More interestingly, varying the ACN content leads to a transition in the charge storage mechanism of this additional process from non-Faradaic to redox-active. At lower ACN concentrations, strongly solvated Na^+ ions intercalate rapidly through a primarily non-Faradaic process, resulting in even better rate retention (72% at 1 V s^{-1}) than in the pure aqueous electrolyte. Meanwhile, higher ACN content (>50%) promotes ion desolvation, enabling distinct redox activity (confirmed by in-situ UV-vis) but reduces rate capability. These findings demonstrate a clear correlation between solvation structure and charge storage mechanism in 2D materials, offering a rational strategy to optimize performance via co-solvent design.

5

5.1 Introduction

As solar and wind energy become more widespread, stationary electrochemical storage systems are essential for grid stability[1]. Additionally, the rapid rise of portable electronics and electric vehicles is driving the development of energy storage technologies with both high energy and high power density. These requirements call for materials that combine large charge storage capacity, fast charge-discharge capability, and excellent cycling stability[2]. With a high surface-to-volume ratio and large interlayer spacing, two-dimensional (2D) materials possess a favorable structure that allows easy access of electrolyte ions to their extensive interlayer surface area with low resistance and helps maintain structural integrity during repeated cycling[3]. Among these, transition metal carbides and nitrides MXenes ($M_{n+1}X_nT_x$), particularly $Ti_3C_2T_x$, stand out due to their great mechanical strength, superior electrical conductivity, tunable surface chemistry, and good hydrophilicity[4–6].

MXenes have demonstrated superior charge storage performance in acidic and organic electrolytes, where fast surface redox reactions enable both high capacitance and excellent rate capability. However, safety concerns in these environments have motivated interests in neutral aqueous electrolytes[7], which offer milder, safer conditions but often suppress surface redox activity of MXene, resulting in moderate capacitance[8,9]. In dilute neutral aqueous electrolytes, cations such as Na^+ and Li^+ are strongly solvated, forming a tightly coordinated structure with four to six water molecules surrounding each ion. This strong coordination makes complete desolvation (or dehydration) difficult, leading to the frequent co-intercalation of water molecules with the ions in MXenes[10]. The co-inserted water molecules reduce interaction between the cation and MXene surface terminations, suppressing charge transfer[9]. As a result, charge storage in dilute neutral aqueous electrolytes is often dominated by electric double-layer (EDL) behavior, yielding relatively low capacitance[11].

Electrolyte modification has been explored as a powerful strategy to improve electrochemical performance for different neutral aqueous electrochemical energy storage systems, including aqueous Li-ion batteries, capacitors and zinc-metal batteries. Common approaches include increasing salt concentration, introducing molecular crowding agents such as polyethylene glycol (PEG), or incorporating organic co-solvents[11–13]. These strategies not only suppress water activity and expand the electrochemical stability window but also reshape the solvation structure, which in turn influences the charge storage behavior[14].

Modifying solvation structure has also been shown to alter ion intercalation behavior and affect the charge storage for MXene electrodes[15]. For example, both water-in-salt (WIS) and molecular crowding electrolytes (MCEs) can enable additional intercalation steps into MXenes' interlayer at relatively high potentials, contributing to extra capacity[16,17]. In MCEs,

5

modified Li$^+$ hydration promotes a new intercalation step at - 0.25 V, involving the insertion of strongly solvated Li$^+$ ions, possibly along with PEG molecules, leading to ~25% higher capacitance compared to dilute electrolytes[17]. In 19.8 m LiCl WIS electrolytes, Li$^+$ ions are coordinated with ~2.85 water molecules, which favors direct intercalation at more positive potentials without prior desolvation[16,18]. This desolvation-free intercalation involves minimal charge transfer, causes a sharp 1.9 Å increase in interlayer spacing, and contributes to enhanced capacitance. Compared to WIS and MCEs, whose high viscosities significantly reduce ionic conductivity, introducing organic co-solvents into aqueous electrolytes has emerged as an effective strategy to tune ion solvation while preserving sufficient ionic transport. Acetonitrile (ACN), with its low viscosity (~0.37 cP), and moderate dielectric constant (~37.5), can efficiently disrupt the water-water hydrogen bonding network and modulate cation solvation through ion-dipole interactions[19,20]. This solvation tuning has been shown to suppress parasitic water decomposition reactions and inhibit dendrite formation in zinc-metal batteries, highlighting ACN's potential to enhance interfacial stability and electrochemical performance in aqueous energy storage systems[21–23]. However, the impact of ACN as a co-solvent on ion intercalation in MXenes remains to be systematically understood.

In our study, we reveal how systematically tuning the Na$^+$ solvation structure using ACN-water hybrid electrolytes can regulate ion intercalation and charge storage mechanisms of MXenes. Interestingly, the introduction of ACN activates an additional ion intercalation step (S1 or S1') at more positive potentials (**Figure 5.1**, middle & right panel) beyond the typical ion intercalation (S2) (**Figure 5.1,** left panel). As the ACN content increases, nuclear magnetic resonance (NMR) and Fourier transform infrared (FTIR) spectroscopy confirm a progressive weakening of Na$^+$-H$_2$O interaction with increasing ACN content. This change modulates the nature of high-potential intercalation (S1 or S1'), shifting from a non-faradaic process at low ACN concentration (**Figure 5.1**, middle panel) to a pseudocapacitive mechanism at higher concentrations (**Figure 5.1**, right panel). Specifically, in 75 H$_2$O:25 ACN electrolyte, additional intercalation of solvated Na$^+$-H$_2$O clusters occurs with rapid kinetics, resulting in a ~30% increase in capacitance along with superior rate capability, retaining 72% of the capacitance at 1 V s^{-1} compared to 62% in pure water. Our findings offer fundamental insights into the charge storage process in co-solvent systems and provide guidance for the rational design of electrolytes to enhance the energy storage performance of 2D material-based electrodes.
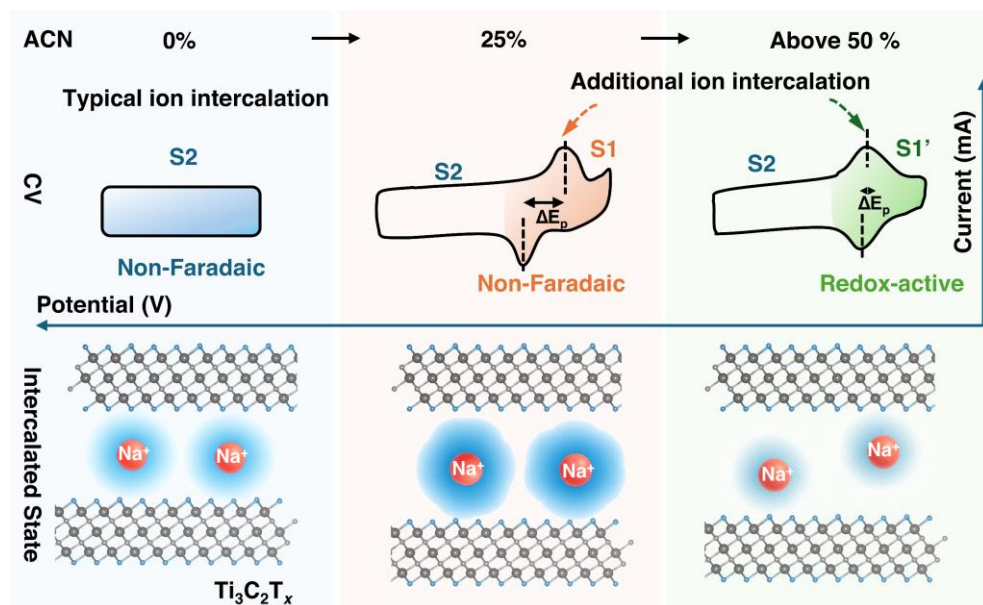
Figure 5.1 Schematic illustration showing cyclic voltammograms (CVs) and corresponding charge storage mechanisms of $Ti_3C_2T_x$ MXene in 2 M $NaClO_4$ aqueous electrolytes with varying ACN content: pure H_2O (left panel), 25% ACN (middle panel), and above 50% (right panel). Red spheres represent Na^+ ions, each surrounded by a blue, diffuse layer denoting the solvation shell. Grey, silver, and blue spheres represent Ti, C, and O atoms in the MXene layers, respectively. Incorporation of ACN introduces a distinct high-potential intercalation step (S1/S1') alongside the typical ion intercalation process (S2). In 75 H_2O:25 ACN, this new step proceeds through intercalation of strongly solvated Na^+-H_2O species without significant charge transfer (non-Faradaic). In 50 H_2O:50 ACN, weaker interaction between Na^+ and H_2O facilitates Na^+ desolvation, leading to redox-active process (S1').

5.2 Results and discussions

5.2.1 Electrochemical behavior of $Ti_3C_2T_x$ in ACN-containing electrolytes

To investigate the influence of ion solvation on the electrochemical performance of $Ti_3C_2T_x$ MXene, acetonitrile (ACN) was introduced as a co-solvent into aqueous electrolytes to prepare 2 M $NaClO_4$ solutions (denoted as 2 M $NaClO_4$ x H_2O: y ACN, where x, y represents the respective volume parts of H_2O and ACN, respectively). Cyclic voltammetry measurements were conducted in a three-electrode configuration using $Ti_3C_2T_x$ as the working electrode, activated carbon as the counter electrode, and an Ag wire as the reference electrode in H_2O:ACN hybrid electrolytes. In 2 M $NaClO_4$ H_2O, $Ti_3C_2T_x$ exhibited a nearly rectangular cyclic voltammogram (CV) from -1.1 V to 0 V vs. Ag (**Figure 5.2 a**), characteristic of EDL behavior. Upon introducing ACN as a cosolvent, the electrochemical response changed markedly (**Figure 5.2 a**). The applicable voltage window of $Ti_3C_2T_x$

improves with increasing ACN content, as evidenced by a lower steady-state leakage current measured at 0.2 V vs. Ag (**Figure S 5.1**). This improvement is attributed to reduced free water reactivity and suppressed oxidative degradation of MXene. Notably, distinct redox peaks emerged in ACN-containing electrolytes, which were absent in pure aqueous electrolytes. In 75 H_2O:25 ACN, a sharp cathodic peak appeared at - 0.09 V, accompanied by an anodic peak at +0.1 V, yielding a peak separation (ΔE_p) of 0.19 V at 5 mV s^{-1} (**Figure 5.2 a**). In 50 H_2O:50 ACN, the CV became more symmetric, with a broader and less intense cathodic peak at - 0.11 V and a reduced ΔE_p of 0.03 V. The capacity contribution of the redox peaks (S1 or S1') in the CV was estimated by subtracting the baseline contribution, approximated as a rectangular area using the current at -0.3 V, from the total integrated area under the CV curve. Based on this method, the peaks contribute to 35% and 30% of the overall capacity in 75 H_2O:25 ACN and 50 H_2O:50 ACN electrolytes, respectively. Importantly, the differences in peak shape and ΔE_p indicate that the charge storage mechanisms at the corresponding peak potentials differ between the 75:25 and 50:50 electrolytes. Further increasing the ACN content to 75% merely shifted the redox peaks negatively to - 0.15 V, with minimal change in CV shape or peak intensity. Galvanostatic charge-discharge (GCD) measurements further confirmed these findings (**Figure S 5.2**). In 2 M $NaClO_4$ H_2O, the GCD curve displayed a nearly triangular shape, consistent with rectangular CV profiles. In 75 H_2O:25 ACN, the GCD curve became asymmetric with sloped plateau. In contrast, more symmetric GCDs with short plateaus were observed in 50 H_2O:50 ACN and 25 H_2O:75 ACN, consistent with the redox features seen in the corresponding CV curves.
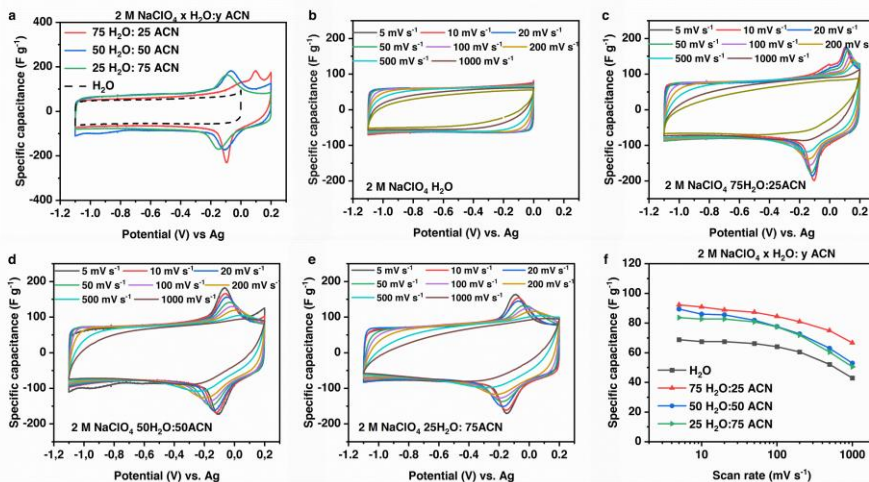
5

Figure 5.2 Electrochemical behavior of $Ti_3C_2T_x$ MXene (a) Cyclic voltammograms (CV) of $Ti_3C_2T_x$ in different 2 M NaClO$_4$ H$_2$O: ACN electrolytes at 5 mV s^{-1}. CV of $Ti_3C_2T_x$ in 2 M NaClO$_4$ in (b) H$_2$O. (c) 75 H$_2$O:25 ACN. and (d) 50 H$_2$O:50 ACN. e) 25 H$_2$O: 75 ACN at different scan rates ranging from 5 mV s^{-1} to 1 V s^{-1}. and (f) Rate performance in 2 M NaClO$_4$ H$_2$O:ACN electrolytes.
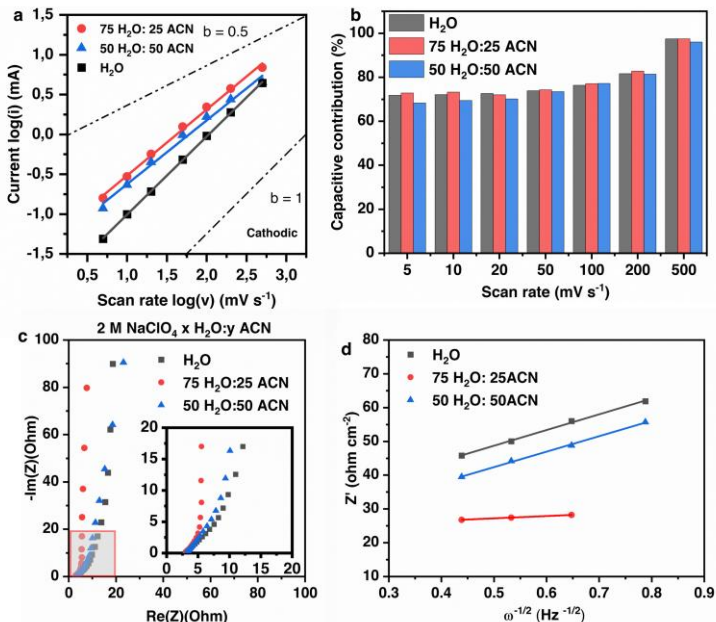

Figure 5.3 Charge storage kinetics of $Ti_3C_2T_x$ in 2 M NaClO$_4$ H$_2$O, 75 H$_2$O:25 ACN and 50 H$_2$O:50 ACN. (a) Linear fitting of logarithm of cathodic peak currents log(i) versus the logarithm of scan rates log(v) for

127

$Ti_3C_2T_x$. **(b) Surface-contributed capacitance contribution at different scan rates. (c) Nyquist plots of f-$Ti_3C_2T_x$ at open circuit voltage. (d) Linear fit of real impedance Z' versus the inverse square root of angular frequency $\omega^{-1/2}$ in the Warburg frequency region.**

To elucidate the nature of the additional process, charge storage kinetics were evaluated by analyzing the slope of log(i)-log(v) plots (b-value) at cathodic peak potential[24]. The extracted b-values were 0.85, and 0.8 for 75 H_2O:25 ACN and 50 H_2O:50 ACN, respectively (**Figure 5.3 a**), suggesting this process was dominated by surface-controlled behavior. In comparison, a b-value of 0.95 was obtained in 2 M $NaClO_4$ H_2O, where the peak feature is absent, indicative of ideal capacitive behavior. To further distinguish between surface and diffusion-controlled contributions, the current response was analyzed using Dunn's method, where the measured current i(V) at a given potential is expressed as the sum of a capacitive contribution k_1v and a diffusion-controlled contribution $k_2v^{1/2}$ [25]. Using this approach, the surface-controlled (capacitive) contribution at 500 mV s^{-1} was determined to be 97.5% for both H_2O and 75 H_2O:25 ACN, and 96.1% for 50 H_2O:50 ACN (**Figure 5.3 b**). Electrochemical impedance spectroscopy (EIS) further confirmed the capacitive-dominated behavior, showing nearly vertical slopes in the low-frequency region of Nyquist plots (**Figure 5.3 c**). Among them, the steepest low-frequency slope was shown in 75 H_2O:25 ACN, while 50 H_2O:50 ACN showed the shallowest slope and the lowest phase angle at 0.01 Hz in Bode plots (**Figure S 5.3**), suggesting slower kinetics at higher ACN content. A magnified view of the high-frequency region showed no clear semicircle, indicating negligible charge-transfer resistance in all electrolytes (**Figure 5.3 c**). To study the ion transport kinetics further, the Warburg coefficient (σ) was extracted from the linear region of real impedance Z' versus $\omega^{-1/2}$ [26]. The lowest σ was obtained for 2 M 75 H_2O:25 ACN (6.8 Ω cm^{-2} s$^{1/2}$) compared to H_2O (45.7 Ω cm^{-2} s$^{1/2}$) and 50 H_2O:50 ACN (46.5 Ω cm^{-2} s$^{1/2}$), indicating faster ion diffusion in $Ti_3C_2T_x$ within 75 H_2O:25 ACN electrolytes (**Figure 5.3 d**). Therefore, while the additional electrochemical process in ACN-containing electrolytes remain surface-controlled, their charge transport kinetics depend on ACN content. Despite the large ΔE_p in 75 H_2O:25 ACN, the process (S1) exhibits high capacitive contribution and fastest kinetic, indicating that the peak separation arises from a distinct intercalation mechanism rather than sluggish ion diffusion. In contrast, 50 H_2O:50 ACN shows more symmetric redox peaks (S1') but exhibits slower kinetic.

5.2.2 Tunable charge storage mechanisms at different ACN ratio: From non-Faradaic to redox-active

To gain a deeper insight into the charge storage mechanisms underlying the additional electrochemical process, operando Ultraviolet-visible spectroscopy (UV-Vis) was conducted during electrochemical cycling. This method tracks variations in light absorbance as a function of applied potential, which reflects changes in the electron density of the electrode

128

material. Recently, this method has been employed to probe redox activity, enabling the differentiation of charge storage mechanisms based on characteristic patterns in absorbance changes[27]. In EDL-type charge storage, the observed absorbance change remains relatively constant with respect to potential, reflecting continuous electronic changes. Pseudocapacitive processes typically exhibit a modest slope change in absorbance with respect to potential, indicating subtle potential-dependent redox activity. In contrast, battery-type mechanisms produce sharp and intense absorbance changes within a narrow potential range, associated with phase transitions[27]. To implement this approach, a custom three-electrode spectroelectrochemical cell was constructed, using a thin $Ti_3C_2T_x$ film spray-coated on a glass substrate as the working electrode, a thicker spray-coated $Ti_3C_2T_x$ film as the counter electrode, and an Ag wire as the reference electrode. **Figure 5.4 a-c** presents the full UV-Vis absorption spectra of $Ti_3C_2T_x$ during the cathodic scan. At OCP, a peak centered at 750 nm was observed, corresponding to the surface plasmon resonance of $Ti_3C_2T_x$. Upon cathodic polarization, a blueshift was observed in all electrolytes, indicative of increased electron density of Ti species. **Figure S 5.4** shows the relative absorbance changes of the plasmonic peak at different potential. In both 2 M $NaClO_4$ H_2O and 75 H_2O:25 ACN, linear relative absorbance changes (normalized by film thickness and potential) were observed across the full voltage window with a slope of 0.82 V^{-1} μm^{-1} and 0.75 V^{-1} μm^{-1}, respectively. In contrast, an increase of the slope from 0.78 V^{-1} μm^{-1} to 1.89 V^{-1} μm^{-1} was seen in 50 H_2O:50 ACN under the redox potential (+ 0.1 V), suggesting that the additional process in 75 H_2O:25 ACN (S1) and 50 H_2O:50 ACN (S1') corresponds to different charge storage mechanism.
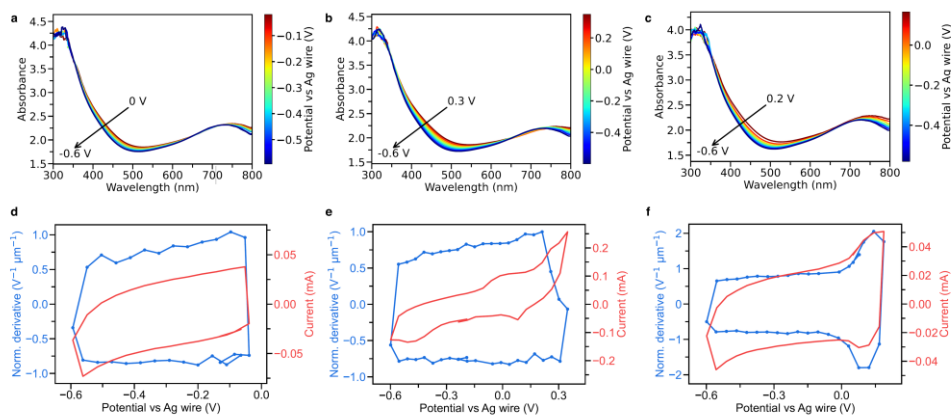

5

Figure 5.4 Operando UV-Vis absorption spectra of $Ti_3C_2T_x$ MXene during cathodic scan at a scan rate of 1 mV s^{-1} in 2 M $NaClO_4$ dissolved in (a) H_2O, (b) 75 H_2O:25 ACN and (c) 50 H_2O:50 ACN. Electrochemical (in red) and UV-Vis absorbance derivative CV (in blue) curves of $Ti_3C_2T_x$ in 2 M $NaClO_4$ dissolved in (d) H_2O, (e) 75 H_2O:25 ACN and (f) 50 H_2O:50 ACN acquired at a scan rate of 1 mV s^{-1}.

To better distinguish between EDL and pseudocapacitive behavior, we analyzed the potential-dependent derivative of absorbance at a characteristic wavelength at 450 nm, where the spectral response was most significant. This approach provides a more direct view of redox activity change across different electrolytes[27]. In 2 M NaClO$_4$ H$_2$O, the absorbance derivative remained nearly constant at 0.8 V^{-1} µm^{-1} throughout the potential window (-1 V - 0 V vs. Ag). This uniform response indicates that charge storage process is primarily non-Faradaic (**Figure 5.4 d**). In 75 H$_2$O:25 ACN, despite the presence of broad redox peaks with a large peak separation in the CV, the absorbance derivative exhibited a similar rectangular shape and magnitude as in H$_2$O, indicating minimal charge transfer (**Figure 5.4 e**). Similar characteristics have been reported in LiCl-based water-in-salt (WIS) electrolytes, where additional desolvation-free Li$^+$ intercalation at positive potential induces significant interlayer expansion with increased intersheet resistance[16]. Despite these structural and resistance changes, this desolvation-free Li$^+$ intercalation involves minimal Faradaic reaction[27]. In contrast, a different absorbance feature was seen in 50 H$_2$O:50 ACN electrolyte. The derivative curve resembles the shape of the CV curve, with a rectangular region (1.0 V^{-1} µm^{-1}) at negative potentials indicative of non-Faradaic behavior, and a pronounced peak (2.5 V^{-1} µm^{-1}) at the redox potentials, characteristic of a pseudocapacitive charge storage process (**Figure 5.4f**).

5.2.3 Solvation structure evolution of NaClO$_4$ electrolytes with different ACN content

To understand the origin of different charge storage mechanisms in 2 M NaClO$_4$ with varying ACN content, we first examined the evolution of the Na$^+$ solvation structure using NMR and FTIR spectroscopy. As shown in **Figure 5.5 a**, the ^{1}H NMR signal of water progressively shifts upfield from 3.82 ppm in 2 M NaClO$_4$ H$_2$O to 3.71 ppm in 75 H$_2$O:25 ACN, 3.45 ppm in 50 H$_2$O:50 ACN, and 3.19 ppm in 25 H$_2$O:75 ACN. This trend suggests disruption of the water-water hydrogen bonding network by enhanced interactions between H$_2$O and ACN[28]. FTIR analysis of the -OH stretching region (**Figure 5.5 b**) corroborates this trend, showing an increasing contribution of the weak hydrogen bonding (~ 3620 cm^{-1}) as the ACN content rises[29]. Meanwhile, the C≡N stretching vibration band of ACN shows a redshift from 2258.8 cm^{-1} in 75 H$_2$O:25 ACN to 2256.7 cm^{-1} in 25 H$_2$O:75 ACN (**Figure 5.5 d**). This redshift could arise either from strengthened dipolar interactions between ACN and water molecules or from the enhanced ion-dipole interactions between ACN and Na$^+$ ions. However, the complex shift trend observed in the ^{1}H NMR spectra of ACN suggests that the latter scenario dominates. The ^{1}H NMR signal of ACN (**Figure 5.5 c**) initially shifts slightly upfield from 1.73 ppm in 75 H$_2$O:25 ACN to 1.71 ppm in 50 H$_2$O:50 ACN, followed by a pronounced downfield shift to 1.90 ppm in 25 H$_2$O:75 ACN. This trend reflects the evolving role of ACN in the Na$^+$ solvation. At lower ACN content, ACN molecules primarily interact with water

130

through dipole-dipole interaction, while Na^+ ions remain predominantly solvated by water molecules (**Figure 5.5 g**, middle), resulting in the initial upfield shift. As the ACN content increases to 50 %, stronger coordination between Na^+ and ACN induces deshielding of ACN protons, causing a noticeable downfield shift in the ^1H NMR signal when comparing 25 H_2O:75 ACN to 50 H_2O:50 ACN.

Further insight on Na^+ ion solvation is provided by ^{23}Na NMR (**Figure 5.5 e**), which shows a continuous upfield shift from -1.48 ppm in H_2O to -1.73 ppm in 75 H_2O:25 ACN, -2.83 ppm in 50 H_2O:50 ACN, and -3.18 ppm in 25 H_2O: 75ACN. This reflects increased shielding of Na^+ nuclei, as more ACN molecules and ClO_4^- coordinate with Na^+ ions and weaken the interaction between Na^+ and water (**Figure 5.5 g**, right). FTIR spectra in the ClO_4^- stretching region (**Figure 5.5 f**) reveals a redshift of the asymmetric ClO_4^- band and new vibrational features which may be associated with contact ion pair formation around 1038 cm^{-1}, supporting increased Na^+-ClO_4^- interactions at high ACN content[30,31].

5
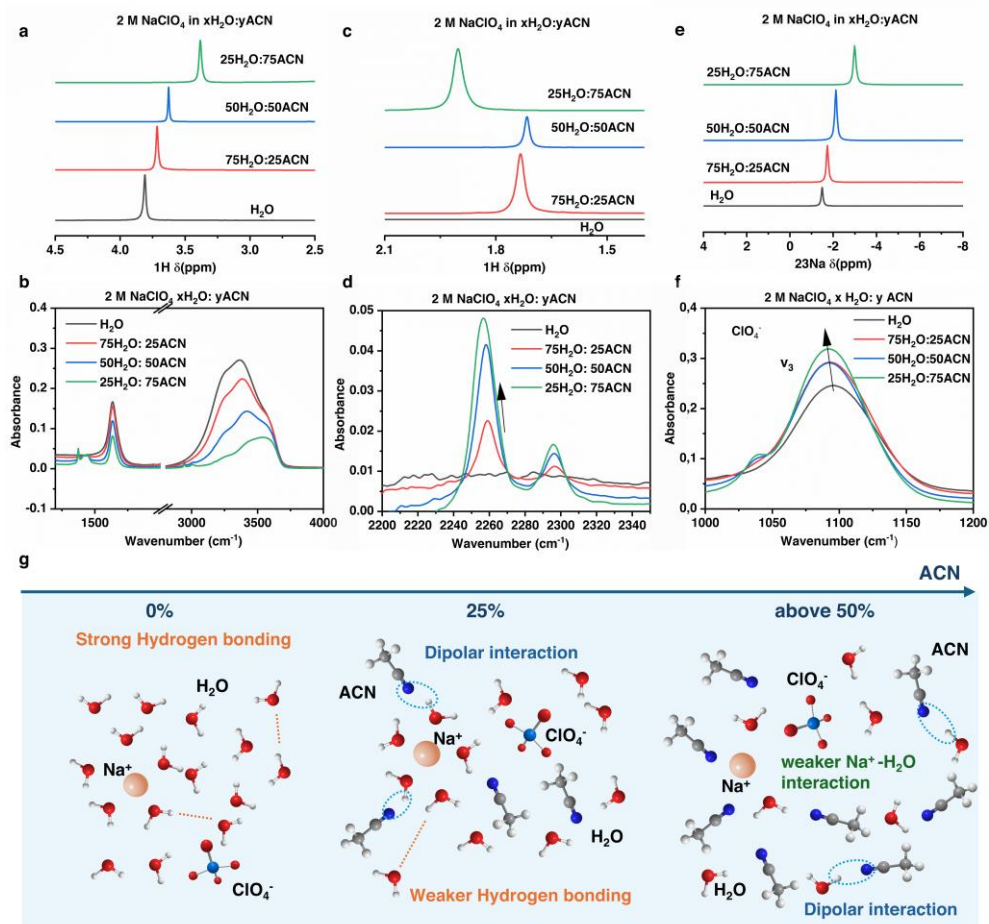
Figure 5.5 . Ion Solvation structure in different electrolytes. (a) ^{1}H NMR and (b) FTIR spectra of water. (c) ^{1}H NMR and (d) FTIR spectra of ACN. (e) ^{23}Na NMR spectra. (f) FTIR spectra of ClO4- in 2 M NaClO4 H2O, 75 H2O:25 ACN and 50 H2O:50 ACN. (g) Schematic illustration showing evolution of Na+ ion solvation structure with increased ACN ratio. Red sphere: O atom; White sphere: H atom; Grey sphere: C atom; Blue sphere: Cl atom; Cyon sphere: N atom; Orange sphere: Na+ cation.

5.2.4 Potential-dependent Na$^+$ intercalation with different solvation level enabled by ACN-containing electrolytes
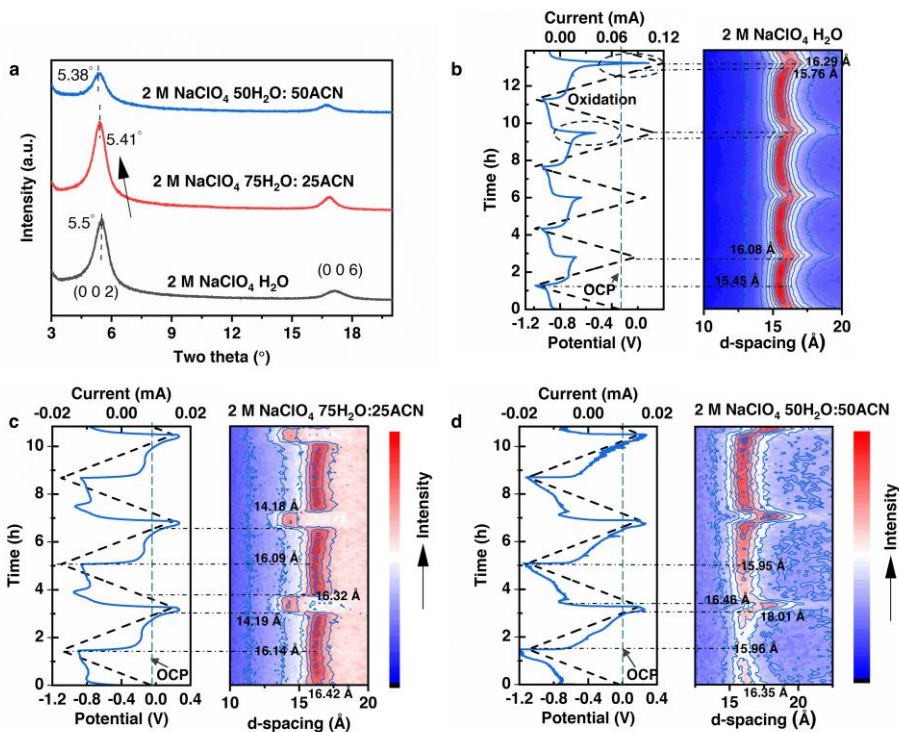
Figure 5.6 Operando X-ray diffraction (XRD) patterns of Ti$_3$C$_2$T$_x$ MXene in 2 M NaClO$_4$ electrolytes with different solvent compositions: H$_2$O, 75 H$_2$O:25 ACN and 50 H$_2$O:50 ACN. (a) XRD patterns after immersing Ti$_3$C$_2$T$_x$ in 2 M NaClO$_4$ H$_2$O, 75 H$_2$O:25 ACN and 50 H$_2$O:50 ACN. Current-voltage curve and corresponding XRD contour plots during the first three electrochemical cycles in 2 M NaClO$_4$ (b) H$_2$O and (c) 75 H$_2$O:25 ACN. (d) 50 H$_2$O:50 ACN.

The dominant charge storage mechanism in MXenes, either through non-Faradaic or surface redox reaction, is influenced by ion desolvation prior to ion intercalation[8,9]. This desolvation process is strongly affected by the surface terminations of the MXenes and the composition of the electrolytes. Surface terminations directly affect the ion-surface interactions and interlayer spacing, which govern how easily ions can shed their solvation shells when entering the interlayer[32,33]. On the other hand, adjusting the electrolyte composition alters the solvation structure in the bulk electrolyte and the interaction with electrodes, which in turn affect the desolvation energy and subsequent ion intercalation behavior[15,34,35]. Since direct ion-surface contact is a prerequisite for efficient charge transfer, the degree and nature of ion intercalation can serve as an indirect probe of the underlying charge storage

133

mechanism[9]. Therefore, to correlate ion solvation with tunable charge storage behavior across different ACN ratios, it is essential to investigate how ion intercalation evolves in different electrolytes. To this end, operando XRD was employed to monitor the structural evolution of $Ti_3C_2T_x$ electrodes during electrochemical cycling under varying solvation conditions.

Figure 5.6 a-d show the d-spacing evolution of (0 0 2) plane of $Ti_3C_2T_x$. Upon immersion in the electrolytes, large d-spacing of approximately 16.08 Å, 16.35 Å, and 16.44 Å was observed for 2 M $NaClO_4$ in H_2O, 75 H_2O:25 ACN, and 50 H_2O:50 ACN, respectively, due to spontaneous co-intercalation of Na^+ with different solvent molecules (**Figure 5.6 a**). The spontaneous intercalation of Na^+ ions was further confirmed by X-ray photoelectron spectroscopy (XPS), which indicated approximately 0.06-0.08 Na^+ ions per $Ti_3C_2T_x$ unit (**Figure S5.5**). Moreover, FTIR spectroscopy on $Ti_3C_2T_x$ after electrolyte immersion and high-vacuum drying (10^{-7} mbar) revealed a broad O-H stretching band at 3426 cm^{-1} in 2 M $NaClO_4$ H_2O and 75 H_2O:25 ACN, strongly suggesting the confined water molecules in the interlayer (**Figure S5.6**)[36]. This peak shows a blueshift to 3445 cm^{-1} in 50 H_2O:50 ACN, suggesting weaker hydrogen bonding remained in MXene's interlayer. Additionally, the vibrational band corresponding to dangling -OH on the MXene surface at 3622 cm^{-1} was more pronounced in 50 H_2O: 50 ACN. Noteworthy, during the first cathodic scan, no distinct reduction peak is observed in any of the electrolytes (**Figure S5.7**), while operando XRD reveals a gradual decrease in interlayer spacing, reaching 15.45 Å, 16.14 Å, and 15.96 Å at -1.1 V in H_2O, 75 H_2O:25 ACN, and 50 H_2O:50 ACN respectively (**Figure 5.6 b-d**). These moderate decreases (by 0.6 Å, 0.21 Å, and 0.48 Å) suggested the electrochemical intercalation of partially desolvated Na^+ ions into MXene interlayers at negative potential, driven by electrostatic attraction between Na^+ and negatively charged $Ti_3C_2T_x$[37]. However, different structural evolution emerged in different electrolytes during the subsequent anodic scan. In 2 M $NaClO_4$ H_2O, the d-spacing increased gradually from 15.45 Å at -1.1 V to 16.08 Å at 0 V, attributed to the de-intercalation of partially desolvated Na^+ ions (**Figure 5.6 b**). In contrast, a two-step de-intercalation process was evident in ACN-containing electrolytes: a subtle, continuous interlayer spacing change at negative potential and a sharp, and a substantial interlayer spacing change at more positive potential above open-circuit potential (OCP). Upon the first anodic sweep in 75 H_2O:25 ACN, the d-spacing of $Ti_3C_2T_x$ initially increased slightly from 16.14 Å to 16.32 Å as the potential rose from -1.1 V to -0.05 V, followed by an abrupt contraction to 14.19 Å at -0.05 V (**Figure 5.6 c**). The initial gradual expansion is likely due to the de-intercalation of partially desolvated Na^+ ions. While the subsequent sharp shrinkage by ~2.1 Å is potentially attributed to the electrochemical de-intercalation of strongly solvated Na^+-H_2O clusters. These Na^+-solvent clusters were spontaneously pre-inserted upon immersion and remained in the interlayer during the initial

cathodic scan. Once the applied potential exceeded the OCP, the positive bias triggered the de-insertion of Na^+ along with coordinated solvent molecules, resulting in a pronounced reduction in interlayer spacing. To further investigate whether ACN co-solvents accompanied Na^+ during de-intercalation, supplementary measurements were performed in 2 M $NaClO_4$ 75 H_2O:25 DMF. DMF was selected due to its larger molecular size and higher donor number, while the latter factor results in stronger coordination with Na^+ ions. If organic cosolvents were de-inserted together with Na^+ ions, the larger size of DMF would be expected to cause a noticeable difference in the degree of *d*-spacing contraction compared to ACN. However, a similar *d*-spacing contraction of ~2.0 Å was observed, suggesting that Na^+ ions were primarily de-inserted together with water molecules (**Figure S5.8**). This indicates that organic cosolvents did not directly participate in de-intercalation but instead modified the Na^+-H_2O coordination, as evidenced by FTIR and NMR. Such modulation of the Na^+-H_2O interaction is necessary to enable electrochemical de-intercalation. Supporting this, applying a potential of +0.2 V in 2 M $NaClO_4$ H_2O only led to severe oxidation with a minor *d*-spacing increase of ~0.2 Å (**Figure 5.6 b**). During the subsequent cathodic sweep in 75 H_2O:25 ACN, the *d*-spacing abruptly expanded from 14.19 Å to 16.32 Å when the potential reached the reduction peak potential (- 0.15 V), corresponding to the electrochemical intercalation of Na^+-H_2O cluster (**Figure 5.6 c**). This was followed by gradual contraction to 16.09 Å until -1.1 V, as partially desolvated Na^+ ions were inserted, confirming a reversible two-step electrochemical intercalation behavior.

A similar two-step (de-)intercalation behavior was also observed in the 50 H_2O:50 ACN system, albeit with different trends (**Figure 5.6 d**). Starting from the fully intercalated state at -1.1 V, the *d*-spacing gradually increased from 15.96 Å to 16.35 Å as the potential swept anodically toward 0 V. Upon reaching 0 V, a sharp increase in d-spacing to 18.01 Å (~1.7 Å jump) was observed near the oxidation peak. Although FTIR and NMR analyses suggest enhanced coordination between ClO_4^- anion and Na^+ ions with increased ACN ratios, direct intercalation of anions into MXene interlayers is energetically unfavorable[30]. Therefore, the observed expansion in *d*-spacing is likely attributed to the de-intercalation of bare or weakly solvated Na^+ ions, which strongly interact with the negatively charged MXene surfaces and help maintain a compact interlayer structure. Removal of these Na^+ ions may reduce electrostatic attraction with MXene layer, allowing the residual confined solvent molecules to reorient or redistribute more freely, resulting in a looser molecular packing and expanded interlayer spacing. During the subsequent cathodic scan, the *d*-spacing abruptly reduced to 16.46 Å at the cathodic peak potential, indicating reversible insertion of bare or weakly solvated Na^+ ions and re-establishment of compact interlayer structure. If a greater number of Na^+ ions or strongly solvated Na^+ species were intercalated, interionic repulsion or steric effects would likely lead to interlayer expansion instead. This limited ion insertion in 50

5

H_2O:50 ACN, despite enhanced redox activity observed from UV-Vis, may explain the comparable overall capacitance to the 75 H_2O:25 ACN system.

In summary, the incorporation of ACN into the electrolyte alters the solvation structure of Na^+ ions, thereby modulating the intercalation behavior and charge storage mechanisms of $Ti_3C_2T_x$ MXene. This solvation structure modification activates a two-step Na^+ intercalation process in $Ti_3C_2T_x$ MXene upon cathodic sweep. At higher potential (S1 & S1'), sharp interlayer spacing changes are observed near the cathodic peak when ACN is employed as the cosolvent. In 75 H_2O:25 ACN, the interlayer spacing expands abruptly by 2.1 Å at high potential, indicating the intercalation of strongly solvated Na^+-H_2O clusters. While this step does not contribute to significant charge transfer, it enables additional ion storage with rapid kinetics (**Figure 5.1**, middle). This intercalation behavior leads to an overall ~30% increase in capacitance and improved rate performance compared to pure water. In contrast, in 50 H_2O:50 ACN, $Ti_3C_2T_x$ undergoes an abrupt contraction in d-spacing by 1.6 Å, likely due to the intercalation of weakly solvated or bare Na^+ ions and the solvent reorganization, accompanied by enhanced redox activity (**Figure 5.1**, right). At more negative potential (S2), both systems involve the intercalation of partially desolvated Na^+ ions. This behavior is consistent with that observed in pure aqueous electrolytes and is non-Faradaic in nature (**Figure 5.1**, left).

5.3 Conclusion

This study demonstrates that modifying the electrolyte composition by introducing ACN as cosolvent alters the Na^+ solvation structure and thus the charge storage behavior in $Ti_3C_2T_x$ MXene. As Na^+-H_2O interactions weaken with ACN addition, a distinct high-potential intercalation step emerges alongside the conventional low-potential EDL process. Importantly, we show that the nature of this additional intercalation step, whether non-Faradaic or pseudocapacitive, is correlated to the solvent-ion interactions. These findings establish a clear relationship between ion solvation and intercalation behavior in MXenes, offering a practical approach to enhance both capacitance and rate capability through electrolyte design. Extending such co-solvent strategies to other ion-electrode systems may provide a rational pathway to optimize electrochemical performance through controlled ion-solvent interactions.

Methods

Synthesis of Ti₃C₂Tₓ: To synthesize $Ti_3C_2T_x$, 1 g Ti_3AlC_2 was gradually added into a solution of 1.6 g LiF and 20 ml of 9 M HCl. This mixture was kept at 35 °C and stirred for 24 hours for etching. Subsequently, the etched material was washed several times with deionized water through centrifugation at 8000 rpm until the pH of the supernatant was neutralized to 6. The remaining sediment was re-dispersed in 40 ml of deionized water and subjected to 1 hour of sonication under an argon atmosphere to facilitate the delamination of the multilayers. The suspension was then centrifuged at 3500 rpm for 1 hour, and the black supernatant was collected, yielding a few-layered $Ti_3C_2T_x$ colloidal solution. The $Ti_3C_2T_x$ film was then obtained through vacuum-assisted filtration and stored in a desiccator before subsequent characterization.

Electrochemical measurements: Electrochemical performance was evaluated using Swagelok cells configured in a three-electrode setup with a Biologic VSP-300 potentiostat. In this configuration, the free-standing $Ti_3C_2T_x$ films served as the working electrode, an Ag wire and activated carbon were used as the reference and counter electrodes, respectively, while Whatman GF-A films served as separators. Cyclic voltammetry was conducted over scan rates ranging from 5 mV s⁻¹ to 1 V s⁻¹. For galvanostatic charge and discharge (GCD) tests, current densities varied from 0.2 A g⁻¹ to 10 A g⁻¹. Electrochemical impedance spectroscopy was performed with a 10 mV amplitude across a frequency range from 10 mHz to 200 kHz. The gravimetric specific capacitance derived from cyclic voltammetry is calculated using the formula:

$$C(\mathrm{F\,g^{-1}}) = \frac{\int i\,\mathrm{d}v}{m\,s\,\Delta V}$$

where i represents the current (A), s is the scan rate (V s⁻¹), m is the mass of the working electrode (g), and ΔV is the applied voltage window (V).

Material characterization: X-ray diffraction (XRD) analysis was performed using a PANalytical X'Pert Pro diffractometer with Cu K_α radiation ($\lambda = 0.1542$ nm) at an operating voltage of 45 kV and a current of 40 mA. In-situ XRD patterns were obtained over a 2θ range of 3°-15° with a step size of 0.02° and a scan rate of 2.5°/min. These measurements were conducted simultaneously with cyclic voltammetry (CV) at a scan rate of 0.2 mV s⁻¹, using a Biologic VSP-300 potentiostat. NMR spectra were acquired using a Bruker 600 MHz (14.1 T) Ascend magnet equipped with a NEO console. For NMR measurements, $NaClO_4$ salts were dissolved in a mixture of deuterated water (D_2O) and ACN in different volume ratio. The Larmor frequencies were 600.13 MHz for ¹H and 158.76 MHz for ²³Na. The 90° pulse lengths were determined to be 16.2 μs for ¹H and 13.4 μs for ²³Na. Spectra were recorded

137

using a 30° excitation pulse with a 2 s recycle delay, collecting 4 scans for ^{1}H and 8 scans for [23]Na. A 2 M NaCl solution in D_2O served as the reference for [23]Na, while tetramethylsilane (TMS), sealed in a capillary and immersed in the electrolyte, was used as the ^{1}H reference. Fourier-transform infrared (FTIR) spectroscopy was employed to analyze the solvation structure of electrolytes using a Thermo Scientific Nicolet iS50 spectrometer equipped with an iS50 ATR module. X-ray photoelectron spectroscopy measurements were performed on a Thermo Scientific K-Alpha Spectrometer with an Al K-alpha (1486.6 eV) monochromator. The spot diameter was set to 400 μm. Survey spectra were recorded with a pass energy of 200 eV and step size of 0.5 eV, while high-resolution spectra were recorded with a pass energy of 50 eV and step size of 0.1 eV. The binding energies were referenced to adventitious carbon at 284.8 eV. Operando UV-Vis spectroscopy was performed using a Thermo Scientific Pro Evolution One Plus spectrophotometer, equipped with a xenon flash lamp as the light source. The system was operated with a spectral bandwidth of 1 nm and a beam size of 0.46 mm × 2.5 mm. Thin $Ti_3C_2T_x$ working electrodes and thick $Ti_3C_2T_x$ counter electrodes were prepared by spray-coating a ~5 mg mL^{-1} $Ti_3C_2T_x$ aqueous dispersion onto pre-cleaned glass substrates at 60 °C. Prior to measurement, a reference spectrum was acquired using a clean glass-glass configuration without electrolyte. The absorbance of the as-prepared electrode was recorded across 300-800 nm to estimate film thickness and serve as the initial baseline. Using a previously reported linear relation ($A = 0.005 \times l$), where A is the absorbance and l is the thickness of the $Ti_3C_2T_x$ working electrode[38]. The thicknesses were calculated for absorbance minima ranging from 0.6 to 1.8, corresponding to 120-360 nm, allowing us to obtain the normalized absorption. While this relation was originally validated for thinner coatings (5-70 nm), its consistent application across all samples allows for comparative analysis within this study. Subsequently, the in-situ cell was filled with electrolytes and sealed with UV-curable resin to prevent electrolyte evaporation and aligned in the beam path. Then the UV-Vis spectra were collected simultaneously with cyclic voltammetry. Under the scan mode, full absorbance spectra were captured every ~ 45 mV by synchronizing with a 1 mV s^{-1} CV scan. To visualize spectral evolution, absorbance curves at selected potentials during anodic and cathodic sweeps were extracted. For quantitative evaluation, the fixed wavelength mode was used by monitoring a single wavelength (450 nm), which corresponds to the wavelength with the most pronounced optical response, was collected as a function of potential. The normalized absorbance derivative was calculated using the following equation:

$$\text{Normalized absorbance derivative} = (A_V - A_{V-dV}) / (dV \times l)$$

where A_V is the absorbance at potential V, dV is the potential difference between measurement points, l is the thickness of the $Ti_3C_2T_x$ working electrode. This normalization accounts for

138

both the potential scan resolution and film thickness, enabling direct comparison of optical behavior across different electrolyte systems.

5.4 Supplementary information
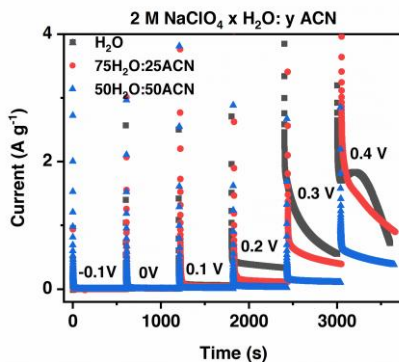
Figure S 5.1 Chronoamperometry data collected at different potentials (vs. Ag) in 2 M NaClO₄ electrolytes with different solvent compositions: H₂O, 75 H₂O: 25 ACN and 50 H₂O: 50 ACN.
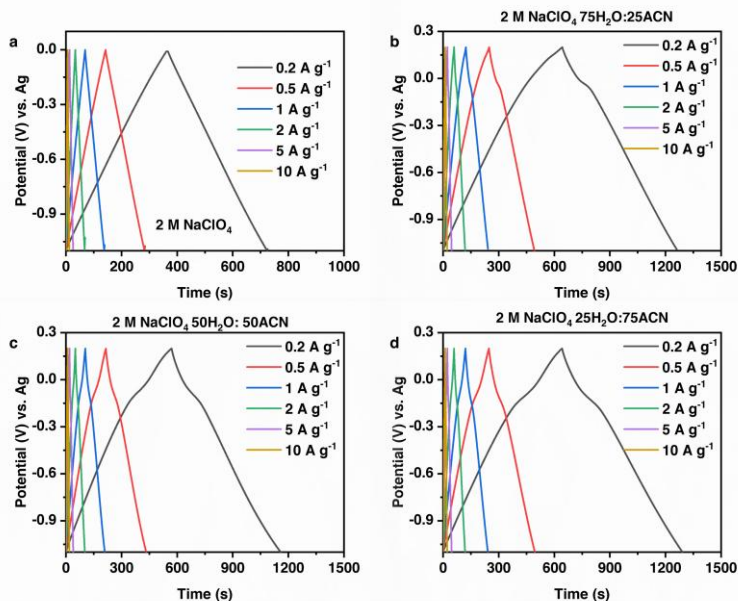

Figure S 5.2 Three-electrode galvanostatic charge-discharge curves of Ti₃C₂Tₓ MXene in 2 M NaClO₄ dissolved in (a) H₂O, (b)75 H₂O: 25 ACN, (c) 50 H₂O: 50 ACN. and (d) 25 H₂O: 75 ACN at current densities of 0.2, 0.5, 1, 2, 5 and 10 A g⁻¹.
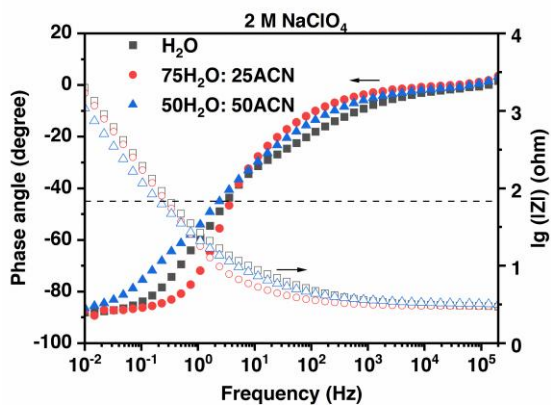
Figure S 5.3 Bode plots showing resistance and phase angle as a function of frequency.
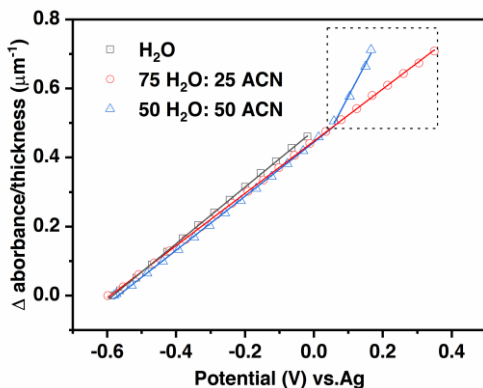
Figure S 5.4 Linear fitting of relative absorbance changes versus potential during the cathodic scan.
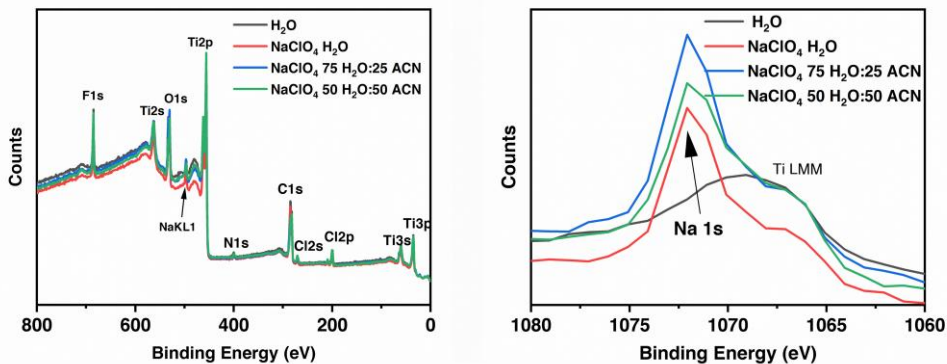
Figure S 5.5 (a) Full range and (b) High-resolution Na1s XPS spectra of Ti$_3$C$_2$T$_x$ MXene after immersing in different solution for 4 h.
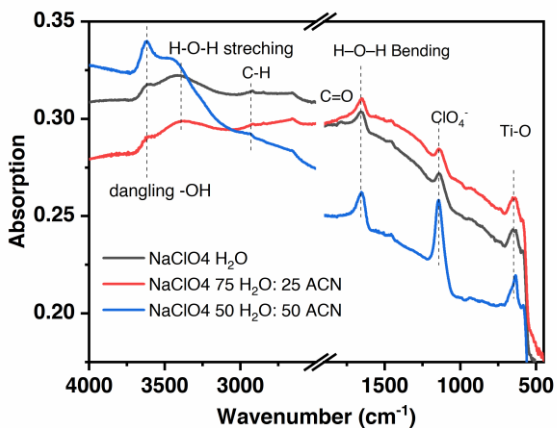
Figure S 5.6 FTIR spectra of Ti$_3$C$_2$T$_x$ MXene after immersing in different electrolytes for 4 h and drying under high-vacuum.

5
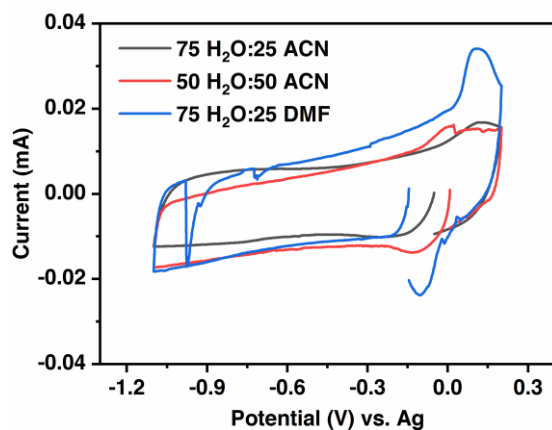
Figure S 5.7 CV curves of Ti$_3$C$_2$T$_x$ MXene at a scan rate of 0.2 mV s^{-1} during the first cycle in in-situ cell.
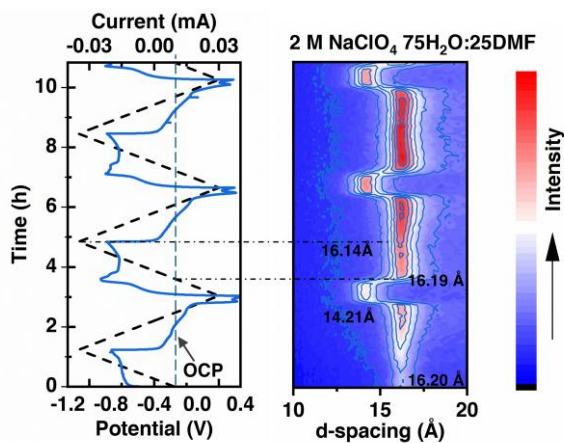
Figure S 5.8 Operando X-ray diffraction (XRD) patterns of Ti$_3$C$_2$T$_x$ MXene in 2 M NaClO$_4$ 75 H$_2$O:25 DMF electrolytes.

5.5 Reference

[1]   N. Kittner, F. Lill, D. Kammen, *Nat. Energy* **2017**, *2*,17125.

[2]   Y. Liu, Y. Zhu, Y. Cui, *Nat. Energy* **2019**, *4*, 540-550.

[3]   S. Fleischmann, J. B. Mitchell, R. Wang, C. Zhan, D. Jiang, V. Presser, V. Augustyn, *Chem. Rev.* **2020**, *120*, 6738.

[4]   M. Naguib, V. N. Mochalin, M. W. Barsoum, Y. Gogotsi, *Adv. Mater.* **2014**, *26*, 992.

[5]   M. R. Lukatskaya, S. Kota, Z. Lin, M.-Q. Zhao, N. Shpigel, M. D. Levi, J. Halim, P.-L. Taberna, M. W. Barsoum, P. Simon, Y. Gogotsi, *Nat. Energy* **2017**, *2*, 17105.

[6]   X. Li, Z. Huang, C. E. Shuck, G. Liang, Y. Gogotsi, C. Zhi, *Nat. Rev. Chem.* **2022**, *6*, 389.

[7]   D. Chao, W. Zhou, F. Xie, C. Ye, H. Li, M. Jaroniec, S. Qiao, *Sci. Adv.* **2020**, *6,* eaba4098.

[8]   M. Okubo, A. Sugahara, S. Kajiyama, A. Yamada, *Acc. Chem. Res.* **2018**, *51*, 591.

[9]   Y. Ando, M. Okubo, A. Yamada, M. Otani, *Adv. Funct. Mater.* **2020**, *30*, 2000820.

[10]   Q. Gao, W. Sun, P. Ilani-Kashkouli, A. Tselev, P. R. C. Kent, N. Kabengi, M. Naguib, M. Alhabeb, W.-Y. Tsai, A. P. Baddorf, J. Huang, S. Jesse, Y. Gogotsi, N. Balke, *Energy Environ. Sci.* **2020**, *13*, 2549.

[11]   F. Ming, Y. Zhu, G. Huang, A. Emwas, H. Liang, Y. Cui, H. Alshareef, *J. Am. Chem. Soc.* **2022**, *144*, 7160.

[12]   L. Suo, O. Borodin, T. Gao, M. Olguin, J. Ho, X. Fan, C. Luo, C. Wang, K. Xu, *Science* **2015**, *350*, 938.

[13]   J. Xie, Z. Liang, Y.-C. Lu, *Nat. Mater.* **2020**, *19*, 1006.

[14]   D. Chao, S. Qiao, *Joule* **2020**, *4*, 1846.

[15]   X. Wang, T. S. Mathis, K. Li, Z. Lin, L. Vlcek, T. Torita, N. C. Osti, C. Hatter, P. Urbankowski, A. Sarycheva, M. Tyagi, E. Mamontov, P. Simon, Y. Gogotsi, *Nat. Energy* **2019**, *4*, 241.

[16]   A. Perju, D. Zhang, R. J. Wang, P.-L. Taberna, Y. Gogotsi, P. Simon, *Adv. Energy Mater.* **2025**, *15*, 2405028.

[17]   C. Chen, A. de Kogel, M. Weijers, L. J. Bannenberg, X. Wang, *2D Mater.* **2023**, *11*, 015001.

[18]   X. Wang, T. S. Mathis, Y. Sun, W.-Y. Tsai, N. Shpigel, H. Shao, D. Zhang, K. Hantanasirisakul, F. Malchik, N. Balke, D. Jiang, P. Simon, Y. Gogotsi, *ACS Nano* **2021**, *15*, 15274.

[19]   R. J. Sengwa, P. Dhatarwal, S. Choudhary, *J. Mol. Liq.* **2018**, *271*, 128.

[20]   Y. Sun, Y. Wang, L. Liu, B. Liu, Q. Zhang, D. Wu, H. Zhang, X. Yan, *J. Mater. Chem. A* **2020**, *8*, 17998.

[21]   J. Chen, J. Vatamanu, L. Xing, O. Borodin, H. Chen, X. Guan, X. Liu, K. Xu, W. Li, *Adv. Energy Mater.* **2020**, *10*, 1902654.

[22]   Q. Dou, S. Lei, D.-W. Wang, Q. Zhang, D. Xiao, H. Guo, A. Wang, H. Yang, Y. Li, S. Shi, X. Yan, *Energy Environ. Sci.* **2018**, *11*, 3212.

[23]   J. Shi, K. Xia, L. Liu, C. Liu, Q. Zhang, L. Li, X. Zhou, J. Liang, Z. Tao, *Electrochim. Acta* **2020**, *358*, 136937.

[24]   S. Yadav, N. Kurra, *Energy Storage Mater.* **2024**, *65*, 103094.

[25]   J. Wang, J. Polleux, J. Lim, B. Dunn, *J. Phys. Chem. C* **2007**, *111*, 14925.

[26]   N. O. Laschuk, E. B. Easton, O. V. Zenkina, *RSC Adv.* **2021**, *11*, 27925.

[27]   D. Zhang, R. (John) Wang, X. Wang, Y. Gogotsi, *Nat. Energy* **2023**, *8*, 567.

[28]   Y. Wang, T. Ou, Y. Dong, L. Chen, Y. Huang, D. Sun, W. Qiang, X. Pei, Y. Li, Y. Tan, *Adv. Mater.* **2024**, *36*, 2311009.

[29]   Z. Wu, Y. Li, A. Amardeep, Y. Shao, Y. Zhang, J. Zou, L. Wang, J. Xu, D. Kasprzak, E. J. Hansen, J. Liu, *Angew. Chem.* **2024**, *136*, e202402206.

[30]   J. S. Loring, W. R. Fawcett, *J. Phys. Chem. A* **1999**, *103*, 3608.

[31]   Y. Chen, Y.-H. Zhang, L.-J. Zhao, *Phys. Chem. Chem. Phys.* **2004**, *6*, 537.

[32]   Z. Bo, R. Wang, B. Wang, S. Sunny, Y. Zhao, K. Ge, K. Xu, Y. Song, E. Raymundo-Piñero, Z. Lin, H. Shao, Q. Yu, J. Yan, K. Cen, P.-L. Taberna, P. Simon, *Nat. Commun.* **2025**, *16*, 3813.

[33]   T. Zhang, L. Chang, X. Zhang, H. Wan, N. Liu, L. Zhou, X. Xiao, *Nat. Commun.* **2022**, *13*, 6731.

[34]   G. A. Ferrero, G. Åvall, K. Janßen, Y. Son, Y. Kravets, Y. Sun, P. Adelhelm, *Chem. Rev.* **2025**, *125*, 3401.

[35]   M. L. Divya, Y.-S. Lee, V. Aravindan, *ACS Energy Lett.* **2021**, *6*, 4244.

5

[36]   M. Lounasvuori, Y. Sun, T. S. Mathis, L. Puskar, U. Schade, D.-E. Jiang, Y. Gogotsi, T. Petit, *Nat. Commun.* **2023**, *14*, 1322.

[37]   M. R. Lukatskaya, O. Mashtalir, C. E. Ren, Y. Dall'Agnese, P. Rozier, P. L. Taberna, M. Naguib, P. Simon, M. W. Barsoum, Y. Gogotsi, *Science* **2013**, *341*, 1502.

[38]   K. Hantanasirisakul, M.-Q. Zhao, P. Urbankowski, J. Halim, B. Anasori, S. Kota, C. E. Ren, M. W. Barsoum, Y. Gogotsi, *Adv. Electron. Mater.* **2016**, *2*, 1600050.

5

Solvation Structure Engineering with Co-Solvents Enables Tunable Charge Storage Mechanisms in MXenes

5

6 Enhancing Zn Deposition Reversibility on MXene Current Collectors by Forming ZnF$_2$-Containing Solid-Electrolyte Interphase for Anode-Free Zinc Metal Batteries

Enhancing Zn Deposition Reversibility on MXene Current Collectors by Forming ZnF2-Containing Solid-Electrolyte Interphase for Anode-Free Zinc Metal Batteries

Abstract

Anode-free aqueous zinc metal batteries (AZMBs) offer significant potential for energy storage due to their low cost and environmental benefits. $Ti_3C_2T_x$ MXene provides several advantages over traditional metallic current collectors like Cu and Ti, including better Zn plating affinity, lightweight, and flexibility. However, self-freestanding MXene current collectors in AZMBs remain underexplored, likely due to challenges with Zn deposition reversibility. This study investigates the combination of a $Ti_3C_2T_x$ self-freestanding film with advanced electrolyte engineering, specifically examining the effects of Li-salt and propylene carbonate (PC) as additives on Zn plating reversibility. While using Li^+ ions as additive alone facilitates uniform Zn deposition on bulk metals through electrostatic shielding effect, addition of Li-salt negatively impacts Zn plating uniformity on $Ti_3C_2T_x$. Meanwhile, using PC additive alone forms an organic solid electrolyte interphase (SEI) layer on $Ti_3C_2T_x$ and causes Zn agglomeration. The use of both additives together results in a ZnF_2-containing hybrid SEI layer with improved interfacial kinetics, promoting more uniform Zn deposition. This approach achieves an average Coulombic efficiency (CE) of 96.8% over 150 cycles (a maximum CE of 97.8%). The study highlights the strategic difference in electrolyte design, emphasizing the need for tailored approaches to optimize Zn deposition on MXenes, contrasting with traditional metallic current collectors.

6

6.1 Introduction

The pursuit of advanced energy storage solutions with economic viability, environmental sustainability, and prolonged cycle life, has prompted extensive exploration of advanced electrochemical energy storage devices[1,2]. Moreover, concerns regarding the scarcity of lithium resources, escalating costs, and safety issues associated with organic electrolytes have intensified efforts to explore promising alternatives to current lithium-ion batteries[3,4]. Aqueous zinc metal batteries (AZMBs) have emerged as promising devices for stationary energy storage due to their low cost, material abundance and low toxicity[5]. The relatively high theoretical capacity of 820 mA h g^{-1} (or 5855 mAh cm^{-3}), low redox potential of zinc metal (-0.762 V versus the standard hydrogen electrode) and good stability further enhance its appeal, positioning AZMBs as standout candidates for next-generation EES devices. Despite its high theoretical capacity and low redox potential, the practical energy densities of AZMBs are limited by heavier battery designs due to the use of excessive Zn metal anodes ($\geq$100 μm). Reasonable modifications on Zn anode, including applying thinner Zn foil, pre-depositing Zn on metallic or carbonaceous substrates, or especially exploring anode-free configurations can reduce the weight and space demand for anode materials, improve the Zn utilization level, thereby enabling a higher energy density at potentially lower costs[6].

Specifically, the anode-free AZMBs are composed of an electron-conductive current collector and a Zn-rich cathode host. In this design, the traditional anode is replaced by a "Zn-free" anode that is not only used directly for Zn deposition but also functions as the current collector, thereby significantly simplifies the production processes[7,8]. To unify the description in this study, we use "anode-free" to represent the "Zn-free" anode. Compared to the other methods applied to improve the Zn utilization level, anode-free configurations can limit the Zn corrosion reactions, due to the minimal amount of Zn that is exposed to the electrolyte[9]. Indeed, in such an anode-free battery, the charging process involves de-intercalation of Zn^{2+} ions from the cathode and subsequent deposition of these ions on the current collector. Since all the active Zn^{2+} ions are stored in the cathode material, and there is no oversupply of Zn ions as in traditional zinc ion batteries, the Coulombic efficiency (CE) becomes crucial. Generally, the plating/stripping process on the current collector exhibits lower CE compared to that of an insertion cathode. Therefore, the challenge is to improve the Zn plating efficiency, which is primarily determined by the side reactions (such as the hydrogen evolution reaction), and the dendrite growth[10]. Such an improvement relies on optimizing both the current collector and the electrolytes.

MXenes have attracted many research interests in AZMBs due to their high conductivity, open layered structure, and unique surface chemistry. MXenes ($M_{n+1}X_nT_x$, where M represents early transition metals, X is C and/or N, and T_x represents surface functional

6

groups (-O, -OH, -F)) are a family of two-dimensional transition metal carbides and/or nitrides, synthesized by selectively etching the A layer from MAX ceramic precursors[11,12]. Their rich surface groups make them both hydrophilic and zincophilic, lowering the energy barrier and facilitating uniform Zn deposition[13–15]. Moreover, owing to its hexagonal structure inherited from the precursor MAX phase, MXenes have minimal lattice mismatch with the (002) facet of Zn, which crystallizes in a hexagonally closed packed structure. As such, MXene can forester the thin hexagonal flakes of Zn depositing horizontally to the film surface and thus achieve a desired morphology for achieving cycling longevity[16]. Compared to other MXenes such as Ti_2CT_x, Nb_2CT_x, $Nb_4C_3T_x$, and V_2CT_x, $Ti_3C_2T_x$ has demonstrated the highest electronic conductivity (~24,000 S cm⁻¹) alongside a great chemical stability[17]. As the most extensively studied MXene, $Ti_3C_2T_x$ has demonstrated exceptional potential for enhancing the Zn deposition reversibility when used as coating layer for Zn metal or substrates for Zn pre-deposition[18–20]. For instance, by pre-electroplating 2 µm Zn on $Ti_3C_2T_x$ film in 2 M $ZnSO_4$ electrolyte, a self-freestanding $Ti_3C_2T_x$ MXene@Zn paper with better electrolyte wettability and lower overpotential than Zn metal can be obtained[14]. The MXene@Zn paper enables a dendrite-free Zn deposition and a good cycling stability with a high average Coulombic efficiency (ACE) of 94.13% for Zn plating/stripping[14].

In addition to serving as surface modifiers for Zn electrodes, MXene films offer significant potential as current collectors in anode-free aqueous zinc metal batteries (AZMBs), which could greatly enhance energy density. Their lower material density, combined with a superior affinity for Zn plating compared to traditional metallic current collectors like Cu and Ti, makes self-standing $Ti_3C_2T_x$ films especially advantageous. Despite this potential, there are currently no reports of $Ti_3C_2T_x$ films being directly employed for Zn plating/stripping in AZMBs, though they have shown notable performance as current collectors in other energy storage systems [21,22]. This absence may stem from challenges in achieving high Zn deposition reversibility on pure MXene films, with prior studies primarily exploring composite-based electrodes instead. For instance, A flexible 3D $Ti_3C_2T_x$/graphene aerogel fabricated by the directional freezing method has been utilized directly as the framework for Zn plating/stripping[23]. The 3D porous structures are capable of effectively encapsulating Zn, leading to a dendrite-free Zn deposition on $Ti_3C_2T_x$/graphene. Consequently, a superior reversibility for Zn plating and stripping with an ACE of ~ 99.67% upon 600 cycles at 10 mA cm⁻² was achieved. Even at a high deposition capacity of 5 mAh cm⁻², Zn is uniformly deposited inside the micropores of the MXene/graphene 3D framework with minimal granular protrusions on the surface, which significantly prevents the formation of Zn dendrites. Combining $Ti_3C_2T_x$ with Antimony (Sb) or nanocellulose to prepare MXene-based composite as current collector for AZMBs also demonstrated good reversibility for Zn plating/stripping[24,25].

150

Addressing this gap could open new pathways for MXene applications in AZMBs. Rationally designing electrolyte systems could enhance the reversibility of Zn plating on $Ti_3C_2T_x$ self-freestanding films in anode-free AZMBs, offering a solution that maintains a straightforward electrode production process. Optimizing the electrolytes, by modifying the salt concentration, introducing ionic additives, organic molecules and polymers, stands out as another practical solution to facilitate the Zn deposition on Zn metal or other metallic current collectors[7,26–28]. The modification of electrolytes can change the solvation structure, influencing charge transfer and Zn^{2+} ion transport process. This, in turn, affects the nucleation and growth of Zn on the electronic conductive substrates[29,30]. Additionally, some additives may participate in the formation of solid electrolyte interphase (SEI), concurrently inhibiting the hydrogen evolution reaction (HER), side reactions and the dendritic growth[31–33]. Optimizing electrolytes for reversible Zn plating on $Ti_3C_2T_x$ presents unique challenges compared to conventional electrolyte design strategies aimed at enhancing Coulombic efficiency (CE) on metal surfaces. This challenge arises from the intercalation process of ions and subsequent deposition, both of which are dependent on the electrolyte composition. Moreover, the presence of intercalated ions can affect the charge distribution within the MXene's structure, further impacting the subsequent Zn deposition behavior. Therefore, traditional electrolyte designing strategies that promote reversible Zn deposition on metal may not work for 2D $Ti_3C_2T_x$ MXenes. This motivates studies towards the influence of electrolytes on the Zn deposition behavior on MXenes, which to the best of our knowledge, has yet to be explored.

In this work, we demonstrate that the co-addition of LiTFSI and polyethylene carbonate (PC) into $Zn(OTF)_2$ electrolytes (denoted as Zn-Li-PC-H_2O) can significantly improve the reversibility of Zn plating/stripping on $Ti_3C_2T_x$ MXene due to the formation of ZnF_2-containing SEI layer. The Li-salt is selected since Li^+ ions are capable of homogenizing the ion-flux on metal surface due to the electrostatic shielding effect, leading to a uniform metal deposition (**Figure 6.1 a** left) [34]. PC is chosen as an aprotic organic solvent that interacts strongly with both H_2O molecules and ions, which may affect the ion intercalation process and/or the interfacial properties[35]. Using either Li-salt or PC as additives has been reported to facilitate the reversible Zn^{2+} ion deposition on metal[7,34]. On 2D $Ti_3C_2T_x$, surprisingly, we find that the addition of Li-salt alone (Zn-Li-H_2O) unexpectedly leads to severe dendritic Zn growth, possibly due to the intercalation of Li^+/Zn^{2+} into 2D $Ti_3C_2T_x$ sheets (**Figure 6.1 a** middle). When combining PC and Li-salt as co-additives, although the intercalation behavior of cations was not changed, we observed the formation of a ZnF_2-containing organic/inorganic hybrid SEI layer. This ZnF_2-containing SEI layer functionalizes as an effective charge regulator, leading to a homogenous Zn deposition (**Figure 6.1 a** right). Consequently, a reversible and uniform Zn plating was realized in Zn-Li-PC-H_2O electrolytes

6

on $Ti_3C_2T_x$ surface with a high maximum CE of 97.8 % and an ACE of 96.8 % (including first cycle) over 150 cycles (**Figure 6.1 b-d**) in a $Zn//Ti_3C_2T_x$ half-cell. This work demonstrates the impact of electrolytes on Zn deposition behavior is different on 2D materials than on metal surfaces. It also provides a general strategy for rational electrolyte design to improve the reversibility of Zn plating on $Ti_3C_2T_x$ MXene for anode-free AMZB.

6.2 Results and discussions

6.2.1 Zn deposition behavior on self-freestanding $Ti_3C_2T_x$

$Ti_3C_2T_x$ films were obtained by selectively etching Ti_3AlC_2 through a mild *in-situ* HF method reported earlier and a subsequent filtration process[36]. The as-resulted $Ti_3C_2T_x$ films were flexible and self-freestanding (**Figure S6.1**), thus they were directly employed as the current collectors for Zn plating/stripping in anode-free AZMBs. As shown in the X-ray diffraction pattern (**Figure S6.2**), the disappearance of peaks attributed to Ti_3AlC_2 and the downshift of (0 0 2) peak indicate successful synthesis of $Ti_3C_2T_x$. Additionally, the $Ti_3C_2T_x$ films display significant preferred orientation along c-axis, which is beneficial for the Zn growth along the (0 0 2) plane[20,24]. The successful exfoliation was further confirmed by Raman spectroscopy and X-ray photoelectron spectroscopy (XPS) (**Figure S6.3**).
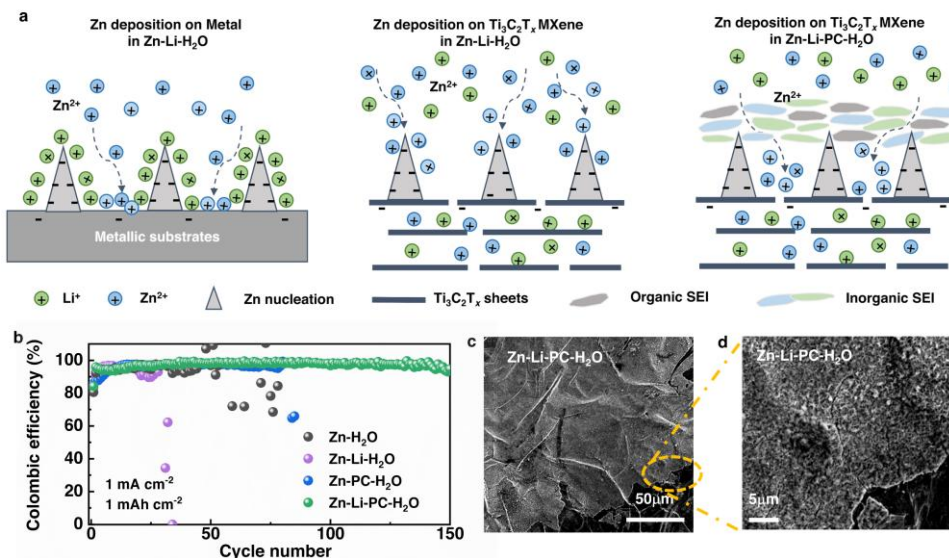
Figure 6.1 (a) Schematic illustration of the Zn deposition process on Metal substrates, $Ti_3C_2T_x$ MXene surface in Zn-Li-H₂O electrolytes and the Zn deposition process on $Ti_3C_2T_x$ MXene in Zn-Li-PC-H₂O electrolytes. (b) Coulombic efficiency measurements of $Ti_3C_2T_x//$Zn cell with a deposition capacity of 1 mAh cm⁻² at a current

density of 1 mA cm^{-2} in different electrolytes. (c)-(d) SEM images of Ti$_3$C$_2$T$_x$ electrode after plating 1 mAh cm^{-2} of Zn at 1 mA cm^{-2} in Zn-Li-PC-H$_2$O.

To investigate the deposition behavior of Zn on Ti$_3$C$_2$T$_x$, cyclic voltammograms (CV) were recorded using a Ti$_3$C$_2$T$_x$//Zn half-cell with a scan rate of 0.5 mV s^{-1} in 1 M Zn(OTF)$_2$ electrolyte (Zn-H$_2$O) (**Figure 6.2 a**). A slightly larger initial Zn plating/stripping potential located at -0.08 V/0.15 V was observed, compared to -0.055 V/0.105 V in 2 M ZnSO$_4$ electrolyte[14], due to the large size of OTF$^-$ than SO$_4$$^{2-}$. The Zn plating/stripping reversibility was then evaluated by galvanostatic discharge/charge profiles with a deposition capacity of 1 mAh cm^{-2} (at a current density of 1 mA cm^{-2}) and a stripping cutoff voltage of 0.5 V. A low initial CE of 80.0 % was observed in the Zn-H$_2$O electrolyte, possibly due to HER and dendrite formation. Moreover, only moderate cycling stability was achieved, with an ACE of 94.5 % and a short lifetime of just 40 cycles (**Figure 6.1 b**).

Figure 6.2 (a) CV curves of Ti$_3$C$_2$T$_x$//Zn cell in Zn-H$_2$O, Zn-Li-H$_2$O, Zn-PC-H$_2$O, and Zn-Li-PC-H$_2$O electrolytes at a sweep rate of 0.5 mV s^{-1}. **(b)** Voltage profiles (1st cycle) and corresponding nucleation overpotential values of Ti$_3$C$_2$T$_x$//Zn cell at a current density of 1 mA cm^{-2} in different electrolytes. **(c)** Charge/discharge curves of Ti$_3$C$_2$T$_x$//Zn cell in Zn-Li-PC-H$_2$O (Capacity: 1 mAh cm^{-2}, current density: 1 mA cm^{-2}). SEM images of Ti$_3$C$_2$T$_x$ electrode after plating 1 mAh cm^{-2} of Zn at 1 mA cm^{-2} in **(d)** Zn-H$_2$O electrolyte and **(e)** Zn-Li-H$_2$O electrolyte **(f)** Zn-PC-H$_2$O electrolyte.

To evaluate the impact of Li-salt additive on Zn deposition process, 1 M LiTFSI was added to the Zn-H$_2$O electrolyte to prepare a Zn-Li-H$_2$O electrolyte (1 M LiTFSI+1 M Zn(OTF)$_2$ in

153

6

water). Li-salt additive was reasonably chosen since the Li^+ ions are capable of enhancing the Zn deposition/stripping reversibility on Zn metal due to the electrostatic shielding effect[34]. Li^+ ion, has a more negative deposition potential than Zn^{2+} ion and is known to create a positively charged electrostatic shielding around the initial growth tip [37,38]. In turn, this can homogenize the Zn^{2+} ion flux on the dendrite surface (**Figure 6.1 a** left) and thereby inhibit further dendrite growth on metallic substrates. Unexpectedly, the CE became more fluctuating, and the $Ti_3C_2T_x$//Zn half-cell can only be cycled 25 times with an ACE of 90.6% (**Figure 6.1 b**). Additionally, the $Ti_3C_2T_x$ displayed a larger nucleation overpotential (61.9 mV) and deposition overpotential (77.7 mV) in Zn-Li-H2O electrolytes compared to that obtained in Zn-H2O electrolytes (**Figure 6.2 b**). The nucleation overpotential gradually decreased and stabilized at the 5th cycle (**Figure S6.4 & S6.5**), attributed to better electrolyte wettability upon cycling.

The morphologies of the deposited Zn on $Ti_3C_2T_x$ with a deposition capacity of 1 mAh cm^{-2} was further examined using scanning electron microscopy (SEM) analysis. Zn flakes that protrude upwards with large irregular Zn agglomerations were observed on the $Ti_3C_2T_x$ surface in both pristine Zn-H2O electrolyte (**Figure 6.2 d**, **Figure S6.6**) and Zn-Li-H2O electrolyte (**Figure 6.2 e**, **Figure S6.7**). This observation suggests that the addition of Li-salt alone does not effectively function as a charge regulator. The redox-active $Ti_3C_2T_x$ with large interlayer spacing allows the intercalation of different cations, contributing to pseudocapacitance. Previous report showed that Zn^{2+} ions can reversibly (de-)intercalate in $Ti_3C_2T_x$, leading to a Zn^{2+} ion storage capacity of 78.4 mAh g^{-1} at 0.2 A g^{-1} [39]. Such intercalative behavior may lead to a different charge distribution on the $Ti_3C_2T_x$ surface than on regular metallic current collectors, since, in the latter case, the electric double layer is formed only on the metal surface.

The intercalative behavior of MXene was accessed by collecting CVs in Zn-H2O and Zn-Li-H2O electrolytes within a narrower voltage window, where no Zn^{2+} ion deposition occurs. **Figure S6.8** shows the CVs of $Ti_3C_2T_x$ in Zn-H2O and Zn-Li-H2O electrolytes. $Ti_3C_2T_x$ displayed a pair of redox peaks at 0.75 V/0.83 V in Zn-H2O electrolyte. Additionally, a higher current density was observed when the cell was discharged to 0.3 V vs. Zn. Correspondingly, a broad oxidation peak at 0.3 V during the charge process can be observed. The presence of peaks in CV is in good agreement with the sloping region observed in the voltage profile in **Figure S6.4**, contributing to an intercalative capacity of 0.05 mAh cm^{-2} at the 1st cycle. Therefore, the first deposition process of Zn on MXenes involves two steps: the intercalation of Zn^{2+} ions into the interlayer spacing of $Ti_3C_2T_x$ at a relatively positive potential and the subsequent Zn plating process on the $Ti_3C_2T_x$ surface at more negative potential. This intercalation process is partially irreversible, as evidenced by the significant decrease in intercalation capacity observed in the following cycles (**Figure S6.4**). When Li^+ ions are

introduced into the electrolyte, a different electrochemical feature with a much broader and less intense oxidation peak at 0.35 V was observed, possibly caused by the de-intercalation of Zn^{2+} and/or Li^+. Also, considering the similar sizes of Li^+ and Zn^{2+}, Li^+ can be easily intercalated into MXene before Zn^{2+} deposition occurs. XRD and inductively coupled plasma (ICP) analysis are conducted to examine the d-spacing change and the Li^+ content change after Zn deposition. The (0 0 2) diffraction peak of $Ti_3C_2T_x$ locates at $2\theta = 5.84°$ and $5.77°$ in Zn-H$_2$O, and Zn-Li-H$_2$O electrolyte, correspond to d-spacings of 1.51 nm and 1.53 nm, respectively (**Figure S6.9**). Although the XRD results do not provide direct insight into Li^+ intercalation, the slight increase in d-spacing may suggest potential difference in intercalative behavior. Furthermore, ICP analysis indicates a reduction of Li^+ concentration in the electrolytes after the first discharge (**Table S6.1**), supporting our assumption of Li^+ co-intercalation into the $Ti_3C_2T_x$ prior to Zn metal deposition. Consequently, Li^+ ions likely reside within the interlayer spacing of $Ti_3C_2T_x$ rather than accumulating on the surface, thereby failing to form an effective positive electrostatic field near the surface and limiting its ability to regulate Zn^{2+} ion flux (**Figure 6.1 a**). Additionally, the presence of TFSI$^-$ anions in Zn-Li-H$_2$O electrolytes may adversely affect Zn deposition reversibility. When TFSI$^-$ was replaced with OTF$^-$ at the same concentration, the CE and cycling performance of Zn plating on $Ti_3C_2T_x$ in Zn-LiOTF-H$_2$O electrolyte, while not superior, were comparable to those in Zn-H$_2$O electrolyte (**Figure S6.10**).

Achieving an effective regulation of Zn deposition by Li^+ requires rational modification on the absorption behavior of Li^+ on the MXenes surface. Such a modification can be realized through tuning the solvation structure of electrolyte. As a commonly used solvent in Li-ion batteries, PC shows high polarity and a high dielectric constant. Therefore, PC can interact strongly with cations and water molecules through dipolar interaction, enabling effective modification of solvation structure. As a result, introducing PC as a co-solvent in the Zn(OTF)$_2$ aqueous electrolyte has been shown to significantly improved the CE of Zn plating/stripping on Cu foil, raising it from 92.5% to 99.7%[7]. Moreover, it has been shown that the using PC as solvent may induce a different intercalative behavior of Li^+ ions into $Ti_3C_2T_x$[35]. Given this consideration, in our system, PC was introduced as a co-additive into Zn-Li-H$_2$O to prepare Zn-Li-PC-H$_2$O electrolyte (1 M LiTFSI +1 M Zn(OTF)$_2$ in 50%PC/50%H$_2$O). A more reversible plating/stripping behavior can be observed in the Zn-Li-PC-H$_2$O electrolyte with a high maximum CE of 97.8 % and an ACE of 96.8 % (including first cycle) over 150 cycles with minimal fluctuation over 150 cycles (**Figure 6.1 b**). $Ti_3C_2T_x$ displayed a slightly larger nucleation overpotential (61.9 mV) and deposition overpotential (77.7 mV) in Zn-Li-PC-H$_2$O electrolytes during the first plating/stripping (**Figure 6.2 b**). One can also observe the decreased nucleation overpotential and the more negative plateau in the subsequent cycles (**Figure 6.2 c**), possibly caused by dynamics difference[22]. The Zn

6

plating morphological evolutions on $Ti_3C_2T_x$ in Zn-Li-PC-H_2O were further investigated. A smooth and dense deposition of Zn was observed (**Figure 6.1 c-d** and **Figure S6.11**). When PC was used as the only additive into the electrolyte (1 M $Zn(OTF)_2$ in 50%PC/50%H_2O, denoted as Zn-PC-H_2O), we observed a relatively lower ACE of 95.1%, a life span of only 80 cycles (**Figure 1b**), and a dendritic Zn growth behavior (**Figure 6.2 f** and **Figure S6.12**). Moreover, a much higher overpotential (121 mV) was observed in Zn-PC-H_2O electrolyte, due to the absence of Li^+ ions.

6.2.2 Impact of Zn-Li-PC-H₂O electrolytes on HER and Zn corrosion

To understand the diverse Zn plating reversibility on $Ti_3C_2T_x$ in different electrolytes, the electrolyte structures need to be firstly explored. Liquid-state nuclear magnetic resonance (NMR) spectroscopy of ^{17}O and ^{67}Zn was performed to investigate the solvation structure of different electrolytes. In the spectrum measured on the Zn-H_2O electrolyte, two ^{17}O peaks which located at -2.87 ppm and 155.04 ppm were observed, corresponding to the ^{17}O signal in water and OTF^-, respectively. When Li^+ ions are introduced into the electrolyte (Zn-Li-H_2O), the ^{17}O signal of OTF^- shifted to upfield (154.87 ppm), suggesting enhanced shielding effect due to a weaker interaction between Zn^{2+}/Li^+ and OTF^- (**Figure 6.3 a**). In contrast, addition of PC leads to an upshift (downfield) of the ^{17}O peak (OTF^-) to 157.03 ppm and 156.30 ppm in Zn-PC-H_2O, and Zn-Li-PC-H_2O, respectively. This shift suggests that the presence of PC enhances the interactions between Zn^{2+} and OTF^-, likely due to a stronger ion-pairing effect facilitated by the reduced dielectric constant of solvent[40]. Additionally, substantial downshift of the ^{17}O signal in H_2O from -3.83 ppm (Zn-Li-H_2O) to -5.33 ppm (Zn-Li-PC-H_2O) was observed, attributed to the reduced hydrogen bond in water due to PC-H_2O interaction (**Figure 6.3 b**), which is conducive to alleviating HER. Furthermore, as shown in **Figure 6.3 c**, the ^{67}Zn signal displayed significant broadening in Zn-PC-H_2O and Zn-Li-PC-H_2O electrolyte, indicating a reduced Zn^{2+} mobility due to a stronger interaction between Zn^{2+} and OTF^- with the introduction of PC[7].

6

Figure 6.3 (a) and (b) ^{17}O NMR spectra for different electrolytes (Zn-H$_2$O, Zn-Li-H$_2$O, Zn-PC-H$_2$O, and Zn-Li-PC-H$_2$O). (c) ^{67}Zn NMR spectra for different electrolytes. (d) Linear polarization curves in different electrolytes at a scan rate of 5 mV s^{-1}. (e) Tafel polarization plots and (f) corresponding linear fitted region.

The HER and Zn corrosion process in aqueous electrolytes determine the CE and cycling stability of ZIBs. The HER behavior in different electrolytes was investigated by linear sweep voltammetry (LSV) experiments (**Figure 6.3 d**). The Zn-Li-PC-H$_2$O electrolyte demonstrated the most negative HER onset potential (-1.23 V vs. Ag) and the lowest HER current densities, which is followed by the Zn-PC-H$_2$O, Zn-Li-H$_2$O and Zn-H$_2$O electrolytes, indicative of the synergistic effect of Li-salt and PC on suppressing the HER. **Figure 6.3 e** and **Figure 6.3 f** showed the Tafel polarization plots and the corresponding fitted linear portion in different electrolytes. Typically, a higher exchange current density and a lower Tafel slope suggests stronger Zn corrosion[41]. In the Zn-Li-PC-H$_2$O electrolyte, the corrosion of Zn metal can be partially inhibited, as indicated by the higher Tafel slope (75.9 mV dec^{-1}), compared to that in Zn-Li-H$_2$O (39.1 mV dec^{-1}), Zn-PC-H$_2$O (37.5 mV dec^{-1}), and Zn-H$_2$O (19.3 mV dec^{-1}) electrolyte. This improvement on the HER and corrosion behavior in Zn-Li-PC-H$_2$O electrolyte is beneficial for achieving better cycling stability.

6.2.3 Function of adding PC in Zn-Li-H$_2$O electrolyte and the SEI formation

To better understand the influence of the electrolytes on the deposition behavior of Zn on Ti$_3$C$_2$T$_x$, we performed XPS to investigate the surface of MXene after Zn plating/stripping for 3 cycles in Zn-H$_2$O, Zn-Li-H$_2$O and Zn-Li-PC-H$_2$O electrolytes. **Figure 6.4 a-c** shows the C1s, F1s and Zn2p spectra of Ti$_3$C$_2$T$_x$ in Zn-H$_2$O and Zn-Li-H$_2$O. The C1s spectra were fitted with five peaks, corresponding to C-Ti (282.0 eV), C-Ti-O (283.3 eV), C-C/C-H (284.8

eV), C-O (286.3 eV), and O-C=O (288.7 eV) (**Figure 6.4 a**), matching well with the C1s peaks of original $Ti_3C_2T_x$ film (**Figure S6.3**). In addition, the F1s spectra can be deconvoluted into Ti-F (685.1 eV) and Al-F (686.0 eV) signals, respectively, which are commonly observed in pure $Ti_3C_2T_x$ (**Figure 6.4 b**). Therefore, no SEI layer was formed on $Ti_3C_2T_x$ after cycling in either $Zn-H_2O$ or $Zn-Li-H_2O$ electrolyte. The peak observed at 1045.3 eV and 1022.1 eV in the XPS spectrum (**Figure 6.4 c**) represents the binding energies (BE) associated with the Zn2p1/2 and Zn2p3/2 orbitals, respectively, due to the intercalated Zn^{2+} into $Ti_3C_2T_x$. Moreover, no significant difference in the C1s, F1s and Zn2p spectra were observed between the surface of $Ti_3C_2T_x$ cycled in $Zn-H_2O$ and the one cycled in $Zn-Li-H_2O$, suggesting that the introduction of Li-salt has a negligible impact on interfacial chemistry.

In contrast to the $Zn-H_2O$ and $Zn-Li-H_2O$ electrolytes, when PC is introduced into the $Zn-Li-H_2O$ aqueous electrolyte, a SEI layer is formed in the $Zn-Li-PC-H_2O$ system. Introducing PC into the Zn^{2+} aqueous electrolyte as co-solvent can facilitate the PC and anions to enter the primary solvation sheath, which are adsorbed and decomposed on the electrode surface, and thus contribute to SEI formation[7,42]. In this case, the C1s spectrum of the $Ti_3C_2T_x$ cycled in $Zn-Li-PC-H_2O$ electrolyte (**Figure 6.4 d**) can be fitted into seven peaks, corresponding to the C-Ti (281.9 eV), C-Ti-O (283.8 eV), C-C/C-H (284.8 eV), C-O (285.9 eV), O=C (288.1 eV), O-C=O (289.0 eV) and C-F* (289.9 eV), respectively[32,43]. The appearance of C=O and C-F* clearly indicates the formation of an organic SEI layer on the MXene surface after cycling in $Zn-Li-PC-H_2O$ electrolyte. Additional support is found in the F1s spectrum, where an extra peak located at 683.6 eV can be observed on $Ti_3C_2T_x$ in $Zn-Li-PC-H_2O$ that we attribute to ZnF_2 and is the result of the reduction of OTF⁻ (**Figure 6.4 e**)[13]. Furthermore, the Zn2p1/2 and Zn2p3/2 peak located at 1044.6 eV and 1021.6 eV, respectively (**Figure S6.13**), show a downshift compared to that observed in $Zn-H_2O$ and $Zn-Li-H_2O$, which may be explained by instrumental factors such as a charge shift or a different interaction between Zn^{2+} and $Ti_3C_2T_x$ on the surface[20].

 XPS in combination with depth profiling using Ar^+ etching was utilized to characterize the SEI and indicates that the SEI layer is very thin. After sputtering for only 10 s, roughly corresponding to 5 nm, the intensity of C-C (C-H), C=O and C-F* of C1s signal as well as that of the Zn-F of F1s signal decreased dramatically, indicating a thin layer of organic-inorganic hybrid SEI (**Figure 6.4 d-e**). Moreover, the results of the Ti2p spectra are consistent with the formation of a thin SEI. **Figure S6.13** shows the high-resolution Ti2p and Zn2p XPS depth profiling of $Ti_3C_2T_x$ after 3 cycles in $Zn-Li-PC-H_2O$ electrolyte. The intensity of the Ti2p peaks is enhanced with increased etching time (**Figure S6.13 a**), which also suggests that the $Ti_3C_2T_x$ surface is covered by SEI layer. An upshift of 0.7 eV in BE to 1045.3 eV (Zn2p1/2) and 1022.3 eV (Zn2p3/2) of the Zn2p spectrum was observed, as the etching time

158

increased up to 10 s. In addition, the Zn2p signal remains after 350 s etching, indicating the intercalation of Zn^{2+} into $Ti_3C_2T_x$ in Zn-Li-PC-H_2O electrolyte.

Figure 6.4 High-resolution XPS spectra of $Ti_3C_2T_x$ after plating 1 mAh cm^{-2} of Zn at a current density of 1 mA cm^{-2} in Zn-H_2O and Zn-Li-H_2O electrolytes. (a) C1s spectra. (b) F1s spectra and (c) Zn2p spectra. XPS depth profiling of $Ti_3C_2T_x$ after Zn plating at 1 mAh cm^{-2} in the Zn-Li-PC-H_2O electrolyte. High-resolution XPS measurements of (d) C1s (e) F1s of $Ti_3C_2T_x$. The top panel shows a detailed scan before etching, the central panel shows a contour plot as a function of etching time where 1s of etching roughly corresponds to 0.5 nm of material. The bottom panel shows the scan after etching for 380 s. The dots indicate the measured points, and the continuous line indicates the fit to the data. (f) Arrhenius plots and corresponding activation energy values for $Ti_3C_2T_x$//Zn cell in Zn-H_2O, Zn-Li-H_2O, and Zn-Li-PC-H_2O. (g) The charge transfer resistance and activation energy values of the $Ti_3C_2T_x$//Zn asymmetric cell at room temperature in Zn-H_2O, Zn-Li-H_2O, and Zn-Li-PC-H_2O electrolyte.

The introduction of PC may affect cation intercalation within the MXene's interlayers and influence subsequent Zn plating behavior. To investigate this, we collected XRD patterns of $Ti_3C_2T_x$ after Zn deposition. As shown in **Figure S6.9**, a slight reduction in d-spacing to 1.49 nm in the Zn-Li-PC-H_2O electrolyte was observed compared to that seen in the Zn-H_2O and Zn-Li-H_2O electrolytes. This shift may suggest that existence of PC modified the intercalation behavior of MXene. Additionally, no obvious zinc hydroxysulfate (ZHS) byproduct was detected in all electrolytes, consistent with the idea that the anode-free

159

configuration effectively suppresses side reactions. Furthermore, the addition of PC to the electrolyte promoted Zn deposition preferentially on the (002) crystal plane, as evidenced by the increased intensity ratio of the (0 0 2) to (1 0 0) peaks in Zn-PC-H$_2$O and Zn-Li-PC-H$_2$O, compared to that in Zn-H$_2$O and Zn-Li-H$_2$O.

The interfacial kinetics was investigated by conducting electrochemical impedance spectroscopy (EIS) at different temperatures (**Figure S6.14, S6.15&S6.16**). Ti$_3$C$_2$T$_x$ showed the highest charge transfer resistance (283.8 Ω) in Zn-Li-PC-H$_2$O at 24°C, whereas much smaller resistances were observed in Zn-Li-H$_2$O (162.0 Ω) and Zn-H$_2$O (125.6 Ω), suggesting slower interfacial charge transfer in Zn-Li-PC-H$_2$O due to the SEI formation and/or the de-solvation process. The activation energy (E$_a$) values in different electrolytes are determined by the Arrhenius equation (**Figure 6.4 f**):

$$1/R_{ct} = A \exp(-E_a/RT)$$

where R_{ct} denotes the interfacial charge transfer resistance, A represents the pre-factor, R is the ideal gas constant and T is the absolute temperature. **Figure 6.4 g** displays the activation energy for different electrolytes. The activation energy is calculated to be 29.8 kJ mol^{-1} in Zn-Li-PC-H$_2$O electrolyte, which is almost three times as high as that in Zn-Li-H$_2$O (11.2 kJ mol^{-1}) and Zn-H$_2$O (10.6 kJ mol^{-1}). The increased activation energy can be attributed to the difficult de-solvation process when PC is present in the solvation sheath.

6.2.4 Function of Li-salt additives in the presence of SEI.

Furthermore, the impact of Li-salt on Zn plating behavior was investigated. In Zn-PC-H$_2$O electrolyte, Ti$_3$C$_2$T$_x$ MXene exhibited higher overpotential and lower CE, compared to Zn-Li-PC-H$_2$O electrolyte. Additionally, dendritic Zn plating behavior was shown. **Figure 6.5 d** illustrates the voltage profiles of the first three cycles for Zn plating/stripping in Zn-PC-H$_2$O and Zn-Li-PC-H$_2$O electrolytes. With the Zn-Li-PC-H$_2$O electrolyte, an initial CE of 84.3% was obtained, due to the reduction of PC and the OTF$^-$ anion. The CE increased to 95.9% for the second cycle after the SEI layer was formed. In contrast, the CE in Zn-PC-H$_2$O gradually increased from 85.8% for the initial cycle to 87.8% for the 3rd cycle, indicative of a less-stable SEI layer, if there is any, without Li-salt additive. Additionally, the overpotential of Zn plating significantly increased to -0.2 V after 20 cycles (**Figure S6.17**), suggesting sluggish kinetics without Li-salt additive.

The interfacial chemistry of Ti$_3$C$_2$T$_x$ in Zn-PC-H$_2$O was revealed by XPS results. **Figure 6.5 a** shows the high resolution C1s depth profiling spectra of Zn deposited Ti$_3$C$_2$T$_x$. In the Zn-PC-H$_2$O electrolyte, we can also observe the presence of organic SEI components (C=O and C-F*) due to the decomposition of OTF$^-$. Compared to Zn-H$_2$O and Zn-Li-H$_2$O, the existence

of SEI layer in Zn-PC-H$_2$O and Zn-Li-PC-H$_2$O electrolyte indicates that PC is essential for the generation of organic SEI layer. Additionally, a similar upshift of binding energy can be noticed in the Zn2p spectrum with increased etching time (**Figure 6.5 b**). However, no trace of ZnF$_2$ was observed in **Figure 6.5c**, differing from the Zn-Li-PC-H$_2$O electrolyte (See **Figure 6.4**). The ZnF$_2$ component is known as a superior Zn^{2+} conductor with a low Zn diffusion energy barrier of only 0.45 eV[44], which is beneficial for the homogeneous distribution of Zn^{2+}[32]. The existence of ZnF$_2$ in the SEI layer explains the improved interfacial kinetics observed with the Zn-Li-PC-H$_2$O electrolytes than with Zn-PC-H$_2$O, which is indicated by the lower interfacial charge transfer resistance observed in Nyquist plot (**Figure 6.5 e**). The Zn deposition behavior with a reduced Li-salt concentration of 0.1 M was also examined (**Figure S6.18**). This lower concentration resulted in an ACE of 91.9 % over 80 cycles, along with a higher overpotential, indicating reduced stability in Zn plating/stripping and slower reaction kinetics as compared to the 1 M Li-salt.

Therefore, the Li-salt additive has demonstrated its significant role in the formation of highly conductive ZnF$_2$ inorganic SEI layer with the co-existence of PC, without which a dendritic growth of Zn occurs (schematic illustration in **Figure 6.5 f**). Based on previous results and discussions, it is reasonable to conclude that the co-addition of PC and Li-salt into Zn^{2+} aqueous electrolyte is essential to generate a ZnF$_2$ containing organic-inorganic hybrid SEI layer that can effectively modulate the homogenous Zn plating behavior on Ti$_3$C$_2$T$_x$ surface. Moreover, the as-formed SEI layer directly regulates uniform Zn deposition, rather than redistributes the Zn^{2+} ions indirectly by influencing the intercalation behavior. Furthermore, we evaluated the Zn plating/stripping behavior on Ti$_3$C$_2$T$_x$ in Zn-LiOTF-PC-H$_2$O electrolytes, achieving an ACE of 97.0 %, over 115 cycles (**Figure S6.10**). This demonstrates that the type of anion has little impact on the Zn deposition reversibility in the presence of PC. Also, the presence of both Li-salt and PC is essential for achieving high CE. In summary, the Zn deposition behavior on Ti$_3$C$_2$T$_x$ shows significant dependence on the electrolyte systems. Specifically, the open interlayer of Ti$_3$C$_2$T$_x$ enables the intercalation of cations into the interlayer spacing, which may result in different surface charge distribution than on a metal substrate. As such, Li$^+$ ions, which can effectively smooth the Zn growth on metal surface when serving as co-ions of Zn^{2+}, do not function properly for improving the reversibility of Zn deposition on 2D Ti$_3$C$_2$T$_x$ MXene. Instead, the addition of Li-salt leads to the formation of large irregular Zn agglomerations during Zn plating. However, when Li-salt is introduced as the additive together with PC, although the intercalation behavior is unaltered, the Li$^+$ ions assist in the formation of an organic-inorganic hybrid SEI layer. The *in-situ* formed ZnF$_2$-containing SEI layer can effectively guide the uniform deposition of Zn (**Figure 6.1 c**), resulting in a highly reversible Zn plating behavior with an ACE of 96.8% over 150 cycles (**Figure 6.1 b**). When PC is introduced into the aqueous electrolyte alone, though the SEI

6

layer also exists, the absence of ZnF_2 in the SEI layer cannot effectively suppress dendritic Zn growth due to the slow interfacial charge transfer process (**Figure 6.5 f**). Noteworthy, while our findings highlight the compatibility of the electrolyte system with $Ti_3C_2T_x$ MXene, further investigation is needed to assess the compatibility of these optimized electrolytes with other MXenes.
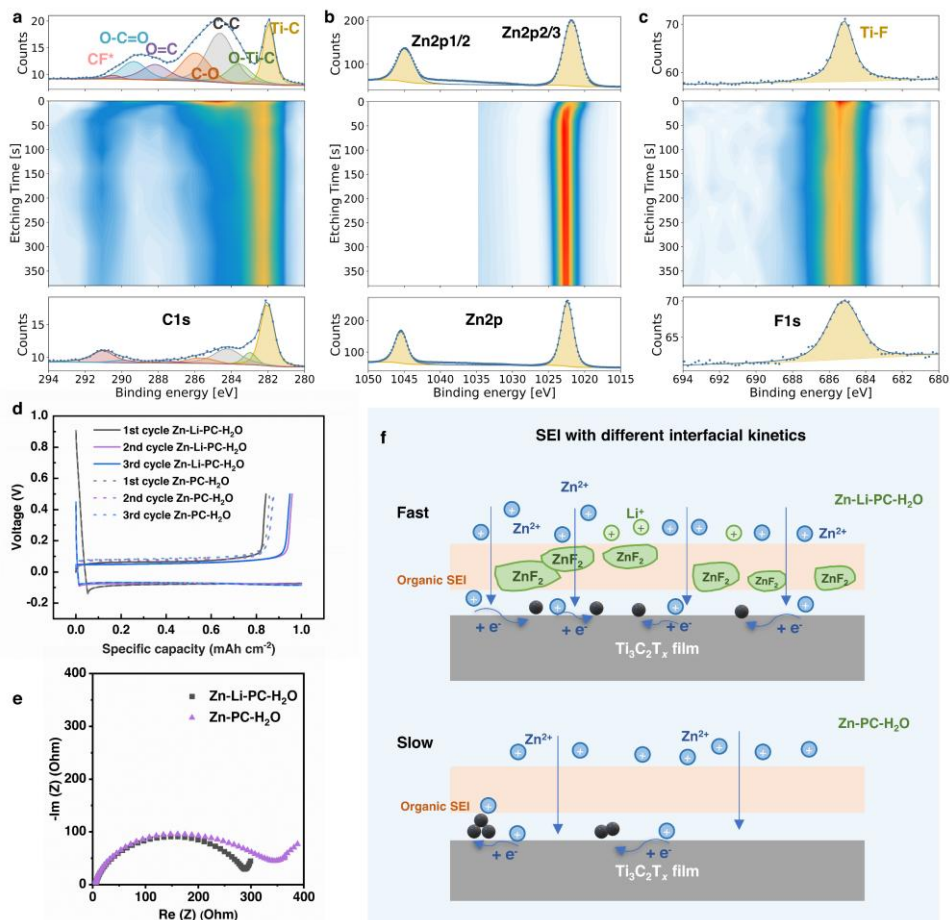
Figure 6.5 XPS depth profiling of $Ti_3C_2T_x$ after plating 1 mAh cm^{-2} of Zn at a current density of 1 mA cm^{-2} in Zn-PC-H$_2$O electrolyte. High resolution XPS (a) C1s (b) Zn2p (c) F1s of $Ti_3C_2T_x$. (d) Charge/discharge curves of $Ti_3C_2T_x$//Zn cell in Zn-PC-H$_2$O and Zn-Li-PC-H$_2$O electrolyte of the first 3 cycles (Capacity: 1 mAh cm^{-2}, current density: 1 mA cm^{-2}). (e) Nyquist plots of the $Ti_3C_2T_x$//Zn asymmetric cell at room temperature in Zn-PC-H$_2$O and Zn-Li-PC-H$_2$O electrolyte. (f) Schematic illustration of the influence of diffusion interfacial kinetics in SEI on Zn deposition process on $Ti_3C_2T_x$ MXene in Zn-PC-H$_2$O electrolytes and Zn-Li-PC-H$_2$O electrolytes.

6.3 Conclusion

Our study demonstrates the importance of rational electrolyte design in enhancing the performance of MXene-based anode-free AZMBs. In our pursuit of enhancing the performance of anode-free AZMBs, we initially explored the application of Li-salt additive to improve Zn deposition behavior on $Ti_3C_2T_x$ MXene surfaces through the electrostatic shielding effect. Contrary to our expectations, this led to unstable cycling performance and the formation of irregular Zn agglomerations. However, this setback prompted further investigation into the role of electrolyte additives. Through our experiments, we discovered the critical role of Li-salt and PC co-additives in $Zn(OTF)_2$ electrolytes. The introduction of PC reinforced Zn^{2+} coordination with OTF^- anion and facilitated the formation of an organic SEI layer, while Li-salt promoted the formation of ZnF_2-rich inorganic SEI layer with fast interfacial kinetics. The formation of this ZnF_2-containing organic/inorganic hybrid SEI layer guides a reversible and uniform Zn plating and suppresses the HER, resulting in an enhanced ACE of 96.8% for Zn plating/stripping over 150 cycles (a stabilized CE of 97.8 %). Our findings highlight the differences in electrolyte design for uniform Zn plating on 2D and bulk metallic substrate and provide valuable guidelines for designing electrolytes for reversible ion plating on 2D and layered materials. A crucial future direction is to comprehensively evaluate the full cell performance of MXene-based anode-free AZMBs to determine how enhanced Zn deposition reversibility translates into electrochemical performance, cycling stability for practical applications.

6.4 Supplementary Information

Methods

Materials synthesis: The $Ti_3C_2T_x$ was synthesized by etching Ti_3AlC_2 precursor (purchased from 11 Technology Co. Ltd.) using a mixture of LiF and HCl. Briefly, 1.6 g of LiF was slowly added to 30 mL of 9 M HCl under stirring, after which 1 g of Ti_3AlC_2 powder was slowly added into the solution and continuously stirred at 35°C for 24 hours. The resulting solution was repeatedly centrifuged with deionized water until the pH reaches ~7. Afterward, the swollen $Ti_3C_2T_x$ slurry was separated from the mixture by centrifugation at 3500 rpm for 2 min. Finally, the delaminated $Ti_3C_2T_x$ colloidal dispersion could be obtained after ultrasonication for 1 h under the protection of Ar gas, which was followed by vacuum-assisted filtration to get self-freestanding $Ti_3C_2T_x$ film.

Electrochemical Characterization: $Ti_3C_2T_x$ films were directly used as working electrode for Zn deposition. Four different electrolytes are prepared by dissolving 1 M $Zn(OTF)_2$ in water, 1 M $Zn(OTF)_2$ in PC/Water (1:1 v:v), 1 M $Zn(OTF)_2$ and 1 M LiTFSI in Water, and 1

M Zn(OTF)$_2$ and 1 M LiTFSI in PC/Water (1:1 v:v), respectively. Electrochemical analyses were performed assembling CR2032 coin cell batteries with GF-A films separators in Ti$_3$C$_2$T$_x$//Zn half-cell. The galvanostatic charging-discharging processes were carried out on a Lanhe electrochemical workstation. To evaluate the Coulombic efficiency (CE) of Zn plating/stripping, a certain amount of Zn (1 mA cm^{-2}, 1 mA cm^{-2} for 1 h) were deposited on the Ti$_3$C$_2$T$_x$ electrode and charged to 0.5 V for stripping. Cyclic voltammetry measurements were collected at a scan rate of 0.5 mV s^{-1} on Biologic VSP-300 potentiostat. EIS was tested at a frequency range varying from 0.001 to 100 kHz with an amplitude of 5 mV. The activation energy can be calculated from the EIS performed at different temperatures (ranging from 24°C to 50°C). Tafel plots were collected by Linear scanning voltammetry from -1.3 V to -1.0 V (vs. Ag) at a scan rate of 1 mV s^{-1} with a three-electrode set-up, where Carbon rod and Ag wire was employed as counter and reference electrode, respectively.

Materials Characterization: Zn deposition morphology on Ti$_3$C$_2$T$_x$ film was studied by SEM analysis using JEOL JSM-6010LA equipment (SED mode) at 10 kV. Additionally, energy dispersive X-ray (EDX) elemental maps were performed at an accelerating voltage of 15 kV to gain more information about the element's distribution. X-ray diffraction (XRD) analysis was employed to examine the interlayer space of Ti$_3$C$_2$T$_x$, utilizing an X'Pert Pro diffractometer (PANalytical, operated at 45 kV and 40 mA) with Cu-Kα radiation (λ = 1.54 Å). NMR spectra were recorded using a Bruker 600 MHz (14.1 T) Ascend magnet equipped with a NEO console. ^{1}H, ^{17}O and ^{67}Zn had Larmor frequencies of 600.13, 81.36 and 37.55 MHz, respectively, at that field strength. The Zn(OTF)$_2$ and LiTFSI salts were dissolved in deuterated oxide (D$_2$O) for NMR measurements. 90-degree pulse lengths of 16.2,14.7 and 25.0 μs were determined for ^{1}H, ^{17}O and ^{67}Zn. ^{1}H spectra were collected using a 30º excitation pulse followed by acquisition with a recycle delay of 2 s and 4 scans. ^{17}O and ^{67}Zn NMR spectra were recorded using standard single pulse experiment (Bloch decay) by collecting 1024 scans with a recycle delay time of 0.5 s and 0.2 s, respectively. Raman spectroscopy was conducted using the Renishaw instrument with a 488 nm laser. XPS measurements were performed with a ThermoFisher K-Alpha spectrometer to investigate the chemical state of the elements present. The spectrometer is equipped with a focused monochromatic Al kα source (1486.6 eV) anode operating at 36 W (12 kV, 3 mA), a flood gun operating at 1 V, 100 μA, and the base pressure in the analysis chamber is approximately 2×10^{-9} mbar. The spot-size is approximately 800 x 400 μm^2. Etching was performed using a 3 kV Ar$^+$ ion gun at a rate of approximately 0.5 nm s^{-1} as calibrated on Ta$_2$O$_5$. The sample was etched for (cumulative) 10, 20, 40, 60, 100, 140, 180, 220, 260, 300, 340 and 380 s and the measurements were performed in 'snap mode' with the pass energy of the analyzer set to 120 eV. Detailed measurements before and after etching were performed in 'scan mode' with a pass energy of 50 eV. Charge referencing was performed using the hydrocarbon C1s line at

6

284.8 eV as the reference. All peaks were fitted using 70% Gaussian and 30% Lorentzian line shapes (weighted least-squares fitting method) and nonlinear Shirley-type background using the ThermoFisher Avantage software.

Figure S 6.1 Digital Photograph of the Ti$_3$C$_2$T$_x$ film.
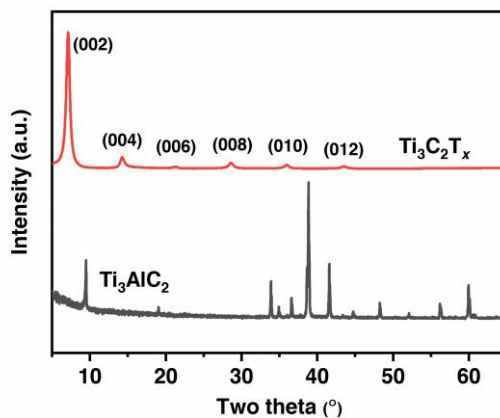
Figure S 6.2 XRD patterns of Ti$_3$AlC$_2$ and Ti$_3$C$_2$T$_x$ film.
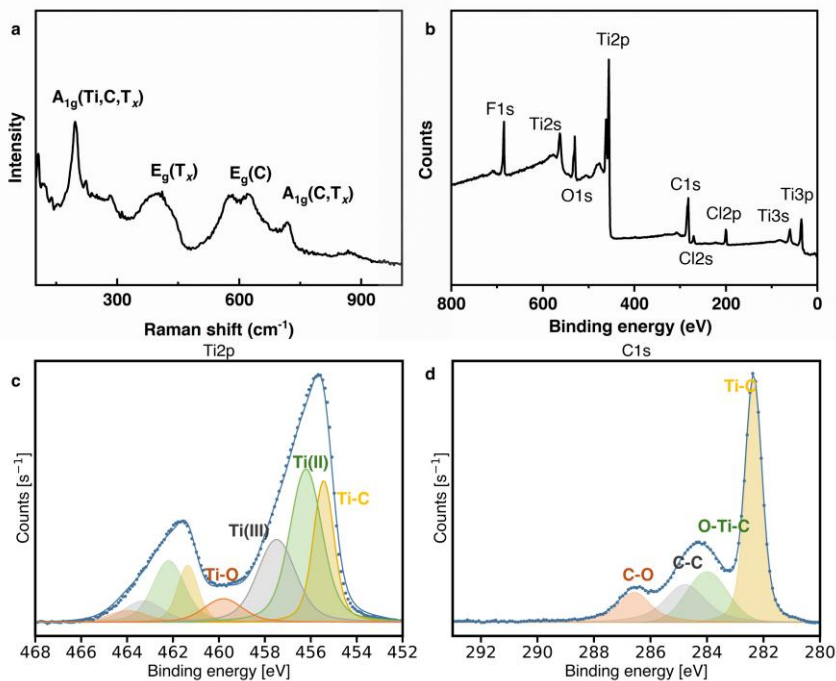
Figure S 6.3 Raman and XPS spectroscopy of Ti$_3$C$_2$T$_x$ film. (a) Raman Spectroscopy. (b) XPS Survey of Ti$_3$C$_2$T$_x$. (c) High-resolution Ti2p and (d) high-resolution C1s XPS spectrum of Ti$_3$C$_2$T$_x$.
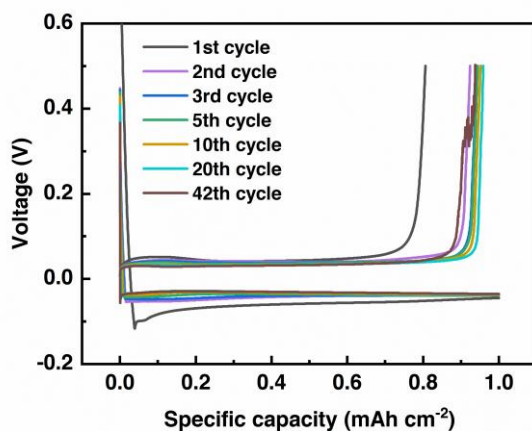
Figure S 6.4 Selected charge/discharge curves of Ti$_3$C$_2$T$_x$//Zn cell in Zn-H$_2$O electrolyte (Capacity: 1 mAh cm^{-2}, current density: 1 mA cm^{-2}).

Enhancing Zn Deposition Reversibility on MXene Current Collectors by Forming ZnF2-Containing Solid-Electrolyte Interphase for Anode-Free Zinc Metal Batteries
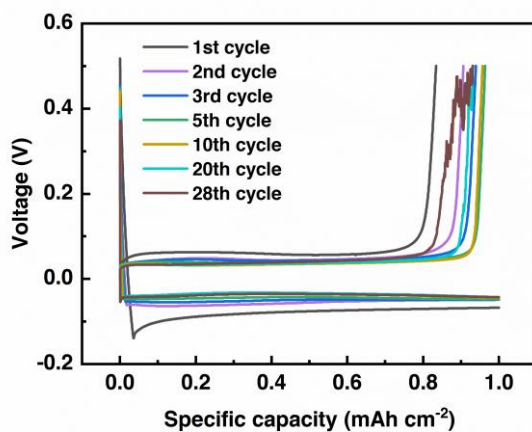
Figure S 6.5 Selected charge/discharge curves of Ti$_3$C$_2$T$_x$ //Zn cell in Zn-Li-H$_2$O electrolyte (Capacity: 1 mAh cm^{-2}, current density: 1 mA cm^{-2}).
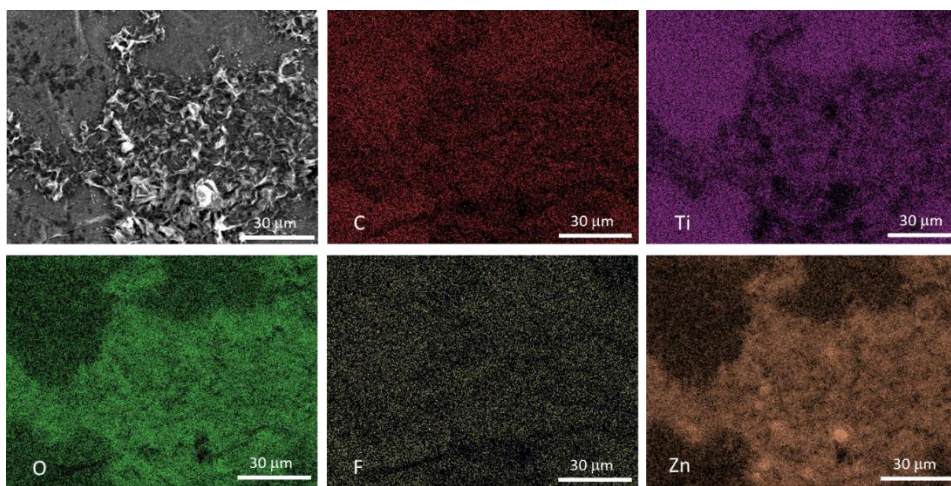
Figure S 6.6 SEM-EDS element mapping of Ti$_3$C$_2$T$_x$ after plating 1 mAh cm^{-2} of Zn at 1 mA cm^{-2} in Zn-H$_2$O.

6

Enhancing Zn Deposition Reversibility on MXene Current Collectors by Forming ZnF2-Containing Solid-Electrolyte Interphase for Anode-Free Zinc Metal Batteries
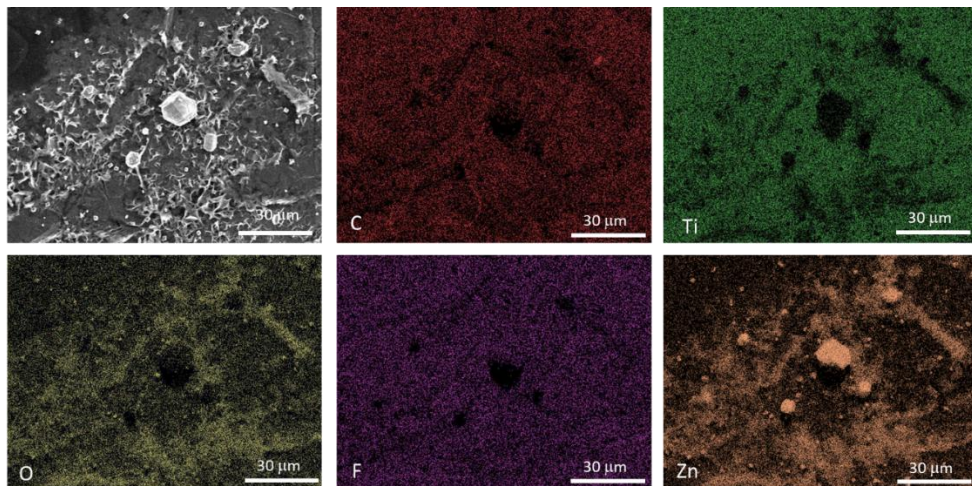
Figure S 6.7 SEM-EDS element mapping of $Ti_3C_2T_x$ after plating 1 mAh cm^{-2} of Zn at 1 mA cm^{-2} in Zn-Li-H$_2$O.
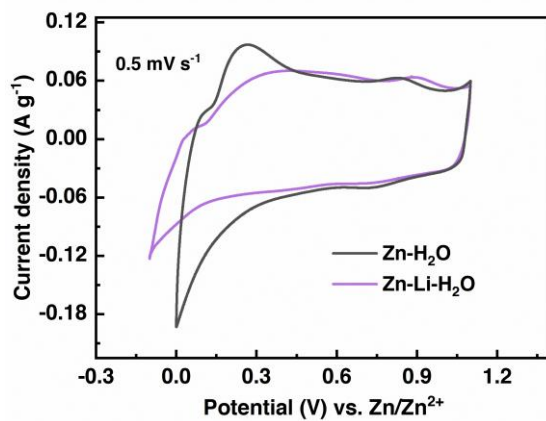
Figure S 6.8 The CV curves of $Ti_3C_2T_x$//Zn cell in Zn-H$_2$O and Zn-Li-H$_2$O electrolyte (3rd cycle) showing the intercalative behavior at a scan rate of 0.5 mV s^{-1}.
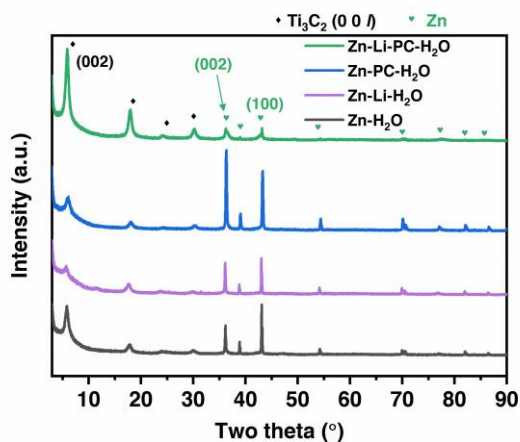
Figure S 6.9 The XRD patterns of $Ti_3C_2T_x$ deposited with 1mAh cm^{-2} Zn in different electrolytes. The symbols indicate the material to which the XRD peak corresponds to.
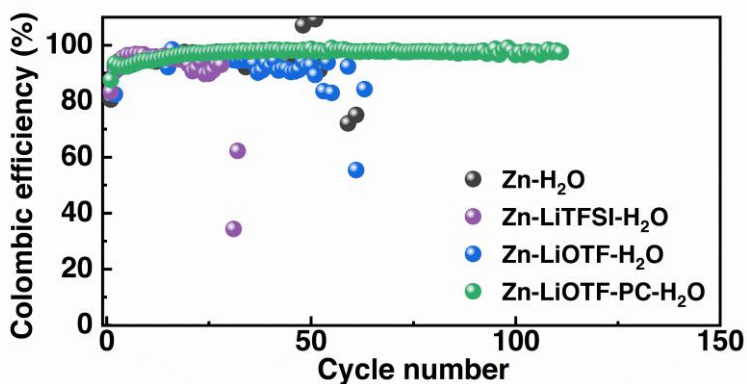
Figure S 6.10 Coulombic efficiency measurements of $Ti_3C_2T_x$@Zn cell with a deposition capacity of 1 mAh cm^{-2} at a current density of 1 mA cm^{-2} in Zn-H$_2$O, Zn-Li-H$_2$O, Zn-LiOTF-H$_2$O, Zn-LiOTF-PC-H$_2$O electrolyte.

6

Figure S 6.11 SEM-EDS element mapping of $Ti_3C_2T_x$ after plating 1 mAh cm^{-2} of Zn at 1 mA cm^{-2} in Zn-Li-PC-H$_2$O electrolyte.
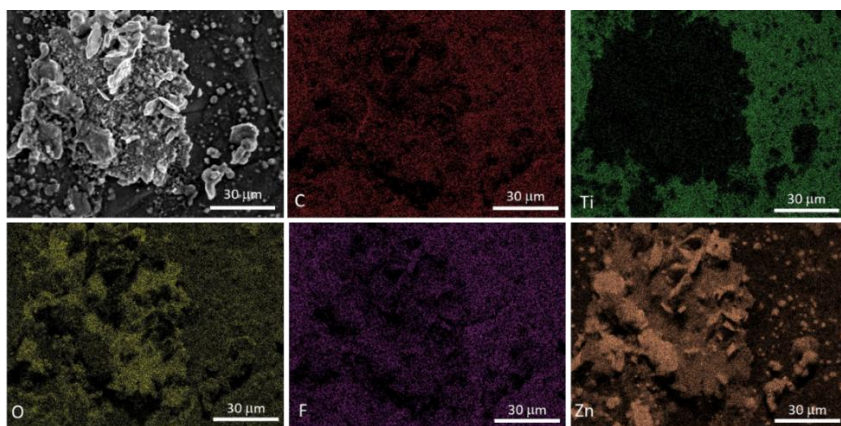
Figure S 6.12 SEM-EDS element mapping of $Ti_3C_2T_x$ after plating 1 mAh cm^{-2} of Zn at 1 mA cm^{-2} in Zn-PC-H$_2$O electrolyte.

Enhancing Zn Deposition Reversibility on MXene Current Collectors by Forming ZnF2-Containing Solid-Electrolyte Interphase for Anode-Free Zinc Metal Batteries
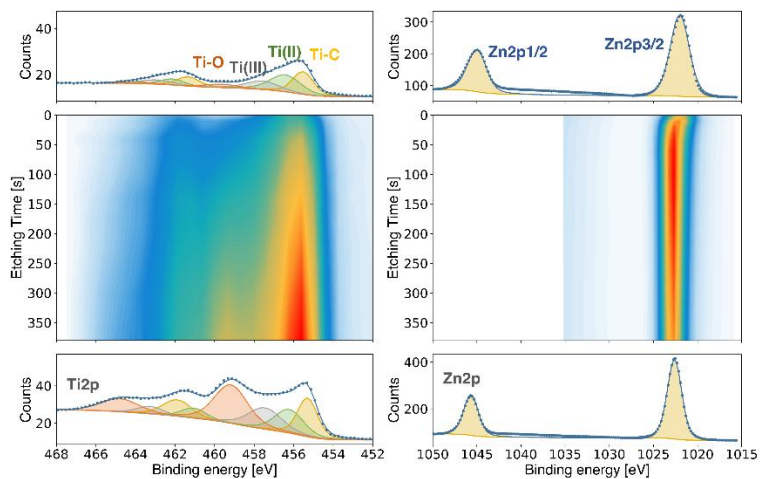
Figure S 6.13 (a) Ti2p and (b) Zn2p XPS depth profiling of $Ti_3C_2T_x$ after plating 1 mAh cm^{-2} of Zn at a current density of 1 mA cm^{-2} in Zn-Li-PC-H$_2$O electrolyte.
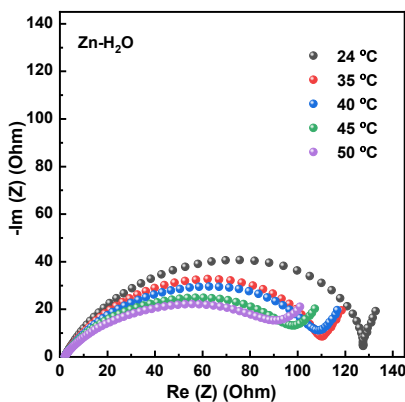
Figure S 6.14 Nyquist plots of the $Ti_3C_2T_x$//Zn asymmetric cell at different temperatures in Zn-H$_2$O electrolyte.

6

Enhancing Zn Deposition Reversibility on MXene Current Collectors by Forming ZnF2-Containing Solid-Electrolyte Interphase for Anode-Free Zinc Metal Batteries
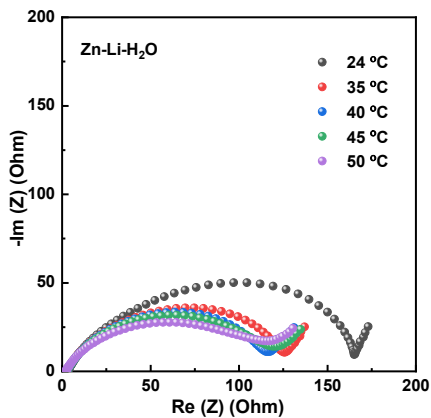
Figure S 6.15 Nyquist plots of the Ti$_3$C$_2$T$_x$//Zn asymmetric cell at different temperatures in Zn-Li-H$_2$O electrolyte.
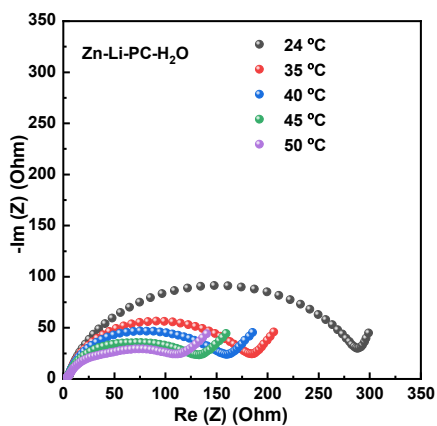
Figure S 6.16 Nyquist plots of the Ti$_3$C$_2$T$_x$//Zn asymmetric cell at different temperatures in Zn-Li-PC-H$_2$O electrolyte.

6

Enhancing Zn Deposition Reversibility on MXene Current Collectors by Forming ZnF2-Containing Solid-Electrolyte Interphase for Anode-Free Zinc Metal Batteries

Figure S 6.17 Charge/discharge curves of Ti$_3$C$_2$T$_x$//Zn cell in Zn-PC-H$_2$O electrolyte of cycle 20th and 50th.
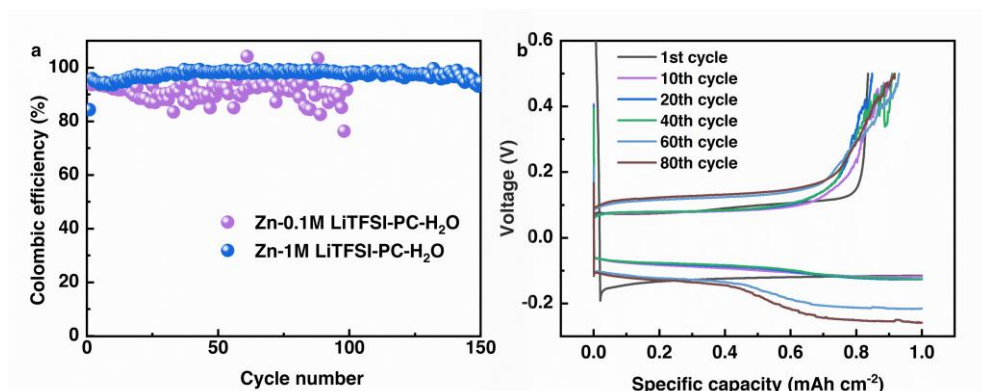
Figure S 6.18 (a) Coulombic efficiency measurements of Ti$_3$C$_2$T$_x$//Zn cell with a deposition capacity of 1 mAh cm^{-2} at a current density of 1 mA cm^{-2} in Zn-Li-PC-H$_2$O electrolyte with different concentration of LiTFSI additive. and (b) Charge/discharge curves of Ti$_3$C$_2$T$_x$//Zn cell in Zn-0.1M Li-PC-H$_2$O electrolyte.

Table S 6.1 Inductively Coupled Plasma (ICP) analysis of the Zn-Li-H$_2$O electrolyte before and after the first discharge process.

Sample (electrolyte)	Molar concentration of Li$^+$ in the electrolyte
1M Zn-Li-H$_2$O pristine	1.16 M
1M Zn-Li-H$_2$O after first discharging	1.075 ±0.015 M

6

6.5 Reference

1   N. Kittner, F. Lill and D. Kammen, *Nat. Energy*, 2017, **2**, 17125.

2   M. Li, J. Lu, Z. Chen and K. Amine, *Adv. Mater.*, 2018, **30**, 1800561.

3   R. Schmuch, R. Wagner, G. Hörpel, T. Placke and M. Winter, *Nat. Energy*, 2018, **3**, 267–278.

4   B. Dunn, H. Kamath and J. Tarascon, *Science*, 2011, **334**, 928–935.

5   D. Chao, W. Zhou, F. Xie, C. Ye, H. Li, M. Jaroniec and S.-Z. Qiao, *Sci. Adv.*, 2020, **6**, eaba4098.

6   X. Zhang, L. Zhang, X. Jia, W. Song and Y. Liu, *Nano-Micro Lett.*, 2024, **16**, 75.

7   F. Ming, Y. Zhu, G. Huang, A. Emwas, H. Liang, Y. Cui and H. Alshareef, *J. Am. Chem. Soc.*, 2022, **144**, 7160–7170.

8   J.-G. Zhang, *Nat. Energy*, 2019, **4**, 637–638.

9   O. Blumen, G. Bergman, K. Schwatrzman, S. Harpaz, S. H. Akella, M. S. Chae, N. Bruchiel-Spanier, N. Shpigel and D. Sharon, *J. Mater. Chem. A*, 2023, **11**, 19970–19980.

10   Z. Cao, P. Zhuang, X. Zhang, M. Ye, J. Shen and P. Ajayan, *Adv. Energy Mater.* **2020**, 10, 2001599.

11   M. Naguib, V. N. Mochalin, M. W. Barsoum and Y. Gogotsi, *Adv. Mater.*, 2014, **26**, 992–1005.

12   X. Li, Z. Huang, C. E. Shuck, G. Liang, Y. Gogotsi and C. Zhi, *Nat. Rev. Chem.*, 2022, **6**, 389–404.

13   T. Wang, K. Yao, K. Li and J. S. Yu, *Energy Storage Mater.*, 2023, **62**, 102921.

14   Y. Tian, Y. An, C. Wei, B. Xi, S. Xiong, J. Feng and Y. Qian, *ACS Nano*, 2019, **13**, 11676–11685.

15   H. Li, R. Zhao, W. Zhou, L. Wang, W. Li, D. Zhao and D. Chao, *JACS Au*, 2023, **3**, 2107–2116.

16   R. Guo, C. Chen, L. J. Bannenberg, H. Wang, H. Liu, M. Yu, Z. Sofer, Z. Lei and X. Wang, *Small Methods*, 2023, **7**, 2201683.

6

17   T. S. Mathis, K. Maleski, A. Goad, A. Sarycheva, M. Anayee, A. C. Foucher, K. Hantanasirisakul, C. E. Shuck, E. A. Stach and Y. Gogotsi, *ACS Nano*, 2021, **15**, 6420–6429.

18   N. Zhang, S. Huang, Z. Yuan, J. Zhu, Z. Zhao and Z. Niu, *Angew. Chem. Int. Ed.*, 2021, **60**, 2861–2865.

19   F. Tian, F. Wang, W. Nie, X. Zhang, X. Xia, L. Chang, Z. Pang, X. Yu, G. Li, S. Hu, Q. Xu, H.-Y. Hsu, Y. Zhao, L. Ji, X. Lu and X. Zou, *Angew. Chem. Int. Ed.*, 2024, **63**, e202408996.

20   X. Li, Q. Li, Y. Hou, Q. Yang, Z. Chen, Z. Huang, G. Liang, Y. Zhao, L. Ma, M. Li, Q. Huang and C. Zhi, *ACS Nano*, 2021, **15**, 14631–14642.

21   W. Yang, J. Yang, J. J. Byun, F. P. Moissinac, J. Xu, S. J. Haigh, M. Domingos, M. A. Bissett, R. A. W. Dryfe and S. Barg, *Adv. Mater.*, 2019, **31**, 1902725.

22   Z. Wang, C. Wei, H. Jiang, Y. Zhang, K. Tian, Y. Li, X. Zhang, S. Xiong, C. Zhang and J. Feng, *Adv. Mater.*, 2024, **36**, 2306015.

23   J. Zhou, M. Xie, F. Wu, Y. Mei, Y. Hao, L. Li and R. Chen, *Adv. Mater.*, 2022, **34**, 2106897.

24   H. Chen, M. Chen, W. Zhou, X. Han, B. Liu, W. Zhang and J. Chen, *ACS Appl. Mater. Interfaces*, 2022, **14**, 6876–6884.

25   Y. Tian, Y. An, C. Liu, S. Xiong, J. Feng and Y. Qian, *Energy Storage Mater.*, 2021, **41**, 343–353.

26   Z. Khan, D. Kumar and X. Crispin, *Adv. Mater.*, 2023, **35**, 2300369.

27   S. Guo, L. Qin, T. Zhang, M. Zhou, J. Zhou, G. Fang and S. Liang, *Energy Storage Mater.*, 2021, **34**, 545–562.

28   D. Wang, Q. Li, Y. Zhao, H. Hong, H. Li, Z. Huang, G. Liang, Q. Yang and C. Zhi, *Adv.Energy Mater.* 2022, **12**,2102707.

29   L. Cao, D. Li, E. Hu, J. Xu, T. Deng, L. Ma, Y. Wang, X. Yang and C. Wang, *J.Am. Chem. Soc.*, 2020, **142**, 21404–21409.

30   M. Han, T. Li, D. Li and H. Yang,*Batteries Supercaps,* 2023, **6**, e202200560.

31   Y. Li, Z. Yu, J. Huang, Y. Wang and Y. Xia, *Angew. Chem. Int. Ed*. 2023, **62**,*e202309957.*

6

32   L. Cao, D. Li, T. Pollard, T. Deng, B. Zhang, C. Yang, L. Chen, J. Vatamanu, E. Hu, M. Hourwitz, L. Ma, M. Ding, Q. Li, S. Hou, K. Gaskell, J. Fourkas, X. Yang, K. Xu, O. Borodin and C. Wang, *Nat. Nanotechnol.* 2021, **16**,902.

33   Y. Chu, S. Zhang, S. Wu, Z. Hu, G. Cui and J. Luo, *Energy Environ. Sci.* 2021, **14**, 3609.

34   X. Guo, Z. Zhang, J. Li, N. Luo, G. Chai, T. Miller, F. Lai, P. Shearing, D. Brett, D. Han, Z. Weng, G. He and I. Parkin, *ACS Energy Lett.*, 2021, **6**, 395–403.

35   X. Wang, T. S. Mathis, K. Li, Z. Lin, L. Vlcek, T. Torita, N. C. Osti, C. Hatter, P. Urbankowski, A. Sarycheva, M. Tyagi, E. Mamontov, P. Simon and Y. Gogotsi, *Nat. Energy*, 2019, **4**, 241–248.

36   M. Alhabeb, K. Maleski, B. Anasori, P. Lelyukh, L. Clark, S. Sin and Y. Gogotsi, *Chem. Mater.*, 2017, **29**, 7633–7644.

37   F. Ding, W. Xu, G. L. Graff, J. Zhang, M. L. Sushko, X. Chen, Y. Shao, M. H. Engelhard, Z. Nie, J. Xiao, X. Liu, P. V. Sushko, J. Liu and J.-G. Zhang, *J. Am. Chem. Soc.*, 2013, **135**, 4450–4456.

38   M. Xue, X. Ren, Y. Zhang, J. Liu and T. Yan, *ACS Appl. Mater. Interfaces*, 2024, **16**, 33559–33570.

39   F. Li, Y. Liu, G.-G. Wang, S.-Y. Zhang, D.-Q. Zhao, K. Fang, H.-Y. Zhang and H. Y. Yang, *Chem. Eng. J.*, 2022, **435**, 135052.

40   X. Chen and Q. Zhang, *Acc. Chem. Res.*, 2020, **53**, 1992–2002.

41   S. Yang, A. Chen, Z. Tang, Z. Wu, P. Li, Y. Wang, X. Wang, X. Jin, S. Bai and C. Zhi, *Energy Environ. Sci.*, 2024, **17**, 1095–1106.

42   B. Kakoty, R. Vengarathody, S. Mukherji, V. Ahuja, A. Joseph, C. Narayana, S. Balasubramanian and P. Senguttuvan, *J. Mater. Chem. A*, 2022, **10**, 12597–12607.

43   P. H. Nguyen, D. H. Nguyen, D. Kim, M. K. Kim, J. Jang, W. H. Sim, H. M. Jeong, G. Namkoong and M. S. Jeong, *ACS Applied Mater. Interfaces*, 2022, **14**, 51487–51495.

44   D. Wang, H. Liu, D. Lv, C. Wang, J. Yang and Y. Qian, *Adv. Mater.*, 2023, **35**, 2207908.

6

7 Summary

Summary

Aqueous energy storage devices are gaining attention as safer and more cost-effective alternatives to conventional EES systems that use flammable organic electrolytes. Their high ionic conductivity also enables fast charge-discharge processes, making them suitable for high power applications. In this context, MXenes, particularly $Ti_3C_2T_x$, have emerged as promising electrode material because of their excellent electrical conductivity, hydrophilic surfaces, and tunable interlayer spacing that supports fast charge transport. Depending on the electrolyte environment, MXenes can store charge through EDL or pseudocapacitive mechanisms. The electrochemical performance is closely linked to how solvated ions adsorb onto MXenes' surface or intercalate into MXenes' interlayer spacing. However, the influence of ion solvation on MXenes' charge storage behavior in aqueous systems remains insufficiently understood.

This thesis addresses this knowledge gap by investigating how solvation of different charge carriers governs ion intercalation and charge transport in $Ti_3C_2T_x$ MXene. Chapters 2 and 3 investigate the charge storage behavior of $Ti_3C_2T_x$ MXene toward non-metallic cations, with a focus on the sustainable ammonium ion (NH_4^+). Chapter 2 investigates how ion solvation affects the intercalation behavior of ammonium (NH_4^+) and a series of tetraalkylammonium (TAA^+) ions, such as TMA^+, TEA^+, and TPA^+. These ions differ in size and solvation strength, offering a systematic platform to examine solvation-governed charge storage mechanisms. Small, hydrophilic NH_4^+ ions intercalate in a partially desolvated state, forming hydrogen bonds with surface terminations, their insertion induces negligible interlayer spacing change and yields EDL-like behavior. In contrast, the bulky, weakly solvated TAA cations, which often have hydrated sizes exceeding the MXene interlayer spacing, undergo reversible intercalation accompanied by substantial water co-insertion. This process results in pronounced interlayer spacing expansions (up to 20.7 Å) and distinct intercalative CV features. Importantly, the intercalative contribution to capacitance increases with alkyl chain length, which possibly correlates with reduced hydration and more compact solvation shells of larger TAA cations. Unlike metallic ions, which typically require desolvation prior to insertion, the reversible intercalation of hydrophobic, weakly solvated non-metallic cations in MXene may rely on water co-insertion to overcome size constraints or stabilize the MXene structure.

Building on the findings from Chapter 2, which demonstrated the reversible intercalation of non-metallic ammonium ions into $Ti_3C_2T_x$ MXene with moderate capacitance and limited rate performance, Chapter 3 aims to address these performance bottlenecks. The focus is on enhancing both the redox activity and ion transport kinetics of $Ti_3C_2T_x$ for NH_4^+ storage. In this chapter, a superlattice-like heterostructure is constructed through electrostatic self-assembly between $Ti_3C_2T_x$ and a water-soluble n-type conjugated polyelectrolyte (CPE) p(cNDI-gT2). By systematically varying the CPE loading, the MXene interlayer spacing can
178

be expanded from 1.21 nm to 2.36 nm, while maintaining an ordered stacking pattern. This ordered structure not only increases interfacial contact between MXene and CPE for efficient electron transfer but also suppresses MXene restacking, thereby improving ion accessibility. At the optimal MXene: CPE mass ratio of 2:1, molecular dynamics simulations reveal a pseudo-bilayer CPE alignment within MXene's interlayer. This configuration creates abundant micropores with sizes (~3 Å) comparable to NH_4^+ ions, which may promote ion desolvation and thereby enhance the charge transfer. As a result, the Ti_3C_2:CPE 2:1 heterostructure demonstrated superior electrochemical performance, delivering a higher capacity of 126.1 C g^{-1} at 0.1 A g^{-1} with 81.5% retention at 10 A g^{-1} in 1 M NH_4Cl. Importantly, this work illustrates that fine-tuning MXene interlayer structure can affect the ion desolvation behavior and ion transport kinetics of NH_4^+ ions.

Chapters 4 and 5 investigate how the solvation structure of metallic cations influences their intercalation behavior in $Ti_3C_2T_x$ MXene through electrolyte design. In Chapter 4, we found that tailoring the solvation environment of Li^+ ions using molecular crowding electrolytes (MCEs) activates additional intercalation processes and enhances the electrochemical performance of $Ti_3C_2T_x$ MXene. By introducing polyethylene glycol (PEG) as a molecular crowding agent into 2 m LiTFSI aqueous electrolytes, the water activity is reduced and the solvation structure of Li^+ can be modified. This change in ion solvation resulted in the appearance of a new pair of redox peaks at -0.25 V and -0.05 V (vs. Ag) in CV, contributing approximately 25% additional capacitance compared to dilute aqueous electrolyte. Operando XRD result showed that this process was coupled with a sharp expansion of the interlayer spacing from 16.9 Å to 20.1 Å, attributed to the insertion of strongly solvated Li^+ species, possibly along with PEG-400. As the potential became more negative, a second intercalation stage occurred, involving less-solvated Li^+ ions and resulting in interlayer contraction to 15.4 Å. When PEG-400 was replaced with the bulkier PEG-8000, the sharp interlayer spacing expansion was no longer observed. However, the CV peaks persist, indicating that the altered solvation environment in the bulk electrolyte, rather than PEG co-intercalation, is primarily responsible for activating the additional intercalation step.

While employing MCE enables additional intercalation step and improves the capacitance, the high viscosity of the electrolyte impedes ion transport, therefore leads to worse rate capability. In chapter 5, acetonitrile (ACN) is introduced into aqueous $NaClO_4$ electrolytes as a low-viscosity co-solvent to modulate Na^+ solvation while preserving fast ion mobility. Similar to PEG-based molecular crowding electrolytes (MCEs), the introduction of ACN activated a distinct high-potential intercalation process in addition to the conventional low-potential insertion of partially desolvated ions. This behavior was evident from CV, where ACN-containing electrolytes displayed clear redox peaks compared to the nearly rectangular CVs seen in dilute aqueous systems. The shape and separation of these peaks vary with the

Summary

ACN ratio, reflecting differences in charge storage mechanisms. In the 75:25 H_2O:ACN electrolyte, broad peaks with large peak separation were observed, corresponding to the intercalation of less desolvated Na-H_2O clusters. This process led to a sharp interlayer expansion (~2.1 Å) during insertion but involved minimal charge transfer, as confirmed by operando UV-Vis spectroscopy. This behavior resembles the solvated-ion intercalation seen in PEG-based MCEs. In contrast, in 50:50 H_2O:ACN, the reduced Na^+-H_2O interaction promotes greater ion desolvation. At onset potential of the reduction peak, bare Na^+ ions intercalated, leading to a sharp interlayer contraction (~1.7 Å) and more symmetric CV peaks with smaller separation. This was accompanied by a clear shift in UV-Vis absorbance peak, indicating a pseudocapacitive charge storage mechanism. Together, these works underscore the importance of electrolyte design in optimizing both energy and power performance of MXene-based systems.

Chapter 6 explores the use of $Ti_3C_2T_x$ MXene as a self-freestanding current collector in anode-free aqueous zinc metal batteries (AZMBs), focusing on how electrolyte engineering modulates Zn deposition behavior through interfacial effects such as SEI formation. In a baseline $Zn(OTF)_2$ aqueous electrolyte, Zn deposition on $Ti_3C_2T_x$ was less reversible due to dendritic growth and side reactions. When 50 vol% propylene carbonate (PC) was introduced into the aqueous electrolyte, the altered ion solvation environment facilitated the formation of an organic-rich SEI. While this SEI layer helps reduce water-induced side reactions, it also increases interfacial charge-transfer resistance, limiting its ability to support efficient Zn^{2+} transport and prevent dendritic growth. In contrast, introducing Li-salts and PC as co-additive leads to the formation of a thin, ZnF_2-containing organic-inorganic hybrid SEI layer. This SEI enhanced interfacial ion transport kinetics, enabling uniform Zn deposition with suppressed dendrite formation. These findings highlight that the ion solvation structure, tuned via electrolyte formulation, plays a decisive role in determining the SEI chemistry and, consequently, the Zn deposition behavior on MXene.

Overall, this thesis demonstrates that ion solvation plays a critical role in governing the charge storage behavior of $Ti_3C_2T_x$ MXene in aqueous electrolytes. By optimizing the solvation environments, it is possible to control the solvation level of intercalated ions and the kinetics of intercalation, as well as the interfacial chemistry. Looking ahead, further performance improvements could be achieved by coupling electrolyte design with structural and chemical modifications of the MXene itself. In particular, surface terminations play a critical role in mediating ion-electrode interactions and could be engineered to promote desired intercalation or redox pathways. Additionally, controlling interlayer spacing through pre-intercalation or molecular pillars may enhance ion accessibility. Together, these strategies offer a promising roadmap toward the development of high-rate, high-capacitance MXene-based aqueous EES systems.

8 Samenvatting

Energieopslagsystemen op waterbasis staan bekend als veiliger en kostenefficiënter dan conventionele elektrochemische energieopslagsystemen die gebruikmaken van brandbare organische elektrolyten. Dankzij hun hoge ionische geleidbaarheid zijn deze waterbasis systemen bovendien geschikt voor toepassingen met een hoge vermogensdichtheid. In dit kader zijn MXenes, met name $Ti_3C_2T_x$, veelbelovende elektrode materialen vanwege hun hoge elektrische geleidbaarheid, hydrofiele oppervlak en regelbare interne laagafstanden die snelle ioneninterclatie ondersteunen. Afhankelijk van het elektrolyt kunnen MXenes lading opslaan via elektrochemische dubbellaagcapaciteit (EDL) of pseudocapacitieve mechanismen. De elektrochemische eigenschappen zijn nauw verbonden met hoe gesolvateerde ionen adsorberen aan het oppervlak, of intercaleren in de binnenste lagen van de MXene. Toch is de invloed van ionensolvatie op de ladingsopslag in elektrolyten op waterbasis nog onvoldoende begrepen.

Dit proefschrift vult deze kenniskloof door te onderzoeken hoe de solvatietoestand van verschillende ionen het intercalatie- en transportgedrag in $Ti_3C_2T_x$ MXene bepaalt. Hoofdstukken 2 en 3 richten zich op niet-metallische kationen, in het bijzonder op het duurzame ammoniumion (NH_4^+). In hoofdstuk 2 wordt onderzocht hoe solvatiestructuur het intercalatiegedrag beïnvloedt van NH_4^+ en een reeks tetraalkylammoniumionen (TMA⁺, TEA⁺, TPA⁺). Deze ionen verschillen in grootte en solvatiegraad en kunnen daardoor systematisch bestudeerd worden om de invloed van solvatie op de ladingsopslagmechanismen te achterhalen. Kleine, hydrofiele NH_4^+-ionen intercaleren in een gedeeltelijk gedesolvateerde toestand, waarbij ze waterstofbruggen vormen met oppervlaktegroepen van de MXene. Hun intercalatie veroorzaakt nauwelijks verandering in de interne laagafstand en vertoont EDL-achtig gedrag. Daarentegen kunnen de grotere, zwak gesolvateerde TAA⁺-ionen—ondanks hun gehydrateerde grootte die groter is dan de interne laagafstanden—reversibel worden geïntercaleerd met aanzienlijke co-insertie van water. Dit leidt tot duidelijke toename van de interne laagafstand (tot 20.7 Å) en laat bijbehorende zien pieken in cyclovoltammetrie. De contributie van intercalatie op de totale capaciteit neemt toe met de lengte van de alkyl groep, wat mogelijk correleert met de compactere hydratie van grote TAA kationen. De reversibele intercalatie van hydrofobe, zwak gesolvateerde niet-metallische kationen hangt waarschijnlijk af van de co-insertie van water om de MXene structuur te stabiliseren. Dit is in tegenstelling tot metaalionen, die normaal gesproken gedesolvateerd moeten zijn voor insertie mogelijk is.

In hoofdstuk 2, waar de reversibele intercalatie van het niet-metallische ammonium ion in $Ti_3C_2T_x$ MXene wordt beschreven, zijn de capaciteit en laadsnelheid zijn nog niet optimaal. Hoofdstuk 3 poogt deze knelpunten op te lossen door de redoxactiviteit en transport kinetiek van $Ti_3C_2T_x$ voor NH_4^+ opslag te verbeteren. Hiervoor is een superroosterachtige heterostructuur opgebouwd via elektrostatische zelfassemblage tussen $Ti_3C_2T_x$ en een

wateroplosbaar n-type geconjugeerd polyelektrolyt (CPE) (p(cNDI-gT2)). Door de verhouding tussen MXene en CPE te variëren, wordt de interne laagafstand vergroot van 1.21 nm tot 2.36 nm, met behoud van een geordende stapeling. Deze geordende structuur verbetert het contact tussen MXene en CPE, wat de elektronische geleidbaarheid ten goede komt. Ook wordt het herstapelen van MXene tegengegaan, wat het geheel meer toegankelijk maakt voor ionen. De optimale verhouding tussen MXene:CPE is 2:1. In dit systeem tonen simulaties aan dat er een pseudo-bilaag CPE structuur in de interne lagen van MXene wordt gevormd. Dit veroorzaakt microporiën (~3 Å), die goed overeenkomen met de grootte van NH_4^+-ionen en de desolvatie en ladingsoverdracht bevorderen. De Ti_3C_2:CPE 2:1 heterostructuur heeft een hoge capaciteit (126.1 C g^{-1} bij 0.1 A g^{-1}) en goede capaciteitsretentie (81.5% bij 10 A g^{-1}) in 1 M NH_4Cl, waarmee wordt aangetoond dat de aanpassing aan de interne laagafstanden de NH_4^+ ionentransportkinetiek en redoxactiviteit aanzienlijk beïnvloedt.

Hoofdstukken 4 en 5 richten zich op metaalionen (Li$^+$ en Na$^+$) en laten zien hoe het intercalatiegedrag in $Ti_3C_2T_x$ MXene wordt beïnvloed door de samenstelling van het elektrolyt. In hoofdstuk 4 wordt polyethyleenglycol (PEG) gebruikt om een moleculair crowding elektrolyt (MCE) te creëren met verlaagde wateractiviteit. Dit activeert een extra intercalatieproces en verbeterd de elektrochemische eigenschappen van $Ti_3C_2T_x$ MXene. Dit leidt tot gewijzigde solvatie van Li$^+$ en de opkomst van nieuwe redoxpieken rond -0.25 V en -0.05 V (vs. Ag) in cyclovoltammetrie, die ~25% extra capaciteit bijdragen vergeleken met het elektrolyt zonder PEG-400. Operando XRD toont aan dat deze pieken gepaard gaan met een plotselinge vergroting van de interne laagafstand van 16.9 Å naar 20.1 Å, veroorzaakt door de intercalatie van sterk gesolvateerde Li$^+$ (mogelijk samen met PEG-400). Bij verdere verlaging van de potentiaal vindt een tweede intercalatiestap plaats met minder gesolvateerde Li$^+$ en krimpt de interne laagafstand tot 15.4 Å. Het gebruik van PEG-8000 in plaats van PEG-400 elimineert deze zwelling, maar niet de redoxactiviteit, wat erop wijst dat de veranderde solvatie in de bulk van het elektrolyt verantwoordelijk is voor het ontstaan van de extra intercalatiestap.

Het gebruik van MCEs geeft een extra intercalatiestap, en verbeterd de capaciteit. Echter, de hoge viscositeit van het elektrolyt hindert ion transport en de laadsnelheid. In hoofdstuk 5 wordt acetonitril (ACN) geïntroduceerd als co-oplosmiddel in $NaClO_4$-oplossingen om de viskeuze MCE's te vermijden en toch het intercalatiegedrag te verbeteren met hoge ionische mobiliteit. Net als bij PEG activeert ACN een extra intercalatieproces op hoge potentialen, bovenop de gebruikelijke intercalatie van gedeeltelijk gedesolvateerde ionen op lage potentiaal. Dit blijkt uit scherpe redoxpieken in de CV, die niet zichtbaar zijn in de systemen zonder ACN. De vorm en afstand tussen de pieken hangt af van de verhouding tussen ACN:H_2O, wat verschillen in het ladingsopslagmechanisme suggereert. Bij 75:25 H_2O:ACN worden brede pieken die ver uit elkaar liggen waargenomen, corresponderend met

intercalatie van minder gesolvateerde Na^+-H_2O complexen. Dit proces leidde tot een grote toename van de interne laagafstand van ~2.1 Å, maar operando UV-Vis spectroscopie wees uit dat er bijna geen ladingsoverdracht plaatsvond. Dit gedrag doet denken aan de intercalatie van gesolvateerde ionen, zoals dat in MCEs op PEG basis. In 50:50 H_2O:ACN neemt de solvatie af doordat Na^+ minder interactie heeft met H_2O. Na^+ ionen intercaleerden op de beginpotentiaal van de reductiepiek, wat zorgde voor een snelle contractie van de interne laagafstand (~1.7 Å). De reductiepieken stonden dichter bij elkaar en waren meer symmetrisch. Dit viel samen met een duidelijke verschuiving in de UV-Vis absorptie piek, wat duidt op een pseudocapacitief ladingsopslagmechanisme. Deze hoofdstukken laten zien hoe belangrijk het ontwerp van elektrolyten is, om de energie- en vermogensdichtheid van MXene systemen te optimaliseren.

Hoofdstuk 6 behandelt het gebruik van $Ti_3C_2T_x$ als zelfstaande stroomcollector in anodeloze zinkmetaalbatterijen op waterbasis (AZMB's). Er wordt onderzocht hoe de samenstelling van het elektrolyt invloed heeft op de depositie van Zn door oppervlakte-effecten zoals SEI groei. In standaard $Zn(OTF)_2$-oplossingen leidt zinkdepositie op $Ti_3C_2T_x$ tot dendrietgroei en beperkte reversibiliteit door nevenreacties. Toevoeging van 50% propyleencarbonaat (PC) verandert de solvatie van Zn^{2+}, wat de groei van een organisch SEI bevordert. Dit SEI remt de nevenreacties met water, maar het verhoogt ook de ladingsoverdrachtsweerstand op het oppervlak. Hierdoor kan de dendrietgroei niet effectief worden geremd, en het Zn^{2+} transport is niet efficiënt. Als er ook nog lithiumzouten bij worden gevoegd als een co-additief, wordt een dun ZnF_2-rijk anorganisch hybride SEI gevormd. Dit SEI verbeterd de oppervlaktekinetiek van Zn^{2+} ionen, en faciliteert uniforme zinkdepositie waar dendrietgroei geremd wordt. Deze resultaten laten zien dat de ionsolvatie, aangepast door elektrolytontwerp, een cruciale rol speelt in de samenstelling van het SEI en daardoor de depositie van Zn op MXene.

Samenvattend toont dit proefschrift aan dat de solvatie van ionen een fundamentele rol speelt in de ladingopslag van $Ti_3C_2T_x$ MXene in elektrolyten op waterbasis. Optimalisatie van de solvatie maakt het mogelijk om de solvatiegraad van geïntercaleerde ionen te bepalen, evenals de kinetiek en oppervlaktechemie. In de toekomst kunnen verdere verbeteringen worden behaald door elektrolyt ontwerp te combineren met aanpassingen aan de structuur en chemie van MXene. Vooral de oppervlaktegroepen bepalen de interactie tussen de electrode en het ion, en zouden kunnen worden ontworpen om de gewenste redox reactie te faciliteren. Ook kan de interne laagafstand worden geoptimaliseerd om ionen toe te laten door pre-intercalatie of moleculaire pilaren. Deze strategieën vormen een stappenplan om snelle, energiedichte MXene energieopslagsystemen op waterbasis te ontwikkele.

Acknowledgement

help. On days when the weather is pleasant, we would sometimes go out together for walks, and those moments have been a well balance to the challenges of research life. Her hard work, passion for science, patience, and encouragement have been a constant source of motivation for me. I could not have asked for a better supervisor, colleague, and friend.

I would also like to thank Dr. Lars Bannenberg, for his generous help with XPS measurements, data analysis, as well as for sharing his deep knowledge of the physical principles behind characterization techniques. I have greatly benefited from his encouragement that helped me gain confidence. His valuable suggestions whenever I felt uncertain, and kind reminders to maintain a healthy work-life balance, have been truly appreciated. Next, I would like to extend my sincere thanks to Dr. Swapna Ganapathy for her guidance with NMR measurements and data analysis. She patiently showed me how to operate the NMR instrument, interpret spectra, and troubleshoot issues along the way. Her deep knowledge, combined with an approachable and easy-going manner, made the learning process both efficient and enjoyable. I have always appreciated her willingness to help whenever I had questions, as well as her strong sense of responsibility in ensuring that experiments were conducted with precision. I am also grateful to Dr. Alex Vasileiadisand Dr. Erik Kelder who I had the pleasure of working with as a teaching assistant for the battery course. From them, I learned how to communicate complex concepts clearly, and approach teaching with patience and enthusiasm.

My heartfelt gratitude also goes to our outstanding supporting team: Frans, Esther, Katarina, Nirmal, Dan, Michael, Jouke, and Robert, for their invaluable contributions to my research and to Martine, Ilse, and Nicole for their help with contracts and daily administrative matters. Frans was particularly supportive during my first few weeks in the Netherlands, when my spoken English was still far from fluent, he somehow managed to understand exactly what I wanted to say, often before I even finished a sentence. We faced numerous challenges together while setting up the tube furnaces and other equipment for the new lab. I will never forget the excitement of synthesizing my first batch of MXene on December 18, a milestone that would not have been possible without his tireless assistance in the lab. Katarina, as the area supervisor of the HF lab, ensured that all safety procedures were strictly followed, making HF-based synthesis possible in the first place. Her sense of responsibility, patience, and exceptional organizational skills from ordering supplies to keeping the lab running smoothly have been instrumental in enabling my experiments. While Dan and Nirmal always kindly helped me with daily lab work and troubleshot the equipment whenever I needed.

I would also like to thank my collaborators, Benjamin, Glenn, Ricardo, Jaehoon, Chengzhi, Ruipeng, Hongjun, Dingding, Xiaoyang, for their invaluable contributions to my research work and the insightful discussions we shared, as well as Dr. Simon Fleischmann, Dr. Weiwei

with whom I have shared many enjoyable moments. I truly appreciate their accompany and the warmth they brought into my life along the way.

Last but not least, I owe my deepest thanks to my parents, my brother, and my best friend Li, who have always encouraged and supported me and to dear "little sheep". A tree does not see its roots, yet all its strength and growth come from them. The people who have surrounded me, my family, my friends, my mentors, and my colleagues, are my roots. To all of you, you are the power that allows me to face life's uncertainties with courage and gratitude.

Publication list

Publication lists as the first author (2021-2025)

1. Enhancing Zn Deposition Reversibility on MXene Current Collectors by Forming ZnF_2-Containing Solid-Electrolyte Interphase for Anode-Free Zinc Metal Batteries. Small. 2025, 2407226.

2. High-rate polymeric redox in MXene-based superlattice-like heterostructure for ammonium ion storage. Advanced Energy Materials. 2024, 2402715.

3. Enhancing pseudocapacitive intercalation in $Ti_3C_2T_x$ MXene with molecular crowding electrolytes. 2D Materials. 2024, 11, 015001.

4. (co-first author) Acidic "Water-in-salt" Electrolyte Enables High Energy Symmetric Supercapacitor Based on Titanium Carbide MXene. ACS Appl. Mater. Interfaces. 2024, 16(41), 55189–55197.

5. (co-first author) Interfacial Designs of MXenes for Mild Aqueous Zinc-Ion Storage. Small Methods. 2023, 7, 2201683.

6. Ion intercalation process in MXene pseudocapacitors with aqueous and non-aqueous electrolytes. Encyclopedia of Materials: Electronics. 2023, 237-249. (Book chapter)

7. Solvation Structure Engineering with Co-Solvents Enables Tunable Charge Storage Mechanisms in MXenes. Energy Storage Materials. (Under revision)

Curriculum Vitae

Chaofan Chen was born on June 3, 1998, in Henan Province, China. She started her undergraduate studies in Applied Physics at Jilin University in 2014 and received her Bachelor's degree in 2018. That same year, she began her Master program in Condensed Matter Physics at Jilin University. Her research focused on the synthesis and electrochemical energy storage applications of Two-dimensional Vanadium Carbides (MXenes), under the supervision of Prof. Yury Gogotsi, Dr. Yu Gao and Dr. Yohan Dall'agnese.

Supported by the China Scholarship Council (CSC), she began her PhD studies from October 2021 in the department of Radiation Science and technology at Delft University of Technology. Her study is conducted in the Storage of Electrochemical Energy (SEE) group under the supervision of Prof. dr. ir. Marnix Wagemaker and Dr. Xuehang Wang. The focus of her research is on understanding the influence of ion solvation on the charge storage behavior of Titanium Carbides MXene material in different energy storage systems, such as supercapacitors and zinc-ion batteries.